Spring 2019

Role of Size, Concentration, and Natural Organic Matter on the Fate, Behavior, and Toxicity of Nanoparticle in Aquatic Environment

Mithun Sikder

ROLE OF SIZE, CONCENTRATION, AND NATURAL ORGANIC MATTER ON THE FATE, BEHAVIOR, AND TOXICITY OF NANOPARTICLE IN AQUATIC ENVIRONMENT

by

Mithun Sikder

Bachelor of Science
Bangladesh University of Engineering & Technology, 2012

Master of Science
University of Nottingham, 2013

Submitted in Partial Fulfillment of the Requirements

For the Degree of Doctor of Philosophy in

Environmental Health Sciences

The Norman J. Arnold School of Public Health

University of South Carolina

2019

Accepted by:

Mohammed Baalousha, Major Professor

George T. Chandler, Committee Member

Jamie R. Lead, Committee Member

Bo Cai, Committee Member

Cheryl L. Addy, Vice Provost and Dean of the Graduate School

DEDICATION

To my family, friends, and colleagues for their endless support, and to those who might read this dissertation and use this for the development of science.

ACKNOWLEDGEMENTS

It would have been impossible for me to complete this thesis without support and help of many outstanding people in my family, at the University of South Carolina, and those whom I met along the way. First, I would like to thank my advisor, Dr. Mohammed Baalousha for giving me the opportunity to attempt and finally finish this degree. Without Mohammed's support and guidance, it would have been exceedingly difficult to complete this degree. I also want to thank my co-advisor, Dr. G. Thomas Chandler. Despite his busy schedule as the dean of Arnold School of Public Health, his door was always open for me. He played an instrumental role in this thesis and taught me about toxicological assays from scratch. I would like to thank Dr. Jamie Lead, whose input through questions and suggestions after a seminar/presentation helped me to think critically. I would like to convey my gratitude to Dr. Bo Cai, as I was always able to stop by his office and talk about statistical problems I faced throughout this journey. I would like to thank Dr. Marie N. Croteau, Dr. Brett Poulin, and David Barasch at USGS, who helped me a lot in Summer-2017 during my research internship at the USGS. Special thanks to Emily Eudy and Mark Losavio, who helped me with the copepod assays. I am also grateful to all my colleagues in CENR for their continued support, encouragement, and collaboration. Finally, a big thanks to my wife, who has been there to support me through some of my most difficult hurdles outside of this degree and she has been nothing but helpful.

ABSTRACT

Understanding the impact of engineered nanoparticles (ENPs) physicochemical properties such as size, surface coating and concentration; and environmental factors such as ionic strength, media composition and natural organic matter (NOM) on NP fate, behavior, and toxicity is crucial for ENP risk assessment. Thus, the overall aim of this dissertation is to evaluate the effects of ENP properties and water chemistry on the behavior, bioavailability, and toxicity of AgNPs and PtNPs.

The aggregation behavior of PtNPs was typical of Derjaguin, Landau, Verwey, and Overbeek (DLVO) type aggregation and the critical coagulation concentration of PtNPs was independent of particle size. PtNPs aggregate size increased with increases in NP concentration and with decreases in PtNP primary particle size in moderately hard water (MHW) and synthetic seawater. NOM enhanced the aggregation of 20 nm PtNPs ($PtNP_{20}$) in MHW due to the bridging of NOM-coated PtNPs by divalent counterions but had no effect on the aggregation of 95 nm PtNPs ($PtNP_{95}$). $PtNP_{20}$ aggregate size increased with the increase in NOM elemental ratio of H to C and the relative abundance of lignin formulae. However, $PtNP_{20}$ aggregate size decreased with the increase in NOM molecular weight, $SUVA_{254}$, elemental ratio of O to C, and the relative abundance of condensed hydrocarbon and tannin. Whereas PtNPs did not undergo significant dissolution (i.e., < 15% after 24 h) in synthetic seawater regardless of the NP exposure concentration; AgNPs dissolved faster and to a greater extent with the decrease in NP concentration. This finding

suggests that NP aggregation became less significant and NP dissolution became more dominant at lower concentrations.

PtNP influx rate constant (k_{uw}) in *Lymnaea stagnalis* decreased with decreases in PtNP size, possibly due to increased aggregation with the decrease in PtNP size. NOM did not have a significant impact on the bioavailability of $PtNP_{20}$ but suppressed the bioavailability of $PtNP_{95}$. The bioavailability of $PtNP_{95}$ increased by 6-fold (from k_{uw}= 0.075±0.05 to 0.456±0.037 L g^{-1} D^{-1}) with the increase in NOM sulfur content. Reduced sulfur (S_{red}) content - in form of exocyclic and heterocyclic reduced sulfur- in the NOMs exhibited a strong positive correlation with k_{uw}, which was attributed to the higher affinity of reduced S to PtNPs relative to the oxidized S.

A concentration dependent increase in *Amphiascus tenuiremis* mortality was observed in AgNPs and dissolved Ag exposures, at environmentally relevant sub-lethal concentrations (i.e., 20-75 µg L^{-1}). A sharp decline of 1.8-7 folds in the reproduction (i.e., fecundity) were observed in the $AgNO_3$ exposure, whereas, fecundity was not impacted by the AgNPs exposure. Slower release of dissolved Ag from AgNPs and/or reduced Ag uptake in the nano form attributed these sharp contrasts in responses.

Overall, the results suggest that the NP's physio-chemical properties, water chemistry, and NOM compositions are key factors that contribute to the behavior, transformation, bioavailability, and toxicity of metallic NPs in the aquatic environment. Hence, scientists, regulators, and policy makers should carefully consider NP colloidal stability, NP concentration, and NP-NOM interactions while assessing the risk of released NPs from consumer products.

TABLE OF CONTENTS

LIST OF TABLES

LIST OF FIGURES

CHAPTER 1

INTRODUCTION

1.1. Nanoparticles and the environment

Engineered nanoparticle (NP) are generally defined as any particle with at least one dimension between 1-100 nm [1]. At this scale, materials exhibit unique and novel properties (e.g., mechanical, optical, reactivity *etc.*) relative to their bulk material and dissolved counterparts [2]. NP vary widely in their composition and include metal or metal oxide based NPs (*e.g.*, Ag, Au, Pt, TiO_2, CuO etc.), carbon based NPs (e.g., fullerenes, carbon nanotubes etc.), and composite NP (*e.g.*, bimetallic, core-shell NP etc.) [3].

Metal and metal oxide NPs have been widely used in consumer products (e.g., clothes, cosmetics *etc.*) [4-7], food packaging [8], medicine [9, 10], and environmental remediation [11, 12] based on the NP composition, size, and coating [3, 13-17]. AgNPs are widely used because of their antimicrobial properties and they could be found in textiles, wound dressing, soaps, personal care products, and plastic-based medical equipment [18]. TiO_2 and ZnO are generally used because of their photocatalytic properties and found in sunscreens, solar cells, paints, and product packaging [19-21]. CeO_2 is used as a fuel additive to boost the combustion of fuel in diesel engine [22], while PtNPs are used as catalyst in vehicle's catalytic convertor that reduce pollutants in the exhaust [23]. AuNPs are used as seeds for creating other composite NPs and are used to increase drug delivery efficacy [24, 25]. The use of NPs in consumer products is predicted to increase as new and novel uses of these NPs are being discovered. According to the Nanotechnology Consumer Products Inventory, the number of nano-enabled products increased from 50 to nearly 2000 products in past decade [26]. Disposal of nano-enabled products at the end of their life creates scenarios where these NPs may potentially be released in the environment and human systems. Hence, NPs are listed as emerging contaminants of environmental concerns (CEC) [27] and there is imminent

need for in-depth understanding of NPs' environmental and biological interactions. Understanding the environmental fate, transformation, and behavior of NPs is a research priority not only for the fundamental understanding of the NPs, but also for the regulatory purpose to protect environmental public health. This dissertation focuses specifically on metallic NPs (e.g., Ag and Pt) because of their greater potential environmental risk compared to other types of nanomaterials due to their elevated, and thus their release, use compared to other materials [13, 17].

1.2. Silver nanoparticles' application and release

Silver nanoparticles (AgNPs) are the most widely used NPs in consumer products due to their antimicrobial, electrical, and optical properties [18]. Several studies reported Ag release from nano-enabled products including fabrics [28], paints [29], building facades [30], and plastic food containers [31]. The use of AgNPs in a high number of consumer products will likely result in increased AgNPs release, and thus concentration, in the environment, which may pose potential risk to environment and human health [2]. In wastewater treatment plants (WTP) employing activated sludge for treatment, probabilistic flow modeling suggest that NPs will partition into the sludge phase. A small fraction might remain in aqueous phase after treatment and will be released in WTP effluent [32, 33]. of AgNPs are in range of 0.01-0.1 ng L^{-1} in surface water and 1.6 mg Kg^{-1} in sludge [32, 33]. Despite the low PEC (ng L^{-1} to μg L^{-1}) of AgNPs in different environmental media, environmental loadings are likely to increase with time as AgNPs use increases.

Despite the low PEC of AgNPs, most studies have focused on evaluating the fate and behavior of AgNPs at relatively high concentrations (*ca.* mg L^{-1}) [34-42]. This is mainly because of the high detection limit of the popular analytical techniques (e.g., dynamic light

scattering (DLS), Ultraviolet visual spectroscopy (UV-vis) etc.) typically used to investigate the AgNPs behavior [43]. In environmental and biological media, AgNPs undergo numerous transformations; among others, aggregation, and dissolution are the key processes which determine AgNPs fate, behavior and effects [44, 45]. Several studies investigated the transformations of AgNPs under variety of experimental conditions [34, 35, 42, 46-50]. These studies demonstrated that transformations (e.g., dissolution and aggregation) of AgNPs depends on their physicochemical properties (e.g., size, shape, surface coatings etc.), concentration [51], aggregation [52-54] and the characteristics of surrounding media (e.g., pH, temperature, presence of natural organic matter, and ligand type and concentration, *etc.*) [55]. However, most studies were performed at relatively high NP concentrations (*ca.* mg L^{-1}) [56, 57] using different analytical techniques, complicating direct comparison between the measured aggregation and/or dissolution rates. Hence, there is a need to (re)evaluate the transformations and behaviors of AgNPs at low environmentally relevant concentrations.

1.3. Platinum nanoparticles' application and release

The global production of platinum group elements (PGE) has grown steadily since 1970, and the global production of platinum (Pt) alone increased to 190 tons with an annual demand of 257 tons in 2016 [58]. The main use of Pt is in the catalytic convertors of cars, trucks, and buses, accounting for approximately 50% of Pt demand each year. Mandatory installation of catalytic convertors in motor vehicles reduced the emission of harmful exhaust emissions (e.g., carbon monoxide, nitrogen and sulfur oxides, hydrocarbons, aldehydes, and heavy metals etc.) [59, 60], but it resulted in an increased release of PGE (i.e., Pt, Pd, Rh, Ru, Os and Ir) to the environment [61], and some studies demonstrated the release

of Pt in the form of nanoparticles (PtNPs) [62, 63]. The concentration of Pt in environmental samples, such as road dust, soil, surface water, sediments and plants has increased significantly in recent decades [64-68]. The concentration of Pt in aquatic ecosystems (0.4-10.8 ng-Pt L^{-1}) is relatively low compared to their concentration in the immediate vicinity of roads (50 ng-Pt g^{-1} of road dust) [60]. Even higher Pt concentration (> 300 µg g^{-1}) has been reported in Mexico city road dust [66]. Additionally, Pt complexes (e.g., cisplatin, carboplatin) are used for cancer treatment [69], and PtNPs have shown promise in this use [9]. The majority of drugs containing Pt complexes are excreted in patients' urine (about 70%) and enter wastewater systems [61]. Treatment removal methods for these active compounds are lacking which contributes to environmental Pt contamination [61, 70].

Despite of PtNPs application in different commodities the release of PtNPs into the environment, and reported toxicity of Pt and/or PtNPs to aquatic organisms [71], freshwater oligochaetes [72], freshwater microalgae [73], and marine [74], very little is known about the environmental behaviors of PtNPs such as aggregation and dissolution in environmental media. Understanding the nature of exposure and the transformations of PtNPs' physiochemical properties during toxicology exposures is essential to interpret and quantify any dose-response relationships. These transformations, which are likely to occur in toxicological media during acute to chronic exposure periods, have been investigated extensively for other NPs (e.g., AgNPs, AuNPs, CeO_2-NPs etc.) [75-77], but not for PtNPs. According to previous studies (with other NPs), aggregation and/or dissolution can significantly alter NP behavior (e.g., dosimetry, uptake, toxicity) and fate (e.g., pharmacokinetics, bioavailability, and biodistribution) [78-80]. Hence, there is a need to understand the aggregation and/or dissolution behavior of PtNPs in different environmental

media, at low concentrations and evaluate the subsequent uptake, bioaccumulation, and toxicity.

1.4. Natural organic matter and interaction with nanoparticles

Natural organic matter (NOM) is ubiquitous in the environment with concentrations in the range of 0.1 to 10 mg-C L^{-1}, depending on biochemical and climatic conditions [81, 82]. NOM is a complex mixture of polyelectrolytic and polyfunctional organic molecules (e.g., polysaccharides, proteins, lipids, nucleic acids, and fulvic and humic substances) [83, 84] that vary spatially and temporally in terms of molecular composition, acidity, molecular weight, structure, and charge density [85]. Adsorption of natural organic matter (NOM) on NP surfaces results in formation of a surface coating (i.e., NOM-corona). NOM-corona is the primary interface that determines NP environmental *(*e.g., *aggregation, dissolution, and sulfidation)* and biological interactions (e.g., bioavailability and toxicity). The widely diverse composition and properties of NOM will significantly impact the molecular composition of NOM-corona, thereby influencing NPs fate, behavior, bioavailability and toxicity.

Adsorption of NOM on NPs [86] results in the formation of NOM-corona [87], giving NPs unique surface identity. This unique surface identity is determined by the ligands that interact with the NP surface with the highest affinity for adsorption [88]. The molecular composition of NOM-corona is determined by the competitive sorption of NOM molecules on the NP surface. The composition of NP NOM-corona depends on: **1)** NP properties such as composition, size, surface charge, and functional groups [89], **2)** NOM properties such as composition, hydrophobicity, charge, and functional groups [90], and **3)** water chemistry such as pH, ionic strength and ionic composition. Furthermore, NOM-NP interactions can be

driven by one of the following mechanisms: **1)** electrostatic interactions, **2)** hydrophobic interactions, **3)** hydrogen bonding, **4)** cation bridging, **5)** ligand exchange-surface complexation, and **6)** chelation (**Figure 1.1**) [91-93]. In most systems, a combination of several interactions describes the complex behavior of NOM. Thus, there an imminent need for in-depth investigation of the molecular composition of NOM-corona formed on the surface of NPs via sorption of NOM, having different properties and subsequent fate, behavior, and bioavailability.

1.5. Environmental transformations of nanoparticles

The environmental fate and behavior of NPs are determined by physical, chemical, and biological transformation of NPs as described in Figure 1.2 [44]. Physical factor include formation, replacement, or degradation of surface coating, dispersion, advection, aggregation, disaggregation, deposition, and re-suspension [2, 17 44, 94]. Chemical factors include dissolution, complexation with other chemicals, redox reactions, sulfidation, and phase transformations [2, 17, 45, 95]. Biological factors include degradation of the capping agent or phase transformations [45]. Interaction between NP and NOM also affects the transformations, fate, bioavailability, and toxicity of NP by altering their surface properties, and reactivity [96-99].

1.5.1. Effect of NP intrinsic properties on transformations

Transformations (e.g., Aggregation and dissolution) of NP depend on nanoparticle's intrinsic properties (e.g., NP size, shape, surface charge, concentration etc.) [45]. Currently there is a limited and often contradictory knowledge on the effect of intrinsic properties of NP (on the aggregation of NPs. For instance, recent studies reported

contradictory results on the dependence of critical coagulation concentration (CCC), the minimum counterion concentration required to fully destabilize the dispersion [100], on NP size. Results from previous studies include a decrease in CCC with a decrease in NP size (e.g., hematite [101], TiO_2 [102]), with an increase in NP size (*e.g.* CdSe NP [103]), and an independence of CCC of NP size (e.g., AuNPs [104], AgNPs [94], PtNPs [105]). In addition, some studies reported a linear correlation between the CCC and NP size (e.g., anatase TiO_2 [102]), others found that the CCC better correlated with NP specific area (e.g., TiO_2 [102], CdSe NP [103]), and another study reported no correlation between CCC and NP size and/or surface area in presence of monovalent and divalent electrolytes (e.g., PtNP [105]). Previous studies also reported the important role of stabilizing agent [103], impurities introduced during synthesis process [106] on NPs aggregation. However, a systematic approach to evaluate the role of NP intrinsic properties on NP aggregation is lacking.

Although the concentration of NPs does not influence the sticking efficiency (slow/fast aggregation rates), the decrease in NP concentration results in lower collision frequency, and the formation of smaller NP aggregates [107]. Additionally, at lower concentrations, NPs (e.g., AgNPs) are more susceptible to dissolution [51]. The concentration-dependent behaviors (e.g., aggregation and dissolution) of NPs are critical as they are likely to determine the fate and transport of NPs in the environmental media. For instance, smaller aggregates are known to remain in suspension, travel for long distances. At higher concentrations, NPs forms larger aggregates and are more prone to sedimentation. In contrast, at lower concentrations, increased dissolution of NPs will complicate the assessment of NP-specific toxicity and may result in a wide spread of NP byproduct (e.g., dissolved ions) [108]. Studies investigating NP transformation, fate, and

effects at environmentally relevant low concentrations are scarce in the literature, and further research is required to fill this knowledge gap.

1.5.2. Effect of media chemistry on transformations

The physiochemical properties of media – such as ionic strength, counter-ion concentration and valency, type of counter-ions, and pH – are key determinant of NP aggregation and dissolution [34, 35, 42, 45-50, 55, 94]. The increase in media ionic strength increases NP aggregation [109]. Multivalent electrolytes are more efficient in destabilizing NP suspension compared to monovalent electrolytes according to Schulze-Hardy rule [110]. Although buffers are used to maintain a constant pH in the suspension, but their presence can result in substantial changes in NP surface chemistry [111] and stability [112]. Dissolution is a key environmental transformation process that may determine the effects of NPs (i.e., AgNPs) in the environment and within the organisms. Liu et al. (2010) concluded that silver ion (Ag^+) released from AgNPs is a cooperative oxidation process requiring both protons and dissolved O_2 [49]. The effects of dissolved O_2, pH, ionic strength, chloride and ammonia content, and salinity on the dissolution of AgNPs are well documented in the literature [35, 49, 113-115]. Additionally, aggregation was found to become an important factor controlling silver release in natural surface water [35]. Unlike AgNPs, PtNPs are resistant to oxidative dissolution and release of dissolved Pt ions and present at low natural background concentration. Although Pt exhibit significant effects on aquatic organisms [71-74, 116], little is known about PtNP transformation in different environmental media, especially at environmentally relevant low concentrations.

1.5.3. Effect of NOM on NP transformations

NOM can act as a competitor to displace intentional engineered coatings (*e.g.*, citrate, PVP) on NPs. For instance, NOM molecules (i.e., both HA and FA) were reported to displace citrate coatings from the surfaces of AgNPs [117] and AuNPs [118] due to the higher affinity of NOM molecules to NP surfaces. Likewise, cysteine can replace a PVP coating on AgNPs via strong chemical interaction (thiolate bonding) [119] and possibly reduce environmental bioavailability.

NOM enhances NP stability by enhancing NP electrostatic repulsion and/or steric hindrance [120-122]. Also, the introduction of NOM to aggregated NPs may lead to disaggregation [122]. The role of NOM in aggregating/disaggregating NPs depends on the physicochemical properties of NOM such as charge density, functional groups, and molecular weight [123]. For instance, higher molecular weight NOM increases the stability of AuNPs due to increased electrosteric repulsion [123-126]. Another study demonstrated that aggregation of ZnS NPs decreased with increasing NOM concentration, molecular weight, and aromatic content of NOM fractions, while carboxylate and reduced sulfur had little effect [127].

The literature presents conflicting results regarding NOM effect on NP (*e.g.*, Ag, Cu and ZnO) dissolution. Some studies reported that Suwannee River humic acid (SRHA) and fulvic acid (SRFA) did not affect AgNP dissolution [128], while other studies reported suppression of AgNP dissolution by SRHA and SRFA [129]. Similarly, whereas one study reported that Pony Lake fulvic acid (PLFA) decreased AgNP dissolution due to PLFA's sulfur and nitrogen content [128], others reported that PLFA increased AgNP dissolution [130]. Furthermore, NOM has been shown to enhance the dissolution of other NPs such as ZnO

[131] and Cu [132], due to complexation between Zn^{2+} and Cu^{2+}, and NOM functional groups. These variable results likely can be attributed to differences in the molecular composition of the studied NOMs [128]. Thus, to explain the discrepancies of NOM effects on NP environmental behaviors, there is a critical need for **1)** studying NOM:NP interactions over a library of NOMs having a wide range of properties compared to the few NOMs that have been studied to date, and **2)** molecular-level characterizations of NOM and NOM-corona.

1.6. Nanotoxicity

Toxicity testing for NPs initially focused on establishing toxicity tests that relate nominal dose to observed effects. These effects vary based on particle type, exposure concentration, test media, and organism type [133] with reported effects ranged from mortality [134] to change swimming behavior [135], reproduction [136] or no toxicity at all [133]. Despite the abundance of reported toxicity data, toxicity evaluation of NPs has been overwhelmed by a number of issues specific to NPs, such as general inability to maintain exposure dose over the course of the test and co-toxicity of carrier solvents [133, 137]. Dose changes observed in a test can be caused by NP aggregation, dissolution, sulfidation or a combination of all these processes [138]. To overcome this variable nature of organism dose, researchers started to perform static renewal tests to continually maintain the desired dose and include dissolved fraction controls to elucidate potential dissolution based effects of NPs during exposure testing [108, 136, 139]. Moreover, majority of previous studies employed high NPs concentrations (e.g., mg L^{-1}) with far less than lifecycle exposure times for most multicellular models. However, few studies have measured chronic toxicity under lower concentrations (e.g., µg L^{-1}) for AgNPs [108] and other NPs [140-142]. Another fundamental question driving toxicity testing for metal NPs is whether the metallic NPs are more or less

toxic and bioaccumulate than their simple mass equivalent dissolved fractions. This type of experimental setting is required for NPs where dissolution is possible (i.e., AgNPs). Hence, comparative toxicity and/or accumulation study of metal NPs and equivalent dissolved fractions with a NP (e.g., PtNPs), that shows no or minimum dissolution in exposure media, is required to tackle this challenge.

Natural organic matter (NOM) can significantly impact NP bioavailability and toxicity to aquatic organisms by altering NP dissolution, aggregation, and sedimentation. The role of NOM on NP bioavailability and toxicity is complex; *i.e.*, even for the same type of NPs, enhanced [96], mitigated [97, 98] and non-significant effects [99] have been observed. For instance, uptake of PVP-AgNPs by a freshwater gastropod was either increased or not strongly affected in the presence of 1-10 mg L^{-1} SRHA. In contrast, cysteine substantially reduced PVP-AgNP uptake [143]. This was attributed to the fact that humic substances contain relatively few strong ligands for Ag^{+}, whereas cysteine is rich in thiol groups with high affinity for Ag^{+}. Similarly, PLFA mitigated AgNPs toxicity to the nematode *Caenorhabditis elegans* more effectively than SRFA [144], which was attributed to the higher metal binding capacity of PLFA compared to SRFA due to compositional differences between these two NOMs. PLFA has higher N and S content (6.5% N, 3.0% S) than SRFA (0.72% N, 0.44 % S), suggesting that PLFA has a higher percentage of amine ligands and reduced sulfur groups that provide more binding sites for Ag^{+} and AgNPs surfaces [145, 146]. Tannic acid (TA) has also been shown to reduce ZnO toxicity more efficiently than FA and HA by reducing bioavailability of free Zn^{2+} in aqueous media [147]. This is because TA has the highest complexation ability among tested NOMs due to formation of stable TA-Zn^{2+} complexes with the highly concentrated O-diphenol groups on the TA surface. These

differences in the role of NOM in NP uptake and toxicity may be due to differences in NOM molecular composition and consequently NOM-corona molecular composition; and schematic approach to evaluate both is highly required.

1.7. Dissertation organization

The environmental behavior and effects of NPs at environmentally relevant concentration are not yet fully understood. In particular, the role of NP's physiochemical properties (e.g., particle size, capping agent etc.) and environmental condition (e.g., NP concentration, presence of NOM, interaction with NOM etc.) on NPs behavior (i.e., aggregation, dissolution etc.), fate (i.e., bioavailability), and toxicity is not fully understood yet. Therefore, the aim of this dissertation is to investigate the effects of NP properties (i.e., particle size, NP concentration) and media compositions (i.e., Chloride concentrations, NOM composition, and NOM-NP interaction) on nanoparticle aggregation, dissolution, bioavailability, bioaccumulation, and toxicity. This dissertation is organized into seven chapters.

Chapter 1 provides a general overview of NP characterization, environmental fate and effect. It also includes the overall research goals of this work and overall dissertation organization.

Chapter 2 describes the synthesis, characterization, and dissolution behavior of polyvinylpyrrolidone coated silver nanoparticles (PVP-AgNPs) in synthetic seawater (SW).

Chapter 3 reports a reproducible protocol for the synthesis of citrate- and PVP-coated PtNPs of five different sizes (i.e., 20, 30, 50, 75, and 95 nm), together with the characterization of their properties and environmental behaviors in relevant biological and

toxicological media using a multimethod approach including DLS, UV-vis, TEM, AFM, sp-ICP-MS, and FFF.

Chapter 4 investigates the life-cycle chronic toxicity of sublethal exposures of PVP-AgNPs relative to a dissolved silver nitrate ($AgNO_3$) for the estuarine meiobenthic copepod, *Amphiascus tenuiremis*, over a range of environmentally relevant concentrations (i.e., 20, 30, 45, and 75 µg-Ag L^{-1}).

Chapter 5 investigates the role of NP size and NOM composition on the colloidal stability of PtNPs in MHW using PtNPs of five different sizes of PtNPs (i.e., 20, 30, 50, 75, and 95 nm) and six different NOM fractions, isolated from surface waters.

Chapter 6 investigates the influence of PtNP size and NOM composition on the bioavailability, uptake, elimination, and bioaccumulation of PtNPs and dissolved Pt (added as H_2PtCl_6) using a model freshwater snail, *Lymnaea stagnalis*.

Chapter 7 discusses the overall conclusions of the dissertation, the environmental implications of the different studies performed as part of this PhD dissertation, and the recommendations for future studies.

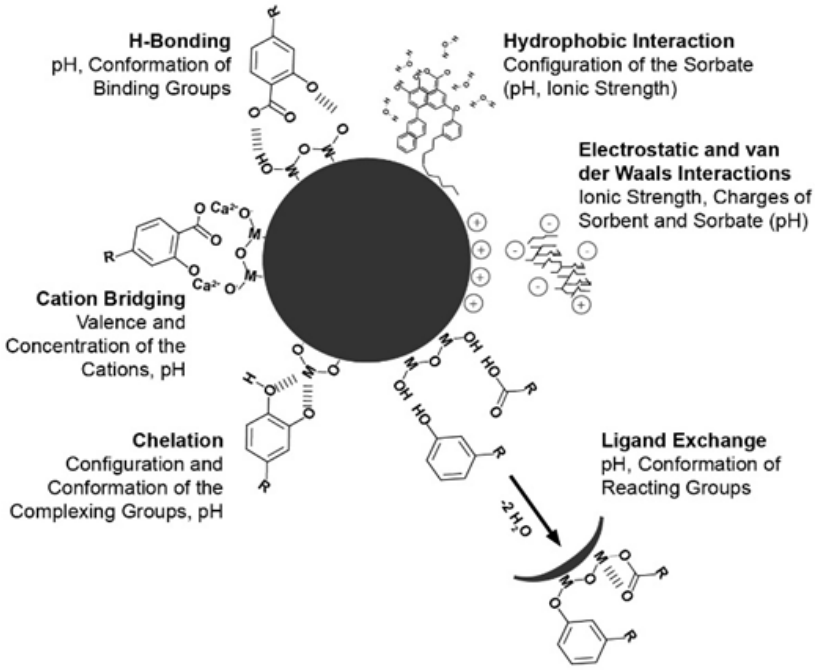

Figure 1.1. Mechanisms of NOM sorption on the NP surface. Modified from Philippe, et al. (2014) [93]

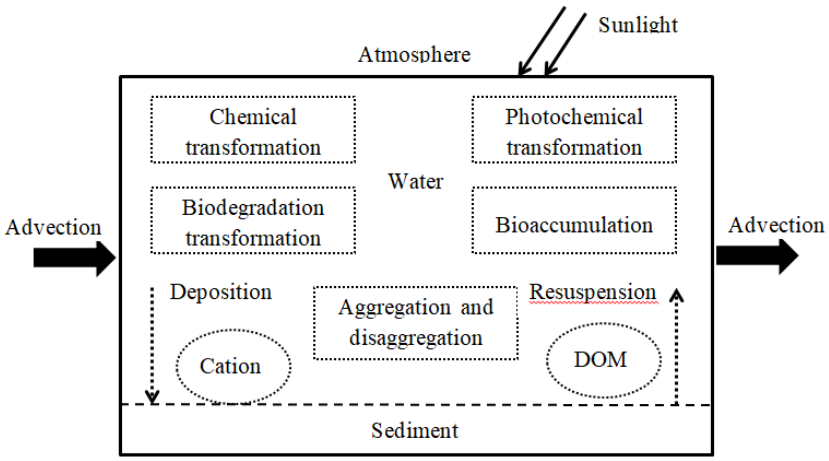

Figure 1.2. Schematic overview of the processes affecting the transport, behavior, and fate of nanoparticles. Modified from Peijnenburg et al. (2015) [45]

CHAPTER 2

A RAPID APPROACH FOR MEASURING SILVER NANOPARTICLE CONCENTRATION AND DISSOLUTION IN SEAWATER BY UV-VIS[1]

[1] Sikder, M., Lead, J.R., Chandler, G.T., Baalousha, M. "A rapid approach for measuring silver nanoparticle concentration and dissolution in seawater by UV-vis", *Science of the Total Environment*, 2018, 618, 597-607

Running title: A rapid approach for measuring silver nanoparticle concentration and dissolution in seawater by UV-vis

Author for correspondence:

Dr. Mohammed Baalousha, Ph.D. Center for Environmental Nanoscience and Risk, Department of Environmental Health Sciences, Arnold School of Public Health, University South Carolina, Columbia, South Carolina 29208, United States; Phone: (803)-777-7177; email: mbaalous@mailbox.sc.edu.

Abstract

Detection and quantification of engineered nanoparticles (NPs) in environmental systems is challenging and requires sophisticated analytical equipment. Furthermore, dissolution is an important environmental transformation process for silver nanoparticles (AgNPs) which affects the size, speciation and concentration of AgNPs in natural water systems. Herein, we present a simple approach for the detection, quantification and measurement of dissolution of PVP-coated AgNPs (PVP-AgNPs) based on monitoring their optical properties (extinction spectra) using UV-vis spectroscopy. The dependence of PVP-AgNPs extinction coefficient (ε) and maximum absorbance wavelength (λ_{max}) on NP size was experimentally determined. The concentration, size, and extinction spectra of PVP-AgNPs were characterized during dissolution in 30 ppt synthetic seawater. AgNPs concentration was determined as the difference between the total and dissolved Ag concentrations measured by inductively coupled plasma-mass spectroscopy (ICP-MS); extinction spectra of PVP-AgNPs were monitored by UV-vis; and size evolution was monitored by atomic force microscopy (AFM) over a period of 96 hours. Empirical equations for the dependence of maximum absorbance wavelength (λ_{max}) and extinction coefficient (ε) on NP size were derived. These empirical formulas were then used to calculate the size and concentration of PVP-AgNPs, and dissolved Ag concentration

released from PVP-AgNPs in synthetic seawater at variable particle concentrations (*i.e.* 25-1500 μg L^{-1}) and in natural seawater at particle concentration of 100 μg L^{-1}.

These results suggest that UV-vis can be used as an easy and quick approach for detection and quantification (size and concentration) of sterically stabilized PVP-AgNPs from their extinction spectra. This approach can also be used to monitor the release of Ag from PVP-AgNPs and the concurrent NP size change. Finally, in seawater, AgNPs dissolve faster and to a higher extent with the decrease in NP concentration toward environmentally relevant concentrations.

2.1. Introduction

Silver nanoparticles (AgNPs) are the most frequently used type of NPs in nano-enabled consumer products; AgNPs are used in 435 out of 1814 consumer products [26]. Several studies have demonstrated the release of AgNPs from nano-enabled consumer products such as fabrics [28, 148] and building facades [30, 149], resulting in increased AgNPs concentration in the environment and posing potential risk to environmental and human health [2, 150]. Currently modelled predicted environmental concentrations (PEC) of AgNPs are in the range of 0.01 ng L^{-1} to 10 μg L^{-1} in surface waters [32, 33]. These predicted AgNP concentrations might not be an accurate representation of the actual environmental exposure concentration to AgNPs as they are predicted based on mathematical models that have not yet been validated [151]. Additionally, these concentrations are expected to increase in the future with the increased use of AgNPs in nano-enabled consumer products [152]. Despite the low predicted environmental concentrations of AgNPs, most studies have focused on evaluating the fate and behavior of AgNPs at relatively high concentrations (*ca.* mg L^{-1}) [34-42]. Recent studies at near-environmentally relevant NP concentrations

demonstrated faster dissolution of NPs such as AgNPs [51], formation of smaller aggregates of NPs such as AuNPs [51], lower removal of NPs such as AuNP from the water column in aquatic systems [153].

In environmental and biological media, AgNPs undergo numerous transformations. Among others, dissolution is one of the key processes which determines AgNPs fate, behavior and effects [44, 45]. Several studies investigated the dissolution kinetics of AgNPs under a variety of experimental conditions [34, 35, 42, 46-50]. These studies demonstrated that dissolution of AgNPs depends on their physicochemical properties (e.g., size, shape, surface coatings etc.), concentration [51], aggregation [52-54] and the characteristics of surrounding media (e.g., pH, temperature, presence of natural organic matter, and ligand type and concentration etc.) [55]. However, most studies were performed at variable NP concentrations [56, 57] using different analytical techniques, complicating direct comparison between the measured dissolution rates.

The most commonly applied approach to measure NP dissolution is based on separation of dissolved ions from the NPs using ultrafiltration [154], or dialysis [155, 156] followed by detection of the dissolved Ag ions by *ca.* inductively coupled plasma-mass spectroscopy (ICP-MS). Other methods such as atomic force microscopy (AFM) and UV-vis monitor changes in particle size and plasmon resonance to quantify NP dissolution [114, 157]. ICP-MS along with centrifugal ultrafiltration has the advantage of directly measuring the dissolved ions at low concentrations (*ca.* ng L^{-1}) but falls short in providing a direct measure of silver concentration remaining in AgNPs when conditions favor Ag precipitation (e.g., formation of AgCl precipitates). AFM has the advantage of directly measuring NP size and provides an evaluation of the evolution of NP size distribution

during the dissolution process. However, size measurement obtained by AFM can be biased by the formation of salt precipitates. UV-vis is one of the most widespread analytical techniques due to its simplicity, reliability, and low-cost instrumentation. It also does not require a separation step to measure the dissolution of AgNPs, and thus is a rapid measurement. However, assessment of AgNP dissolution can be complicated by NP aggregation and sorption of ligands that could influence NP extinction coefficients [157]. Dissolution data obtained by ultrafiltration coupled with ICP-MS, UV-vis and AFM have not been systematically compared yet, leading to a knowledge gap in understanding of the comparability of the dissolution data obtained by these different methods.

Furthermore, NP detection and quantification in environmental systems is challenging and requires sophisticated equipment such as transmission electron microscopy (TEM) or AFM [114, 158, 159], field flow fractionation coupled with ICP-MS [34, 48, 160], or single particle-ICP-MS [161]. The distinct optical properties of plasmonic NPs (e.g., Ag and Au) can be used for their detection and quantification in environmental systems [162, 163]. Analysis of NP extinction spectra can provide valuable information about NP size, structure, concentration and aggregation properties [164].

The aims of this paper are: **1)** to develop a fast method, based on surface plasmon resonance (SPR), to detect and quantify sterically-stabilized AgNPs, **2)** investigate and rationalize the observed variability in PVP-AgNPs dissolution behavior measured by ICP-MS and UV-vis, **3)** investigate the dissolution behavior of PVP-AgNPs in synthetic seawater at a range of AgNPs concentration (25-1500 μg L^{-1}) and **4)** compare the dissolution of PVP-AgNPs in synthetic and natural seawater.

2.2. Materials and methods

2.2.1. Materials/Chemicals

A 99% pure sodium citrate ($Na_3C_6H_5O_7$) supplied by VWR (West Chester, USA), 99.9% pure silver nitrate ($AgNO_3$), greater than 98% pure sodium borohydride ($NaBH_4$) supplied by Alfa Aesar (Ward Hill, USA), and 99% pure polyvinylpyrrolidone of molecular weight 10,000 (PVP10) supplied by Sigma Aldrich (St. Louis, USA) were used for synthesis of AgNPs. Trace metal grade nitric acid (68-70% HNO_3) supplied by Fisher Scientific (Nazareth, USA) was used to acidify samples for ICP-MS analysis. An internal standard mix supplied by Perkin Elmer Pure Plus was used as internal standard for ICP-MS analysis, and the ARISTAR PLUS silver (Ag) standard manufactured by British Drug House (BDH chemicals) was used to prepare standards for ICP-MS calibration. A natural seawater was collected near the cost of Charleston in South Carolina, USA.

2.2.2. Synthesis and characterization of PVP-AgNPs

Citrate-coated AgNPs (cit-AgNPs) were synthesized by reduction of Ag^+ ions using sodium borohydride as a reducing agent and citrate as a capping agent following methods described elsewhere [165]. Briefly, 100 mL of 0.31 mM sodium citrate, 100 mL of 0.25 mM silver nitrate and 10 mL of 0.25 mM sodium borohydride ($NaBH_4$) were prepared in ultrahigh purity water (UPW, 18.2 MΩ.cm) and kept in dark at 4°C for 30 minutes. Silver nitrate and sodium citrate were mixed in a flask and stirred at 700 rpm for 10 minutes. Then 6 mL of $NaBH_4$ was added and the resulting mixture was heated for 90 minutes at 115°C while stirring at 350 rpm. The resulting AgNPs suspension was then left overnight at room temperature to cool. cit-AgNPs were then washed by ultrafiltration (Amicon, 1 kDa

regenerated cellulose membrane, Millipore) to remove the excess reagents. 200 mL of cit-AgNPs suspension was cleaned by pressurized stirred-cell ultrafiltration (Amicon, 1 kDa regenerated cellulose membrane, Millipore) to remove excess reagents before use. AgNPs suspension volume was reduced to 100 mL and then replenished by 100 mL of 0.31 mM sodium citrate solution. This process was repeated at least three times to avoid further AgNP growth.

PVP-AgNPs were obtained by a ligand exchange approach using cit-AgNPs as precursors [75]. Briefly, 200 mL cit-AgNPs were converted into PVP-AgNPs by adding 1 mL of 0.94 M PVP10 solution under vigorous stirring (e.g. 700 rpm) for at least 1 hour. This amount of PVP was required to obtain full surface coverage of AgNPs by PVP molecules to impart full steric stabilization [12] .

AgNPs were characterized using a multi-method approach including surface plasmon resonance (SPR), dynamic light scattering (DLS), zeta potential, inductively coupled plasma mass spectroscopy (ICP-MS) and atomic force microscopy (AFM) [166-168]. Both cit-AgNPs and PVP-AgNPs had a single peak plasmon resonance centered on 393nm and 404nm, respectively. The z-average hydrodynamic diameter (Z-avg), polydispersity index and zeta potential of cit-AgNP were 17.2 ± 0.2 nm, 0.26 ± 0.01, and -37.3 ± 1.1 mV, respectively. The z-average hydrodynamic diameter, polydispersity index and zeta potential of PVP-AgNPs were 21.6 ± 0.3 nm, 0.27 ± 0.01, and -23.4 ± 5.4mV. The number average particle size (N-avg) measured by AFM was 10.1 ± 1.3 nm and 12.3 ± 2.0 nm for cit- and PVP-AgNPs, respectively. The shift in the UV-vis absorbance, the increase in the Z-avg- and N-avg- diameters and the decrease in AgNPs zeta potential further confirms the

replacement of citrate molecules by PVP molecules. The concentration of PVP-AgNPs stock suspension was measured by ICP-MS and was 10.81 ± 0.28 mg L^{-1}.

PVP coated AgNPs were used to avoid interferences in the UV-vis signal caused by NP aggregation. The lowest concentration of AgNPs selected was 25 μg L^{-1} due to the detection limit of UV-vis. The highest AgNPs concentration of 1500 μg L^{-1} was used as a benchmark to enable comparison with data widely available in the literature.

2.2.3. Monitoring PVP-AgNP properties during dissolution in synthetic seawater

A 100 mL of 100 μg Ag L^{-1} PVP-AgNP suspension was prepared by diluting 0.925 mL of AgNPs stock suspension in 75 mL of 30 ppt synthetic seawater (Crystal Seas® bioassay grade sea salts in carbon-scrubbed 18-mΩ deionized H_2O). All samples were prepared in triplicate. A 10 mL aliquot of PVP-AgNPs suspensions in seawater was withdrawn at different time points (*ca.* 1, 3, 6, 9, 24, 48, and 72 hours post mixing with seawater) for analysis by UV-vis, ICP-MS and AFM. Samples were processed prior to analysis as described below. Solution pH was monitored throughout the experiment and was approximately 8.1 ± 0.1.

2.2.4. Total, dissolved and AgNP concentration measurement by ICP-MS

Dissolved Ag species were separated from PVP-AgNPs using centrifugal ultrafiltration units (3KDa regenerated cellulose membranes, Amicon Ultra-4). The samples were centrifuged at 3250 g for 15 minutes using an Eppendorf 5810R centrifuge. The original and filtered samples were then acidified to 10% HNO_3 using concentrated acid (70% HNO_3). Finally, all samples were diluted 200-fold in 1% HNO_3 prior to the analysis by ICP-MS (NexION™ 350D, PerkinElmer Inc., Massachusetts, USA) in order

to minimize matrix effects and avoid salt formation. Indium (In_{115}) was used as an internal standard to correct for non-spectral interferences during analysis [169]. Each sample was measured in triplicate and data are presented as mean ± 1 standard deviation.

The potential retention of dissolved Ag, or Ag-PVP complexes on the ultrafilters [170, 171] plus their sorption to the ultrafiltration unit itself, was evaluated by filtering 101.0 ± 2.6 µg L^{-1} Ag (as $AgNO_3$) dissolved in 30 ppt seawater in the absence/presence of 0.036 µg L^{-1} PVP (equivalent to the total PVP in PVP-AgNPs suspension). Samples were ultrafiltered in triplicate as described above. Ag ion recoveries in absence/presence of PVP (97.9 ± 1.5% and 95.9 ± 1.8% Ag respectively) were not significantly different (two tailed T-test, *p-value* = 0.083). Thus, under the experimental conditions of this study, there was no retention of Ag ions due to interaction with PVP, complexation to ultrafiltration membranes, or sorption to the walls of the ultrafiltration unit.

2.2.5. Size evolution measured by AFM

The evolution of NP size distribution during the dissolution processes was monitored using AFM in order to achieve better understanding of NPs dissolution processes and comparability among results obtained by the different analytical techniques. AFM was selected because of **1)** the low particle concentration used in this study; which limits the utility of other NP sizing techniques such as DLS, and **2)** the higher sensitivity of AFM compared to light scattering methods (e.g., DLS), allowing measurements of small changes in NP size due to dissolution.

The size of PVP-AgNPs (100 µg-Ag L^{-1}) was monitored over time (e.g., 0, 24, 72 and 96 hour) following mixing with synthetic seawater by AFM (Cypher ES™ AFM, Asylum Research, an Oxford Instruments company, Santa Barbara, USA). Height

measurements of AgNPs were made using Igor Pro data analysis software (Asylum Research, an Oxford Instruments company, Santa Barbara, USA).

AFM samples were prepared by ultracentrifugation of PVP-AgNPs suspensions at 163,000 g for 1 hour onto a freshly cleaved mica substrate using an ultracentrifuge (Sorvall MTX 150 Micro-ultracentrifuge, Thermo Fisher Scientific Inc., USA) with a swing out rotor. Mica substrates were then rinsed thoroughly with UHPW three times and left to dry under ambient air conditions in a covered petri dish. In order to create a flat support for the mica substrate a Teflon insert was inserted at the bottom of each centrifuge tube [158]. All samples were diluted 10 times in synthetic seawater to avoid overloading of PVP-AgNPs onto the AFM substrate.

AFM analyses were carried out in true non-contact mode under ambient conditions. All images were recorded in ACAirTopography mode with 256x256 pixel size resolution and a scan rate of 1.0 Hz. At least five different areas on each substrate were analyzed and a minimum five images from each area were collected, resulting in at least 25 images per analysis for each substrate. At least 140 height measurements were performed for each sample, which are sufficient to produce a representative particle size distribution (PSD) [166]. In order to construct number particle size distribution histograms (NPSD) measured heights were classified into intervals of 1 nm. The NPSD was then converted to volume PSD (VPSD) as described elsewhere [172].

2.2.6. Extinction spectra evolution by UV-vis

Extinction spectra of PVP-AgNPs aliquots collected at different time points following suspension in seawater were recorded over the wavelength range of 200 to 800 nm using a UV-vis spectrometer (UV 2600, Shimadzu Co., Kyoto, Japan) with a 10-cm

path-length quartz cuvette. PVP-AgNPs with full surface coverage by PVP molecules are sterically stabilized and do not undergo aggregation even at very high salt concentrations [46] (the absence of aggregation is discussed further in the results and discussion section). Thus, the observed reduction in UV-vis absorbance at λ_{max} is attributed to the dissolution of PVP-AgNPs [157]. The % of Ag released from PVP-AgNPs after mixing with seawater can be calculated according to Equation. 2.1 assuming that the extinction coefficient of AgNPs does not change with size. Zook et al. (2011) [157] suggested that in the absence of aggregation this decrease in absorbance is a robust measure of AgNPs dissolution, and the results obtained by UV-vis absorbance loss correlates well with dissolution measurements obtained by ultrafiltration coupled with ICP-MS. Here, we first test this hypothesis, and then we account for size-dependent extinction coefficient as discussed below.

$$Ag\ released\ from\ Ag\ NPs\ (\%) = \frac{UV_{\lambda max,t0} - UV_{\lambda max,t}}{UV_{\lambda max,t0}} x100 \qquad \text{Equation 2.1}$$

2.2.7. Calculation of NP concentration and dissolution from UV-vis

The extinction coefficient (ε) of light is the net effect of scattering and absorption and describes the effect of the interaction between radiation and the matter upon which it impinges. The extinction coefficient can be calculated from NPs absorption *(A)* at maximum absorbance wavelength *(λ_{max})* and molar concentration *(C, mol L^{-1})* using the Beer-Lambert law [173]

$$\varepsilon = \frac{A}{C.L} \qquad \text{Equation 2.2}$$

$$C = \frac{N}{N_A} \qquad \text{Equation 2.3}$$

$$C_{NP} = N m_{NP} \qquad \text{Equation 2.4}$$

$$m_{NP} = V_{NP}\rho = \frac{\pi}{6} d^3 \rho \qquad \text{Equation 2.5}$$

Where L is path length of light through the sample (i.e., 10 cm), N is number density of NPs (NP L^{-1}), N_A is Avogadro's number, C_{NP} is the total mass of silver in PVP-AgNPs suspension, m_{NP} is mass of a single NP, V_{NP} is volume of a single NP, d is the diameter of a single NP and ρ is density of the nanoparticle material (i.e., 10.5 x 10^4 kg m^{-3} for AgNPs). Substituting equations 2.3-2.5 in equation 2.2 results in equation 6, which relates the total mass of silver in PVP-AgNP to their size and extinction coefficient

$$C_{NP} = \frac{\pi d^3 \rho A N_A}{6 L \varepsilon} \qquad \text{Equation 2.6}$$

The volumetric cross-section of AgNPs plays an important role in changing NP extinction spectra. For a population containing equal concentrations of two sizes of AgNPs, the larger NPs contribute more to the extinction spectra, or extinction coefficient value. Therefore, we used volume weighted mean size (v-avg.) to calculate AgNPs extinction coefficients. Additionally, despite having small differences in theoretically calculated extinction coefficient depending on NPSD and VPSD, Paramelle et al. (2014) suggested that volume average size would be more accurate in calculating these parameters (e.g., λ_{max}, ε) particularly when AgNPs are smaller than 20 nm [173]. The λ_{max} was measured for each of the collected spectra (Table S1) and was correlated to volume-weighted mean size of PVP-AgNPs to obtain an empirical equation describing the dependence of λ_{max} on AgNP size.

The dissolution of PVP AgNPs in synthetic seawater was also measured at different NP concentrations (i.e., 25, 50, 500, 1000 and 1500 μg-Ag L^{-1}). All samples were prepared in triplicate and analyzed by UV-vis as discussed above. The λ_{max} was measured for each of the collected spectra, which was then used to calculate PVP-AgNPs volume average size (Equation 2.8), extinction coefficient (Equation 2.9) and concentration (Equation 2.6) (see

results and discussion). The % Ag released from PVP-AgNPs can then be calculated according to Equation 2.7

$$\%\ Ag\ released\ from\ AgNPs\ in\ seawater = \frac{C_{NP,t0} - C_{NP,ti}}{C_{NP,t0}} * 100 \qquad \text{Equation 2.7}$$

Where $C_{NP,t0}$ and $C_{NP,ti}$ are the total mass of silver in PVP-AgNPs suspension at time 0 and *i=3, 6, 9, 24, 30, 48, 72 and 96 h* following mixing in seawater. The % dissolved Ag over time was then fitted using a first order kinetic dissolution model as described elsewhere [34] and dissolutions rates are summarized in **Table A.2**.

2.3. Results and discussion

2.3.1. Concentration of dissolved Ag measured by ICP-MS

Total and dissolved silver concentrations [Ag] as a function of time after mixing with synthetic seawater and measured by ICP-MS with ultrafiltration are presented in **Figure 2.1**. Total [Ag] was 97.9 ± 4.5 µg-Ag L^{-1} and dissolved [Ag] was approximately 23.6 ± 0.7 µg-Ag L^{-1} immediately (within the preparation and centrifugation time *ca.* 20 minutes) after mixing with seawater and increased to 89.8 ± 1.6 µg-Ag L^{-1} within 168 hours (7 days). **Figure 2.1** demonstrates that under the experimental conditions of this study, the dissolution of PVP-AgNPs does not reach equilibrium (*i.e.*, no plateau of dissolved [Ag]) and AgNPs almost completely (*ca.* 92%) dissolved within 7 days. The absence of equilibrium is due to the high concentration of Cl^-, which acts as a sink for Ag^+ ions released from PVP-AgNPs following oxidative dissolution of PVP-AgNPs through the formation of $AgCl_2^-$ and $AgCl_3^{2-}$ complexes, thus maintaining a high Ag^+ gradient between the surface of AgNPs and the bulk solution [174]

2.3.2. Particle size evolution due to dissolution

Representative AFM micrographs of PVP-AgNPs in UHPW and at different time points (*i.e.* 0, 24, 48, 72, 96 hours) after dilution in 30 ppt seawater are shown in **Figure A.1a and A1(b-f)**, respectively. Qualitatively, AFM images show that PVP-AgNPs are randomly distributed on the mica substrate. The number particle size distributions (NPSD) of PVP-AgNPs in UHPW and at different time points (*i.e.* 0, 24, 48, 72, 96 hours) after dilution in 30 ppt seawater are shown in **Figure 2.2**. These NPSD were converted to volume particle size distributions (VPSD), which is required for the calculation of [Ag] in NPs using UV-vis (see materials and methods). Number and volume weighted average size (*n-avg.* and *v-avg.*, respectively) and polydispersity indices are presented in **Table 2.1**.

In UHPW, PVP-AgNPs show a monomodal distribution with number (*n-avg.*) and volume average sizes (*v-avg.*) of 14.7 ± 5.0 and 19.4 ± 5.1 nm, respectively (**Figure 2.2a**). Immediately after mixing with 30 ppt seawater, the NPSD and VPSD of PVP-AgNPs shifts to slightly higher sizes with number and volume average sizes of 15.8 ± 5.2 and 20.6 ± 5.3 nm, respectively. This change in NP size after mixing with seawater is small but statistically significant (Two-tailed t-test for unequal variances; *p-value* = 0.018). This size shift in the NPSD and VPSD can be attributed to the rapid dissolution of smaller AgNPs (*ca.* < 7nm) immediately after mixing with seawater [39]. The disappearance of smaller PVP-AgNPs is congruent with the faster dissolution rates of smaller AgNPs relative to larger ones [46].

As PVP-AgNPs dissolve over time (> 24 hours, **Figure 2.2c-f**), the NPSD and VPSD of PVP-AgNPs shift towards smaller sizes, with a decrease in the number- and

volume-weighted average sizes, increased frequency of smaller NPs and narrower size distributions (i.e., reduced polydispersity, Table 1).

In sum, AFM analysis suggests that in seawater smaller PVP-AgNPs (*ca.* < 7 nm) fully dissolve rapidly (within hours), but larger NPs dissolve at slower rates and become smaller over time. This decrease in NP size over time may complicate the assessment of AgNPs size relationships relative to fate and toxicity. For instance, many studies have reported size-dependent toxicity of AgNPs [36, 175-177], while others did not find any correlation between NP size and toxicity [41].

2.3.3. Evolution of PVP-AgNPs extinction spectra in seawater

Extinction spectra of 97.9 ± 4.5 µg-Ag L^{-1} PVP-AgNPs in seawater at different time points following mixing of PVP-AgNPs with seawater are presented in **Figure 2.3a**. PVP-AgNPs have a single plasmon resonance peak, which decreases with time. The decrease in the UV-vis absorbance is attributed to NP dissolution due to the absence of peak broadening, shoulder formation or the formation of a second peak at higher wavelengths that can be attributed to NP aggregation and/or shape transformation [178, 179]. Several studies used the loss in UV-vis absorbance as a measure of NP dissolution [51, 129, 157, 180-182]. **Figure 2.3b** shows the % loss in UV-vis absorbance with time which follows the same trend as the increase in dissolved Ag concentration measured by ICP-MS coupled with Ag separation by ultrafiltration (**Figure 2.1**). However, the dissolved Ag (%) calculated from the loss in UV-vis absorbance assuming a constant extinction coefficient of PVP-AgNPs during the dissolution process is higher than those calculated from direct measurement of dissolved ions by ICP-MS following ultrafiltration (**Figure 2.4**). The differences in the % dissolved Ag measured by UV-vis from ICP-MS along with ultrafiltration could be

attributed to several factors; **1)** sorption of dissolved Ag ions to free PVP molecules, **2)** formation of AgCl precipitates in the seawater matrix, and/or **3)** reduction in the extinction coefficient of AgNPs correlated with a decrease in NP size due to dissolution, as demonstrated by AFM [173]

PVP released from AgNPs could contain some Ag ions that can be retained on the filter during the ultrafiltration step. It is well known that there is a strong interaction between functional groups (C=O and C-N, more likely with C-N in case of Ag) of PVP and metal ions [170, 171, 183]. PVP may provide adsorption sites for the removal of Ag ions. However, control experiments using 101.0 ± 2.6 µg-Ag L^{-1} (from $AgNO_3$) in 30 ppt seawater containing 0.036 µg L^{-1} PVP (i.e., equivalent to the total [PVP] in the 97.9 ± 4.5 µg-Ag L^{-1} PVP-AgNPs suspension) showed no significant reduction of dissolved Ag ion (total dissolved Ag concentration is 95.3 ± 3.0 µg-Ag L^{-1} after ultrafiltration) attributable to sorption onto free PVP molecules. Thus, PVP molecules do not account for the differences in the measured dissolution between UV-vis and ICP-MS.

The concentration of silver used was below the saturation level of silver chloride (AgCl) in seawater. Thus, within the concentration range used in this study (25-1500 µg L^{-1}), no AgCl precipitates would be expected. Therefore, the quantitative differences in the measured % dissolved fraction by UV-vis and ICP-MS can be attributed to the reduction in extinction coefficient occurring with the decrease in NP size due to their dissolution in seawater [173]. The UV-vis absorbance depends not only on NPs concentration, but also on their extinction coefficient. Thus, the reduction in UV-vis absorbance at λ_{max} is a combined effect of NP dissolution and the corresponding reduction in AgNPs extinction coefficient.

2.3.4. Size-dependent maximum absorbance wavelength and extinction coefficient for PVP-AgNPs

The maximum absorbance wavelength (λ_{max}) for PVP-AgNPs gradually shifts towards shorter wavelengths with time (blue shift, **Figure 2.3a and Table A.1**), which can be attributed to NP size reduction as a result of their dissolution [184]. The spectra of AgNPs are highly sensitive to particle size distribution, where the maximum absorbance wavelength shifts to shorter wavelengths due to decrease in NP sizes as larger AgNPs contribute more to absorbance and scattering [173]. The shift in the λ_{max} is in agreement with the reduction in NP mean size and dispersity observed by direct measurement of NP size distribution by AFM [184]. **Figure 2.5a** and Eq.8 show the correlation (R^2 = 0.96) between PVP-AgNP volume average size and the maximum absorption peak position (λ_{max}), which can be used to calculate PVP-AgNPs size in seawater.

$$d = 0.11\,(\lambda_{max})^2 - 89.88\,(\lambda_{max}) + 17{,}775.94 \qquad \text{Equation 2.8}$$

Similarly, the calculated extinction coefficient of PVP-AgNPs decreases with the decrease in NP volume-weighted mean size (**Figure 2.5b,** Equation 2.9), as reported by others [162, 173]. The calculated extinction coefficients for PVP-AgNPs (2.4 to 34 x 10^8 M^{-1} cm^{-1} for 9.7-20.6 nm volume average size) are lower than those reported for cit-AgNPs (5.56 to 41.8 x 10^8 M^{-1} cm^{-1} for 10-20 nm volume average size) [173]. The difference in extinction coefficient between cit- and PVP-AgNPs might be due to the differences in the capping agent or the media composition [164]. Eq. 6 enables us to calculate the concentration of PVP-AgNPs and dissolved Ag from extinction spectra in a nondestructive way.

$$\varepsilon = 0.202e^{0.251*d} \qquad \text{Equation 2.9}$$

2.3.5. Validation of the concentrations calculated by UV-vis

To validate the results obtained by UV-vis, the concentration of PVP-AgNPs at different nominal [Ag_{total}] concentrations in seawater were measured both by ICP-MS (as the difference between [Ag_{total}] and [$Ag_{dissolved}$]) and UV-vis (**Table 2.2**). The calculated [PVP-AgNPs] by ICP-MS and UV-vis are in good agreement (within <10% error), ensuring the accuracy of UV-vis to measure the concentration of plasmonic NPs.

2.3.6. Case study 1: Impact of NP concentration on their dissolution in synthetic seawater

The dissolution of PVP-AgNPs in synthetic seawater at a range of PVP-AgNP concentrations (25-1500 μg L^{-1}) was investigated using the validated UV-vis spectrophotometry approach. UV-vis was used due to practicality, cost and speed, as UV-vis does not require a fractionation step to separate Ag ions from AgNPs prior to analysis. PVP-AgNP size and the corresponding extinction coefficient were calculated using Eq.8 and 9, respectively. These parameters were then used to calculate the concentration of PVP-AgNPs (using Eq. 6) and the % of Ag ions released from PVP-AgNPs (using Equation. 7). The % loss in UV-vis absorbance of PVP-AgNPs in seawater at different NP concentrations is presented in **Figure 2.6a**, which were converted to % Ag ion released from PVP-AgNPs as described above (**Figure 2.6b**). The maximum absorbance wavelength position (λ_{max}) of PVP-AgNPs in seawater decreases with time (**Figure 2.6c**) due to reduction in NP size by dissolution, which was converted to volume-average particle size (**Figure 2.6d**).

At high NP concentration (1500 μg L^{-1}) only a small fraction of PVP-AgNPs (*ca.* 10 ± 2.5%) undergo dissolution within 96 hours. As the concentration decreases, the

fraction of dissolved AgNPs increases and reaches near complete dissolution (83 ± 4%) within 48 hours at 25 µg L^{-1} Ag concentration. The dissolution profiles were fitted using a first-order kinetic dissolution model [34]. The rate of dissolution increases with the decrease in NP concentration and it follows a logarithmic profile as a function of NPs concentration (**Figure 2.6e, Table A.2**).

AgNPs dissolve via oxidative dissolution mechanisms, where Ag^0 at the surface of AgNPs oxidize and form Ag^+, followed by the diffusion of Ag^+ to the bulk solution due to the concentration gradient of Ag^+ between the surface of AgNPs and the bulk solution [185]. Due to the high concentration of Cl^- in sea water, the speciation of Ag is dominated by the formation of $AgCl_2^-$, and $AgCl_3^{2-}$ complexes. These complexes act as a sink for Ag^+ and therefore maintain Ag^+ gradient between the surface of AgNPs and the bulk solution. The slower dissolution of AgNPs at higher NP concentration may be attributed to the closeness to saturation concentration of $AgCl_2^-$ and $AgCl_3^{2-}$ formation at high NP concentrations.

2.3.7. Case study 2: dissolution of PVP-AgNPs in synthetic *vs.* natural seawater

The extinction spectra of 100 µg-Ag L^{-1} PVP-AgNPs in 20 ppt synthetic and natural seawaters at different time points following mixing PVP-AgNPs with seawater are presented in **Figures 2.7a-b**, respectively. In both cases, PVP-AgNPs have a single plasmon resonance peak, which decreases with time to a larger extent in synthetic compared to natural seawater. The decrease in UV-vis absorbance is attributed to NP dissolution due to the absence of NP aggregation and/or shape transformation as discussed above[51]. The % loss in UV-vis absorbance at λ_{max}, the % Ag released (as calculated from the UV-vis spectra taking into account the size dependent extinction coefficient), the shift in λ_{max} over time and the PVP-AgNP size-change over time are presented in **Figures 2.8a-**

d. **Figure 2.8** shows that the dissolution behavior of PVP-AgNPs in synthetic and natural seawaters follows the same trend with some differences in dissolution rate. PVP-AgNPs dissolve faster (**Table 3**) in synthetic seawater (dissolution rate = 0.008 h^{-1}) compared to natural seawater (dissolution rate = 0.005 h^{-1}) at the same salinity (i.e., *20 ppt*), which can be attributed to the differences in the chemical composition of natural and synthetic seawater, and most notably the presence of natural organic matter in the natural seawater. Natural organic matter has been shown to reduce dissolution of AgNPs under different environmental conditions [49, 115, 186].

2.3.8. Advantages, limitations and potential future development

Advantages of this approach include simplicity, low-cost instrumentation, lower NP size detection compared with many analytical methods, and wide availability of UV-vis instrumentation in most analytical laboratories. This method can be widely used for polymer coated NPs in inorganic media (e.g., exposure media) such as USEPA synthetic waters and natural seawater (see case study presented above), charge stabilized NPs in low ionic strength media or electrolyte solutions [178], and for all NPs in low ionic strength natural waters such as Shield lakes in Canada and northern Scandinavia [187].

Limitations of this approach include interferences in the UV-vis absorbance due to aggregation of electrostatically stabilized NP, chemical sorption of water constituents on the surface of PVP-AgNPs, the poor detection limit of UV-vis when using cuvettes with short path length (e.g., the commonly used 1 cm path length) cuvettes in most laboratories [178, 188], and the lack of tabulated values for NM extinction coefficient as a function of their size in different environmental matrices. The interferences limitation due to NP aggregation can be overcome by developing approaches to break NP aggregates into

primary particles, or by developing approaches to deconvolute the absorbance peaks of individual and aggregated NPs.

The use of liquid waveguide capillary cells – sample cells with optical path length up to 500 cm compared to the conventional UV-vis cuvettes with optical path length of 1 cm – can increase significantly UV-vis sensitivity (up to 500 times) and thus can reduce detection limits (*ca.* sub μg L^{-1}) toward NP concentrations even lower than those studied in this work (e.g., 25 μg L^{-1}) [189]. Such developments will enhance the capability of UV-vis as a NM detection and quantification tool. Future research should generate data on NM extinction coefficient as a function of NP size in different environmental and biological matrices. Finally, further validation of the presented approach for highly polydispersed samples, for NPs with different capping agents, and in the presence of naturally occurring particles is required.

2.4. Conclusions and environmental implications

This study demonstrates the application of UV-vis spectroscopy for the quantification of sterically stabilized PVP-AgNPs concentration and dissolution in a high ionic strength aqueous solution (seawater). We calculated the correlation between NP size, λ_{max} and ε, which overcomes the need to measure NP size by more direct measurement methods. This implies that UV-vis can be used as a detection method to measure the concentration of AgNPs in seawater and potentially other environment matrices. Because NPs exhibit unique size-dependent properties, particle size cannot be overlooked and must be explicitly monitored so that a fundamental understanding of the underlying size-dependent processes and the influence of NP dispersity on the nanoscale can be discerned [46]. The concentration-dependent dissolution of AgNPs in toxicological media (e.g.,

seawater) means that NP size changes differently at different exposure concentrations. At lower concentrations, NP size decreases faster and to a higher extent than at higher NP concentrations. This differential change in NP size should be considered when investigating toxicological effects and risks of AgNPs in the environment. For instance, smaller NPs may be more efficient in crossing biological barriers [175]. For ecotoxicological assays, the nature of the toxicant (e.g., dissolved, number and size of primary AgNPs) will be different at different concentrations due to their concentration-dependent dissolution. Higher dissolution rates and consequently faster reduction in primary NP sizes at lower NP concentrations suggest that, at lower concentrations, NPs and their dissolution products may be more bioavailable than has been considered toxicologically in most cases. Toxicity results obtained at high NP concentration may produce inaccuracies in risk assessments when extrapolated to the often much lower but environmentally-relevant concentrations seen in the field. In order to approach realism and to avoid underestimation of potential risk, we suggest that environmental fate and effects studies of NPs, and the characterization of NPs underpinning these studies, be performed at environmentally-relevant NP concentrations.

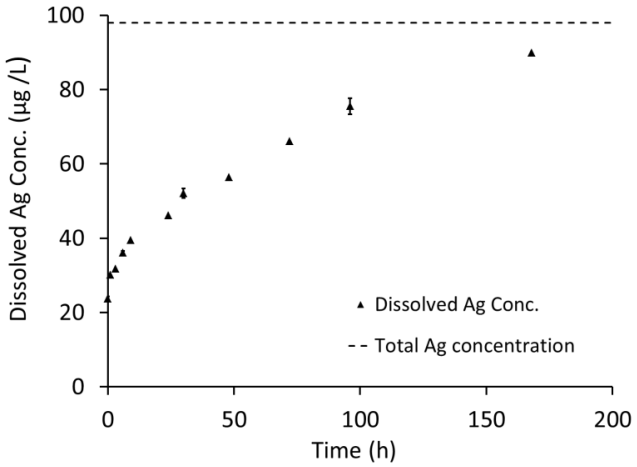

Figure 2.1. Evolution of dissolved [Ag] measured by ICP-MS. All experiments were performed in triplicates and are reported as mean concentration ± standard deviation. The dashed line indicated the total Ag concentration (97.9±4.5 µg-Ag L^{-1})

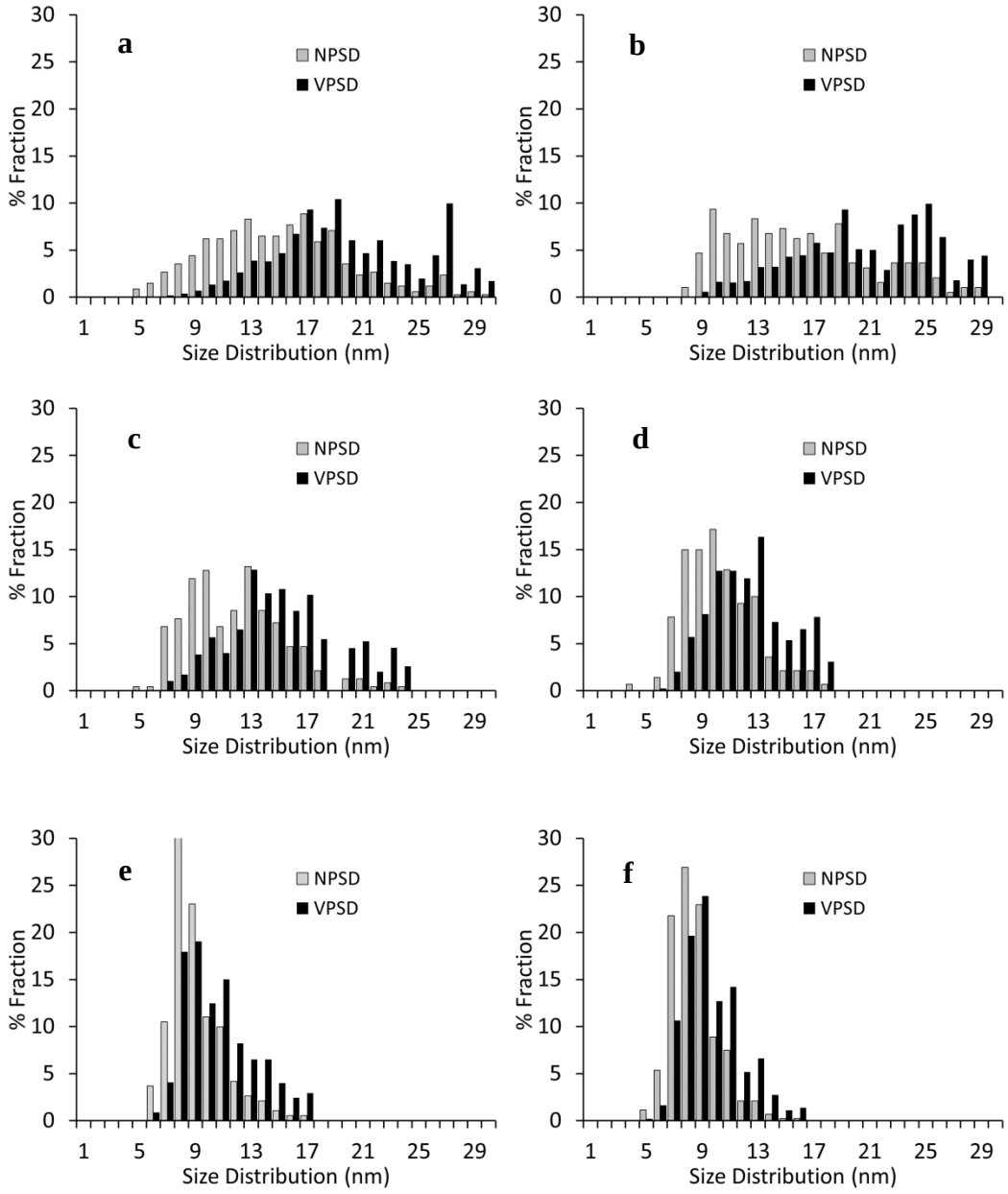

Figure 2.2. Number particle size distribution (NPSD) measured by atomic force microscopy and calculated volume particle size distribution (VPSD) of 97.9±4.5 µg Ag L-1 PVP-AgNPs in (a) ultrahigh purity water, and in synthetic seawater after (b) 0 hr, (c) 24 hr, (d) 48 hr, (e) 72 hr and (f) 96 hr. Corresponding number of measured particles and their number and volume mean sizes are summarized in Table 2.1.

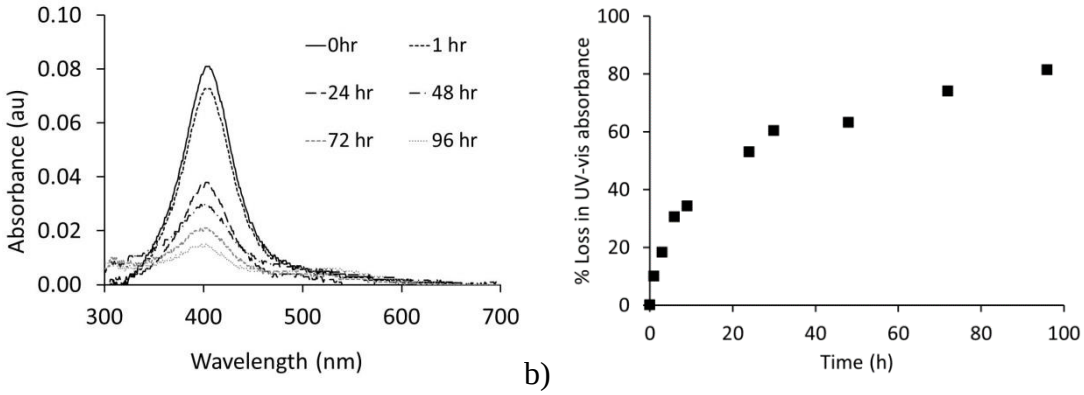

Figure 2.3. (a) UV-vis spectra of 97.9±4.5 µg-Ag L^{-1} PVP-AgNPs in seawater as a function of time, and (b) % loss of UV-vis absorbance at λ_{max}.

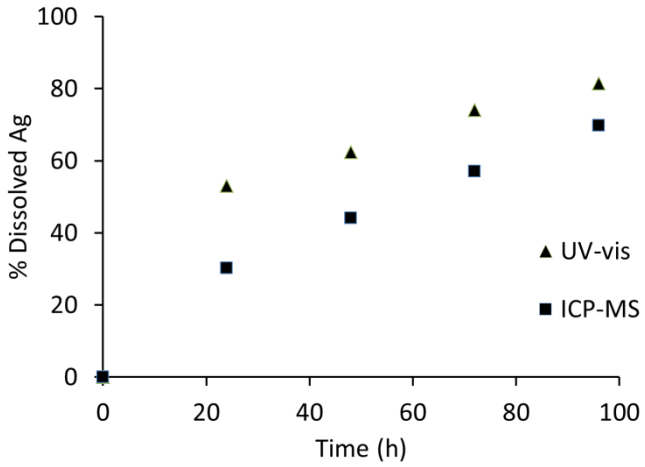

Figure 2.4. Comparison between the measures of PVP-AgNPs dissolution; loss in absorbance measured by UV-vis and release of dissolved Ag ions measured by ICP-MS along with separation by ultrafiltration

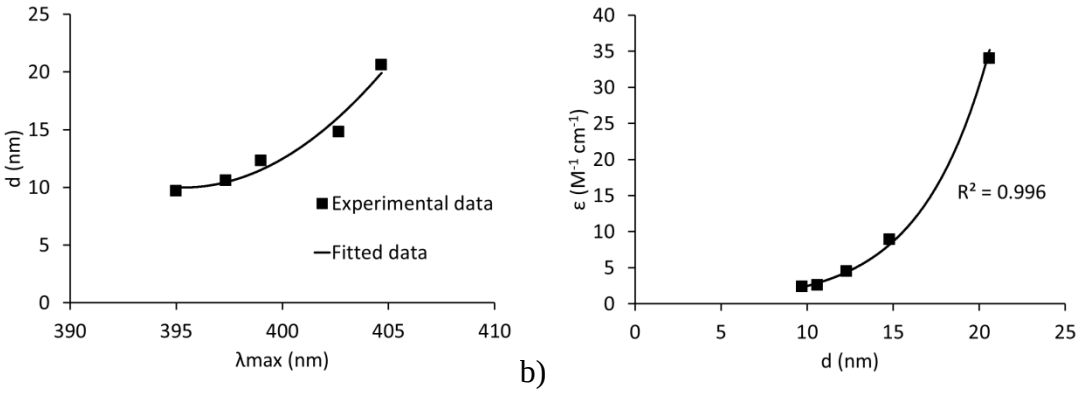

a) b)

Figure 2.5. Correlation between PVP-AgNP (a) volume weighted average size and maximum absorbance wavelength (λ_{max}), and (b) extinction coefficient (ε) and volume weighted average size.

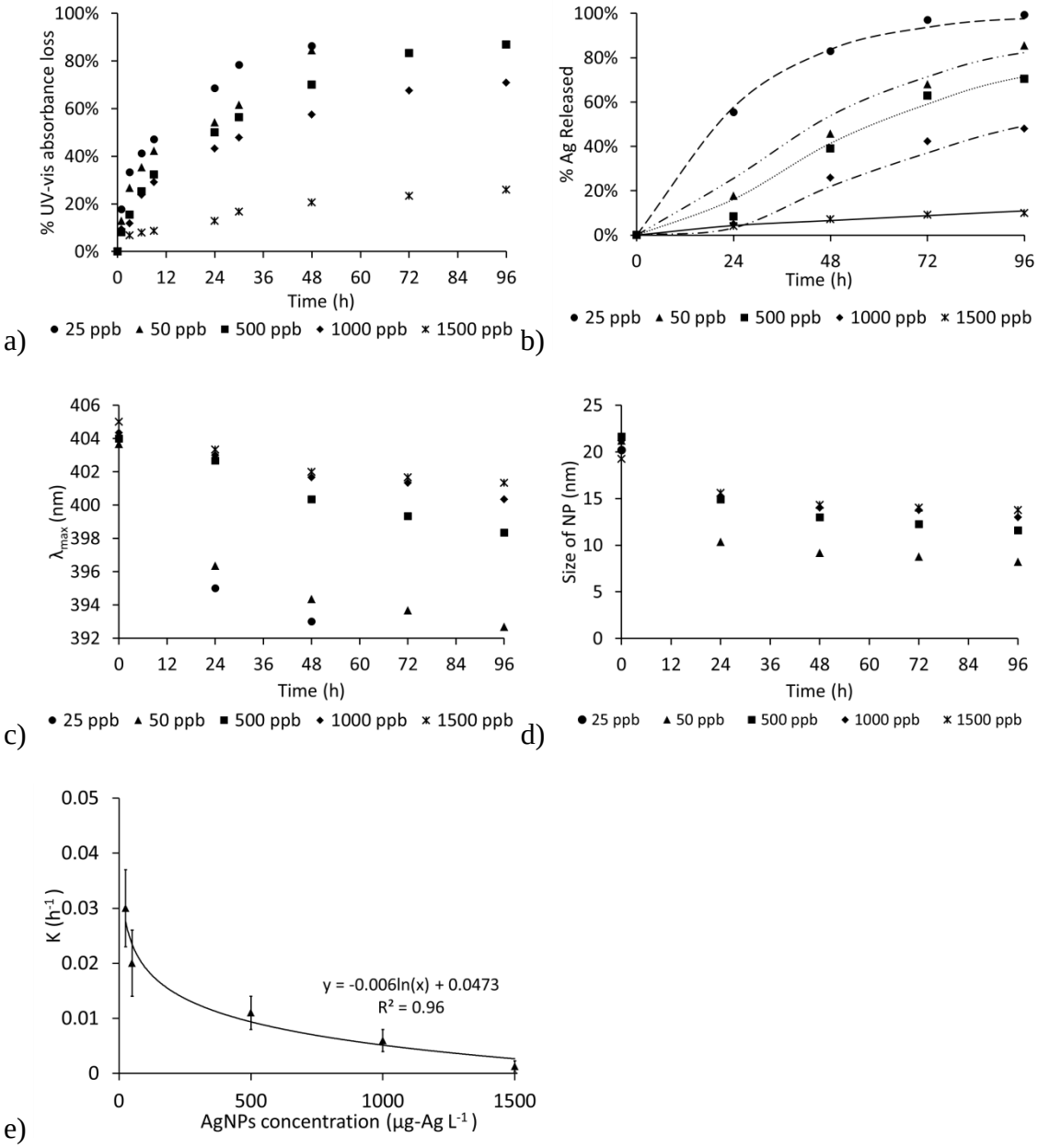

Figure 2.6. Dissolution behavior of PVP-AgNPs in 30 ppt seawater as a function of AgNPs concentration: (a) % loss in UV-vis absorbance, (b) % Ag released from AgNPs calculated by taking into account the size-dependent extinction coefficient, (c) evolution of maximum absorbance wavelength overtime, (d) size evolution calculated from UV-vis spectra, and (e) correlation between AgNPs concentration and dissolution rate

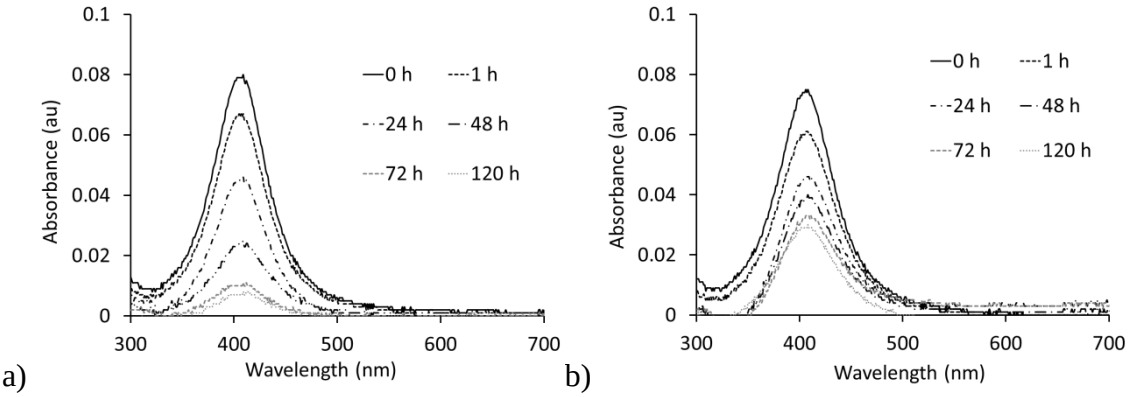

Figure 2.7. Extinction spectra of 100 µg-Ag L^{-1} PVP-AgNPs in (a) 20 ppt synthetic seawater and (b) 20 ppt natural seawater as a function of time

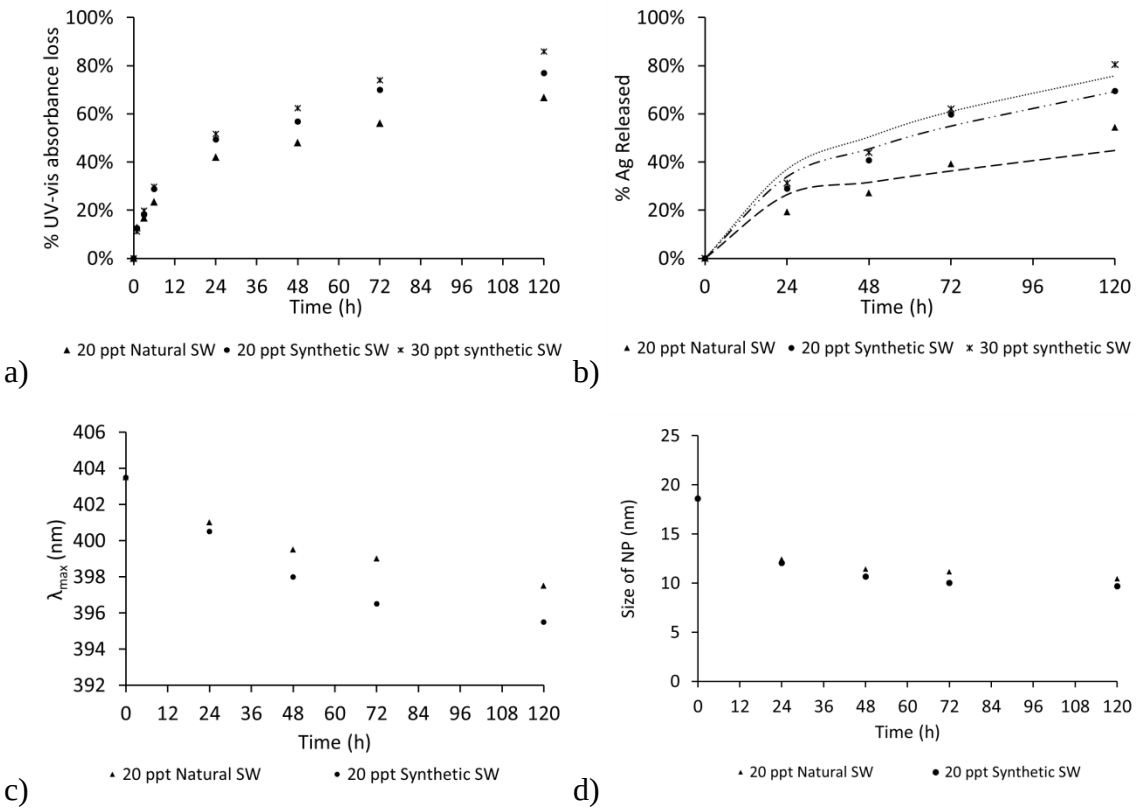

Figure 2.8. Dissolution behavior of PVP-AgNPs (100 µg L^{-1}) in natural and synthetic seawater (SW): (a) % loss in UV-vis absorbance, (b) % Ag released from AgNPs calculated by taking into account the size dependent extinction coefficient, (c) evolution of maximum absorbance wavelength (λ_{max}) over time, and (e) size evolution calculated by UV-vis spectra. Dissolution rates are presented in Table 2.3.

Table 2.1. Number and volume mean size of PVP-AgNPs analyzed by AFM samples at different time points. Corresponding number particle size distribution histograms are presented in Figure 2.

Sample	n-avg. ± SD (PDI) nm.	v-avg. ± SD (PDI) nm	Number of analyzed NPs
NPs in UPW at 0 hr	14.7 ± 5.0 (0.34)	19.4 ± 5.1 (0.27)	235
NPs in SW at 0 hr.	15.8 ± 5.2 (0.33)	20.6± 5.3 (0.26)	192
NPs in SW at 24 hr.	11.6 ± 3.6 (0.31)	14.8 ± 4.0 (0.27)	235
NPs in SW at 48 hr.	10.0 ± 2.6 (0.26)	12.3 ± 2.8 (0.23)	140
NPs in SW at 72 hr.	8.7 ± 2.0 (0.23)	10.6 ± 2.6 (0.24)	191
NPs in SW at 96 hr	8.1 ± 1.7 (0.21)	9.7 ± 2.1 (0.24)	227

n-avg. =number weight mean size
v-avg. = volume weighted mean size
SD= standard deviation
PDI= polydispersity index (=average size/ SD)
SW = seawater

Table 2.2. Comparison of concentration of PVP-AgNP measured by ICP-MS and UV-vis ($\mu g\ L^{-1}$)

Nominal [Ag_{total}]	Measured [AgNP] by ICP-MS = [Ag_{total}]-[$Ag_{ultrafiltered}$]	Calculated PVP-[AgNP] by UV-vis	% error
25	13.8	14.6	5.8
50	34.2	31.9	6.7
500	281.5	268.6	4.6
1000	608.9	550.7	9.5
1500	1083.6	1124.7	3.8

Table 2.3. Dissolution rate (k) and fitted coefficient (A) of 100 µg L^{-1} PVP-Ag NPs in 20 ppt natural seawater and 20 and 30 ppt synthetic seawater. Dissolution rates are presented as a mean and standard deviation of three independent replicates

Media characteristic	**Dissolution rate (k), h^{-1}**	**Fitted Parameter (A)**
20 ppt natural seawater	0.005 ± 0.001	0.80 ± 0.02
20 ppt synthetic seawater	0.008 ± 0.002	0.80 ± 0.01
30 ppt synthetic seawater	0.019 ± 0.004	0.79 ± 0.01

CHAPTER 3

SYNTHESIS, CHARACTERIZATION, AND ENVIRONMENTAL BEHAVIORS OF MONODISPERSED PLATINUM NANOPARTICLES[1]

[1] Sikder, M., Wang, J., Chandler, G.T., Berti, D., Baalousha, M., "Synthesis, characterization, and environmental behaviors of monodispersed platinum nanoparticles", *Journal of Colloid and Interface Science*, 2019, 540, 330-341

Running title: Synthesis, characterization, and environmental behaviors of monodispersed platinum nanoparticles

Author for correspondence:

Dr. Mohammed Baalousha, Ph.D. Center for Environmental Nanoscience and Risk, Department of Environmental Health Sciences, Arnold School of Public Health, University South Carolina, Columbia, South Carolina 29208, United States; Phone: (803)-777-7177; email: mbaalous@mailbox.sc.edu.

Abstract

The release of platinum group elements, including platinum nanoparticles (PtNPs), has been increasing over the past decades. However, few studies have investigated the fate, behavior and effects of PtNPs in environmental media. Here, we report a protocol for the synthesis of five different sizes (8.5±1.2, 10.3±1.3, 20±4.77, 40.5±4.1, and 70.8±4.2 nm) of monodispersed citrate- and polyvinylpyrrolidone (PVP)-coated PtNPs, together with their characterization using a multi method approach and their behavior in relevant biological and toxicological media. In general, PtNPs sizes measured using dynamic light scattering, field flow fractionation, single-particle inductively-coupled plasma-mass spectroscopy, transmission electron microscopy and atomic force microscopy, were all in good agreement when PtNP sizes were larger than the size detection limits of each analytical technique. Slight differences in sizes measured were attributable to differences in analytical techniques, measuring principles, NP shape and NP permeability. The thickness of the PVP layer increased (from 4.4 to 11.35 nm) with increases in NP size. The critical coagulation concentration of cit-PtNPs was independent of NP size, possibly due to differences in the PtNPs surface charge as a function of NP size. PtNPs did not undergo any significant dissolution in any media tested. PtNPs did not aggregate significantly in Dulbecco's modified Eagle's medium, but they formed aggregates in moderately hard water and 30 ppt synthetic seawater, and aggregate size increased with increases in PtNPs

concentration. Overall, this study establishes a general model NP system (i.e., PtNPs) of different sizes and coatings that can be used to investigate the fate, behavior, uptake, and eco-toxicity of NPs in the environment.

3.1. Introduction

The global production of platinum group elements (PGE) has grown steadily since 1970, and the global production of platinum (Pt) alone increased to 190 tons with an annual demand of 257 tons in 2016 [58]. The main use of Pt is in the catalytic convertors of cars, trucks, and buses, accounting for approximately 50% of Pt demand each year. Mandatory installation of catalytic convertors in motor vehicles reduced the emission of harmful exhaust emissions (e.g., carbon monoxide, nitrogen and sulfur oxides, hydrocarbons, aldehydes, and heavy metals etc.) [59, 60], but it resulted in an increased release of PGE (i.e., Pt, Pd, Rh, Ru, Os and Ir) to the environment [61], and some studies demonstrated the release of Pt in the form of nanoparticles (NPs) [62, 63]. The concentration of Pt in environmental samples, such as road dust, soil, surface water, sediments and plants has increased significantly in recent decades [64-68]. The concentration of Pt in aquatic ecosystems (0.4-10.8 ng-Pt L^{-1}) is relatively low compared to their concentration in the immediate vicinity of roads (50 ng-Pt g^{-1} of road dust) [60]. Even higher Pt concentration (> 300 µg g^{-1}) has been reported in Mexico city road dust [66]. Additionally, Pt complexes (*e.g.* cisplatin, carboplatin) are used for cancer treatment [69], and platinum nanoparticles (PtNPs) have shown promise in this use [9]. The majority of drugs containing Pt complexes are excreted in patients' urine (about 70%) and enter wastewater systems[61]. Treatment removal methods for these active compounds are lacking which contributes to environmental Pt contamination [61, 70].

Several studies have reported Pt toxicity to aquatic organisms including water fleas (*Daphnia magna*, 3-weeks LC_{50}= 520 µg L^{-1}) [71], freshwater oligochaetes (*Variegatus lubriculus*, 96-h LC_{50}= 0.4-30 mg L^{-1}) [72], freshwater microalgae (*Pseudokirchneriella subcapitata*, 72-h EC_{50} = 17 mg L^{-1}) [73], and marine bacteria (*Photobacterium phosphoreum*, EC_{50}= 25 µg L^{-1})[74]. A recent study also reported reproductive toxicity of PtNPs to zebra fish after chronic exposure [116].

Currently little is known about the environmental behaviors of PtNPs such as aggregation and dissolution in environmental media. Understanding the nature of exposure and the transformations of PtNP physiochemical properties during (eco)toxicology exposures is essential to interpret and quantify any dose-response relationships. These transformations, which are likely to occur in (eco)toxicological media during acute to chronic exposure periods, have been investigated extensively for other NPs (e.g., AgNPs, AuNPs, CeO_2-NPs etc.) [75-77] but not for PtNPs. According to previous studies (with other NPs), aggregation and/or dissolution can significantly alter NP behavior (e.g., dosimetry, uptake, toxicity) and fate (e.g., pharmacokinetics, bioavailability, and biodistribution) [78-80].

The study aims to 1) develop reproducible protocols for the synthesis of monodispersed PtNPs of five different sizes and two coatings (citrate and polyvinylpyrrolidone; PVP); 2) evaluate the aggregation kinetics of PtNPs in the presence of monovalent (i.e., $NaNO_3$) and divalent electrolyte (i.e., $Ca(NO_3)_2$); and 3) evaluate the colloidal stability (e.g., aggregation and dissolution) of cit- and PVP-coated PtNPs in three different media, moderately hard water (MHW), 30 ppt synthetic seawater (SW), and Dulbecco's modified Eagle's medium (DMEM). Monodispersed PtNPs were synthesized

to avoid confounding results due to NP dispersity [190]. Citrate and PVP surface coatings were used in this study as model surface coatings because they are well-characterized; widely used in published studies; and they impart two mechanisms of NP stabilization (e.g., electrostatic stabilization and steric stabilization, respectively) [94, 191].

3.2. Methodology

3.2.1. Particle synthesis

Citrate- and polyvinylpyrrolidone-coated PtNPs (cit-PtNPs and PVP-PtNPs) of five different hydrodynamic sizes ranging from 20 to 95 nm (labelled as $PtNP_{20}$, $PtNP_{30}$, $PtNP_{50}$, $PtNP_{75}$, and $PtNP_{95}$) were synthesized by modifying the PtNPs synthesis protocol developed by Bigall et al. (2008) [192] as described below.

$PtNP_{20}$. Spherical cit-PtNP seed suspensions (8.7 nm diameter) were synthesized according to previously published synthesis protocols [192, 193]. Briefly, 36 mL of 5 mM chloroplatinic acid hydrate (H_2PtCl_6, ≥ 99.9% pure, supplied by Sigma-Aldrich, St. Louis, USA) was added to 464 mL ultra-high pure water (UHPW, 18.2 MΩ· cm) at boiling point. 50 µL of 1 M sodium hydroxide (NaOH, supplied by Sigma-Aldrich, St. Louis, USA) was then added to the solution because it favors the production of monodispersed small PtNPs (< 10nm) [194]. After 1 minute, 11 mL of 1% sodium citrate solution were added dropwise. After 30 seconds, 5.5 mL of a solution containing 0.08% sodium borohydride ($NaBH_4$, > 98% pure, supplied by Alfa Aesar, Ward Hill, USA) and 1% sodium citrate ($Na_3C_6H_5O_7$, supplied by VWR International, West Chester, USA) were added quickly to the boiling solution. After 10 minutes, the product was left to cool down to room temperature under

ambient conditions. All reactions took place under vigorous stirring (*i.e.*, 700 rpm) in covered Erlenmeyer flask.

$PtNP_{20}$. 10 mL $PtNP_{20}$ suspension were diluted in 290 mL UHPW, to which 450 µL of 0.4 M H_2PtCl_6 were added under constant stirring (700 rpm). 5 mL of 1% sodium citrate and 1.25% L-ascorbic acid (aqueous) were added dropwise (1 drop per 3 seconds) to the PtNP and H_2PtCl_6 mixture. The temperature was slowly raised (~10°C per minute) to boiling under vigorous stirring (i.e., 700 rpm) and then poised at boiling point (100°C) for 30 minutes. The resulting suspension was left to cool at room temperature.

$PtNP_{50}$, $PtNP_{75}$, and $PtNP_{95}$. Larger PtNPs were synthesized by diluting different volumes (40, 10, and 2.5 mL) of the $PtNP_{30}$ in 260, 290, and 297.5 mL UHPW, respectively. 450 µL of 0.4 M H_2PtCl_6 solution were added to the diluted suspensions under vigorous stirring (700 rpm). Then, 5 mL solution containing 1% sodium citrate and 1.25% L-ascorbic acid were added dropwise. The temperature was raised slowly to boiling, as above, under vigorous stirring for 30 minutes and left to cool at room temperature.

Purification of PtNPs. All synthesized cit-PtNP suspensions were washed three times by ultrafiltration to remove excess reagents. 300 mL cit-PtNP suspension were reduced to 150 mL by ultrafiltration over 3 kDa regenerated cellulose membrane using Amicon® stirred-cell ultrafiltration unit (EMD Millipore Corporation, MA, USA) under 15 psi pressure (nitrogen). The PtNP suspension was replenished by 150 mL solution of 1% sodium citrate.

PVP-PtNPs were obtained by a ligand exchange approach using cit-PtNPs as precursors [75]. Briefly, 300 mL cit-PtNPs of different sizes (i.e., $PtNP_{20}$- $PtNP_{95}$) were converted into PVP-PtNPs by adding 1, 0.85, 0.48, 0.20, and 0.12 mL of 7.7 mM PVP

solution, respectively, under vigorous stirring (*e.g.,* 700 rpm) for at least 1 hour. The amount of PVP was selected to obtain full surface coverage of PtNPs by PVP molecules in order to impart full steric stabilization [94], assuming that PtNPs are spherical and that 8 PVP molecules/nm^2 are required to fully cover a PtNP surface.

The concentrations of the synthesized cit- and PVP-PtNPs were measured using a NexION 350D inductively coupled plasma-mass spectrometer (ICP-MS). 1 mL aliquot of each PtNP suspension was digested using 1 mL freshly-prepared aqua regia at room temperature for 24 hours. Aqua regia was prepared by mixing 1 mL hydrochloric acid (trace metal grade, 35-38%, Fisher scientific, MA, USA) and 3 mL nitric acid (trace metal grade, 68-70%, Fisher scientific, MA, USA) in acid cleaned glassware. The digested PtNP solutions were diluted at least 3000 times prior to analysis by ICP-MS, and all samples were measured in triplicate.

3.2.2. Particle characterizations

The z-average diffusion coefficient and electrophoretic mobility (EPM) of the synthesized PtNPs were measured by dynamic light scattering (DLS) and laser Doppler electrophoresis using a Zetasizer Nano-ZS instrument (Malvern Instruments Ltd., MA, USA). All measurements were performed at 25°c after a 2-min temperature equilibration. The z-average hydrodynamic diameter (d_{DLS}) was calculated from the diffusion coefficient using Stokes-Einstein equation. The zeta potential (ζ) was calculated from the electrophoretic mobility using Smoluchowski's assumption[195]. The d_{DLS} and ζ were reported as the mean and standard deviation of five and ten replicates, respectively.

Samples for transmission electron microscopy (TEM) analysis were prepared by depositing a drop of the washed PVP-PtNP suspensions on a copper grid (300 mesh) coated

with a thin film of continuous carbon (Agar Scientific, Stansted, Essex, UK) at room temperature. After 20 mins, the grids were washed thoroughly with UHPW to avoid salt crystallization and NP aggregation artefacts[76]. The grids were then left to dry overnight under ambient conditions in a covered petri dish to avoid atmospheric particle deposition. Samples were analyzed in a LaB_6 Jeol 2100 TEM (Joel USA Inc., MA, USA), operated at 200 keV and equipped with a Jeol EX-230 Silicon Drift Detector (SDD; manufactured by Joel USA Inc., MA, USA) with a 60 cm^2 window of acquisition of Energy Dispersive X-ray Spectroscopy (EDS) analysis of elements. Micrographs were acquired at different magnifications, ranging from 500X to 400,000X, to gather information about the average size, morphology, and degree of aggregation (if any) of nanoparticles on the grid. At least 150 NPs were analyzed for each sample to construct a representative particle-size distribution using a Gatan Digital Micrograph software package (GMS 3) [196].

Samples for atomic force microscopy (AFM) analysis were prepared by depositing a drop of PVP-PtNPs suspension in the presence of 2 mM calcium on a freshly cleaved mica substrate for 20 minutes. That was followed by through rinsing with UHPW to avoid salt crystallization and NP aggregation [158]. The mica sheets were then left to dry overnight under ambient conditions in a covered petri dish. AFM analysis was performed on a Cypher ES™ AFM microscope (Asylum Research, CA, USA). Images were recorded in ACAirTopography mode using a silicon cantilever (Asylum Research, CA, USA) with a spring constant of 26 (11-54) N m^{-1}. The scanning rates were optimized to acquire a stable and clear image without damaging the tip or detaching the NPs from the AFM substrate [76], usually 0.25 to 1 Hz scan rate. At least five different areas on each substrate were analyzed and a minimum of five images (image size = 5 x 5 µm) from each area were collected,

resulting in at least 25 images for each substrate. For each sample, at least 150 height measurements were performed, which is sufficient to produce a representative and robust particle size distribution [166]. This distribution was used to calculate the mean core diameter (d_{AFM}) of each PtNP collection.

Flow-Field flow fractionation (FlFFF) analysis was performed using a Wyatt Ecilipse® DualTec™ asymmetrical FlFFF instrument (Wyatt Technology Corporation, CA, USA). 1 kDa OMEGA™ Polyethersulfone membrane (Pall Corporation, NY, USA) was used as an accumulation wall. The carrier phase was 10 mM $NaNO_3$ (pH 7). The channel flow and cross flow were maintained at 1 mL min^{-1}. The injection volume was 0.25 mL (particle concentration 1 mg L^{-1}), and the focus time was 5 mins. Four polystyrene Nanosphere™ size standards (22 ± 2, 41 ± 4, 81 ± 3, and 152 ± 5 nm manufactured by Thermo scientific, CA, USA) were used to calibrate the effective channel thickness for particle size conversion. All particles were detected with a UV detector at 370 nm. Hydrodynamic diameter (d_{FlFFF}) of PtNPs was calculated using the calibration curve between size and retention time established using polystyrene size standards.

Particle number concentration and number size distribution were measured by single particle ICP-MS (sp-ICP-MS). All sp-ICP-MS[43, 197-200] data were acquired with a NexION™ 350D ICP-MS (PerkinElmer Inc., MA, USA) operating in a single particle mode with the Syngistix Nano Application Module. A standard introduction system consisting of a Meinhard glass concentric nebulizer, a glass cyclonic spray chamber, and a 2 mm ID quartz injector were used. The sample uptake rate was 0.28 mL min^{-1}. Data were acquired at an RF power of 1600 W, a 50 µs dwell time, a 0 µs settling time, and a 60 s acquisition time. The transport efficiency for $PtNP_{50}$, $PtNP_{75}$, and $PtNP_{95}$ were 10.3%,

10.0%, and 11.1%, respectively. NIST™ Au standard reference material (actual TEM size of 56 nm; reference material 8013 manufactured by National Institute of Standard and Technology, MD, USA) was used to determine the transport efficiency. A rinse cycle consisting of 1 min with 1% aqua regia, and 1 min with UHPW was performed after each sample run to ensure cleansing of the sample introduction system between samples. All PtNPs suspensions ($PtNP_{20}$- $PtNP_{95}$) were measured in triplicate at 5 different concentrations (e.g., 100, 200, 400, 600, and 800 ng . L^{-1}), and the results are reported as the mean ± standard deviation of the 3 replicates. ($d_{sp\text{-}ICP\text{-}MS}$). The NIST Au standard reference material was measured after each set as a QA/QC check.

3.2.3. Aggregation kinetics

The aggregation kinetics of all cit-PtNPs were measured in duplicate in the presence of different electrolyte (0-70 mM $NaNO_3$, and 0-10 mM $Ca(NO_3)_2$) concentrations at pH 7. The aggregation kinetics of cit-PtNPs were measured by monitoring the growth of NP z-average hydrodynamic diameter (d_{DLS}), measured by DLS, over time immediately after mixing (within 10 s) with electrolyte ($NaNO_3$, and $Ca(NO_3)_2$) at an interval of 15 s for 10 min at 25±0.5 °C. The count rate during DLS measurement increased with time in the range of 30-200 kcps, due to increasing aggregate sizes. The aggregation rate constant (k) is proportional to rate of change in the d_{DLS} (that is the slope of the hydrodynamic diameter as a function of time, Equation 3.1) [113], which was determined by fitting a linear correlation function to the experimental data collected during the early stage aggregation.

$$k = \frac{1}{oNd_0}\frac{d_r}{d_t} \qquad \text{Equation 3.1}$$

Where N is the initial NP concentration, d_0 is the initial NP diameter, and o is the optical factor.

The attachment efficiency ($\alpha = \frac{1}{W}$) was determined according to Equation 3.2.

$$\alpha = \frac{1}{W} = \frac{K_{slow}}{K_{fast}} \qquad \text{Equation 3.2}$$

Where W is the colloidal stability ratio, and k_{slow} and k_{fast} are the slow and fast aggregation rates representing the aggregation rates under the reaction (RLA) and diffusion (DLA) limited aggregation regimes, respectively. The DLA occurs at counter-ion concentrations above the critical coagulation concentration (CCC); whereas the RLA occurs at counter-ion concentrations below the CCC. The CCC represents the minimum counter-ion concentration required to completely destabilize the NP suspension [201]. The attachment efficiencies under RLA and DLA regimes were fitted by linear functions, with their intersection yielding the respective CCC.

3.2.4. Colloidal stability of PtNPs in (eco)toxicological media

The colloidal stability of citrate- and PVP- $PtNP_{95}$ was investigated as a function of NP concentration (e.g., 20, 200, 2000 µg L^{-1}) in three (eco)toxicological media including MHW, 30 ppt SW, and DMEM. MHW media is widely used for acute and/or chronic toxicity tests with *Daphnia magna* [202] and *Lymnaea stagnalis* [203]. 30 ppt SW is recommended for toxicity tests with *Amphiascus tenuiremis* [204], and DMEM is typically used as a cell culture medium [205]. MHW was prepared according to US environmental protection agency (USEPA) guidelines [206]. Crystal Seas™ bioassay grade synthetic seawater was purchased from Instant Ocean® (Marine Enterprises International, Baltimore, MD, USA). DMEM was purchased from American Type Culture Collection

(ATCC, Manassas, VA, USA). The chemical composition of MHW, synthetic seawater, and DMEM is given in Tables S4-6.

$PtNP_{95}$ was incubated with the (eco)toxicological media in high density polyethylene (HDPE) sterile plastic vials (Fisher Scientific, MA, USA) under static conditions in the absence of light [75]. All vials were washed with 10% nitric acid for at least 24 h and rinsed in UHPW for another 24 h prior to the experiment. PtNP hydrodynamic diameter and zeta potential were measured by DLS and Laser Doppler Electrophoresis. Size distribution and number concentration were measured by sp-ICP-MS, and pH was measured by Mettler Toledo F20-Kit FiveEasy™ Benchtop pH meter (Hogentogler & co. Inc., Columbia, MD, USA). All parameters were measured immediately after mixing and 24 hours after mixing with different media at different NP concentrations. For the colloidal stability test, sp-ICP-MS analysis was performed following the same procedure described above (see particle characterizations section). However, the instrument rinsing time between samples was increased to 5 mins (1 min with 1% nitric acid, 2 mins with 1% aqua regia, followed by 2 mins with UHPW). The increased rinse cycle was important to ensure that all salts, organic matter, and metals were removed from the system as the buildup of these constituents could contribute to cross- contamination, nebulizer fouling, or changes in NP transport efficiency.

3.3. Results and discussions

3.3.1. Particle synthesis

A facile seed-mediated growth synthesis protocol was successfully adapted [192] to produce spherical cit-PtNPs ($PtNP_{20}$- $PtNP_{95}$) of five different sizes, ranging from 9.2 to

72.5 nm. All five cit-PtNP suspensions had a pH of 7.0 ± 0.1, were black in color immediately after preparation, and were stable over several months when stored at 4°C in the dark. Initially, the seed ($PtNP_{20}$) was produced by reducing the Pt precursor (H_2PtCl_6) using a strong reducing agent ($NaBH_4$, redox potential -1.37 to 0.4 V) [207]. Larger cit-PtNPs (cit- $PtNP_{30}$) were produced via a "seed-mediated growth" process using cit- $PtNP_{20}$ as a nucleus to which a Pt precursor was added in the presence of a weak reducing agent (i.e., L-ascorbic acid, redox potential -0.55 to 0.35 V) [208]. The weak reducing agent reduces Pt ions to metallic Pt without inducing a new nucleation event. Thus metallic Pt atoms precipitate on the surface of already existing nuclei resulting in particle growth [207]. Larger cit-PtNPs (cit-PtNP $PtNP_{50}$- $PtNP_{95}$) were synthesized following the same seed-mediated growth process discussed above but using cit- $PtNP_{30}$ as the nucleus seeds. Different cit-PtNP sizes were produced by varying the initial seed concentration. The higher seed concentration, and thus a higher seed number, provided a higher number of sites for the precipitation of metallic Pt atoms resulting in the formation of smaller cit-PtNP sizes, and vice versa. Subsequently, $PtNP_{20}$- $PtNP_{95}$ were obtained from the corresponding cit-PtNPs by ligand exchange.

3.3.2. Particle characterizations

The physicochemical properties of the synthesized PtNPs were measured using a multi method approach [167, 168]. Representative TEM and AFM micrographs of $PtNP_{20}$-$PtNP_{95}$ are presented in **Figure 3.1a-e** and **Figure B.1a-e**, respectively. All TEM and AFM micrographs show randomly-distributed NPs, without agglomerates, indicating robust sample preparation and desired dispersion of PVP-PtNPs [159]. TEM images (Figure 1) show that synthesized PVP-PtNPs ($PtNP_{20}$- $PtNP_{95}$) are spherical. High resolution TEM images

of $PtNP_{50}$- $PtNP_{95}$ (**Figure B.2**) illustrate the formation of a thick PVP coating (2.7-5.6 nm thick) on the surface of PtNPs. Such a PVP coating was not observed on the surface of $PtNP_{20}$ and $PtNP_{30}$, possibly because the PVP coating thickness around $PtNP_{20}$ and $PtNP_{30}$ was not thick enough to be detected by TEM. Elemental analysis (using EDS coupled with TEM) of the synthesized NPs confirmed that they are composed of Pt (**Figure B.3**).

Figure 3.2 presents the PSD of PVP-$PtNP_{20}$- $PtNP_{95}$ obtained by TEM, AFM, sp-ICP-MS, DLS, and FlFFF. The size distributions measured by TEM, AFM, and FlFFF show that PtNPs A, B, D, and E exhibit a monomodal PSD, whereas PVP-PtNPs C exhibits a bimodal PSD. For PtNPs C, the size distribution measured by TEM shows that the main peak (77% of the total number of NPs) is centered at 19 nm and the minor peak of smaller particles (23% of the total number of NPs) is centered at 11-12 nm. The size of the smaller particles in PVP- $PtNP_{30}$ corresponds to that of PVP-$PtNP_{20}$, indicating that some seed nuclei did not grow to larger particles, and possibly due to the limited concentration of added Pt precursor. The size distributions measured by sp-ICP-MS show that PVP- $PtNP_{20}$-$PtNP_{50}$ have similar size distributions within the range 25±2 to 32±3 nm, and that PVP-$PtNP_{75}$ and PVP-$PtNP_{95}$ are characterized by a monomodal PSD. The PSD of PVP- $PtNP_{20}$-$PtNP_{50}$ are characterized by a half Gaussian distribution, possibly due to the detection of the large PVP-PtNPs only (i.e., PtNPs > the lower size detection limit of approximately 20 nm) [209]. The size distributions measured by DLS show that all PVP-PtNPs are characterized by monomodal PSDs because DLS cannot resolve such small differences in NP size distribution due to the lower size resolution of DLS compared to TEM, AFM, and FlFFF.

The mean sizes of PVP- $PtNP_{20}$- $PtNP_{95}$, as measured by five different techniques (**Table 3.1**), are different and generally follow the order $d_{AFM} <\sim d_{TEM} < d_{sp\text{-}ICP\text{-}MS} < d_{FlFFFF}$

< d_{DLS} with few exceptions. These exceptions likely can be attributed to the inherent limitations of each analytical technique. For example, $d_{sp\text{-}ICP\text{-}MS} > d_{FlFFF}$ for PVP-PtNPs A and B, which can be explained by the lower size detection limit of sp-ICP-MS and subsequent overestimation of PVP-PtNPs A and B mean size by sp-ICP-MS. The discrepancies in measured mean sizes obtained by different techniques can be attributed to differences in (i) measurement principles, (ii) the obtained measure versus PSD weighting, and (iii) NP structure [166, 167].

Whereas TEM, AFM, and sp-ICP-MS all measure particle core size, DLS, and FlFFF measure NP hydrodynamic diameter (i.e., core size + diffuse layer). Thus, the NP sizes measured by DLS and FlFFF are generally larger than those measured by TEM, AFM, and sp-ICP-MS. TEM measures a projected surface area from which an equivalent circular diameter can be calculated assuming spherical particle shape. AFM measures NP height, which is typically assumed to be equal to particle diameter assuming all particles are spheres [210, 211]. Both TEM and AFM techniques give number-based PSD and number average size. The mean sizes measured by TEM and AFM were in good agreement (within ± 10%; d_{AFM}/d_{TEM} = 0.92-1.08) for all five PtNPs (**Table 3.1**).

sp-ICP-MS measures NP number-based core size. The measured PtNP mean sizes by sp-ICP-MS are in good agreement with those measured by TEM and AFM for PtNPs (D and E) larger than the lower size detection limit by sp-ICP-MS (i.e., 20 nm for PtNPs) [209]. The PSDs of PtNPs suspension A, B, and, C obtained by sp-ICP-MS are monomodal but represent curtailed log-normal size distribution. This is because the smaller particles detected by TEM, AFM and FlFFF are below the size detection limit of sp-ICP-MS. Hence, the $d_{sp\text{-}ICP\text{-}MS}$ of PtNPs A, B, and C are larger than those measured by TEM.

DLS and FlFFF measure NP diffusion coefficients, from which NP equivalent hydrodynamic diameter can be calculated using Stokes-Einstein equation, assuming that the NPs are hard spheres [212]. D_{DLS}/d_{FlFFF} varied within a range of 0.98-1.39 for PVP-$PtNP_{20}$- $PtNP_{75}$ and was 0.89 for PVP-$PtNP_{95}$. The higher hydrodynamic diameter obtained by DLS compared to FlFFF is because DLS measures intensity-based PSD whereas FlFFF-coupled to UV-vis measures mass-based PSD. The larger hydrodynamic diameter of PVP-PtNPs E measured by FlFFF can be attributed to NP-membrane interaction in the FlFFF channel resulting in retardation in NP elution as indicated by tailing in the FlFFF PSD of PVP-PtNP E (**Figure 3.2e**).

For cit-$PtNP_{30}$, $PtNP_{75}$, and $PtNP_{95}$, the d_{DLS} decreased with the addition of 20 mM $NaNO_3$ compared to d_{DLS} in UPW (**Table 3.1**). This was likely due to shrinkage of the diffuse double layer after addition of $NaNO_3$ [213]. As a result, d_{DLS} of cit-PtNPs measured in 20 mM $NaNO_3$ were in closer agreement to those measured by TEM than to those measured in UHPW. This approach provides a useful way to measure NPs core size using DLS by increasing the NP suspension ionic strength to screen the diffuse layer without inducing NP aggregation. For $PtNP_{20}$ and $PtNP_{50}$, the d_{DLS} did not change with the addition of 20 mM $NaNO_3$ compared to d_{DLS} in UHPW, which might be attributed to the higher polydispersity of $PtNP_{20}$ and $PtNP_{50}$ ($\sigma/d_{TEM} > 0.13$) compared to $PtNP_{30}$, $PtNP_{75}$, and $PtNP_{95}$ ($\sigma/d_{TEM} < 0.09$).

For the same PtNP, the d_{DLS} of PVP-PtNPs were larger than the corresponding d_{DLS} of cit-PtNPs by 9-23 nm, depending on the particle (Table 1). This is attributed to surface coating exchange and the formation of a thick PVP coating (4.4-11.4 nm thick), and is in good agreement with TEM analysis (**Figure B.2a-c**) [214]. Moreover, d_{DLS}/d_{TEM} of cit-PtNPs

range from 1.08-1.69 (**Table 3.1**), and those for PVP-PtNPs range from 1.29-2.88. This variability between small-ion (citrate) stabilized PtNPs and large polymer (PVP) stabilized PtNPs is mainly due to structural differences between PtNPs. The higher ratios (d_{DLS}/d_{TEM}) of PVP-PtNPs are due to polymer softness/permeability and because these particles do not satisfy the assumptions of the Stokes-Einstein relationship for hard spherical NPs. Based on our data, citrate-coated NPs may be considered hard spheres whereas PVP coated NPs behave as soft permeable particles, which agrees with previous studies with different NPs [166, 215].

The magnitude of ζ increase with increase in cit-PtNP size (**Figure B.4**) can be attributed to (1) increases in surface Pt oxidation state (*e.g.,* Pt^0 to Pt^{+2} and/or Pt^{4+}) with decreases in PtNP size, and/or (2) insuffient/partial citrate coating on smaller PtNP surfaces (*i.e.*, variability in the amount of citrate per unit surface area). The concentration of citrate molecules is the same for all PtNPs. The spceific surface area of PtNPs increases with decrease in NP size. Thus the number of available citrate molecules per unit surface area decreases with decrease in PtNP size. The first mechanism can be ruled out because surface Pt oxidation state increases only for PtNPs < 6 nm [216], and all PtNPs used in this study were ≥ 10 nm. To evaluate the second mechanism, the zeta potential of $PtNP_{20}$ was measured as a function of sodium citrate concentration (**Figure B.5**). The ζ of $PtNP_{20}$ increased with increasing sodium citrate concentration which is indicative of an increased surface coating and corresponding surface charge as sodium citrate concentration increased. Conversely, the decrease in magnitude of ζ with decreases in particle size can be attributed to insufficient coating of smaller PtNPs with citrate molecules due to correspondingly larger specific surface areas.

3.3.3. Aggregation behavior of cit-PtNPs

Increases in electrolyte concentrations ($NaNO_3$ and $Ca(NO_3)_2$) lead to a corresponding increase in d_{DLS} as a function of time up to a certain cation concentration, above which the d_{DLS} does not change (**Figure B.6**). In the presence of $NaNO_3$, cit- $PtNP_{20}$ (9.2 nm) did not show any aggregation up to 50 mM $NaNO_3$ as the counter ion concentration was insufficient to screen the cit- $PtNP_{20}$ surface charge. At higher $NaNO_3$ concentrations (55-59 mM), cit-$PtNP_{20}$ aggregation rates slowly increased with increasing $NaNO_3$ concentration as the repulsion barrier decreased according to DLVO (Derjaguin, Landau, Verway, and Overbeek) theory (**Figure B.6a**). At a $NaNO_3$ concentration higher than 60 mM, attractive van der Waals forces dominate over electrostatic repulsive forces, resulting in the fast aggregation of cit-$PtNP_{20}$. Growth in z-average diameter as a function of time did not change further with increases in $NaNO_3$ concentration (up to 90 mM). Similar aggregation behavior was observed for cit-PtNPs B-E (**Figure B.6b-e**). In the presence of divalent electrolyte ($Ca(NO_3)_2$), aggregation of cit-PtNPs was observed at much lower concentration of Ca^{2+} (e.g., 0.5- 2.5 mM) compared to Na^+ concentration (e.g., 55-60 mM). Ca^{2+} ions are more efficient in screening the surface charge of cit-PtNPs compared to Na^+ (**Figure B.6f-j**). Additionally, Ca^{2+} ions can interact specifically with the carboxyl groups of the absorbed citrate molecules on surfaces of the PtNPs [217].

The attachment efficiency of cit-PtNPs as a function of $NaNO_3$ (**Figure B.7a-f**) and $Ca(NO_3)_2$ (**Figure B.7 f-j**) shows two different aggregation regimes, that is RLA and DLA, typical of DLVO type aggregation behavior. The RLA regime for cit-PtNP occurs within a narrow $NaNO_3$ and $Ca(NO_3)_2$ concentration range (*ca.* 53-65 and 1-3 mM for $NaNO_3$ and $Ca(NO_3)_2$, respectively), and the CCC values vary within a narrow counter ion

concentration range for all cit-PtNP sizes. The CCC values in the presence of $NaNO_3$ and $Ca(NO_3)_2$ are presented in **Table 3.2**. The lower CCC values in the presence of Ca^{2+} compared to those measured in the presence of Na^+ is in good agreement with the Schulze-Hardy rule (i.e., the CCC is inversely proportional to counter ion valency) and with previous studies using citrate coated silver nanoparticles [178, 217].

No correlation was observed between CCC and cit-PtNP size (**Table 3.2**) for $NaNO_3$, or $Ca(NO_3)_2$. This is likely due to the increase in ζ magnitude with increasing cit-PtNP size (**Figure B.4**). There are currently contradictory data on the dependence of CCC on NPs size. Studies have reported a decrease in CCC with decreases in NPs size (e.g., hematite NPs [101], TiO_2-NPs [102]), an increase in CCC with decreases in NPs size (e.g. AgNPs [94], CdSe-NPs [103]), and independence of CCC relative to NPs size (e.g. AuNPs [104]). These contradictory results can be rationalized by taking into account the variability in NPs surface charges [94]. Negative correlation between CCC and NP size was observed for NPs characterized by a narrow range of ζ (ca. -33±3 to -35±5 for CdSe-NPs [103]), whereas positive correlation between CCC and NP size, or a size independence for CCC were observed for NPs characterized by variable ζ [101, 102, 104].

Maximum cit-PtNPs aggregate sizes – measured after 10 minutes in electrolyte concentrations (e.g., 70 mM $NaNO_3$ and 10 mM $Ca(NO_3)_2$) greater than the CCC – decreased with increases in cit-PtNPs initial hydrodynamic diameters (**Figure B.8**). Under these experimental conditions, the electrolyte concentration is sufficient to fully screen cit-PtNPs surface charge and dictate cit-PtNPs aggregation based on their diffusion [109]. With mass concentration held constant, smaller cit-PtNPs have a higher NPs number resulting in a higher collision probability and a subsequently larger aggregate size. Thus, under the

same mass concentration and under diffusion limited aggregation conditions, smaller PtNPs form larger aggregates compared to larger PtNPs. Additionally, the maximum aggregate size of cit-PtNPs was larger in the presence of Ca^{2+} compared to Na^{+} (**Figure B.8**), and likely due to cit-PtNPs aggregation enhancement via bridging mechanisms in the presence of Ca^{2+} [178].

3.3.4. The concentration-dependent behavior of PtNPs in toxicological media

The concentration-dependent colloidal stability (e.g., dissolution, aggregation) of cit- and PVP-$PtNP_{95}$ was evaluated by monitoring the change in d_{DLS}, ζ, number particle size distribution, and number particle concentration for $PtNP_{95}$ (d_{TEM}= 72.5±3.9 nm) over 24 h in the three media (i.e., MHW, SW, and DMEM). The pH of the PtNPs in DMEM, MHW, and SW media was 7.3±0.1, 8.0±0.1, and 8.1±0.1, respectively.

The d_{DLS}, and ζ were monitored by DLS at an initial PtNPs concentration of 2000 µg. L^{-1}. The d_{DLS} of cit- and PVP-PtNPs in UHPW (control) were 89.5 ± 1.5 and 88.6 ± 1.9 nm, respectively (**Figure 3.3a, b**). The d_{DLS} of cit- and PVP-PtNPs E increased slightly but significantly (two tailed t-test, *p-value* < 0.05) immediately after mixing with DMEM to 104.7±3.9 and 105.4±2.1, respectively, compared to the UHPW control (**Figure 3.3a, b**). This increase in the NP d_{DLS} might be attributed to sorption of organic compounds from the media [48, 51] and/or the lower viscosity of DMEM media (0.94 mPa. s) compared to UPW (1 mPa s) [218]. The larger PtNPs hydrodynamic diameter in the DMEM media was likely due to the inverse correlation between size and viscosity (Stokes-Einstein relationship). The absolute ζ values of cit- and PVP-$PtNP_{95}$ decreased from 48.3±7.5 and 17.3±1.5 mV in UPW to 11.2±9.2 and 6.9±0.7 mV immediately after mixing with DMEM media (**Figure 3.3c, d**). This indicates the replacement of citrate and PVP coatings by organic compounds

in DMEM, and/or the screening of PtNPs surface charge by the abundant counter ions in DMEM. The d_{DLS} and ζ of cit- and PVP-PtNPs E did not change significantly (t-test, *p-value* > 0.05) in DMEM after 24 h compared to those measured at 0 h, indicating the colloidal stability of both cit-and PVP-PtNPs in DMEM media despite a significant reduction in the ζ absolute value. DMEM media is rich with organic compounds (e.g., amino acids, vitamins, proteins) that are known to sorb on NP surfaces forming a surface coating called "protein-corona" which may enhance NP colloidal stability via steric stabilization [48, 51]. The z-average hydrodynamic diameter decreased after 24 hours and can be attributed to the change in the nature and/or formation mechanisms of the protein-corona over time [87]. Formation of the protein-corona is dynamic in nature. Initially proteins with high concentrations and high association rate constants are adsorbed onto NP surfaces, and then they dissociate quickly to be replaced by proteins of lower concentration, slower exchange, and higher affinity [219]. Hence, the thickness of the protein-corona can change over time due to changes in protein conformation following sorption onto NP surfaces.

The d_{DLS} of cit- and PVP-$PtNP_{95}$ increased immediately after mixing with MHW and SW, and the d_{DLS} increased further after 24 hours (**Figure 3.3a, b**), indicating aggregation of cit- and PVP-PtNPs in both media. At 24 hours, the d_{DLS} of cit- and PVP-PtNPs E was higher in SW (954.3±240.1 and 810±282.4, respectively) compared to those measured in MHW (778.2±140.6 and 670.6±19.8, respectively), indicating higher aggregation in SW. The absolute ζ of cit- and PVP-PtNPs was lower in SW after 24 hours (7.1± 1.2, and 7.6± 0.8 mV) compared to those measured in MHW (22.4± 0.6 and 11.4± 0.9 mV; **Figure 3.3c, d**). The higher aggregation and surface charge screening in SW is due to the to the higher ionic strength of SW compared to MHW.

The cit-PtNPs and PVP-PtNPs did not undergo significant aggregation in DMEM despite the significant reduction in their absolute ζ's, whereas they formed large aggregates in MHW despite the higher absolute ζ's of PtNPs in MHW relative to DMEM. This indicates that PtNPs are charge-stabilized in MHW and sterically stabilized in DMEM. DMEM is rich with organic compounds (e.g., amino acids, vitamins, proteins etc.) whereas MHW does not contain organic molecules. Hence, the organic molecule sorption onto the surface of PtNPs seems to enhance the colloidal stability of PtNPs in DMEM media via steric stabilization [48, 51].

The concentration-dependent aggregation and dissolution of cit- and PVP-$PtNP_{95}$ in DMEM, MHW and SW was further investigated by monitoring NP number concentration and number size distribution using sp-ICP-MS for initial NP concentrations between 20-2000 μg L^{-1}. The higher end of this concentration range coincides with that used to investigate $PtNP_{95}$ aggregation by DLS. The lower end of the concentration range was selected as a more environmentally-relevant concentration [108].

At 2000 μg L^{-1}, PVP-PtNPs size distribution did not change in UPW (**Figure 3.4c and B.9a**), increased slightly in DMEM (**Figure 3.4c and B.9b**), and increased significantly (two tailed t-test, $p > 0.05$) in MWH (**Figure 3.4c and B.9c**) and SW (**Figure 3.4c and B.9d**) over time. These results are in good agreement with the increase in PVP-PtNPs size measured by DLS (**Figure 3.3**). However, the aggregate sizes measured by sp-ICP-MS are generally smaller compared to those measured by DLS due to differences in measured parameters and measurement principles as discussed above.

In DMEM, the size distribution of PVP- and cit-PtNPs did not change over time at 20 μg L^{-1} (**Figure 3.4a and S10a,d**). It increased slightly with the appearance of a second

peak at 90-100 nm at 200 µg L^{-1} (**Figure 3.4b and B.10b,e**) and 2000 µg L^{-1} PtNPs (**Figure 3.4c and B.10c,f**), concurrent with a decrease in the total particle number concentration (**Table B.5**). In MHW and SW, cit- and PVP-PtNPs size distributions extended to larger sizes with mean sizes increasing with PtNPs concentrations (**Figure B11, B12**)**.** Concurrently, primary NP number concentration (**Figure B.11, B.12**) and total particle number concentration (**Table B.5**) decreased with increasing PtNPs concentrations.

For direct comparison, the % change in NP mean diameter and number concentration over 24 hours as a function of NP concentration in the three media is presented in **Figure 3.5**. At a given concentration, PtNPs mean size increased and the particle number concentration decreased following the order SW > MHW > DMEM (**Figure 3.5b, d**). For a given media, the % increase in PtNP mean size and the % decrease in PtNP total number concentration increased with increasing NP concentration. For DMEM, the PtNP mean diameter and number concentration did not change significantly over time (**Figure 3.5 a, c**). For MHW and SW, the particle diameter increased with the increase in initial NP number concentration (**Figure 3.5a, c**) and concurrent with a decrease in total particle number concentration (**Figure 3.5b, d**), indicating particle aggregation.

Despite PtNP aggregation in MHW and SW, a fraction of PtNPs remained as primary particles (**Figures 3.6 and B.9-B.12**). The % of primary (unaggregated) particles increased with the decrease in NP concentration (**Figure 3.6**). This is due to a decrease in collision frequency, resulting in the formation of smaller aggregates and/or the lack of NP aggregation. These findings suggest that NP aggregation becomes less significant at lower concentrations, and that NPs may remain as primary particles for an extended period at environmentally relevant concentrations – even in high ionic strength media such as MHW

and SW. This is in good agreement with the decrease in AuNP aggregate size with the decrease in their concentration [51]. Furthermore, the % of primary particles was higher for MHW than for SW (**Figure 3.6**) due to the lower ionic strength of MHW compared to SW.

Initial dissolved Pt concentration (at 0 h) was < 4% of total PtNPs concentration in all NP suspensions. After 24 h, 5-15% of PtNPs dissolved in different toxicological media (**Figure B.13**). However, the % of dissolved Pt in different media (e.g., DMEM, MHW, and SW) were not statistically different (t-test, *p-value* > 0.05). Moreover, we did not observe any concentration-dependent dissolution of PtNPs, but a previous study has reported concentration-dependent dissolution of AgNPs [108, 220]. This might be attributed to the higher solubility of AgNPs compared to PtNPs (**Figure B.14**). The aggregation and dissolution behavior of cit- and PVP-PtNPs was not significantly different. This might be attributed to the partial surface coating of PVP-PtNPs [94]. Thus, both cit- and PVP-NPs behave as charge-stabilized NPs independent of the media ionic strengths evaluated here.

3.4. Conclusions

Here, we report a reproducible protocol for the synthesis of monodispersed citrate- and PVP-coated PtNPs of five different sizes, together with their characterization using a multi method approach and their behavior in relevant biological and toxicological media. In general, the sizes of PtNPs measured using DLS, FlFFF, sp-ICP-MS, TEM and AFM, were all in good agreement when PtNP sizes were larger than the size detection limits of each analytical technique. The thickness of the PVP layer increased with increases in NP size. The aggregation of PtNPs is typical of DLVO type aggregation behavior as observed for other types of NPs (e.g., Ag, Au, TiO_2, and iron oxide NPs) [109, 221-223]. The critical coagulation concentration of cit-PtNPs was independent of NP size, possibly due to

differences in the PtNPs surface charge as a function of NP size. The aggregation and/or dissolution of PtNPs depend on media composition, NP concentration, and ionic strength. PtNPs tend to remain stable in DMEM regardless of NP surface coating or concentration, whereas they tend to aggregate in MHW and SW for both cit- and PVP-PtNPs. Additionally, PtNPs exhibit an increase in aggregate size concurrent with increases in NP concentration.

The synthesized PtNPs undergo very limited transformations *(*e.g., aggregation and/or dissolution) at environmentally relevant concentrations (< 20 μg L^{-1}) and do not change appreciably over time, even in high ionic-strength SW, in good agreement with the decreased aggregation of other types of NPs (e.g., iron oxide, AuNPs, AgNPs, and Au@Ag core–shell Nanoparticles) with the decrease in their concentration [43, 51, 224]. Taken together, limited aggregation and lack of dissolution suggest that these PtNPs present an excellent model NP for future fundamental studies of NP uptake and NP environmental fate and transport, as they will reflect the behavior of primary NPs and not that of dissolved Pt or aggregates of varying NP clusters.

The concentration of platinum group elements (PGE) in the environment has significantly increased over the past decades due to the increased release of Pt from automotive catalytic converters in the form of nanoparticles. The limited aggregation and dissolution of PtNPs at environmentally-relevant particle concentrations suggest that they may persist in the environment and may travel for longer distances in surface waters than other NPs. The concentration-dependent aggregation of PtNPs implies that in (eco)toxicological studies, the nature of PtNP exposure will change as a function of NP concentration; that is, organisms will likely be exposed to primary nanoparticles at low NP

concentrations (< 20 μg L^{-1}) and predominantly exposed to NP aggregates at higher concentrations. Such concentration-dependent differences in NP exposure dynamics are likely to influence NP uptake, elimination and ultimately toxicity as a result of these unique aggregation behaviors, and they should be investigated further.

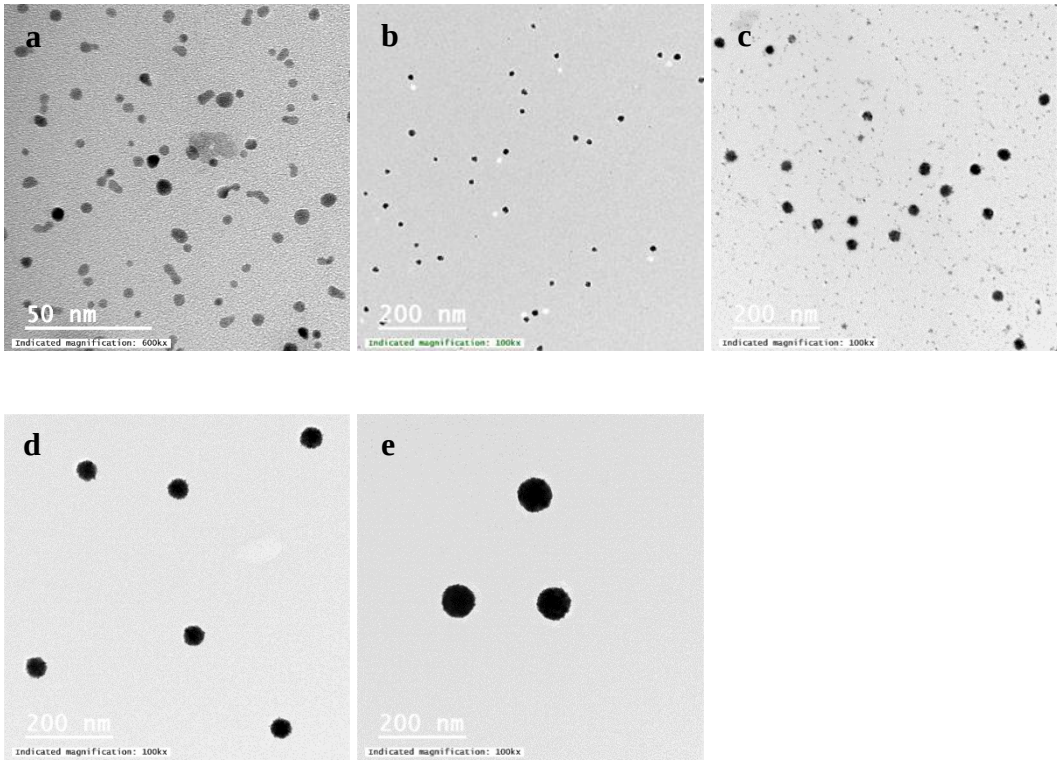

Figure 3.1. Typical transmission electron microscopy (TEM) micrographs of synthesized PVP-PtNPs for (a-e) PVP- $PtNP_{20}$, $PtNP_{30}$, $PtNP_{50}$, $PtNP_{75}$, and $PtNP_{95}$, respectively.

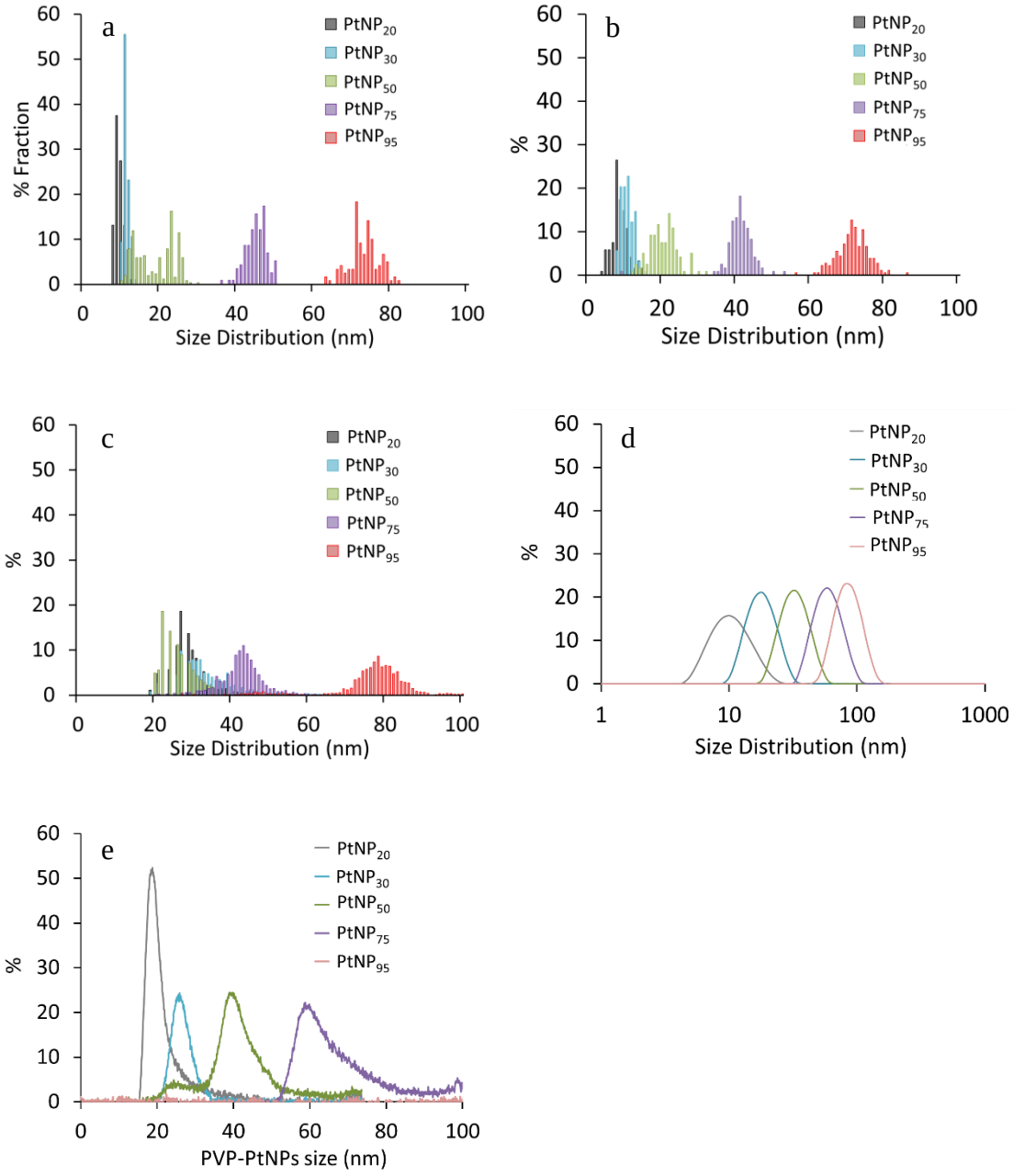

Figure 3.2. Particle size distributions (PSD) of PVP-PtNPs using (a) transmission electron microscopy (TEM), (b) atomic force microscopy (AFM), (c) single particle inductively-coupled plasma mass spectroscopy (sp-ICP-MS), (d) dynamic light scattering (DLS), and (e) field flow fractionation (FFF) with UV-vis as a detector, cross flow and channel flow of 1 mL/min, and elution time of 60 min.

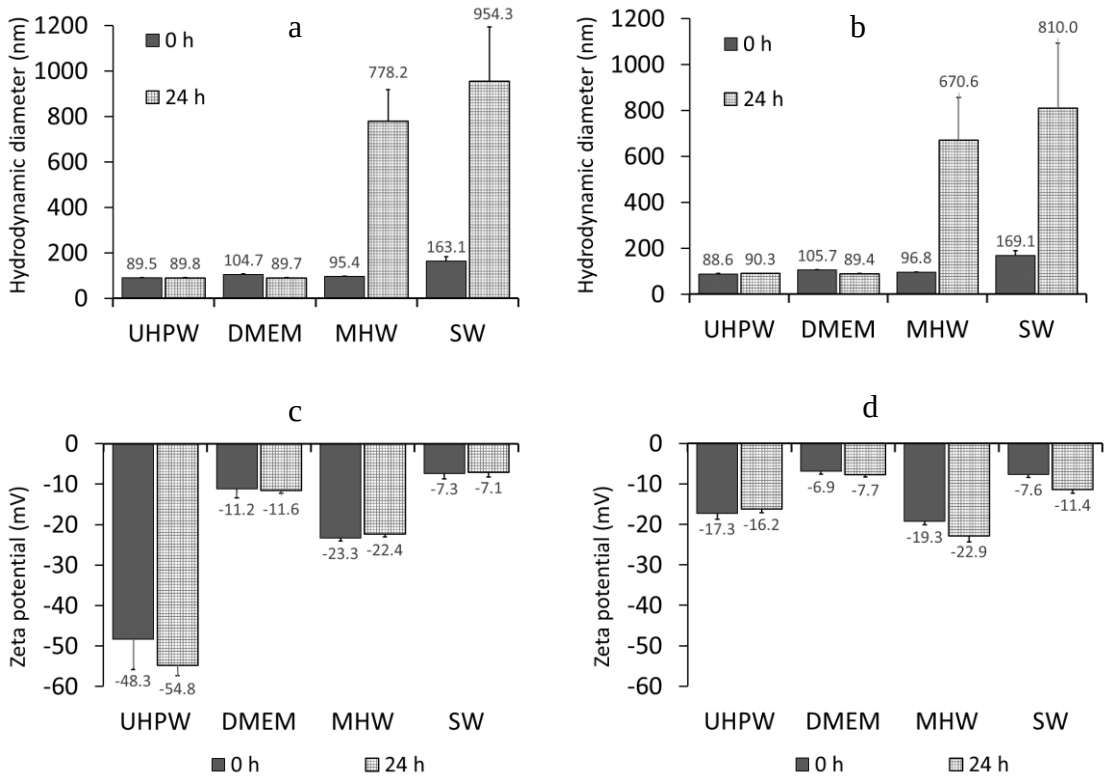

Figure 3.3. (a, b) the equivalent hydrodynamic diameter (d_{DLS}.) and (c, d) the corresponding zeta-potential (ζ) of (a, c) cit-PtNPs and (b, d) PVP-PtNPs in ultra-high pure water (UPW), Dulbecco's modified Eagle's medium (DMEM), Moderately hard water (MHW), and 3030 ppt synthetic seawater (SW) media after 24 h of adding PtNPs in the corresponding media. PtNPs concentration in all suspensions are 2000 µg L^{-1}.

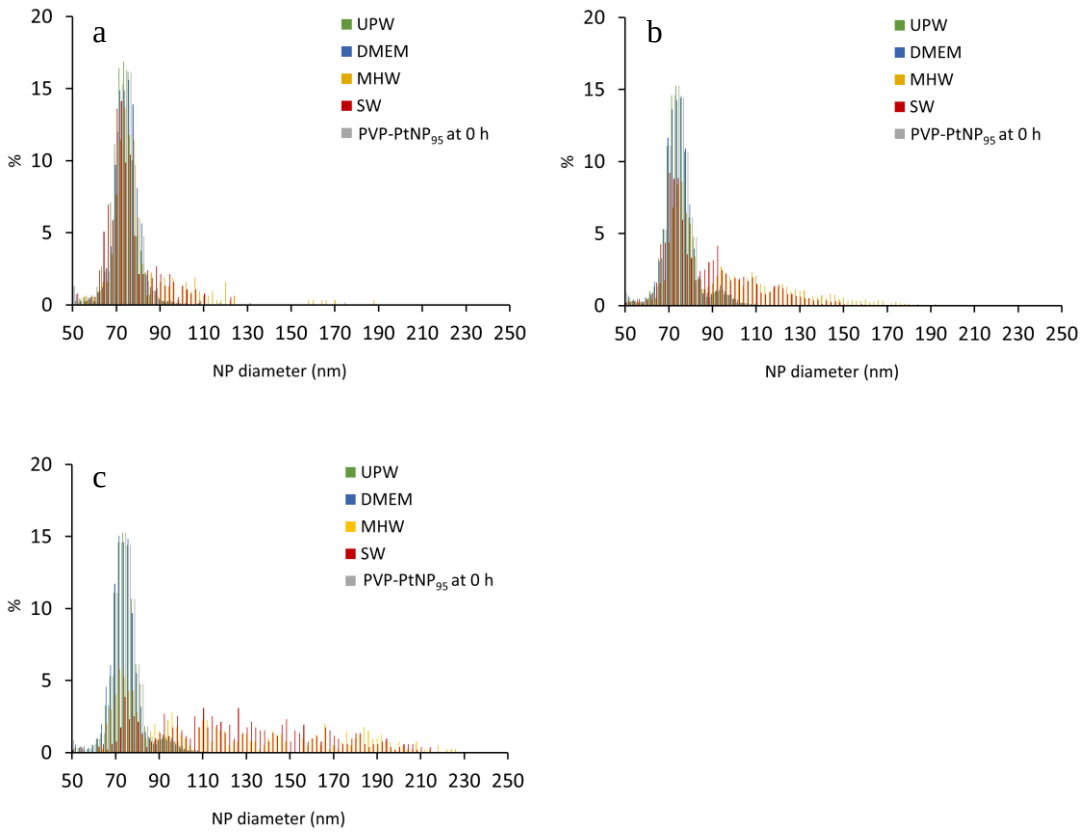

Figure 3.4. Size distribution of PVP-PtNP$_{95}$ after 24 h of adding the NPs to different media at initial exposure concentration of (a) 20 µg L^{-1}, (b) 200 µg L^{-1}, and (c) 2000 µg L^{-1}.

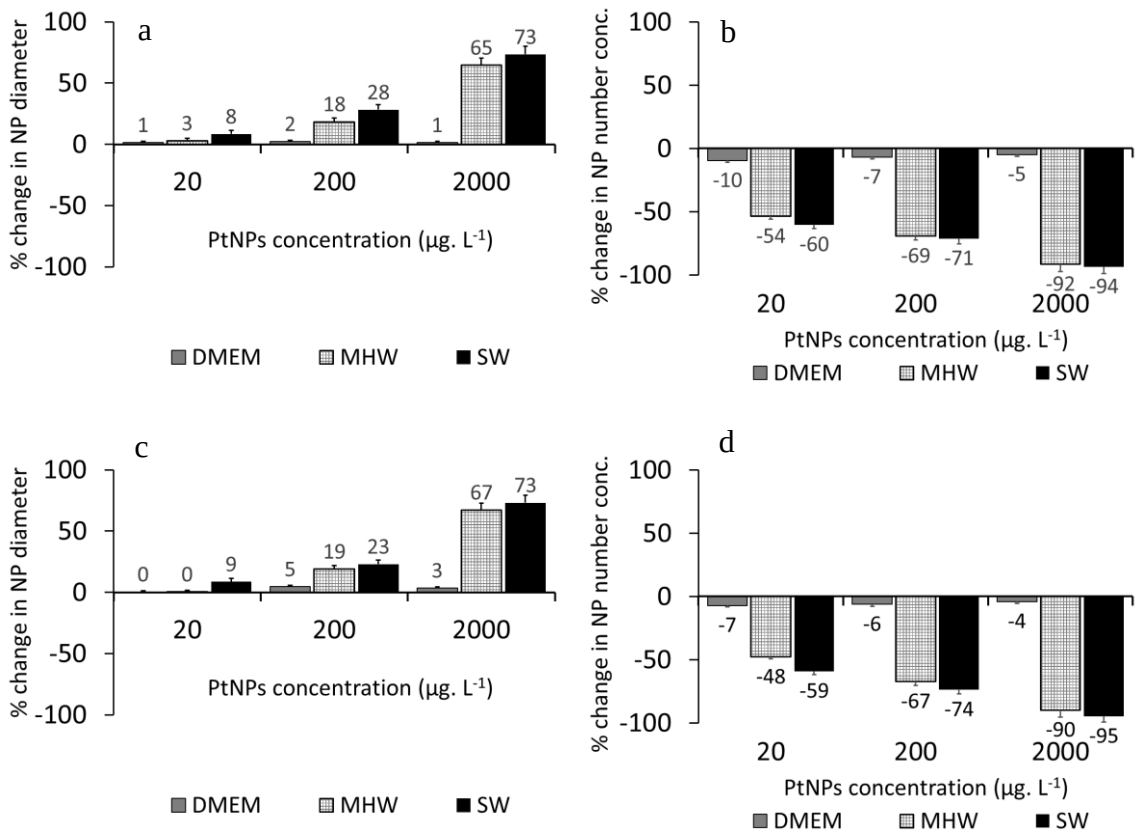

Figure 3.5. (a, c) Change in particle diameter (%), and (b, d) change in particle number concentration (%) after 24 h of adding cit-PtNPs (a, b) and PVP-PtNPs (c, d) to DMEM, MHW, and SW.

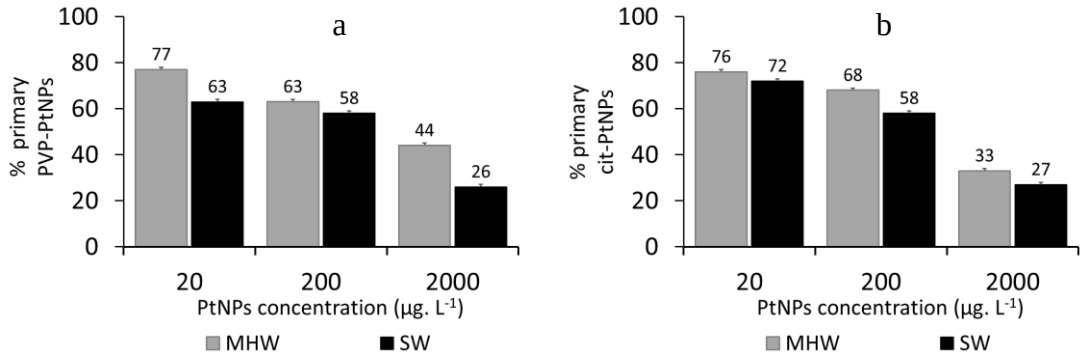

Figure 3.6. The percentage of primary particles remaining in suspension after 24 h of adding (a) PVP-PtNPs and (b) cit-PtNPs to moderately hard water (MHW) and 30 ppt synthetic seawater (SW). % of primary PVP-PtNPs was calculated number of primary NPs in the media after 24 hours relative to the total number of NPs in original suspension.

Table 3.1. Summary of PtNPs sizes measured by different sizing techniques. The reported sizes are for PVP-PtNPs, except where it is mentioned otherwise.

Method/measured or calculated parmaeter	Size of PtNPs suspensions (nm)				
	$PtNP_{20}$	$PtNP_{30}$	$PtNP_{50}$	$PtNP_{75}$	$PtNP_{95}$
AFM, $d_{AFM} \pm \sigma_d$	8.5 ± 1.2	10.3 ± 1.3	20 ± 4.77	40.5 ± 4.1	70.8 ± 4.2
TEM, $d_{TEM} \pm \sigma_d$ (d_{TEM}/ σ_d)	9.2 ± 1.2 (0.13)	10.9 ± 0.8 (0.09)	18.5 ± 5.0 (0.27)	44.5 ± 2.7 (0.06)	72.5 ± 3.9 (0.05)
sp-ICP-MS, $d_{sp\text{-}ICP.MS} \pm \sigma_d$	26.3 ± 1.5	32.4 ± 2.5	24.7 ± 1.6	42.9 ± 0.8	77.1 ± 0.8
FlFFF, $d_{FFF} \pm \sigma_d$	19.3 ± 1.5	25.6 ± 2.7	36.7 ± 3.5	59.6 ± 5.2	105.4 ± 4.1
DLS, $d_{DLS} \pm \sigma_d$ (PDI)	18.9 ± 0.3 (0.36)	31.4 ± 0.8 (0.19)	51 ± 0.7 (0.20)	74.7 ± 0.2 (0.03)	93.4 ± 1 (0.10)
DLS (cit-PtNPs in UPW), $d_{DLS} \pm \sigma_d$	10.0 ± 0.3	17.0 ± 0.3	31.6 ± 0.2	59.3 ± 0.3	83.5 ± 0.3
DLS (cit-PtNPs in 20 mM $NaNO_3$), $d_{DLS} \pm \sigma_d$	10.1 ± 1.9	14.0 ± 0.6	32.6 ± 1.3	52.8 ± 0.7	70.7 ± 0.9
$d_{DLS\text{-}PVP} - d_{DLS\text{-}cit\text{-}20\ mM\ NaNO3}$	8.8	17.4	18.4	21.9	22.7
PVP thickness	4.4	8.7	9.2	11	11.4
d_{AFM}/d_{TEM}	0.9	1	1.1	0.9	1
$d_{sp\text{-}ICP\text{-}MS}/d_{TEM}$	2.9	3	1.3	1	1.1
d_{DLS}/d_{FlFFF}	1	1.2	1.4	1.3	0.9

d_{AFM}: nanoparticle height measured by atomic force microscopy (AFM)
d_{TEM}: nanoparticle equivalent circular diameter measured by transmission electron microscopy (TEM)
$d_{sp\text{-}ICP\text{-}MS}$: nanoparticle equivalent spherical diameter measured by single particle-inductively coupled plasma-mass spectroscopy (sp-ICP-MS)
d_{FlFFF}: nanoparticle equivalent hydrodynamic diameter measured by flow-field flow fractionation (FlFFF)
d_{DLS}: nanoparticle equivalent hydrodynamic diameter measured by dynamic light scattering (DLS)

Table 3.2. Critical coagulation concentration (CCC) of cit-PtNPs in presence of monovalent ($NaNO_3$) and divalent ($Ca(NO_3)_2$) electrolytes

	CCC in $NaNO_3$ (mM)	CCC in $Ca(NO_3)_2$ (mM)
cit-$PtNP_{20}$	63.6	1.1
cit-$PtNP_{30}$	65.2	2.7
cit-$PtNP_{50}$	53.6	2.6
cit-$PtNP_{75}$	61.7	1.5
cit-$PtNP_{95}$	54.2	1.5

CHAPTER 4

COMPARATIVE STUDY OF DISSOLVED AND NANOPARTICULATE AG EFFECTS ON THE LIFE CYCLE OF AN ESTUARINE MEIOBENTHIC COPEPOD, *AMPHIASCUS TENUIREMIS* [1]

[1] Sikder, M., Eudy, E, Chandler, G.T., Baalousha, M. "Comparative study of dissolved and nanoparticulate Ag effects on the life cycle of an estuarine meiobenthic copepod, *Amphiascus tenuiremis*", *Nanotoxicology*, 2018, 12, 1-15

Running title: Comparative study of dissolved and nanoparticulate Ag effects on the life cycle of an estuarine meiobenthic copepod, *Amphiascus tenuiremis*

Author for correspondence:

Dr. Mohammed Baalousha, Ph.D. Center for Environmental Nanoscience and Risk, Department of Environmental Health Sciences, Arnold School of Public Health, University South Carolina, Columbia, South Carolina 29208, United States; Phone: (803)-777-7177; email: mbaalous@mailbox.sc.edu.

Abstract

Many nanotoxicological studies have assessed the acute toxicity of nanoparticles (NPs) at high exposure concentrations. There is a gap in understanding NP chronic environmental effects at lower exposure concentrations. This study reports life-cycle chronic toxicity of sub-lethal exposures of polyvinylpyrrolidone-coated silver nanoparticles (PVP-AgNPs) relative to dissolved Ag ($AgNO_3$) for the estuarine meiobenthic copepod, *Amphiascus tenuiremis*, over a range of environmentally relevant concentrations; that is 20, 30, 45, and 75 µg-Ag L^{-1}. A concentration-dependent increase in mortality of larval nauplii and juvenile copepodites was observed. In both treatment types, significantly higher mortality was observed at 45 and 75 µg-Ag L^{-1} than in controls. In $AgNO_3$ exposures, fecundity declined sharply (1.8 to 7-fold) from 30 to 75 µg-Ag L^{-1}. In contrast, fecundity was not affected by PVP-AgNPs exposures. A Leslie matrix population-growth model predicted sharp 60-86% declines in overall population sizes and individual life-stage numbers from 30-75 µg-Ag L^{-1} as dissolved $AgNO_3$. In contrast, no population growth suppressions were predicted for any PVP-AgNPs exposures. Slower release of dissolved Ag from PVP-AgNPs and/or reduced Ag uptake in the nano form may explain these sharp contrasts in copepod response.

4.1. Introduction

Ever increasing commercial application of engineered nanoparticles (NPs) has led to currently >1800 nano-enabled products in the consumer market, 438 of which contain silver nanoparticles (AgNPs) [26]. Environmental hazards to aquatic ecosystems are on the rise from episodic release of AgNPs from industrial, consumer, and medical products [225-227]. Expected environmental concentrations of AgNPs based on modeling approaches – in the aquatic environment (i.e., surface water, sewage treatment effluent) are estimated between 0.1 ng-Ag L^{-1} to 0.1 µg-Ag L^{-1} [32]. Thus, there is a need for better understanding of AgNPs behaviors and effects at environmentally-realistic low concentrations. Past eco-toxicological studies have focused on acute AgNP toxicity to bacteria [128], algae [228, 229], cladocerans [230, 231], fish [232, 233], aquatic plants [234], estuarine polychaete [235] and cell lines [236-238]. Many studies have demonstrated AgNP-associated lethality, reproductive failures, and embryonic development failures. Consistently, several studies have noted that AgNPs toxic effects might be due to NP dissolution and release of ionic silver [231, 239]. However, most of these studies employed high AgNPs concentrations (e.g., mg-Ag L^{-1}) with far less than lifecycle exposure times for most multicellular models. Furthermore, few studies have measured chronic toxicity under lower concentrations (e.g., µg-Ag L^{-1}) for AgNPs and other NPs [140-142], where dissolution behaviors might be different [51].

The meiobenthos, a group of short-lived micro-invertebrates, has gained attention as a useful collection of species for chronic bioassay of environmentally-realistic sediment and waterborne contaminants over lifecycle [240-242]. Meiobenthic copepods like *Amphiascus tenuiremis*, serve as a predominant food source for juvenile fishes, shrimps, and crabs [243, 244] and are often the most sensitive meiobenthic taxon to pollution [245]. Since *A. tenuiremis*

is at the base of the food web in estuarine ecosystems, changes in its population quantity or quality may result in population changes of other dependent fauna.

The aims of this study were to 1) determine and compare the lifecycle developmental and reproductive response of the model estuarine meiobenthic copepod, *Amphiascus tenuiremis,* to chronic µg-Ag L^{-1} levels of PVP-AgNPs and dissolved Ag using aqueous-renewal microplate-based lifecycle toxicity test [246]; and 2) predict/compare multigenerational effects at the population-growth level using empirical lifetable data collected from each toxicity test.

4.2. Materials and methods

4.2.1. Chemicals

All glassware used for AgNP synthesis was washed with 10% nitric acid followed by thorough washing by ultrahigh purity water (18.2 MΩ.cm). 99% pure sodium citrate ($Na_3C_6H_5O_7$) supplied by VWR (West Chester, USA), 99.9% pure silver nitrate ($AgNO_3$) and greater than 98% pure sodium borohydride ($NaBH_4$) supplied by Alfa Aesar (Ward Hill, USA), and 99% pure polyvinylpyrrolidone (PVP) of molecular weight 10,000 supplied by Sigma Aldrich (St. Louis, USA) were used for synthesis of AgNPs. Trace metal grade nitric acid (68-70% HNO_3) supplied by Fisher Scientific (Hampton, NH, USA) was used to acidify samples for inductively coupled plasma-mass spectroscopy (ICP-MS) analysis. Indium (supplied by PerkinElmer Internal Standard Mix, USA) was used as internal standard for ICP-MS analysis and ARISTAR PLUS silver (Ag) standard manufactured by British Drug House (BDH chemicals) was used to prepare standards for ICP-MS calibration. Crystal Seas™ bioassay grade synthetic seawater (SSW) was

purchased from Instant Ocean® (Marine Enterprises International, Baltimore, MD, USA) and the composition of SW is given in **Table D.1**.

4.2.2. Synthesis of PVP-AgNPs

Citrate-coated precursor AgNPs (cit-AgNPs) were first synthesized by reduction of Ag^+ ions using $NaBH_4$ as a reducing agent and citrate as a capping agent [165]. Briefly, 100 mL of 0.31 mM sodium citrate, 100 mL of 0.25 mM silver nitrate and 10 mL of 0.25 mM sodium borohydride were prepared in ultrahigh purity water (18.2 MΩ.cm) and kept in darkness at 4°c for 30 minutes. Silver nitrate and sodium citrate solutions were stirred in a flask at 700 rpm (50 g) for 10 minutes. After that, 6 mL of $NaBH_4$ was added and the resulting mixture was heated for 90 minutes at 115°C while stirring at 350 rpm (12 g). The resulting AgNP suspension was left overnight at room temperature to cool. Cit-AgNPs were then washed by ultrafiltration (Amicon, 1 kDa regenerated cellulose membrane, Millipore) to remove excess reagents. 200 ml of resulting cit-AgNP suspension was cleaned by pressurized stirred ultrafiltration cell (Amicon, 1 kDa regenerated cellulose membrane, Millipore) to remove excess reagents before use. AgNP suspension volume was reduced to 100 ml and then replenished by 100 ml of 0.31 mM sodium citrate solution. This process was repeated three times to ensure removal of the majority of remaining dissolved Ag. Polyvinylpyrrolidone-coated silver nanoparticles (PVP-AgNPs) were obtained by ligand exchange of the cit-AgNPs precursor [75]. Briefly, 200 mL cit-AgNPs were converted into PVP-AgNPs by adding 1mL of 1.25 mM PVP (molar mass 10,000 g/mol) solution under vigorous stirring (i.e., 700 rpm) for at least 1 hour. This amount of PVP was required to obtain full surface coverage of AgNPs by PVP molecules and thereby gain full steric stabilization [94]. PVP coating was used in this study because it is a nontoxic

polymer widely used to sterically-stabilize NPs, preventing their aggregation even at the high ionic strength of sea water, and thus eliminating any aggregation-influenced toxicity response [247-249].

4.2.3. Characterization of AgNPs

AgNPs were characterized using a multi-method approach including surface plasmon resonance (SPR), dynamic light scattering (DLS), inductively coupled plasma mass spectroscopy (ICP-MS) and atomic force microscopy (AFM) [166-168]. Z-average hydrodynamic diameter (Z-avg.), and polydispersity index (PDI) of synthesized PVP-AgNPs were measured by dynamic light scattering (Malvern zeta sizer nano-ZS, Westborough, MA, USA). Electrophoretic mobility of PVP-AgNPs was measured by laser Doppler electrophoresis (Malvern zeta sizer nano-ZS, Westborough, MA, USA), which was used to calculate the zeta potential using Smoluchowski's assumption [195]. SPR spectra of PVP-AgNPs aliquots were recorded over 200 to 800 nm using a UV-vis spectrometer (UV 2600, Shimadzu Co., Kyoto, Japan) and a 10 cm path-length quartz cuvette. All measurements were performed in triplicate.

Atomic force microscopy (Cypher ES™ AFM, Asylum Research, Santa Barbara, USA) was used to measure the height (core size) and size evolution of PVP-AgNPs over 72 h in 30 ppt Crystal Seas™ bioassay grade SW. AFM samples were prepared by depositing a drop of PVP-AgNPs suspension on freshly cleaved mica substrates for 20 minutes, followed by thorough washing with UPW to avoid salt crystallization and NP aggregation [158]. AFM analyses were carried out in true non-contact mode under ambient conditions. All images were recorded in ACAirTopography mode with 256x256 pixel size resolution and a scan rate of 1.0 Hz. At least five different areas on each substrate were

analyzed and a minimum of five images from each area were collected, resulting in at least 25 images for height analysis on each substrate. At least 140 height measurements were performed for each sample, which is sufficient to produce a representative and robust particle size distribution [166].

4.2.4. Test organism

Amphiascus tenuiremis is a diosaccid harpacticoid copepod that is amphi-Atlantic in distribution ranging from the North Sea/Baltic intertidal to the southern Gulf of Mexico [250]. *A. tenuiremis* is a muddy-sediment dwelling copepod that cultures well in sediments or seawater alone under laboratory conditions. It is a suitable test species for acute-to-lifecycle sediment or water bioassays due to its moderate acute sensitivity, high chronic sensitivity, and its small size (0.4 and 0.25 mm for females and males respectively) [246]. In 30 ppt SSW at 25˚C, *A. tenuiremis* passes through 12 life stages and 3 distinct morphologies (*i.e.*, nauplius, copepodite, and adult), becomes reproductively competent in approximately 15 days, and has a median life time of 49 days. Adult females produce five to seven clutches per lifetime with each clutch averaging six to eight embryos in water-only culture [251, 252]. All *A. tenuiremis* used in this study were obtained from laboratory sediment cultures [253] originally collected from a pristine muddy sediment site in the North Inlet Estuary, South Carolina, USA.

4.2.5. Acute toxicity test

A 96-hour acute toxicity test with adult *A. tenuiremis* was performed to determine median lethal toxicity of PVP-AgNPs and $AgNO_3$. Five nominal Ag concentrations (45, 75, 130, 216, 360 µg-Ag L^{-1}) and a SW control (30 ppt) were tested. All test glassware was

washed with 10% HCl (Fisher Scientific, Hampton, NH, USA) and rinsed with UPW for at least three times. SW (30 ppt salinity; Instant Ocean®, aquarium systems, Mentor, OH, USA) was aerated to > 90% O_2 saturation and then filtered at 0.45 µm. SW was spiked with fully-characterized PVP-AgNPs and $AgNO_3$ (10 mg-Ag L^{-1} stock) in a 100-mL volumetric flask. Each treatment, including control, employed two replicates for a total of 24 polystyrene petri-dishes (Fisher Scientific, Hampton, NH, USA). 20 haphazardly selected adult *A. tenuiremis* were gently transferred into one petri dish using an analytical grade Wire-Trol® glass capillary pipette (Drummond Scientific, Broomall, PA, USA). After the transfer, overlying SW was drawn out under microscopy by analytical grade 500-µL Hamilton® glass syringe (Hamilton, Reno, NV, USA) so that <5 µL of SSW remained. Control (SW) and treatment solutions (6 mL/petri dish) were added back immediately. The petri-dishes were incubated static at 25˚C for 96 h under 12:12 h light: dark conditions. The number of dead in each petri-dish was recorded each day. At the end of the exposure period, the number of surviving copepods in each dish was counted. These data (**Figure 4.3a**) were used to define a lower sublethal range of exposure concentrations (i.e., < 75 µg-Ag L^{-1}) for definitive 35-day lifecycle bioassays in 96-well microplates.

4.2.6. 96-well microplate life cycle toxicity test

Standardized lifecycle microplate bioassay methods [246, 254] were used to measure lethal and sublethal chronic responses of *A. tenuiremis* to PVP-AgNPs at µg L^{-1} concentrations in SW. Using the same methods, PVP-AgNPs toxicity was compared to toxicity from a positive Ag control, i.e., the soluble silver salt – silver nitrate ($AgNO_3$) – dissolved SSW. Life-table data collected from each bioassay were entered into the Leslie (Lefkovich) matrix (LM) to generate comparative projections of future population

abundance and population age/stage structure at the fourth filial generation under each toxicant condition [255]. This bioassay method measures individual mean fecundity through two broods; but females of this species produce on average 5-7 broods during a mean lifetime of 49 ± 2 days [251]. Thus, LM population abundance projections presented for treatments and controls are truncated (lower) than the absolute population sizes possibly achievable by *A. tenuiremis* in the field.

4.2.6.1. Collection of test copepods.

A. tenuiremis for the study were gently sieved from flow-through muddy sediment monocultures in the laboratory [253, 254] with 100's of adults pipetted to a 12-well Costar Netwell® microplate containing SW and 75-µm mesh cup inserts. The inserts allowed hatching nauplii from gravid females to continuously fall ~3 mm to the microwell bottom over an 18-24 h period while retaining the larger adults. Captured nauplii (< 18 h old) were then transferred individually to microwells of sterile 96-well ultra-low attachment polystyrene microplates (Corning Costar, Corning, NY) [246, 254].

4.2.6.2. Preparation of treatment solutions and microplates.

For lifecycle testing, a SSW control and four lower Ag concentrations (20, 30, 45, and 75 µg-Ag L^{-1}) were prepared in SSW as described above. 10 mg-Ag L^{-1} PVP-AgNPs and $AgNO_3$ measured concentrated stocks were used to spike all treatment solutions. Fifteen ultra-low-attachment (*i.e.* hydrophilic) polystyrene 96-well microplates (300 µL well volume) were hydrated with UPW for 1 hour, dumped and allowed to air dry before refilling with 250 µL of 0.2 µm filtered and aerated SSW test solution. Haphazardly selected nauplii were gently transferred into microwells using analytical grade Wire-Trol® glass capillary pipette (Drummond Scientific, Broomall, PA, USA) silanized with an air-

dried solution of 80, 3, and 1.5% ethyl alcohol, isopropyl alcohol, and ethyl sulfate, respectively, to facilitate non-sticky naupliar transfer. After naupliar loading, overlying transferred SSW was drawn out under a stereomicroscope by analytical grade 500-µL Hamilton® glass syringe (Hamilton, Reno, NV, USA) so that < 5 µL of SSW remained. This procedure standardizes the starting test volume in each microwell and allowed minimum dilution of the treatment solutions from the initial nauplius transfer. Treatment and control solutions (250 µL/microwell) were added back to wells within 2-5 minutes using Finnpipette® multichannel analytical pipette (Thermo Labsystems, Vantaa, Finland). Two µL of fresh centrifuged 1:1:1 mixed algal cell (~$2*10^7$ cells/mL) suspension of *Isochrysis galbana, Dunaliella tertiolecta, and Rhodomonas sp.* were then added to each well using a Finnpipette® analytical pipette. Each microplate was covered and placed in a temperature regulated incubator at 25˚C with 12:12 h light:dark photoperiod. Per ASTM [246] and OECD guidelines [254], 96 nauplii were tested over three replicate microplates for each treatment and control. Every other 12-well row was reserved for individual copepod pairing and mating within each treatment or control, usually on days 18-20 of the test. Test solutions in each microwell were aspirated and replaced under microscopy every 3 days by 250-µL Hamilton glass syringe. Care was taken to ensure that no copepods were aspirated into the syringe, and no copepods experienced desiccation stress.

4.2.6.3. Copepod rearing, pairing, and mating.

Survival and development rates of *A. tenuiremis* were recorded daily in each test microwell by inverted microscopy. Copepod sex was recorded at reproductive maturity. Sexually mature males and females were collected and haphazardly paired within each treatment as individual mating pairs – one pair per microwell. All mating microwells were

then reloaded with 250 µL of fresh control or treatment solution, and each mating pair was fed 2 µL of algae mixture as described above. Each mating pair was checked daily for the following end points: male and female survival, mating success, days to 1st and 2nd clutch hatch, days between successive clutches, and total fecundity over two clutches. For all treatments, the test terminated at day 35 or after the 2nd clutch hatch, whichever occurred first.

4.2.7. Stage structured population growth model

Multi-generational population level effects of $AgNO_3$ and PVP-AgNPs were estimated using empirical microplate life cycle data fitted to a stage-structured four generation Leslie matrix model (RAMAS® EcoLab 2.0, Applied Biomathematics, Setauket, NY, USA) [256-258]. A five life-stage (nauplius:copepodite:virgin-male:virgin-female:gravid female) matrix model projected population changes through four generations in each treatment or control based on (a) stage specific survival and next stage transition rates, (b) proportions of copepodites developing into males or females (thereby capturing sex ratio shifts), (c) proportions of females able to become gravid and produce two viable clutches, and (d) fecundity (i.e., number of hatched nauplii per mating pair) through two clutches. Population projections were compared and presented relative to each within-experiment control response rather than as absolute abundance differences across $AgNO_3$ and PVP-AgNPs exposures. Treatment-specific instantaneous rates of population increase (λ) also were calculated for each treatment and control population. At $\lambda=1$ replacements equal loss; thus, population size is projected stable and neither increasing nor decreasing over time.

4.2.8. Transformations of PVP-AgNPs in synthetic seawater (SSW)

For PVP-AgNPs and $AgNO_3$ lifecycle toxicity tests, control and treatment solution samples were collected in triplicate at test initiation and at each renewal period (every 3 d, from microwells). Dissolved Ag species were separated from PVP-AgNPs using centrifugal ultrafiltration (3KDa regenerated cellulose membranes, Amicon Ultra-4) at 3250g for 15 minutes. The original (total Ag) and ultrafiltered (dissolved Ag) samples were acidified to 10% HNO_3 and then diluted 200-fold in 1% HNO_3 prior to ICP-MS (NexION™ 350D, PerkinElmer Inc., Massachusetts, USA) analysis to minimize matrix effects and avoid salt precipitation. Indium (analytical grade, BDH®, VWR International LLC, PA, USA) was used as an internal standard to correct for non-spectral interferences during analysis [169].

Additional experiments were conducted to quantify Ag sorption onto the microplates and onto algal food cells. 20 and 75 µg-Ag L^{-1} (i.e., lowest and highest exposures of the life-cycle test) as $AgNO_3$ or PVP-AgNPs were added to microwells without copepods and algae, followed by sample collection at 0, 24, 48, and 72 h. Sorption of Ag on algal cells was investigated by mixing 20 and 75 µg-Ag L^{-1} (as $AgNO_3$ or PVP-AgNPs) with algae in 100-mL Erlenmeyer flasks at the same concentrations that were given to copepods as food followed by serial SSW sample collection at spaced time points (e.g., 0-72 h). Dissolved Ag in SSW was separated from PVP-AgNPs by centrifugal ultrafiltration. Total and dissolved Ag concentrations were then measured by ICP-MS following sample treatment as described above. All samples and analyses were done in triplicate.

4.2.8. Statistical analysis

All statistical analyses were performed with SAS® version 9.4 software (SAS Institute, Cary, NC, USA). The following dependent variable means were tested for statistical significance: stage-specific survival, development rates, and percent of females becoming gravid (fertility), and brood size through two clutches (fecundity). Copepod survival, percent gravid, and offspring production within treatments and microplates were analyzed using general linear model (GLM) nested ANOVA and Tukey's multiple comparison tests. Statistical significance was set at *p-value* < 0.05.

4.3. Results and discussions

4.3.1. PVP-AgNPs characterization and transformation in synthetic seawater (SSW)

The total and dissolved Ag concentrations in the PVP-AgNPs stock suspension were 11.5 ± 0.08 and 0.45 ± 0.03 mg-Ag L^{-1}, respectively. AFM micrographs show randomly-distributed PVP-AgNPs on the mica substrate with no aggregated particles (**Figure C.1**), indicating good sample preparation quality and good dispersion of synthesized PVP-AgNPs in UHPW [166]. The number-weighted PVP-AgNPs particle height measured by AFM was approximately 11.3 ± 3 nm, with a height distribution range predominantly (>81%) between 8-14 nm (**Figure C>1b**). The Z-average (intensity-weighted) hydrodynamic diameter measured by DLS was 21.6 ± 0.3 nm. The larger Z-average hydrodynamic diameter compared to the particle height measured by AFM can be attributed to the higher light scattering intensity from larger particles resulting in a bias toward larger sizes [166]. The zeta potential of synthesized PVP-AgNPs was -9.6 ± 1.1 mV.

The initial mean PVP-AgNPs particle heights in UHPW and SSW (11.7 ± 3 and 12 ± 3 nm, respectively) were not significantly different (two tailed t-test, $p>0.48$). UV-vis SPR spectra of PVP-AgNPs in UHPW and SSW exhibited a characteristic absorption maximum at 404 nm (**Figure C.2a,b**) without peak, suggesting that PVP-AgNPs remain colloidally stable (i.e., do not aggregate) and do not undergo shape transformation in our SSW [51, 188, 220]. However, PVP-AgNPs did dissolve in SSW in a concentration-dependent manner (**Figure 4.1a**); that is PVP-AgNPs dissolved at a higher rate and to a greater extent as initial NPs concentrations decreased [51, 220]. At low concentrations (e.g., 20 and 30 µg-Ag L^{-1} NPs), PVP-AgNPs dissolved completely (>98%) within 72 h; whereas at higher concentrations (*e.g.*, 45 and 75 µg-Ag L^{-1}) 88% and 78% of NPs mass, respectively, dissolved over 72 h. The dissolution of PVP-AgNPs also resulted in a decrease in particle height (size) over time (**Figure 4.1b and C.3**). PVP-AgNPs particle size distribution shifted toward smaller sizes and narrower size distributions (**Figure C.3**). At 72 h, PVP-AgNPs were not detected at low NP concentrations, which agrees with complete dissolution as supported by ICP-MS analysis. These findings suggest that exposure to PVP-AgNPs in SSW is dynamic with variable NP and dissolved ion concentrations, and NP sizes changing over time.

4.3.2. Acute 96-hour exposure effects

For $AgNO_3$ exposures, measured mean Ag concentrations were 42.5±3.1, 80.5±2.4, 139.9±2.2, 217.3±3.9, and 351.4±6.8 µg-Ag L^{-1} respectively for the nominal target concentrations of 45, 75, 130, 216 and 360 µg-Ag L^{-1} (**Figure C.4a**). Baseline 4.3±0.2 µg-Ag L^{-1} was measured in control treatment during acute exposures. As measured Ag concentrations were ≥ 93% of nominal targets for $AgNO_3$, exposure concentrations are

reported on a nominal basis. Similarly, in PVP-AgNPs exposures, measured Ag concentrations were 49.1±3.8, 77.9±4.5, 138.7±2.6, 217.5±5.3 and 355±7.1 µg-Ag L^{-1} for the same nominal targets; (i.e., ≥ 91% of nominal targets, **Figure C.4a)**. Thus PVP-AgNPs also are reported nominally.

All water quality parameters (e.g., salinity, pH, and dissolved oxygen) met American Society of Testing and Materials (ASTM) guidelines for the acute exposure test [259]. During the acute exposure (**Figure C.10**), control mortality was less than 10%. $AgNO_3$ and PVP-AgNPs were toxic to *A. tenuiremis* at or above 75 µg L^{-1}(**Figure C.10**), with significantly higher acute toxicity for $AgNO_3$ (96-hour LC_{50}= 64.8 < 72.8 < 80.2 µg-Ag L^{-1}) compared to PVP-AgNPs (96-hour LC_{50}= 95.2< 106.8 < 118.4 µg-Ag L^{-1}). Previous tests with the planktonic copepod *Acartia tonsa* reported a 48-h LC_{50} of 43 µg-Ag L^{-1} for dissolved Ag in the same order of magnitude as our present 96-h finding [260].

The toxicity of AgNPs have been attributed to the NPs directly, or the release of Ag^+ from AgNPs dissolution, or both [97, 261, 262]. In this study, the observed differences in the toxicological outcomes for $AgNO_3$ and AgNPs can be attributed to the dynamic nature of the exposure. For $AgNO_3$ treatments, copepods were exposed to the maximal Ag exposure concentration (as dissolved Ag) from the beginning of the test to the end. For PVP-AgNPs treatments, copepods were exposed to a combination of intact PVP-AgNPs and dissolved Ag released from PVP-AgNPs. Thus, for PVP-AgNPs treatments, copepods were exposed for shorter times and/or to lower amounts of the most biologically-active/bio-available dissolved Ag over the 96-hour exposure [203]. Such differences in the nature of the full exposure regime could explain the sharply higher acute toxicity of $AgNO_3$ relative to PVP-AgNPs.

4.3.3. Chronic life cycle exposure effects

4.3.3.1. PVP-AgNP behavior in the bioassay environment

Total Ag concentrations in SSW were measured by ICP-MS at each of ten water changes during the $AgNO_3$ and PVP-AgNPs copepod lifecycle tests. Low Ag concentrations of 4.3±0.6 and 4.8±1.0 µg-Ag L^{-1} were measured in control for the $AgNO_3$ and PVP-AgNPs experiments, respectively. At time-zero in $AgNO_3$ exposures, measured total Ag concentrations (20±2.3, 30±2.4, 46.1±4.3, and 78.1±1.5 µg-Ag L^{-1}) were ≥ 94% of nominal target concentrations (*i.e.*, 20, 30, 45, 75 µg-Ag L^{-1}, **Figure C.4b**). In PVP-AgNPs exposures, measured total Ag concentrations at time-zero (22.3±2.7, 31.4±3.5, 46.1±4.5, and 73.3±3.3 µg-Ag L^{-1}) were ≥ 87% of same nominal targets (**Figure C.4b**). Thus, results are presented with nominal concentrations.

At the end of each 72-h renewal period, dissolved Ag concentrations measured in microwells containing algae and copepods were sharply lower for $AgNO_3$ (only 5-10% initial concentrations) and PVP-AgNPs (15-20% initial) (**Figure C.5**) compared to Ag concentrations in the absence of algae and copepods (**Figure 4.2**). These low dissolved Ag concentrations at 72-h may be attributed to: (1) sorption of dissolved Ag on microplate well walls, (2) sorption of dissolved Ag on algal cells, and/or (3) Ag bioaccumulation by growing copepods. To explore these questions, we conducted additional experiments.

First, 20 and 75 µg-Ag L^{-1} (*i.e.*, lowest and highest exposures in life-cycle test) as $AgNO_3$ and PVP-AgNPs were added to 30 ppt SW in microplate microwells (without copepods and algae) followed by sample collection at 0, 24, 48, and 72 h. Approximately, 90-95% added Ag was recovered from microplates (**Figure C.6a,b**) and total Ag concentrations (at 0 h) were not significantly different ($p>0.97$) compared to recovered

dissolved Ag (after 72 h). These results confirm the absence of Ag losses in the low-adsorption hydrogel-coated microwell. For PVP-AgNPs, the percent dissolved Ag concentration increased with time in organism-free microwells (**Figure C.6c,d**) due to NP dissolution. Dissolution behavior of PVP-AgNPs in microplates was similar to that in batch experiments (**Figure 4.1a**) indicating that the low-adsorption microwell environment *per se* has no impact on PVP-AgNP dissolution behavior.

Second, to evaluate the impact of algae on dissolved Ag concentrations, 20 and 75 µg L^{-1} $AgNO_3$ and PVP-AgNPs were added to microwells loaded with 2 µL algae ($2*10^4$ cells) in SSW under the same exposure but using finer time-sampling conditions. For the 20 µg-Ag L^{-1} $AgNO_3$ exposure, > 90% of total dissolved Ag associated with algae within 30 minutes (**Figure C.7**). For the 75 µg-Ag L^{-1} $AgNO_3$ exposure, 59% of dissolved Ag associated with algae within 30 minutes and then increased to > 90% Ag by 72 h (**Figure C.7**). Similarly, for PVP-AgNPs, dissolved Ag in microwells represented < 20% of the total Ag released by PVP-AgNPs dissolution over the 72-hour renewal period (**Figure 4.2a,b**). For both the 20 and 75 µg-Ag L^{-1} NP exposures, Ag sorption on algae was rapid (**Figure 4.2**) and dissolved Ag decreased with time in the solution phase. After 72 h, only 3.7 and 8.4 µg-Ag L^{-1} respectively remained in solution at 20 and 75 µg-Ag L^{-1} PVP-AgNPs.

4.3.3.2. Copepod survival and development rates in chronic lifecycle exposures

Development of the most sensitive naupliar copepod life-stage was normal in all Ag-free controls with an overall control mortality ≤ 10% (**Figure 3b**). Naupliar mortalities in the 20 and 30 µg-Ag L^{-1} treatment (for both $AgNO_3$ and PVP-AgNPs) were also ≤ 10%. However, significantly higher naupliar mortality was seen at 45 and 75 µg-Ag L^{-1} (*p-value*

< 0.05). Both $AgNO_3$ and PVP-AgNPs produced a concentration-dependent increase in naupliar and copepodite mortality that peaked at 34 and 23 % death, respectively (**Figure 4.3b,c**). As this bioassay is focused on measuring sublethal lifecycle effects, test concentrations were set to achieve ideally ≤ 30% maximum naupliar mortality. This condition was largely met. The highest 75 µg-Ag L^{-1} exposure to $AgNO_3$ and PVP-AgNPs yielded only 23.8% and 17.7% naupliar mortality, respectively. $AgNO_3$ showed consistently higher naupliar mortality than PVP-AgNPs in most treatments; but cross-treatment differences were significant only at 45 µg-Ag L^{-1} (*p-value* < 0.05). $AgNO_3$ and PVP-AgNPs exposures produced lower but similar (*p-value* > 0.05) mortality patterns (**Figure 4.3c**) across the treatment concentration range for the less sensitive juvenile copepodite stage.

Nauplius-to-copepodite development rates (i.e., days to copepodite; **Figure C.8a**) were not significantly different across treatments and control, except at 75 µg-Ag L^{-1} PVP-AgNPs, which was delayed by 2 days (p< 0.05). For the copepodite-to-adult development window, no significant effect of Ag in either form was observed (**Figure C.8b**).

Overall, these results show that larval nauplii are the most sensitive copepod life-stage to Ag generally. Based on naupliar mortality patterns, repeated 72-h exposures to dissolved $AgNO_3$ were more toxic than repeated exposures to PVP-AgNPs. However, juvenile-stage copepodite mortality and development rates (i.e., copepodite-to-adult) were not significantly different between Ag treatments.

4.3.3.3. Reproductive effects

The number of adult mating pairs able to produce viable offspring through ≥ 18 d of mating was significantly reduced in the 30 and 75 µg-Ag L^{-1} $AgNO_3$ treatments relative

to controls ($p < 0.05$, **Figure 4.4**). Reproductive success is defined as proportion of females in each treatment able to produce at least two viable clutches of offspring in $\leq$ 35 days. The 30 and 75 µg-Ag L^{-1} $AgNO_3$ treatments showed 55% and 81% lower mating success, respectively, while 20 and 45 µg-Ag L^{-1} $AgNO_3$ treatments showed decreases of 23% and 25% relative to controls ($\geq$ 67% successful; **Figure 4.4**). Note that higher $AgNO_3$ concentrations (*e.g.*, 45 and 75 µg-Ag L^{-1}) led to low n-sizes of only 4 and 2 mating pairs respectively due to high lifetime copepod mortality. Because of these low n-sizes no statistical inferences can be made regarding actual mating success at these concentrations. For those surviving females able to reproduce, the time required to extrude/hatch two brood sacs was delayed significantly by 2.5 and 3.3 days respectively at 45 and 75 µg-Ag.L^{-1} $AgNO_3$ (*p-value* < 0.05, **Figure 4.5**). In contrast to $AgNO_3$, mating success in PVP-AgNPs treatments was not significantly different from controls at any concentration (*p-value* > 0.37, **Figure 4.4**), and no significant delays in brood sac extrusions/hatch occurred (*p-value* > 0.1, **Figure C.9**).

Mean fecundity was calculated as the average number of hatched offspring through two broods per successful mating pair in $\leq$ 35 days. Increasing $AgNO_3$ concentrations produced a consistent trend of depressed fecundity (19% to 40% lower) compared to the control (*p-value* < 0.05, **Figure 4.6**). In sharp contrast, PVP-AgNPs had no significant effects on fecundity at any concentration (*p-value* > 0.27, **Figure 4.6**) even though Ag was liberated freely by PVP-NPs dissolution over the exposure period.

4.3.3.4. Stage-structured Leslie matrix population growth models

The microplate culturing approach allows life-cycle tracking of each individual's survival, development, sex, fertility, and reproductive output (fecundity). These endpoints

allow population level responses to be predicted over time via a life-stage based adaptation of the Leslie (Lefkovich) matrix (LM) population growth model [256-258]. LM models also predict finite rates of population increase (λ, instantaneous growth rate) based on same measured stage-specific mortality, sexual development, and reproductive endpoints [263]. A λ of unity implies a population is neither growing nor declining. A value less than unity implies population decline, and greater than unity implies population growth. $AgNO_3$ λ's ranged from 0.76 for the highest 75 µg-Ag L^{-1} treatment to 1.21 for the lowest 20 µg-Ag L^{-1} treatment. The instantaneous growth rate for the $AgNO_3$ control population was 1.24, but the 30 and 75 µg-Ag L^{-1} treatment data predicted sharply reduced growth rates (Table 1). In contrast, all PVP-AgNPs copepod populations had λ's in strong excess of unity and similar to Ag-free controls. The highest 45 and 75 µg-PVP-AgNPs L^{-1} treatment showed mildly suppressed λ's relative to controls, but both were well-above "no-growth" unity (**Table 4.1**).

λ provides a single-digit rate estimation of potential population growth but the Leslie matrix gives multi-generational projections of copepod population size and age-stage structure for each treatment and control population at multiple future generations (e.g., four in this study). [Four generations were arbitrarily chosen; see **Figure 4.7a**]. The 30-75 µg-Ag L^{-1} life-table data for $AgNO_3$ predicted sharp decreases of 60-86% in estimated population sizes relative to the control. In contrast, the 30-75 µg-Ag L^{-1} life-table data PVP-AgNPs, predicted 2-5 times **higher** population sizes than for $AgNO_3$, even though measured dissolved Ag in PVP-AgNPs SSW exceeded 30 µg L^{-1} within 24 h in, for example, the 75 µg-Ag L^{-1} PVP-AgNPs treatment (**Figure 4.1a**). $AgNO_3$ life-table data at 30, 45 and 75 µg-Ag L^{-1} similarly predicted sharp depressions in relative abundances of

every individual copepod life-stage (**Figure 4.7b-d**). Relative to PVP-AgNP controls, naupliar larvae projections were depressed 9.8-77.3%, copepodite juveniles by 45.7-81.9%, adult females by 62.6-78.5%, and gravid females by 64.4-89%. In $AgNO_3$, these predicted life-stage declines were primarily driven by low reproductive success (fertility and fecundity) in the bioassay. In contrast, PVP-AgNPs life-table data produced fourth-generation life-stage structures that were all similar to control structure/abundance irrespective of PVP-AgNPs concentration (**Figure 4.7b-d**).

Amphiascus tenuiremis survival and reproductive ability is highly sensitive to dissolved Ag concentration. This is consistent with previous studies where, for example, Ag-related reproductive, histological and biochemical impairment of planktonic copepods (*Acartia tonsa*) and daphniids (*Daphnia magna*) occurred when they were fed algal food incubated in dissolved Ag ($AgNO_3$) at 27-108 µg-Ag.L^{-1} (0.25- 1 nM) [260, 264]. Reduced egg numbers were observed when *A. tonsa* was fed algal food exposed to $AgNO_3$, and total protein concentration per egg (lipovitellin) and percentage of copepod females with developed ovaries decreased with increasing Ag ingestion [260]. Lipovitellin is the predominant soluble egg protein [265] in crustaceans and most invertebrates, and its accumulation in egg follicles is required for maximum egg quality and offspring survival/development [266]. These studies demonstrate that dietary metals' assimilation efficiencies by copepods is strongly related to the metal concentrations inside or on the surface of algal food which potentially become bioavailable during ingestion [267-269].

4.3.3.5. Nature of the exposure: dissolved Ag vs. AgNP effects

Toxicity of AgNPs has been attributed to direct AgNPs effects, the release of Ag^+ from AgNPs dissolution, or to both [97, 261, 262]. In this study, the observed differences in

toxicological response for $AgNO_3$ versus AgNPs can be attributed to the dynamics of $[Ag^+]$ change over each 72-h treatment renewal period. For each $AgNO_3$ test concentration, copepods were exposed for 35 days to the maximal dissolved Ag concentration that could be delivered, in fresh 72-h doses, and with a significant proportion of dissolved Ag rapidly sorbed to the surfaces of algal cell food. For PVP-AgNPs treatments, the actual realized exposure is a combination of intact PVP-AgNPs in suspension and also associated with algal food, plus any released dissolved Ag from the PVP-AgNPs' gradual dissolution and sorption to food. Hence, under similar microplate conditions, PVP-AgNPs exposures likely produced less freely-dissolved Ag than $AgNO_3$ exposures. Thus, for PVP-AgNPs, copepods likely were exposed integratively to lower amounts of the most biologically-active dissolved Ag complexes over each 72-h microwell SW renewal and subsequently to lower total amounts over the full 35-d test duration. This could explain the sharply lower effects of PVP-NPs (i.e., better survival, development, reproduction, and population growth potential) on *A. tenuiremis* compared to the severe chronic effects observed for dissolved $AgNO_3$.

4.4. Environmental Implications

Copepods are the most abundant arthropods on earth, and nearly the most abundant of all metazoans known, rivaled only by nematode round-worms [270]. For aquatic/marine ecosystems they are key to food-web integrity, quality and sustainability [271]. Impacts of contaminants on the reproductive success of any important prey species could affect the population dynamics of that species and possibly other species dependent on it through selective grazing or predation. Since *A. tenuiremis* and other meiobenthic copepods are a

key part of the diet of fishes [244], shrimps, and crabs [243], there is potential for Ag uptake and subsequent transfer to higher level organisms of direct value to humans.

Copepod exposure to PVP-AgNPs had little effect on their ability to survive, reproduce, and increase population size. Environmental release of AgNPs from consumer products, sewage outfalls, etc. would however still pose some risk to marine ecosystems through rapid and complete dissolution of AgNPs in seawater. Therefore, researchers, policy-makers and regulators should carefully consider unintended effects of dissolved Ag release from AgNPs when considering potential risks of AgNPs. For a more informed risk assessment of AgNPs, future studies should evaluate whether dissolved Ag and AgNPs exhibit similar reproductive and population toxicity patterns for a broader spectrum of chronically-exposed invertebrate phyla. Such population-relevant data, along with others, could be used to produce a more useful holistic model for predicting AgNPs risks to estuarine and aquatic ecosystems.

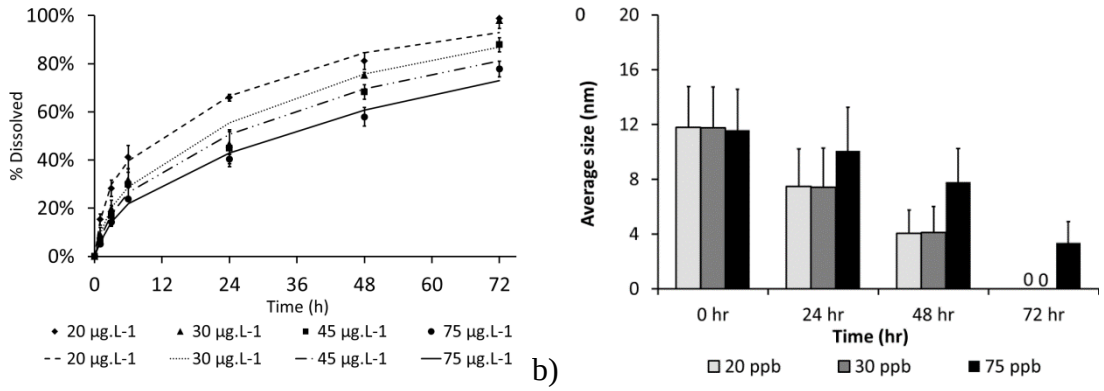

Figure 4.1. Behavior of PVP-AgNPs in 30 ppt synthetic seawater (SW): (a) % dissolved Ag measured by ICP-MS following centrifugal ultrafiltration as a function of time, and (b) average NP size measured by AFM as a function of time after mixing 20, 30, 45, and 75 $\mu g.L^{-1}$ PVP-AgNPs with SW

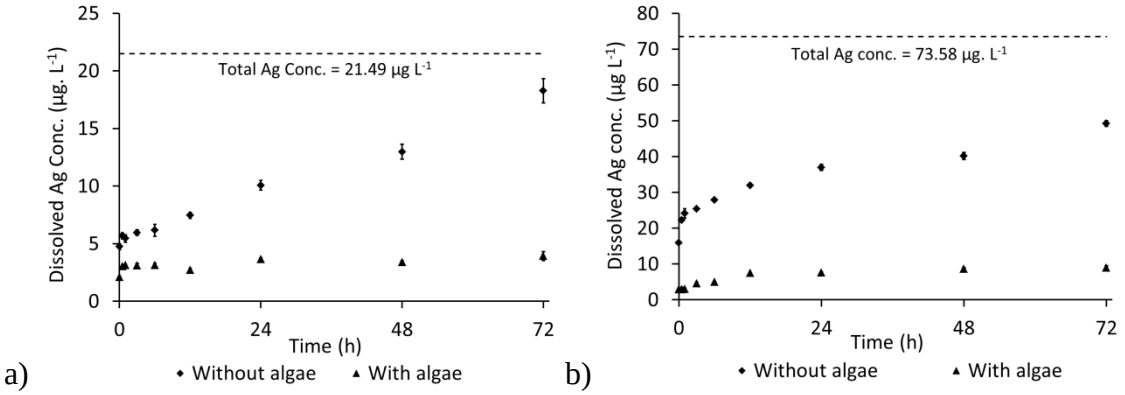

Figure 4.2. Dissolved Ag concentration (< 3 kDa) as a function of time following mixing at (a) 20 µg L^{-1} and (b) 75 µg L^{-1} PVP-AgNPs with 30 ppt SW in presence and absence of algae

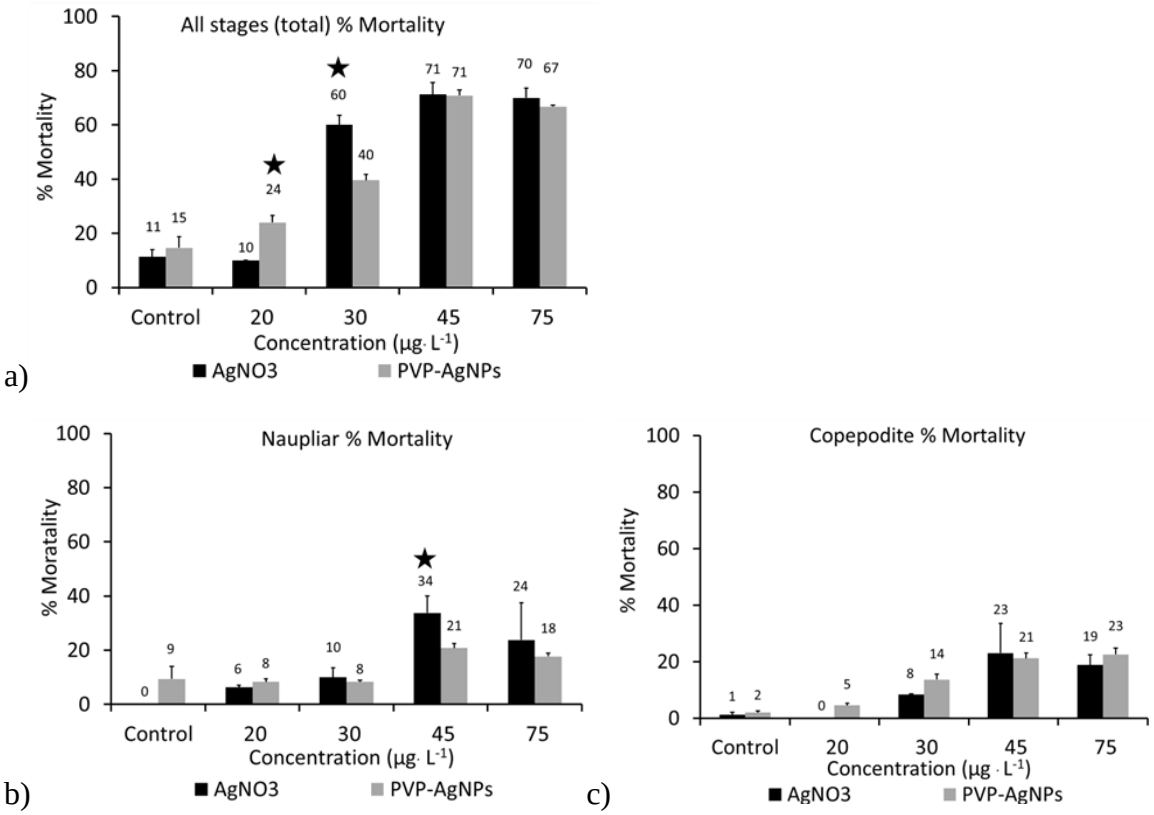

Figure 4.3. (a) All stages (total) mortality, (b) Naupliar mortality, and (c) copepodite (juvenile) mortality in sub-lethal life-cycle exposure to $AgNO_3$ and PVP-AgNPs (* indicates statistically significant difference between mean responses within a given Ag-treatment concentration; *p-value* < 0.05)

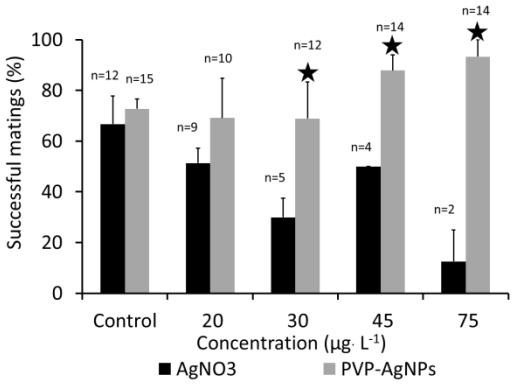

Figure 4.4. Percent of females able to produce two broods of viable offspring over 18-24 d of mating (n-sizes vary across treatments/concentrations depending on survival rates of nauplii to sexually mature adults; * indicates significant difference between mean responses within a given Ag-treatment concentration; *p-value* < 0.05).

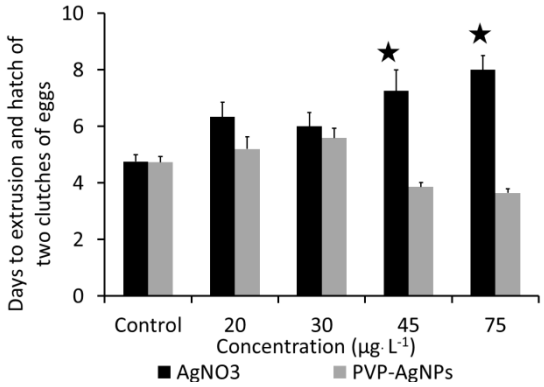

Figure 4.5. Time to extrusion and hatch of two clutches of eggs in $AgNO_3$ and PVP-AgNPs treatments (* indicates significantly delayed extrusion compared to control treatment; *p-value* < 0.05).

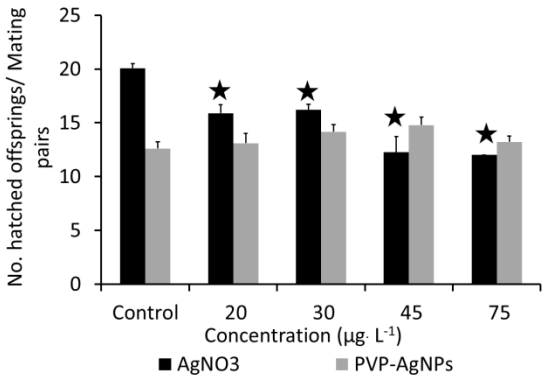

Figure 4.6. Number of hatched offspring through two broods per mating pair (mean fecundity) in $AgNO_3$ and PVP-AgNPs treatments (* indicates significantly reduced number of hatched offspring compared to control; *p-value* < 0.05).

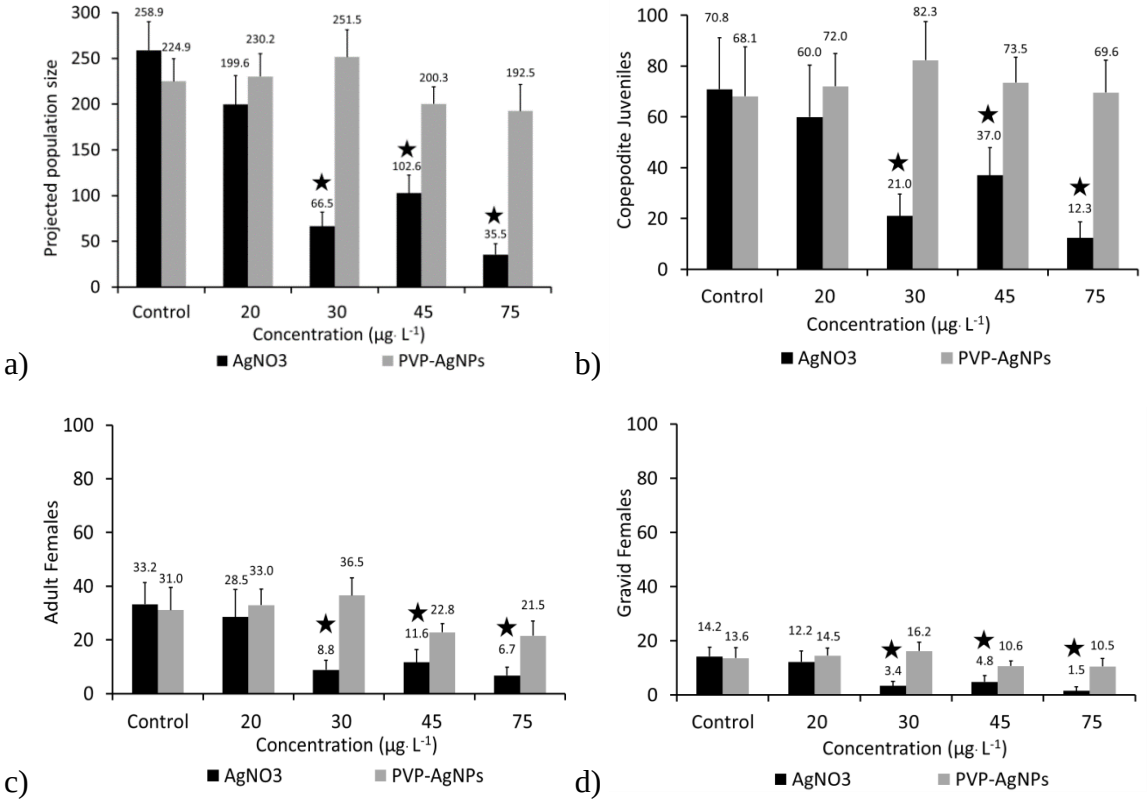

Figure 4.7. (a) Leslie matrix projected $AgNO_3$ and PVP-AgNPs impacts on *Amphiascus tenuiremis* population sizes after four generations. Each treatment-specific mean abundance represents 10,000 replications of a simulated population growth model starting with 38 nauplii, 30 copepodites, 12 males, 6 gravid and 14 non-gravid females (* indicates a significantly depressed (> 2 s difference) population size relative to its within-treatment control). (b), (c) and (d) Final-stage abundance projections of copepodite juveniles, adult females, and gravid females after four generations of exposure. (* indicates a significantly depressed (> 2 s difference) life-stage abundance relative to its within-treatment control).

Table 4.1. Leslie matrix predicted instantaneous population growth rate (I) of *Amphiascus tenuiremis* in presence of $AgNO_3$ and PVP-AgNPs.

Exposure ($\mu g\ L^{-1}$)	Population Growth Rate I in presence of $AgNO_3$	Population Growth Rate I in presence of AgNPs
Control	1.24	1.26
20	1.21	1.25
30	0.89	1.29
45	1.01	1.18
75	0.76	1.17

CHAPTER 5

NANOPARTICLE SIZE AND NATURAL ORGANIC MATTER COMPOSITION DETERMINE AGGREGATION BEHAVIOR OF PLATINUM NANOPARTICLES [1]

[1] Sikder, M., Poulin, B.A., Tfaily, M., Baalousha, M. "Nanoparticle size and natural organic matter composition determine aggregation behavior of platinum nanoparticles". To be submitted as peer-reviewed journal article.

Running title: Nanoparticle size and natural organic matter composition determine aggregation behavior of Platinum nanoparticles

Author for correspondence:

Dr. Mohammed Baalousha, Ph.D. Center for Environmental Nanoscience and Risk, Department of Environmental Health Sciences, Arnold School of Public Health, University South Carolina, Columbia, South Carolina 29208, United States; Phone: (803)-777-7177; email: mbaalous@mailbox.sc.edu.

Abstract

Nanoparticle (NP) size and natural organic matter (NOM) composition play important roles in determining NP environmental behaviors. The aim of this work was to investigate how NP size and NOM composition influence the colloidal stability of PtNPs. We compared the effect of five different nominal sizes of PtNPs (20, 30, 50, 75, and 95 nm, denoted as $PtNP_{20\text{-}95}$) in moderately hard water (MHW) and the effect of six different NOM fractions, that were isolated from surface waters and represented a range of characteristics, on the aggregation of $PtNP_{20}$ and $PtNP_{95}$. NOM isolates were characterized for elemental composition, specific absorbance, and molecular level composition using CHONS elemental analyzer, UV-vis, and electrospray ionization-Fourier-transform ion cyclotron resonance mass spectrometer (ESI-FTICR-MS). Single particle-inductively coupled plasma-mass spectrometer (sp-ICP-MS) was employed to monitor the aggregation of PtNPs at environmentally relevant NP and NOM concentrations (1 μg L^{-1} and 1 mg L^{-1}, respectively). PtNP aggregate size increased with decreasing primary PtNP size likely due to the lower zeta potential and the higher number concentration of smaller NPs compared to larger NPs at the same mass concentration. No aggregation was observed for $PtNP_{95}$ in MHW in presence and absence of the different NOM isolates. $PtNP_{20}$ formed aggregates in MHW in the presence and absence of the same NOM isolates, and aggregate size

increased in the presence of NOM due to interparticle bridging of NOM-coated PtNPs by divalent counterions. $PtNP_{20}$ aggregate size increased with the increase in NOM elemental ratio of H to C and the relative abundance of lignin formulae. However, the aggregate size of $PtNP_{20}$ decreased with the increase in NOM molecular weight, NOM $SUVA_{254}$, elemental ratio of O to C, and the relative abundance of condensed hydrocarbons, and tannin formulae. Overall, the results of this study suggest that the composition and sources of NOM are key factors that contribute to the stabilization/destabilization of PtNPs in the aquatic environment.

5.1 Introduction

The colloidal stability of NP has been studied over the past two decades. Numerous studies measured NP aggregation for different types of NPs with a major focus on investigating the effect of NP surface coating, media ionic strength, ion valency, and natural organic matter (NOM) [94, 191]. Yet, there is a limited and often contradictory knowledge on the effect of NP size and the physicochemical properties of natural organic matter (NOM) on NP aggregation. For instance, whereas some studies reported a decrease in critical coagulation concentration (CCC, the minimum counterion concentration required to fully destabilize the dispersion) with the decrease in NP size (e.g., hematite [101], TiO_2 [102]), others reported an increase in CCC with the increase in NP size (e.g., CdSe NP [103]), or an independence of CCC of NP size (e.g., AuNPs [104], AgNPs [94], PtNPs [272]). In addition, whereas some studies reported a linear correlation between the CCC and NP size (e.g., anatase TiO_2 [102]), others found that the CCC correlated better with NP specific area (e.g., TiO_2 [102], CdSe NP [103]), and another study reported no correlation between CCC and

NP size and/or surface area in presence of monovalent and divalent electrolytes (e.g., PtNPs [272]).

NOM is ubiquitous in the environment with concentrations in the range of 0.1 to 10 mg-C L^{-1}, depending on biochemical and climatic conditions [81, 273]. NOM is a complex mixture of polyelectrolytic and polyfunctional organic molecules (e.g., polysaccharides, proteins, lipids, nucleic acids, and fulvic and humic substances)[83, 84] that vary spatially and temporally in terms of molecular composition, acidity, molecular weight, structure, and charge density[85]. Adsorption of NOM on NP surfaces [86] results in the formation of NOM-corona [87], giving NPs unique surface identity, which may determine NP environmental behavior. NOM can act as a competitor to displace intentional engineered coatings (e.g., citrate, Polyvinylpyrrolidone, PVP) on NPs. For instance, NOM molecules (i.e., both HA and FA) were reported to displace citrate coatings from the surfaces of AgNPs [117] and AuNPs [118] due to the higher affinity of NOM molecules to NP surfaces. Model thiol ligands can (e.g., cysteine) replace the PVP coating on AgNPs[119], which suggests that thiol groups present in in the NOM might interact with NPs in a similar manner. NOM enhances NP stability by enhancing NP electrostatic repulsion and/or steric hindrance [120-122]. The role of NOM on NP environmental behaviors depends on the physicochemical properties of NOM such as charge density, functional groups, and molecular weight [123]. For instance, higher molecular weight NOM increases the stability of AuNPs due to increased electrostatic repulsion [123-126]. Aggregation of ZnS NPs decreased with increasing NOM concentration, molecular weight, and aromatic content of NOM fractions, while carboxylate and reduced sulfur had little effect [127].

Recently, the development of ultra-high resolution mass spectrometry, specifically Fourier transform-ion cyclotron resonance-mass spectroscopy (FT-ICR-MS), offers resolving power sufficient to identify the molecular formulas of the thousands of unique molecules that make up NOM. FT-ICR-MS is a technique that measures the mass-to-charge ratio of organic compounds with up to six decimal place precision [274], and highlights compositional differences between NOMs of varying chemical functionality and structure. Similarly, the recent development in single particle inductively coupled plasma mass spectroscopy (sp-ICP-MS) allows measuring NP size and aggregation at environmentally relevant concentrations [105], and thus enable understanding the interaction of NOM and NPs under realistic environmental scenarios. Such measurements and understanding have been limited by the detection limits of the commonly implemented analytical techniques for NP sizing and aggregation such as dynamic light scattering (DLS) and nanoparticle tracking analysis (NTA). These methods requires high NP concentrations, typically in the mg L^{-1} range [275], which is well above the predicted environmental concentrations (PEC) of most NPs (e.g., ng L^{-1} to µg L^{-1}) [276, 277]. At such high concentrations, NPs aggregate at faster rates, form larger aggregates, are more likely to settle out of solution, and dissolve at slower rates [51].

The release of platinum into the environment has been increasing over the years [64-68, 278] and some studies demonstrated that the released Pt in road dust is in the form of nanoparticles (NPs)[63]. Such increases are due to the increased use of platinum group element (PGE; i.e. Pt, Pd, Rh) in automobile catalysts. The expected Pt concentration is 0.4-10.8 ng L^{-1} in aquatic ecosystems and 50 ng L^{-1} in the road dust [60]. The occurrence of PtNPs in the environment raises concerns regarding the potential environmental

implications (e.g., bioaccumulation and/or toxicity) of PtNPs [61]. Several studies reported bioaccumulation and toxicological effects of Pt in aquatic organisms, such as waterfleas [71], freshwater oligochates [72], microalgae [73], and marine bacteria [74].

Therefore, the aims of this study were to determine the role of NP primary particle size and the role of NOM composition and molecular properties on the aggregation behavior of PtNPs at environmental relevant NP concentration using sp-ICP-MS.

5.2. Methodology

5.2.1. NP synthesis

Polyvinylpyrrolidone coated Platinum nanoparticles (PVP-PtNPs) were synthesized using seed mediated growth approach described by Sikder et al (2018) [272]. Briefly, 19 nm hydrodynamic sized PVP-PtNPs ($PtNP_{20}$) were synthesized by adding 36 mL of 5 mM chloroplatinic acid hydrate (H_2PtCl_6) in 464 mL ultra-pure water (UPW) at boiling temperature (100 °c) followed by addition of 50 µL of 1 M sodium hydroxide and 11 mL of 1% sodium citrate. Half a minute later, 5.5 mL of a solution containing 0.08% sodium borohydride and 1% sodium citrate was injected quickly to the boiling solution. 10 minutes later the suspension was cooled down to room temperature under vigorous stirring (i.e., 700 rpm). 31 nm hydrodynamic sized PVP-PtNPs ($PtNP_{30}$) were synthesized by adding 10 mL of $PtNP_{20}$ in 290 mL UPW at room temperature followed by addition of 450 µL of 0.4 M H_2PtCl_6 under constant stirring (i.e., 700 rpm). 5 mL of a solution containing 1% sodium citrate and 1.25% L-ascorbic acid was added drop-wisely (1 drop per 3 seconds) and temperature was slowly increased to the boiling point (100°c, increment of 10°c per minute). After 30 minutes, the suspension was cooled down to room temperature

under stirring. Larger PVP-PtNPs ($PtNP_{50}$, $PtNP_{75}$, and $PtNP_{95}$) were synthesized by diluting different volumes (40, 10, and 2.5 mL) of $PtNP_{30}$ in 260, 290, and 297.5 mL UPW, respectively, followed by addition of 450 µL of 0.4 M H_2PtCl_6 under constant stirring (i.e. 700 rpm) in room temperature. Then, 5 mL of a solution containing 1% sodium citrate and 1.25% L-ascorbic acid was added dropwise and reaction temperature was increased slowly to boiling point (100°c, increment of 10°c per minute) under stirring (i.e. 700 rpm). The resulting suspension was then cooled down to room temperature after 30 minutes of reaction.

5.2.2. Nanoparticle characterizations

The core size and morphology of the synthesized PtNPs ($PtNP_{20}$-$PtNP_{95}$) were measured using transmission electron microscopy (TEM, LaB_6 Joel 2100, 200 KeV, MA, USA). Samples for TEM analysis were prepared by depositing a droplet of undiluted PVP-PtNP suspension on a 300-mesh carbon coated Cu-grid (Agar Scientific, Stansted, UK) for 15 mins followed by rinsing with UPW. The grids were then left it to dry in room temperature for 48 h in a covered petri dish. The elemental composition of synthesized PtNPs was confirmed by Energy Dispersive X-ray Spectroscopy (EDS, Joel EX-230 Silicon Drift Detector, MA, USA) coupled with the TEM. Particle size was measured using Gatan Digital Micrograph software package (GMS 3) [196] and at least 150 individual NPs were analyzed to determine particle size distribution (PSD) and mean size. The PtNP z-average hydrodynamic diameter (Z_{avg}) and electrophoretic mobility were determined by measured by dynamic light scattering (DLS) and laser Doppler electrophoresis using a Zetasizer Nano-ZS instrument (Malvern Instruments Ltd., MA, USA). The theoretical particle number concentration of 1 µg L^{-1} PtNPs was calculated by dividing the mass

concentration by the average primary particle mass calculated using particle density and diameter measured by TEM.

5.2.3. NOM sampling sites and sample collection

NOM isolates were extracted from different environments (details in **Table D.1**) including three saw-grass dominated wetlands in northern Everglades: water conservation area (WCA) F1 site, 2B south site, and Arthur R. Marshall Loxahatchee National Wildlife Refuge (LOX) 8 site (denoted as NOM 1, 2, and 6 respectively), Suwannee river (NOM 5), Williams lake (NOM 3), and Pacific ocean (NOM 4). All 6 NOM isolates are operationally defined as hydrophobic organic acid (HPOA) fractions isolated on XAD-8 resin [279]. All NOMs, except NOM 4, were isolated in freeze-dried form following the protocol described by Aiken et al. (1992) [279]. Pacific Ocean NOM (NOM 4) was collected and isolated following the protocol described by Green et al. (2017) [280]. The NOM isolates were fully characterized by determining their elemental composition using a CHONS analyzer and specific ultra-violate light absorbance at 254 nm ($SUVA_{254}$) using UV-vis spectrometer as described elsewhere[281, 282], and briefly summarized in the supplemental information (SI) section (see **Table D.1**).

5.2.4. Molecular characterization of NOM using FT-ICR-MS

1 mg of NOM isolates were dissolved directly in 1 ml methanol and analyzed by FT-ICR-MS. A 12 Tesla Bruker Solarix FT-ICR-MS located at the Environmental Molecular Sciences Laboratory in Richland, WA, was used to collect high-resolution mass spectra of the NOM isolates. A standard Bruker ESI source was used to generate negatively charged molecular ions. Samples were introduced directly to the ESI source at a flow rate

of 3 µl/min. The ion accumulation time was varied, from 0.1 to 0.5 s, to account for differences in C concentration between samples and to maintain a final dissolved organic carbon concentration of 20 ppm. The instrument was externally calibrated weekly with a tuning solution from Agilent (Santa Clara, CA), which calibrates to a mass accuracy of <0.1 ppm. Two hundred scans were averaged for each sample and internally calibrated using OM homologous series separated by 14 Da ($-CH_2$ groups). The mass measurement accuracy was less than 1 ppm for singly charged ions across a broad m/z range (i.e. 200 < m/z <1200). To further reduce cumulative errors, all sample peak lists for the entire dataset were aligned to each other prior to formula assignment to eliminate possible mass shifts that would impact formula assignment. Putative chemical formulas were assigned using in-house software based on the Compound Identification Algorithm [283], and modified as previously described [284]. Chemical formulas were assigned based on the following criteria: S/N > 7, and mass measurement error <1 ppm, taking into consideration the presence of C, H, O, N, S and P and excluding other elements. Peaks with large mass ratios (m/z values > 500 Da) were assigned formulas through the detection of homologous series (CH_2, O, H_2). Additionally, to ensure consistent assignment of molecular formula the following rules were implemented: one phosphorus requires at least four oxygens in a formula and when multiple formula candidates were assigned the formula with the lowest error and with the lowest number of heteroatoms was picked. The chemical formulae were grouped into seven heteroatom classes of compounds: CHO, CHON, CHOS, CHOP, CHONS, CHONP, and CHONSP. The chemical compounds were grouped into the eight main families: condensed aromatic compounds, unsaturated hydrocarbon, tannins, lignin, lipids, protein, amino

sugars, and carbohydrate derived. From the formula assignment, the average (by number-weighted) abundance of each class was calculated and compared between samples.

5.2.5. Aggregation of PtNPs

The aggregation behavior of PtNPs (NP_{20}-NP_{95}) was determined by monitoring the evolution of PtNP number size distribution and number and mass concentration by sp-ICP-MS following (e.g., 0 and 24 h) mixing 1 µg L^{-1} PtNPs with ultrahigh pure water (UPW) and moderately hard water (MHW). The effect of NOM on the aggregation of PtNPs in MHW was determined following mixing 1 µg L^{-1} PtNPs ($PtNP_{20}$ and $PtNP_{95}$) with MHW in presence of 1 mg L^{-1} NOM isolates under static condition. All aggregation experiments were conducted in triplicates, and the number and mass concentrations and the number average diameter were presented as average of the three replicates (**Table S7-S12**). All sp-ICP-MS data were acquired with a NexION™ 350D ICP-MS (PerkinElmer Inc., MA, USA) operating in a single particle mode with the Syngistix Nano Application Module. A standard introduction system consisting of a Meinhard glass concentric nebulizer, a glass cyclonic spray chamber, and a 2 mm ID quartz injector were used. The sample uptake rates were 0.28-0.32 mL/min. Data were acquired at an RF power of 1600 W, a 50 µs dwell time, a 0 µs settling time, and a 60 s acquisition time. The transport efficiencies were 9.6-12.7%. NIST™ Au standard reference material (actual TEM size of 56 nm; reference material 8013 manufactured by National Institute of Standard and Technology, MD, USA) was used to determine the transport efficiency. A rinse cycle consisting of 1 min with 1% aqua regia, and 1 min with UPW was performed after each sample run to ensure cleansing of the sample introduction system between samples. The NIST Au standard reference material was measured after each set as a QA/QC check.

5.2.6. Statistical analysis

All the experiments were conducted in triplicates. All statistical analyses were performed with SAS® version 9.4 software (SAS institute, Cary, NC). The correlation coefficient between % mass of aggregated NP and NOM's elemental composition were calculated using Pearson's correlation method. % mass of aggregated NP in presence of six NOM isolates (and control, that is without NOM) were analyzed using ANOVA and Tukey's multiple comparison test. Particle size distribution of PtNPs in absence and presence of different NOMs were analyzed using Kolmogorov-Smirnov (K-S) test with Bonferroni correction. In all cases, the statistical significance was set at *p-value* < 0.05.

5.3. Results and discussions

5.3.1. NOM characterization

The bulk elemental composition of the NOM isolates used in this study are presented in **Table D.1**. The molecular properties of NOM isolated were determined by FT-ICR-MS. The relative abundance of molecules based on heteroatom content and geochemical classification are presented in **Table D.2 and D.3**, respectively. The O/C, H/C, and molecular weight of the NOM isolates are summarized in **Table D.4**. Molecular weight and $SUVA_{254}$ of the NOMs varied between 369-442 Da and 0.8-4.8 L mg^{-1} m^{-1}, respectively. N and S are the other key parameters that varied significantly between NOMs (0.8-1.8% and 0.4-1.9%, respectively; **Table D.1**). CHO and CHON are the main heteroatom classes of compounds in NOM whose abundance is > 5% and varied significantly between the six NOM isolates (**Table D.2**). CHOS and CHONS were generally less abundant (1.6 to 7.5% and 1.9 to 8.1) with few NOM isolates containing >

5% of these two classes of compounds. Other heteroatom classes of compounds (*e.g.*, CHOP, CHONP, CHONSP, and others) represented only < 5% of all formulae in all NOM isolates. Condensed hydrocarbon, lignin, and tannin are the main geochemical classes of compounds in NOM whose abundance is > 5% and varied significantly between the six NOM isolates (**Table D.3**). Other geochemical classes of compounds (e.g., aminosugar, carbohydrates, lipid, unsaturated hydrocarbons, and others) represented < 5% of all formulae in all NOM isolates. The number average elemental ratio of O/C and H/C varies within a narrow range (0.48-0.52 and 1.05-1.26, respectively) between the different NOM isolates. The differences in the molecular properties of NOM isolates are likely due to differences in sources and environmental processing of the NOM samples, rather than due to ionization and detection variations in the measurement technique as all samples were prepared and analyzed using the same protocol and at the same time.

5.3.2. Particle characterization

The physiochemical properties of the PVP-PtNPs were measured using a multimethod approach and reported elsewhere [272], and PtNP properties pertinent to this manuscript are summarized below. TEM analysis show that the synthesized PtNPs are spherical (**Figure D.1a-e**) with $PtNP_{20}$, $PtNP_{30}$, $PtNP_{75}$, and $PtNP_{95}$ exhibiting monomodal PSDs, whereas $PtNP_{50}$ exhibiting a bimodal PSD (**Figure 5.1a**). The mean core diameters of $PtNP_{20,}$ $PtNP_{30}$, $PtNP_{50}$, $PtNP_{75}$, and $PtNP_{95}$ measured by TEM are 9.2±1.2, 10.9±0.8, 18.5±5, 44.5±5, and 72.5±3.9 nm, respectively (**Table D.5**). sp-ICP-MS analysis show that all PtNPs exhibit monomodal PSDs, with mean core diameters of $PtNP_{20}$-$PtNP_{95}$ of 26.3 ± 1.5, 32.4 ± 2.5, 24.7 ± 1.6, 42.9 ± 0.8, and 77.1 ± 0.8 nm, respectively (**Figure 5.1b**). The mean core diameters of $PtNP_{75}$ and $PtNP_{95}$ measured by sp-ICP-MS are in good aggrement

with those measured by TEM (**Table D.5**). However, the mean core diameters of $PtNP_{20}$, $PtNP_{30}$, and $PtNP_{50}$ measured by sp-ICP-MS were larger than those measred by TEM (**Table D.5**), which is attributed to the high lower size detection limit of sp-ICP-MS for PtNP which is 18 nm [209]. The PSD of $PtNP_{20}$, $PtNP_{30}$, and $PtNP_{50}$ obtained by sp-ICP-MS are monomodal but represent curtailed log-normal size distribution, resulting higher mean core size compared to TEM measured core size.

The number concentration of $PtNP_{20}$, $PtNP_{30}$, and $PtNP_{50}$ in UPW measured by sp-ICP-MS represents a small fraction of the theoretical particle number concentration (**Table D.7**). The measured number concentration of $PtNP_{20}$, $PtNP_{30}$, and $PtNP_{50}$ in UPW represented only 0.3, 1.2, and 33.1%, respectively, of the theoretical NP number concentration (**Table D.7**). In contrast, the measured number concentrations of $PtNP_{75}$ and $PtNP_{95}$ in UPW were in good agreement with the theoretical number concentration (**Table D.7**). This is due to the size detection limit of sp-ICP-MS (e.g., 18 nm for PtNPs) [209]. The number PSD measured by TEM illustrates that all NPs in $PtNP_{20}$, and $PtNP_{30}$ and 54% of NPs in $PtNP_{50}$ are below the sp-ICP-MS size detection limit, whereas all particles in $PtNP_{75}$ and $PtNP_{95}$ are greater than the sp-ICP-MS size detection limit for PtNPs (**Figure 5.1b**).

The Zeta potential of PtNPs decreased from -16.9±3.5 to -27.2±1.7 with the increase in particle size (**Table D.6**), which might be attributed to the partial coating of PtNPs. Typically, NPs fully coated with PVP molecules exhibit low zeta potential of approximately -10 mV [75, 285]. Higher zeta potential of PVP-coated NPs has been reported elsewhere and was attributed to the partial surface coating of NPs by PVP molecules [115, 217, 286]. For instance, the magnitude of the zeta potential of PVP-partially coated AgNPs

increased with the decrease in the number of PVP molecules per AgNP unit surface area [94].

5.3.3. Size-dependent aggregation of PtNPs

The number PSDs of $PtNP_{20}$ – $PtNP_{75}$ shifted slightly toward larger sizes relative to the corresponding PSDs of $PtNP_{20}$ – $PtNP_{75}$ measured in UPW immediately after mixing with MHW and shifted further towards larger sizes after 24 h after mixing with MHW (**Figure 5.2a-d**), indicating PtNPs aggregation in MHW. The aggregation of PtNPs in MHW relative to UPW can be attributed to the higher ionic strength in MHW which screens the PtNP surface charge. The magnitude of the zeta potential of each of the PtNP suspensions decreased in MHW at 0 h and further decrease at 24 h relative to the corresponding zeta potential measured in UPW (**Table D.6**). The number PSD of $PtNP_{95}$ did not change in MHW relative to that measured in UPW (**Figure 5.2e**), indicating the colloidal stability of $PtNP_{95}$ in MHW.

The number concentrations of $PtNP_{20}$ and $PtNP_{30}$ increased immediately after mixing with MHW relative to those measured in UPW and increased further after 24 h (**Table D.7**). This is counterintuitive as NP number concentration is expected to decrease with NP aggregation. However, due to the aggregation, PtNP aggregate size became larger than the size detection limit of sp-ICP-MS for PtNPs (i.e., 18 nm). Thus, NP aggregation increased the detectable PtNPs by sp-ICP-MS and increased the measured PtNPs number concentration (**Table D.7 and Figure 5.2a-b**). This is further corroborated by the increase in the mass concentration of $PtNP_{20}$ and $PtNP_{30}$ measured by sp-ICP-MS in MHW relative to those measured in UPW (**Table D.8**).

The number concentration of $PtNP_{50}$ and $PtNP_{75}$ decreased immediately after mixing with MHW relative to the number concentration in UPW and decreased further after 24 h of mixing with MHW (**Table D.7**), which can be attributed to particle aggregation. It might be expected that aggregation of $PtNP_{50}$ should result in the increase in the number particle concentration similar to $PtNP_{20}$ and $PtNP_{30}$. However, a larger fraction (67 %) of NPs in $PtNP_{50}$ was larger than the size detection limit. Thus, aggregation of $PtNP_{50}$ increases the size of undetectable particles to become detectable and thus increase the number particle concentration, but aggregation also reduces the number of NPs larger than the sp-ICP-MS detection limit. Thus, the measured number concentration is influenced by these two processes. All NPs in $PtNP_{75}$ were larger than the size detection limit of sp-ICP-MS and thus the number concentration of $PtNP_{75}$ in MHW decreased relative to that in UPW due to particle aggregation. The number concentrations of $PtNP_{95}$ in UPW and in MHW at t= 0 (i.e., 8 mins, time required from sample collection to reach the plasma of sp-ICP-MS) were not statistically different (*p-value* < 0.05) (**Table D.7**). The number concentration of $PtNP_{95}$ in MHW decreased (*e.g.*, 35% reduction, **Table D.7**) after 24 h in MHW, but the number PSD of $PtNP_{95}$ did not change after 24 h in MHW. This might be due to the aggregation of some PtNPs without a significant shift in the number PSD, or due to sedimentation of some PtNPs, and/or due to both processes. The decrease in $PtNP_{75}$ and $PtNP_{95}$ mass concentration suggest the loss of some PtNPs, most likely due to PtNP sedimentation. Sedimentation of $PtNP_{75}$ and $PtNP_{95}$ was visually observed in the stock suspensions within 24-48 h, mainly because of the high density of PtNPs (= 21.45 g cm^{-3}). Similar gravitational sedimentation of 65 and 87.5 nm AuNPs (density= 19.32 g cm^{-3}) in UPW under static condition was observed after 48 h [287].

The number PSD of $PtNP_{20}$ and $PtNP_{30}$ 24 h after mixing with MHW exhibited broader size distributions compared to $PtNP_{50}$, $PtNP_{75}$, and $PtNP_{95}$ (**Figure 5.1**). This observation indicates that smaller PtNPs are more prone to aggregation and form larger aggregates compared to the larger PtNPs. This is consistent with previous studies demonstrating the increased aggregation of smaller hematite NP [101], TiO_2 NP [102, 288], and cit-PtNPs under the same experimental conditions relative to their larger counterpart [272]. NP aggregation occur because of NP collision and attachment. The former increases with the increase in NP number concentration, whereas the later increase with the decrease in NP zeta potential. At the same mass concentration, NP number concentration increases with the decrease in NP size. The magnitude of the zeta potential of PtNPs decrease with the decrease in NP size (**Table D.6**). Thus, both factors contribute to the increased aggregation with the decrease in PtNPs sizes. However, positive correlation [94, 103] and insignificant correlation [104] between primary particle size and aggregation also reported in literature.

5.3.4. NOM-dependent aggregation of PtNPs

The PSDs of $PtNP_{20}$ and $PtNP_{95}$ (1 μg L^{-1}) in MHW in the presence of 1 mg L^{-1} NOM isolates are presented in **Figure 5.3 and 5.5**, respectively. The PSDs of $PtNP_{20}$ in MHW in the presence of NOM isolates at time 0 h were not statistically different (Kolmogorov-Smirnov test; *p*- value > 0.065) relative to the PSD of $PtNP_{20}$ measured in MHW (without NOM) at time 0 h (**Figure 5.3**), inferring the lack of immediate aggregation of $PtNP_{20}$ in MHW because of the NOM isolates. After 24 h, the PSDs of $PtNP_{20}$ in the presence of NOM isolates shifted toward larger sizes relative to that measured PSD at time

0 h, indicating aggregation of $PtNP_{20}$ in MHW in the presence of all NOM isolates. The PSDs of $PtNP_{20}$ in presence of NOM 1, 2, 3, 5, and 6 after 24 in MHW were not statistically different (Kolmogorov-Smirnov test; *p-value* > 0.4) relative to the PSD of $PtNP_{20}$ after 24 h in MHW without NOM. However, the PSDs of $PtNP_{20}$ in presence of NOM 4 after 24 h in MHW was statistically different (larger, Kolmogorov-Smirnov test; *p-value* < 0.05) relative to the PSD of $PtNP_{20}$ after 24 h in MHW without NOM. Similarly, the mean number diameter of $PtNP_{20}$ in NOM 1, 2, 3, 5 and 6, were not significantly different (t-test; *p*-value > 0.05) relative to the mean diameter of $PtNP_{20}$ after 24 h in MHW without NOM, whereas the mean diameter of $PtNP_{20}$ in presence of NOM 4 was larger than the mean diameter of $PtNP_{20}$ in MHW without NOM and in MHW in presence of all other NOM isolates (t-test; *p*-value < 0.05). These results suggest that NOM isolates differently impact $PtNP_{20}$ aggregation/stability.

To evaluate PtNPs aggregation in the absence and presence of NOM isolates, the number and mass concentrations of PtNPs measured by sp-ICP-MS were compared to the theoretical number and mass concentrations, respectively. The number concentration of $PtNP_{20}$ at 0 h and 24 h after mixing with MHW in presence or absence of NOM isolates represents 0.4-0.6% and 11-52% of the theoretical $PtNP_{20}$ number concentration, respectively (**Table D.9**). This result confirms the aggregation of $PtNP_{20}$ in MHW in presence and/or absence of NOM isolates. In contrast, $PtNP_{20}$ in UPW did not aggregate during 24 h exposure and the number concentration of $PtNP_{20}$ remained constant and represented only 0.7% of the theoretical $PtNP_{20}$ concentration. The mass concentration of $PtNP_{20}$ in presence and absence NOM isolates also followed the same trend. The mass concentration of $PtNP_{20}$ represented 1.6-3.4% and 18.8-97.8% of the theoretical $PtNP_{20}$

mass concentration after 0 and 24 h of mixing with MHW in presence of NOM isolates (**Table D.10**).

The number concentration of $PtNP_{20}$ in presence of NOM 4 was significantly higher than the number concentration of $PtNP_{20}$ in absence of NOM (**Figure 5.4a**; *p*-value < 0.05), whereas the number concentration of $PtNP_{20}$ in presence of NOM 1, 2, 3, 5, and 6 were not significantly different compared to the number concentration of $PtNP_{20}$ in absence of NOM (**Figure 5.4a**; ANOVA with Tuckey's multiple comparison test; $\alpha = 0.05$). Nonetheless, the number concentration of $PtNP_{20}$ in the presence of the different NOM isolates decreased following the order: NOM4 > NOM2 > NOM5 > NOM3 > no NOM > NOM6 > NOM1 (**Table D.9**). The mass concentration of $PtNP_{20}$ in presence of NOM 4 was larger than the mass concentration of $PtNP_{20}$ in absence of NOM and in presence all other NOM isolates. However, the mass concentration of $PtNP_{20}$ in presence of NOM 1, 2, 3, 5, and 6 were not significantly different relative to the mass concentration of $PtNP_{20}$ in absence of NOM (**Figure 5.4b**; ANOVA with Tuckey's multiple comparison; $\alpha = 0.05$). The mass concentration of $PtNP_{20}$ in presence of NOM 1 was lower than the mass concentration of $PtNP_{20}$ in presence of NOM 2 (ANOVA with Tuckey's multiple comparison test; $\alpha = 0.05$), whereas the mass concentration of $PtNP_{20}$ in the presence of NOM2, 3, 5 and 6 were not significantly different among themselves. Nonetheless, the mass concentration of $PtNP_{20}$ in the presence of the different NOM isolates decreased following the order: NOM4 > NOM2 > NOM3 > NOM5 > NOM6 > no NOM > NOM1. These results indicate that NOM isolates impacted $PtNP_{20}$ aggregation to different extents. The extent to which NOM affects $PtNP_{20}$ aggregation can be attributed to the difference in the molecular composition and properties of the six NOM isolates used in this study as discussed in detail below.

The increased aggregation of PtNP20 in presence of NOM is likely due to inter-particle bridging of NOM-coated PtNPs due to complex formation between humic acid macromolecules and divalent counterions (e.g., Ca^{2+} and Mg^{2+}) [178, 289]. MHW contains higher concentrations of divalent counter-ions (e.g., 0.45 Ca^{2+} and 0.5 mM Mg^{2+}, Table S14) than the concentration of monovalent counter-ions (e.g., 1.14 mM Na^{+} and 0.05 mM K^{+}). Such low concentrations of monovalent counterions in MHW are lower than the concentrations of monovalent counterions (e.g., ≥ 50 mM Na^{+}) required to initiate $PtNP_{20}$ aggregation [272]. However, the concentrations of divalent counterions in MHW were shown to result in a significant aggregation of $PtNP_{20}$ and were in close proximity to the critical coagulation concentration (e.g., 1.1 Ca^{2+}) of $PtNP_{20}$ [272]. However, this bridging phenomenon may depend on the type, composition and structure of the natural organic material, which has not been investigated previously.

The PSD of $PtNP_{95}$ in MHW in the presence of NOM isolates at 0 and 24 h (**Figure 5.5**) were not statistically different from those measured in MHW at time 0 h or 24 h (**Figure 5.2e**). This indicates that all NOM isolates did not have significant impact on the colloidal stability of $PtNP_{95}$. The number concentration of $PtNP_{95}$ decreased slightly in MHW relative to that measured in UPW at 24 h (**Table D.11**), indicating slight particle aggregation and/or sedimentation. The mass concentration of $PtNP_{95}$ decreased slightly in MHW relative to that measured in UPW at 24 h (**Table D.12**) indicating slight particle aggregation and/or sedimentation of PtNPs during this period. The number and mass concentrations of $PtNP_{95}$ in MHW increased slightly in the presence of all NOM isolates relative to that in the absence of NOM isolates, suggesting that NOM isolates did not induce $PtNP_{95}$ aggregation.

Taken together, these results suggest that the effect of NOM on PtNP aggregation is size-dependent. Smaller PtNPs were more impacted by NOM, which might be attributed to the size-dependent NOM-corona composition/properties. For instance, Pittibone et al demonstrated difference in adsorption sites or a different distribution of adsorption sites for oxalic acid on the surface of 5 nm and 32 nm TiO_2-NPs, with the presence of lower energy binding sites for adsorption on the surface of the 5 nm TiO_2-NPs that were not present on the 32 nm TiO_2-NPs [288]. The presence of such sites was attributed to the edge and corner sites, which are present in greater abundance for the 5 nm particles relative to the larger 32 nm particles [288]. Such differences in adsorption sites on the NP surfaces can be even more important for the adoption of NOM on NP surfaces due to polydiversity of NOM formulae. Zhang et al. (1999) reported increased adsorption of organic acids with the decrease (e.g., 6-16 nm) in TiO_2 NPs [290]. Smaller particles with increased molar free energy are more prone to adsorb molecules or ions per unit area onto their surfaces in order to decrease the total free energy and to become more stable [290]. Chowdhury et al. (2013) reported that NOM affect the morphology of TiO_2 NP aggregate, where small NPs (e.g., 6 nm) form more compact aggregates than larger NPs in presence of NOM (e.g., 13 nm and 23), suggesting that interactions of NOM with smaller NPs are more significant than those with larger ones [77].

5.3.5. Correlating $PtNP_{20}$ aggregation to NOM properties

The NOM isolates used in this study represents a diverse array of HPOAs. Differences in composition among isolates may explain the variation in observed particle aggregation. To better understand the NOM properties with the greatest influence on observed aggregation, we performed Pearson's correlation analysis between mass of

aggregated $PtNP_{20}$ and specific NOM property. $PtNP_{95}$ were not included in these correlation analysis as they did not exhibit any appreciable aggregation in the absence or presence of NOM isolates. Calculated Pearson's correlation coefficient (r) and *p-values* (**Table 5.1**) were used to assess the correlation quality with each NOM parameter, varied depending on NOM characteristics.

The mass of $PtNP_{20}$ that formed aggregates exhibited negative correlation with $SUVA_{254}$, molecular weight (MW), O/C ratio; relative abundance of condensed hydrocarbon (ConHC), and tannin, and it exhibited positive correlation with H/C ratio, relative abundance of lignin (**Table 5.1, D.2-D.4 and Figure 5.6**). NOM parameters producing the best negative correlations with the mass of aggregated $PtNP_{20}$ were MW (r= -0.979, *p*-value = 0.004), $SUVA_{254}$ (r= -0.763, *p*-value = 0.078), O/C ratio (r= -0.841, *p*-value = 0.036), relative abundance of ConHC (r= -0.766, *p*-value = 0.076), and relative abundance tannin (r= -0.898, *p*-value = 0.015). NOM parameters producing the best positive correlation with the mass of aggregated $PtNP_{20}$ were H/C (r = 0.73, *p*-value = 0.1), and relative abundancies of lignin (r = 0.798, *p*-value = 0.058).

NOM molecular properties associated with higher charge density (*i.e.* O/C) demonstrated negative correlation with the observed aggregation (**Table 5.1, Figure D.2c and D.2g**). In contrast, lower charge density parameters (i.e. H/C) showed positive correlation with the aggregated mass (**Table 5.1, Figure D.2h**). Higher oxygen content and O/C ratio indicates a higher content of functional groups such as carboxylic groups [127]. The higher content of these functional groups is likely to enhance NP surface charge and thus increase the electrostatic repulsive forces between NOM-coated PtNPs, and thus enhance NP stability. While overall aggregation of PtNPs and NOM were influenced by repulsive

forces for aggregation caused by net negative surface charge, the variations between NOM fractions could also be partially explained by properties that influenced steric and hydrophobic effects. An increase in MW would presumably lead to thicker adsorbed layers of NOM on NP surface, particularly by forming loop and tail structure and resulting in increased steric stabilization[291-293]. An increase in $SUVA_{254}$ and the relative abundance of ConHC would presumably lead to higher sorption of these molecules on NP surfaces and thus increasing the NP hydrophobicity, and thus may enhance repulsive forces between NPs. The significant role of these NOM properties can also be related to the selective sorption on the surface of NPs of NOM molecules with high O/C, molecular weight, aromaticity, and hydrophobicity [294-299]. The negative correlation of aggregated $PtNP_{20}$ mass with MW, $SUVA_{254}$ (a proxy indicator of aromaticity), and ConHC are consistent, as the higher MW NOM tends to have more aromatic carbon over aliphatic carbon moieties[300]. Similar trend was observed for ZnS nanoparticles [127] and cit-AuNPs [125]. Thus, larger MW, higher $SUVA_{254}$, and relative abundance of ConHC in NOM isolates enhance NP_{20} stability [125, 127].

Compounds with high O/C (i.e., tannin) demonstrated significant negative correlation, whereas those with low O/C (i.e., lignin, conHC etc.) demonstrated significant positive correlation with the mass of aggregated $PtNP_{20}$, in good agreement with the correlations observed with O/C ratios as discussed above. Lignin and tannin contain the same types of surface functional groups (hydroxyl groups and phenol groups). However, tannin has a higher content of these functional groups. Tannins are high molecular weight polycyclic aromatic compounds with high O/C ratio and charge density, which are likely to enhance the surface charge, and thus, result in higher stability of NPs. Additionally, the

hydrophobic nature and polymer structure of tannins might be responsible for increased NP stability and decreased aggregation [301]. Lignin is a high molecular polyphenolic compounds [301]. These poly-phenol compounds has particular importance as they promote aggregation by forming strong non-covalent bonds [302]. Lignin has hydrophilic regions such as hydroxyls (–OH), carboxylic (–COOH) and small alkyl chains i.e., methane groups (–CH_3). These functional groups and the hydrophobic regions of lignin (e.g., resinol, C-H groups) enable it to bind with organic matter and mineral particles through polar, covalent, and hydrogen bonding as well as Van der Waals forces. These humified and highly decomposed materials, which are more stable, aid in the formation of microaggregates [303]. For instance, lignin has been shown to promote macroaggregation in soil and it increases aggregate stability [303-305]. Application of 1.67-3.34 g-C kg^{-1} soil in the form of sulfuric acid-precipitated lignin from rice straw pulping resulted in more than two fold increase (~ 59%, *p*-value < 0.05) in macroaggregate formation over the control soil during 8 week incubation [305].

5.4. Conclusions

This study demonstrated that the aggregation of PtNPs depend on several factors, including NP size and NOM characteristics. At the same mass concentration, the PtNP aggregate size increased with the decrease in NP primary size due to the increased NP number concentration and this collision. NOM isolates of different elemental composition and properties did not alter the aggregation behavior of $PtNP_{95}$ in MHW. However, the same NOM isolates generally increased the aggregation of $PtNP_{20}$ in MHW to different extents, likely via bridging mechanism in presence of divalent counterions in MHW. The mass of the aggregated $PtNP_{20}$ decreased with the increase in NOM elemental ratio of O to

C, molecular weight, $SUVA_{254}$, and relative abundance of condensed hydrocarbons and tannin formulae due to electrosteric stabilization effects. The mass of the aggregated $PtNP_{20}$ increased with the increase in NOM elemental ratio of H to C and the relative abundance of Lignin formulae. Therefore, the molecular composition and properties, and thus sources, of NOM determine, to a great extent, PtNP colloidal stability in the aquatic environment. Future studies are needed using a larger number of NOM isolates in various environmentally representative media, and higher number of replicates to discern the subtle effects of NOM properties on PtNP, and other NP, colloidal stability and to develop quantitative structure activity relationships between NOM molecular properties and NP environmental behaviors.

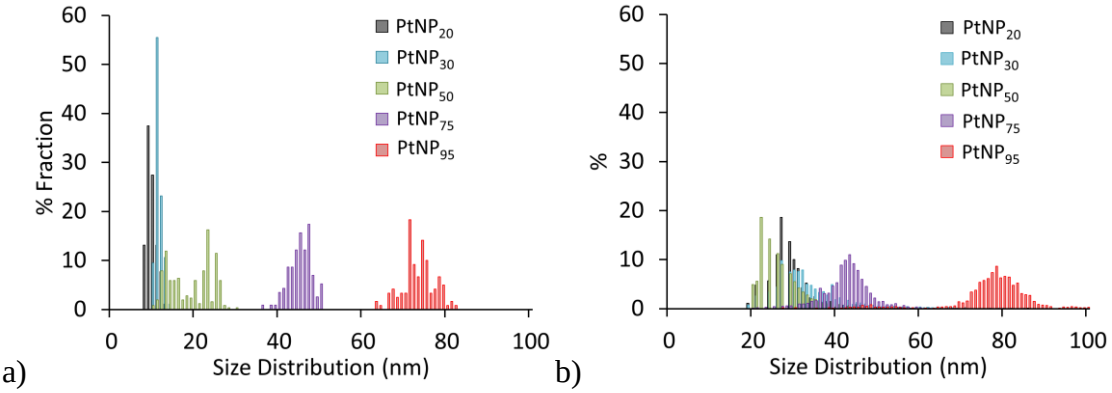

Figure 5.1. Number particle size distribution of polyvinylpyrrolidone-coated platinum nanoparticles of five different nominal sizes ranged from 20 to 95 nm (denoted as $PtNP_{20}$-$PtNP_{95}$) measured by (a) transmission electron microscope, and (b) single particle-inductively coupled plasma-mass spectrometer (sp-ICP-MS). Size detection limit of PtNPs in sp-ICP-MS is 18 nm

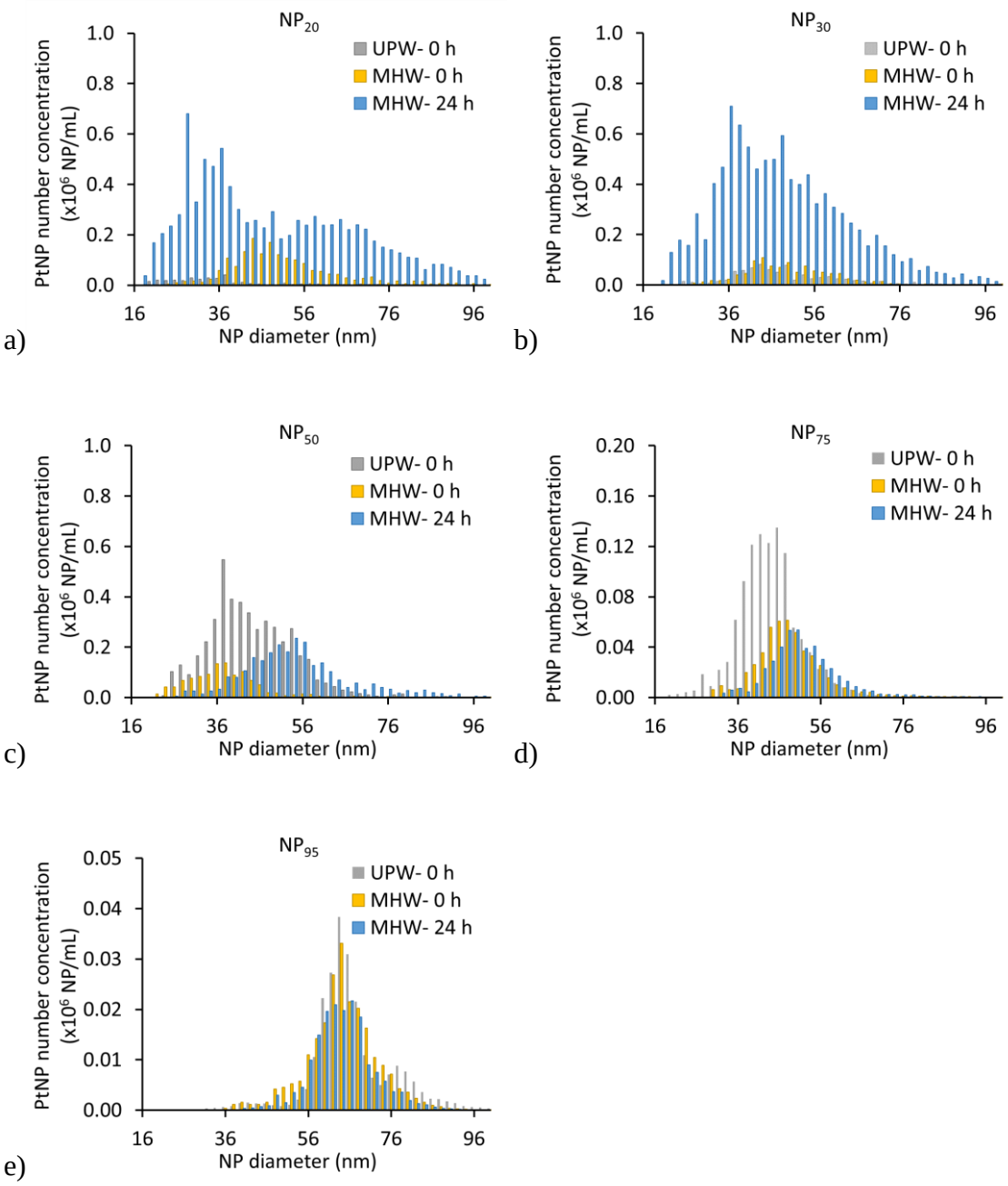

Figure 5.2. Number particle size distribution measured by sp-ICP-MS of 1 µg L-1 PVP-PtNPs in ultrapure water (UPW) and and at 0 and 24 h after mixing with moderately hard water (MHW) of: (a) $PtNP_{20}$, (b) $PtNP_{30}$, (c) $PtNP_{50}$, (d) $PtNP_{75}$, and (e) $PtNP_{95}$.

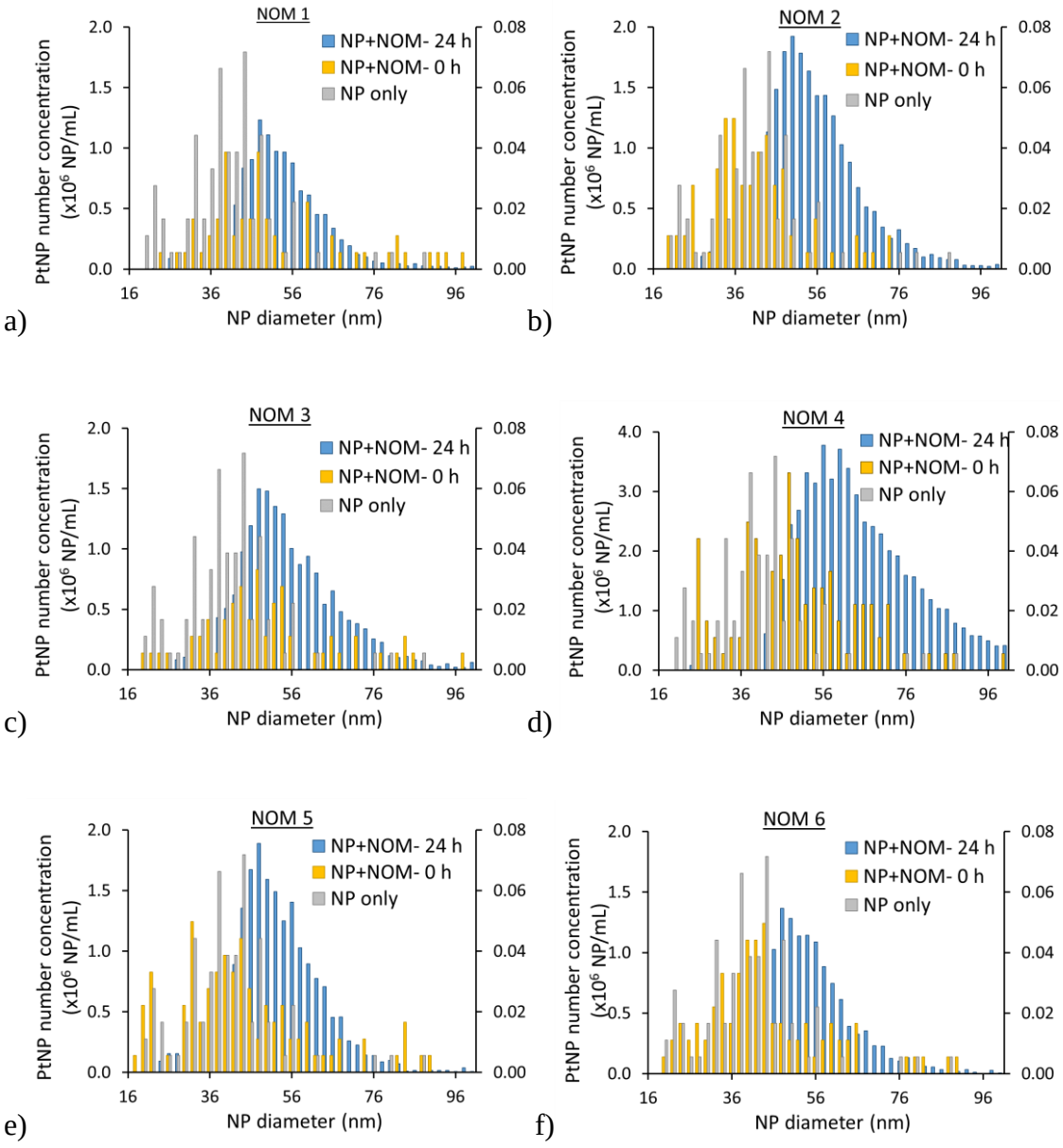

Figure 5.3. Particle size distribution (PSD) measured by sp-ICP-MS of 1 µg L^{-1} $PtNP_{20}$ at 0 and 24 hours after mixing with MHW in presence of 1 mg L-1 (a) NOM 1, (b) NOM 2, (c) NOM 3, (d) NOM 4, (e) NOM 5, and (f) NOM 6. The frequency of PtNPs only and PtNPs+NOM- at 0 h are presented on the secondary Y-axis, which is 25 folds less than the primary Y-axis (both Y-axis represents $x10^6$ NP/mL)

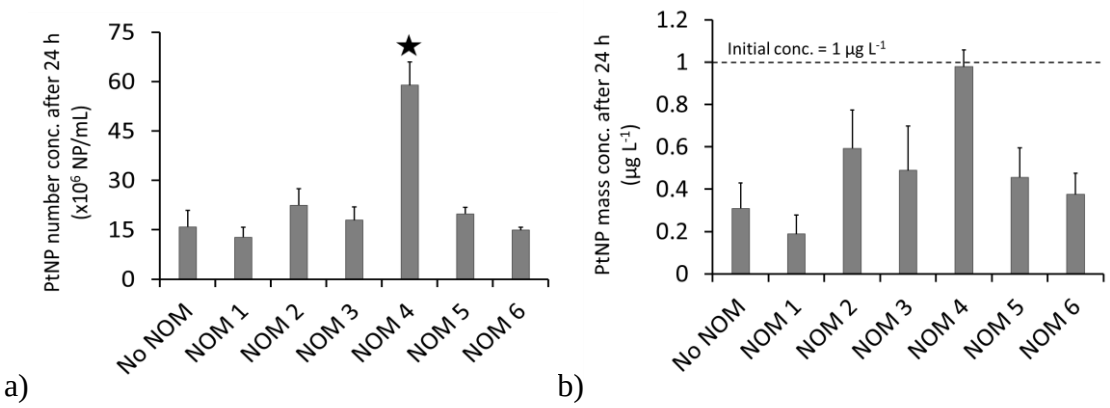

Figure 5.4. (a) Number and (b) mass concentration of 1 µg L^{-1} $PtNP_{20}$ measured by sp-ICP-MS after 24 h of mixing with MHW in absence and presence of 1 mg L^{-1} NOM. * represents a significant increase in measured $PtNP_{20}$ number concentration in presence of NOM compared to that measured in the absence of NOM

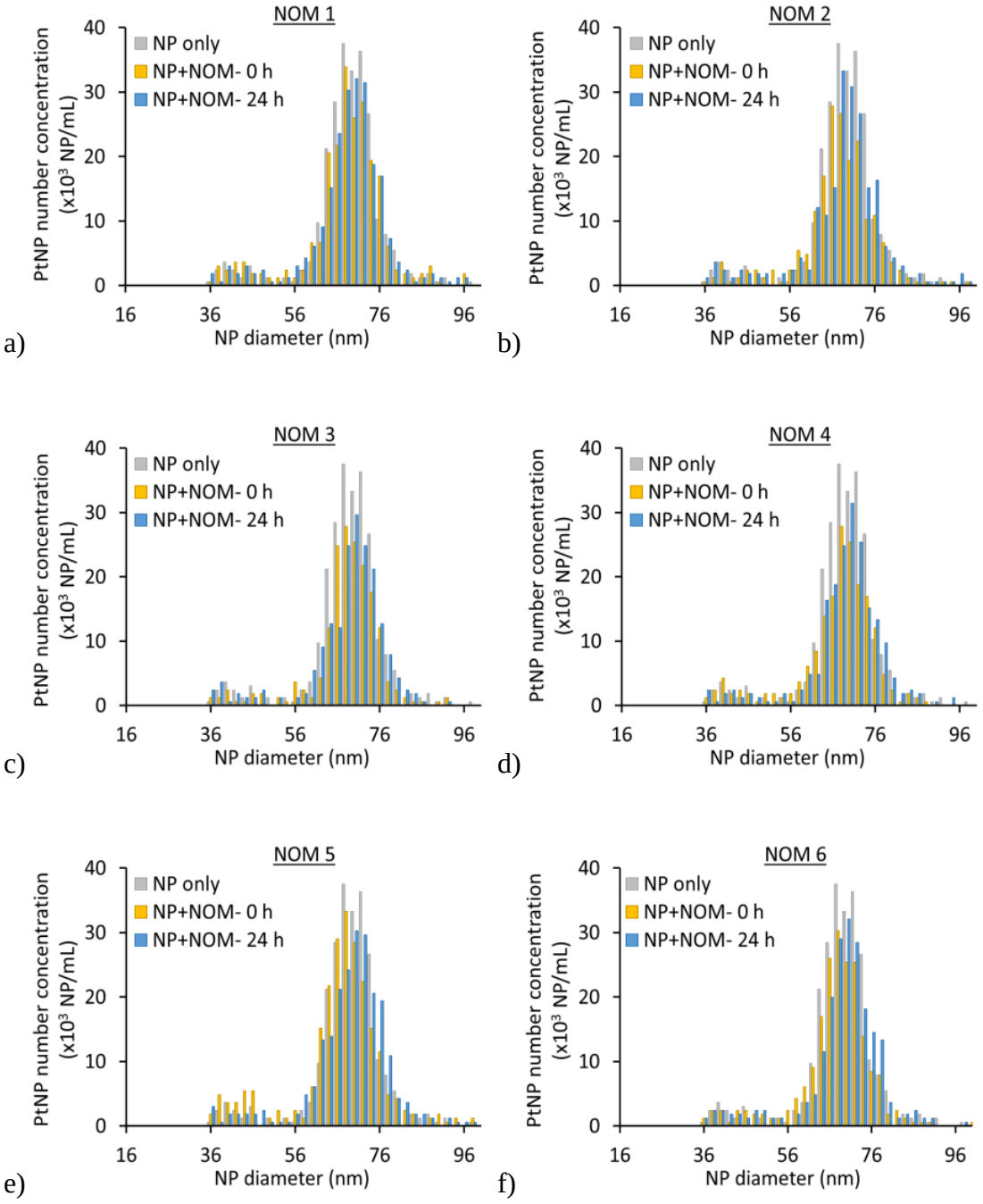

Figure 5.5. Particle size distribution of $PtNP_{95}$ measured by sp-ICP-MS of 1 µg L^{-1} $PtNP_{95}$ at 0 h and 24 h after mixing with MHW in presence of 1 mg L^{-1} (a) NOM 1, (b) NOM 2, (c) NOM 3, (d) NOM 4, (e) NOM 5, and (f) NOM 6

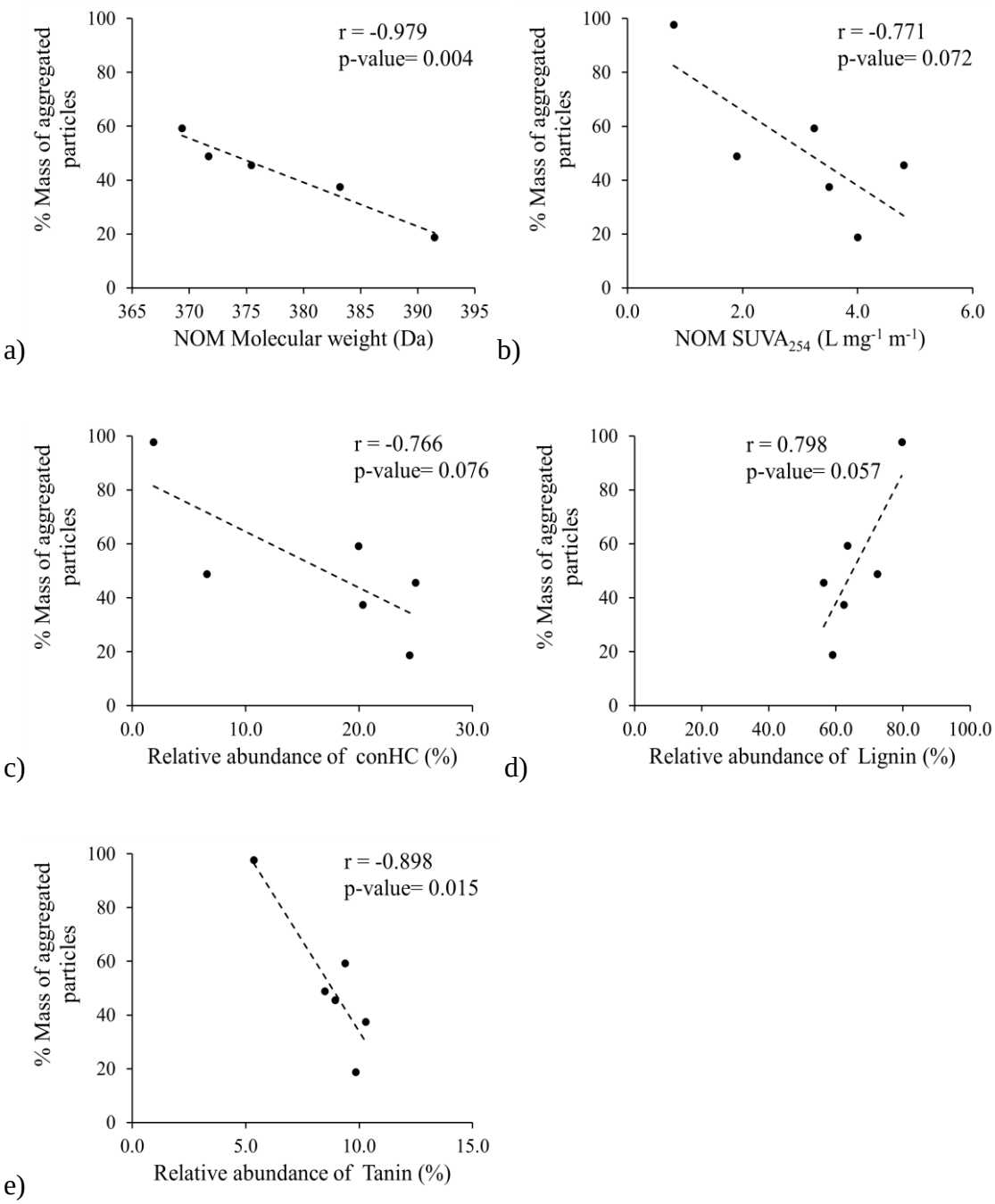

Figure 5.6. Correlation between % of $PtNP_{20}$ mass undergoing aggregation in presence of the different NOM isolates and NOM properties: (a) molecular weight, (b) specific UV absorbance at 254 nm ($SUVA_{254}$), (c) condensed hydrocarbon (ConHC), (e) lignin, and (f) tanin

Table 5.1. Analysis results of Pearson's correlation between % mass of aggregated $PtNP_{20}$ and NOM properties

Variables	Pearson's correlation coefficient (r)	p-value
% mass of aggregated NP vs NOM elemental composition		
O	-0.411	0.418
N	-0.164	0.756
S	-0.429	0.397
$SUVA_{254}$	-0.771	0.072
Molecular weight	-0.979	0.004*
O/C	-0.841	0.036*
H/C	0.730	0.099
% mass of aggregated NP vs NOM geochemical classes of compounds		
Aminosugar	0.709	0.115
Condensed HC	-0.766	0.076
Carbohydrates	-0.746	0.089
Lignin	0.798	0.058
Lipid	0.409	0.420
Protein	0.748	0.087
Tannin	-0.898	0.015*
Unsaturated HC	-0.171	0.745

CHAPTER 6

EFFECT OF SIZE AND NATURAL ORGANIC MATTER COMPOSITION ON THE BIOAVAILABILITY OF PLATINUM NANOPARTICLES TO A MODEL FRESHWATER SNAIL, *LYMNAEA STAGNALIS* [1]

[1] Sikder, M., Barasch, D., Croteau, M.N., Poulin, B.A., Baalousha, M. "Effect of size and natural organic matter composition on the bioavailability of Platinum nanoparticles to a model freshwater snail, *Lymnaea stagnalis*". To be submitted as peer-reviewed journal article.

Running title: Effect of size and natural organic matter composition on the bioavailability of Platinum nanoparticles to a model freshwater snail, *Lymnaea stagnalis*

Author for correspondence:

Dr. Mohammed Baalousha, Ph.D. Center for Environmental Nanoscience and Risk, Department of Environmental Health Sciences, Arnold School of Public Health, University South Carolina, Columbia, South Carolina 29208, United States; Phone: (803)-777-7177; email: mbaalous@mailbox.sc.edu.

Abstract

Nanoparticle's (NP) size, form (i.e. ion vs NP), and natural organic matter (NOM) are key in determining NP environmental fate, behavior, and toxicity. The aim of this work was to investigate how NP size and natural organic matter composition influence the bioavailability of PtNPs to a model freshwater species, the snail Lymnaea stagnalis from aqueous exposure. Bioavailability of dissolved Pt (added as H2PtCl6) and polyvinylpyrrolidone coated PtNPs of five different sizes (e.g., 20, 30, 50, 75, and 95 nm) was investigated using a model freshwater species, the snail Lymnaea stagnalis in controlled laboratory experiments. All forms of Pt were bioavailable to L. stagnalis, and Pt bioavailability was 2.5-times greater for the NPs than for dissolved Pt (kuw of 0.055±0.003 vs 0.139±0.007 L g^{-1} d^{-1}, respectively). PtNP bioavailability decreased with decreasing PtNPs size (from k_{uw}= 0.092±0.011 to 0.751±0.343 L g^{-1} d^{-1}), which might be attributed to the increased aggregation with the decrease in NP size. The influence of NOM isolates on Pt bioavailability was equivocal; that is, NOM did not have a significant impact on the bioavailability of $PtNP_{20}$ but suppressed the bioavailability of PtNP95. The bioavailability of $PtNP_{95}$ increased by 6-fold (from 0.075±0.050 to 0.456±0.037 L g^{-1} d^{-1}) with the increase in NOM sulfur (S) content. This study delineates the effect of NP size and NOM molecular composition on PtNPs interactions in the aquatic environment, which subsequently

influence the environmental fate and bioavailability of PtNPs. PtNP's influx rate constant and efflux rate constant along with NP-NOM interaction characterization could be used to produce a more useful holistic model for predicting PtNPs bioavailability, concentration, and risks to aquatic ecosystems.

6.1. Introduction

Nanoparticle bioaccumulation in organisms depends on NP size, shape, surface charge, NP concentration, media chemistry, and the model organism used in the study [2, 17]. There are currently contradictory data on the dependence of bioaccumulation on NP size, with same exposure conditions and media characteristics. Studies have either reported an increase in uptake or bioaccumulation with increase NP size (*e.g.* AuNP [306, 307], AgNP [308] etc.), a decrease in bio-accumulation with increase in size (*e.g.* Au NP [309], AgNP [310], ZnO-NP [311], SiO_2-NP [312]), or a lack of influence of NP size on bioaccumulation (e.g. AuNP [309, 313, 314], ZnO, TiO_2, SiO_2-NP [315]). Because bioaccumulation is the outcome of both uptake and elimination processes [316], characterizing the influence of NP size on influx and efflux rates might provide clearer insights.

Natural organic matter (NOM) is ubiquitous in the environment with concentrations in the range of 0.1 to 10 mg-C L^{-1}, depending on biochemical and climatic conditions [81, 82]. NOM is a complex mixture of polyelectrolytic and polyfunctional organic molecules (e.g. polysaccharides, proteins, lipids, nucleic acids and fulvic and humic substances)[83, 84] that vary spatially and temporally in terms of molecular composition, acidity, molecular weight, structure, and charge density [85]. Adsorption of NOM on NPs [86] results in the formation of NOM-corona [87], giving NPs unique surface identity. Although NOM is commonly recognized as a series of nontoxic compounds [317, 318], NOM can significantly impact the

bioavailability and toxicity of NPs in aquatic organisms by altering their fate and behavior [191, 319, 320]. The influence of NOM on NP bioavailability and toxicity is complex. Studies have shown that for the same type of NPs, NOM can enhance [96], mitigate [97, 98] or have no significant effects on NP bioavailability [99]. The range of NOM impacts on NP bioavailability and toxicity may be due to differences in NOM molecular composition and consequently NOM-corona composition [87, 294, 317], which are not fully understood at the molecular interaction level. For logistic reasons and cross-lab standardization, the majority of studies in the literature have used single molecules (e.g. cysteine or citric acid) [143], or standard NOM fractions (e.g. SRFA, SRHA and PLFA) [93, 143, 321], which do not always reflect the variability of NOM composition and properties in the environment. Thus, there is currently a limited knowledge on the effect of NOM composition on NP bioavailability.

The increased use of platinum group element (PGE; i.e. Pt, Pd, Rh) in automobile catalysts has led to an increased release of these elements to the environment. The concentration of Pt in environmental samples, such as road dust, soil, surface water, sediments, and plants has increased significantly in recent decades [64-68, 278] and some studies demonstrated that the released Pt in road dust is in the form of nanoparticles (NPs) [63]. Pt deposited on and/or by the road can be washed out during rainfall and transported to urban rivers, posing a threat to aquatic ecosystems [322]. Pt concentrations in aquatic ecosystems range from 0.4 to10.8 ng L^{-1} to as high as 50 ng kg^{-1} in road dust [60]. The occurrence of PtNPs in the environment raises concerns regarding potential environmental implications (*e.g.*, bioaccumulation and/or toxicity) of PtNPs [61]. Several studies reported bioaccumulation and toxicological effects of Pt in aquatic organisms, such as waterfleas [71], freshwater oligochates [72], microalgae [73], and marine bacteria [74]. Most previous studies

assessed bioavailability and/or toxicity at extremely high Pt exposure concentrations (*e.g.* mg L^{-1}). In addition to lacking environmental relevance, at such high concentrations, NPs aggregate at faster rates, form larger aggregates, are more likely to settle out, and dissolve at slower rates, which may reduce the bioavailability and thus uptake of ENPs for pelagic organisms [51].

The aims of this study are to characterize the effects of NP size and NOM composition on PtNP bioavailability to the model freshwater snail, *Lymnaea stagnalis* using the precepts of a bioaccumulation kinetic model [323]. *Lymnaea stagnalis* has been widely used to investigate metal bioaccumulation [203, 324-326], the species has an extensive geographic distribution, and it represents a significant part of the diet of many fish and crayfish [327].

6.2. Methodology

6.2.1. NP synthesis

Polyvinylpyrrolidone coated platinum nanoparticles (PVP-PtNPs) were synthesized using a seed mediated growth approach described by Sikder et al (2019) [272]. Briefly, 19 nm hydrodynamic sized PVP-PtNPs ($PtNP_{20}$) were synthesized by adding 36 mL of 5 mM chloroplatinic acid hydrate (H_2PtCl_6) in 464 mL ultra-pure water (UPW) at boiling temperature (100 °c) followed by addition of 50 µL of 1 M sodium hydroxide and 11 mL of 1% sodium citrate. Half a minute later, 5.5 mL of a solution containing 0.08% sodium borohydride and 1% sodium citrate was injected quickly to the boiling solution. 10 minutes later the suspension was cooled down to room temperature under vigorous stirring (*i.e.* 700 rpm). 31 nm hydrodynamic sized PVP-PtNPs ($PtNP_{30}$) were synthesized by

adding 10 mL of $PtNP_{20}$ in 290 mL UPW at room temperature followed by addition of 450 µL of 0.4 M H_2PtCl_6 under constant stirring (i.e. 700 rpm). 5 mL of a solution containing 1% sodium citrate and 1.25% L-ascorbic acid was added drop-wisely (1 drop per 3 seconds) and temperature was slowly increased to the boiling point (100°c, increment of 10°c per minute). After 30 minutes, the suspension was cooled down to room temperature under stirring. Larger PVP-PtNPs ($PtNP_{50}$, $PtNP_{75}$, and $PtNP_{95}$) were synthesized by diluting different volumes (40, 10, and 2.5 mL) of NP_{30} in 260, 290, and 297.5 mL UPW, respectively, followed by addition of 450 µL of 0.4 M H_2PtCl_6 under constant stirring (*i.e.* 700 rpm) at room temperature. Then, 5 mL of a solution containing 1% sodium citrate and 1.25% L-ascorbic acid was added dropwise and the reaction temperature was increased slowly to boiling point (100°c, increment of 10°c per minute) under stirring (i.e. 700 rpm). The resulting suspension was then cooled down to room temperature after 30 minutes of reaction.

6.2.3 Experimental organisms

Freshwater snails, *Lymnaea stagnalis*, were reared in moderately hard water (MHW, hardness around 80-100 mg of $CaCO_3$ L^{-1}, pH 8.1, **Table E.1**) [206] as described elsewhere [324, 328]. Three days prior to each experiment, juvenile snails of a restricted size range (average soft tissue dry weight 9.9±0.5 mg, n= 344) were transferred to 10-L glass aquarium with freshly prepared MHW without food. Constraining the size of the experimental organisms allowed minimizing possible confounding allometric effects on bioaccumulation [328]. Eight snails were used in each treatment.

6.2.4. The biodynamic model

Biodynamic modeling deconstructs metal bioaccumulation and quantifies its mechanistic components [203]. Pt influx from solution into the snails (Pt_{influx}) is expressed (Eq. 1) as a function of the unidirectional Pt influx rate constant from solution (k_{uw} (L g^{-1} D^{-1})), and the Pt concentration in solution ($[Pt]_{water}$, µg L^{-1}). Pt efflux varies as a function of the rate constant for physiological loss (k_e, d^{-1}), the rate constant for body growth dilution (k_g, d^{-1}), and Pt concentration in the snail ($[Pt]_{snail}$, µg g^{-1}). Pt efflux was modeled by non-linear regression using either a one or two compartment model (equation 2).

$$Pt_{influx} = k_{uw} \times [Pt]_{water} - k_e \times [Pt]_{snail} - k_g \times [Pt]_{snail} \quad \text{Equation 6.1}$$

$$\frac{C}{Co} = C_1 * e^{-ke_1 \times t} + C_2 * e^{-k_{e2} \times t} \quad \text{Equation 6.2}$$

Where, C is Pt exposure concentration at a given time (µg g^{-1}), C_0 is the Pt concentration in the tissue at the beginning of the elimination phase, C_1 and C_2 are Pt concentrations in the fast and slow exchanging compartments (µg g^{-1}), k_{e1} and k_{e2} are the estimated rate constant of loss (d^{-1}) for the fast and slow compartments, and t is the depuration time (d).

Snail growth was determined by fitting the snail's dry weight (wt_{snail}) to an exponential growth function as shown in equation 4, where wt^0_{snail} is the snails' weight at the beginning of the experiment (mg), k_g is the snails' growth rate constant (d^{-1}), and t is the time (d). If growth is negligible ($k_g \leq 0$), then k equals k_e. If growth is significant ($k_g > 0$), then k equals $k_e + k_g$.

$$Wt_{snail} = wt^0_{snail} \cdot e^{-k_g \times t} \quad \text{Equation 6.3}$$

6.2.4. Waterborne uptake experiments

In the first series of experiments, waterborne exposures were conducted to characterize Pt influx rate constant (k_{uw}) after exposure to dissolved Pt (H_2PtCl_6) and PtNP20. Pt exposure concentrations ranged from 0.01 µg L^{-1} to 100 µg L^{-1}, covering the range of concentrations that might be expected in the aquatic environment [60] . k_{uw} was determined from the slope of the linear relationship between Pt influx rates and the measured exposure concentrations. In the second series of experiments, the effect of PtNP size on Pt uptake was investigated using 1 µg L^{-1} PtNPs of five different sizes (*i.e.* 19-93 nm, designated as $PtNP_{20}$, $PtNP_{30}$, $PtNP_{50}$, $PtNP_{75}$, and $PtNP_{95}$) in MHW. k_{uw} was determined by dividing the measured uptake rates by the measured exposure concentrations. In the third series of experiments, the effect of NOM on Pt influx rate constant was evaluated by exposing the snails to 1 µg L^{-1} of dissolved Pt, $PtNP_{20}$ and $PtNP_{95}$ in the presence of 1 mg L^{-1} of different NOM isolates (designated as NOM 1- NOM 6). k_{uw} was determined similarly as in the second series of experiments.

For each experiment, snails (n= 8 per treatment) were randomly transferred to acid-washed high-density polyethylene (HDPE) containers filled with 1 L MHW and spiked with different concentrations of H_2PtCl_6 and/or PtNPs and NOM (as per requirement). Snails were not fed during the 24-h exposure period to minimize fecal scavenging [203]. The exposure was short enough to ensure sufficient Pt accumulation for accurate detection. After the exposure, snails were removed from experimental media, rinsed with UPW, and frozen. Water aliquots (2 mL) were taken from each vial after gentle stirring before and after exposure to determine the actual Pt exposure concentrations. The water aliquots were digested using concentrated aqua regia (freshly prepared from double distilled HNO_3 and

HCl) and diluted to 1% final concentration prior analysis by inductively coupled plasma-mass spectrometer (ICP-MS).

6.2.5. Elimination experiments

To characterize and compare the physiological elimination of Pt accumulated after waterborne exposure, 65 snails were exposed to either 10 µg L^{-1} dissolved Pt from H_2PtCl_6, $PtNP_{20}$, or $PtNP_{95}$ for four days. Snails were not fed during the exposure period to minimize fecal scavenging. After 4 days, snails were removed from the exposure media, rinsed thoroughly with MHW, distributed into seven 150 mL acid-washed low-density polyethylene vials (each containing 8 snails) that were partially submerged in a 40 L glass tank filled with 20-L freshly prepared MHW. Snails were fed during the depuration period and fecal material was removed from each depuration chamber prior to adding fresh food and MHW every 2 days to minimize the confounding influence of Pt re-ingestion and re-uptake. At each sampling time point (i.e. 0, 1, 2, 3, 5, 7, and 10 days), snails were collected, rinsed with UPW, and frozen. Aliquots of water (n=3) were collected at each sampling time point and were acidified with concentrated aqua regia and diluted to 1% final concentration before analysis using ICP-MS. The Pt efflux rate constants (k_e) were determined by non-linear regression of tissue concentration over time and expressed as the natural logarithm (ln) of the retained proportion (%) of initial accumulated Pt concentration at t=0 (i.e., immediately after collecting them from the exposure).

6.2.6. Sample preparation for Pt analysis

To minimize inadvertent metal contamination, labware, vials, and Teflon sheeting were soaked in acid (10% HNO_3 and/or 5% HCl) for 24 h, followed by rinsing several times with UHPW, and finally dried under a laminar flow hood prior to use.

Partially thawed *L. stagnalis* were dissected using stainless tweezers to remove soft tissues, placed individually on a piece of acid-washed Teflon sheeting, and allowed to dry at 40°c for 3 d. The dry weight of soft tissues was determined to the nearest µg on a microbalance (Sartorius model M2P). Snail tissues were digested in a PTFE vials with 200 µL aqua regia (freshly prepared from double distilled HNO_3 and HCl) for 3 h at 125°c in an autoclave. Digested water and tissue samples were diluted using UPW (final volume 4 mL) and an internal standard (thallium) was added to control signal drift. Diluted samples were filtered (0.45 µm, Pall) and analyzed for Pt by inductively coupled plasma mass spectroscopy (ICP-MS, PerkinElmer NexION 300Q). The ICP-MS were calibrated with 10, 100, 1000, and 10000 ng L^{-1} Pt standards and Thallium (Tl) was used the internal standard in all the standards and samples. One of the standards was analyzed after every 10 samples to quantify any deviations in the concentrations due to instrumental drift. Deviations from the standard values were less than 10% for the analyzed Pt isotope (^{195}Pt). Similar weight samples of an in-house reference tissue material (Supporting Information) were subjected to the same digestion procedure during each analytical run and recovery of the standard reference material was 95±3%. Procedural blanks were also digested with samples during each analytical run and were below the method detection limit (MDL) of 0.005 µg L^{-1}.

6.2.7. Natural organic matter isolates

Natural organic matter (NOM) isolates were extracted from different environments (**details in Table E.4**): water conservation area (WCA) F1 site, 2B south site, and Arthur R. Marshall Loxahatchee National Wildlife Refuge (LOX) 8 site (denoted as NOM 1,2, and 6 respectively), Suwannee river (NOM 5), Williams lake (NOM 3), and Pacific ocean HPOA (NOM 4) (**Table E.4**). All 6 NOM isolates were isolated as hydrophobic organic acid (HPOA) fraction. All NOMs, except NOM4, were isolated in freeze-dried form following the protocol described in Aiken et al. (1992) [279]. The Pacific ocean HPOA (NOM 4) was collected and isolated following the protocol described in Green et al. (2017) [280]. The NOM isolates were fully characterized by determining their elemental composition [281], specific ultra-violate light absorbance at 254 nm ($SUVA_{254}$) [282], and sulfur speciation [329], and properties are briefly summarized in the supplemental information (SI) section (**Table E.4**).

6.3. Results and discussions

6.3.1. Particle characterization and behavior in moderately hard water

The physiochemical properties of the synthesized PVP-PtNPs were measured using a multimethod approach [272] and are briefly summarized below. The mean core sizes measured by TEM were 9.2±1.2, 10.9±0.8, 18.5±5, 44.5±5, and 72.5±3.9 nm, respectively for the $PtNP_{20}$, $PtNP_{30}$, $PtNP_{50}$, $PtNP_{75}$, and $PtNP_{95}$ (**Table E.2**). The corresponding mean hydrodynamic diameters measured by DLS were 18.9±0.3, 31.4±0.8, 51±0.7, 74.7±0.2, and 93.4±1, respectively (**Table E.2**). The Zeta potential of $PtNP_{20}$-$PtNP_{95}$ decreased from -16.9±3.5 to -27.2±1.7 mV with the increase in particle size (**Table E**).

The aggregation behavior of PVP-PtNPs ($PtNP_{20}$-$PtNP_{95}$) in MHW was measured at environmentally-relevant low NP concentration (e.g., 1 µg L^{-1}) using sp-ICP-MS. Briefly, PtNP aggregate size decreased with the increase in primary particle size. While $PtNP_{20}$-$PtNP_{75}$ formed aggregates in MHW, $PtNP_{95}$ remained stable during the exposure duration. $PtNP_{20}$ aggregate size did not change significantly in MHW in presence of NOM 1, 2, 3, 5, and 6 compared to $PtNP_{20}$ aggregate size in MHW in absence of NOM (ANOVA with Tuckey's multiple comparison test, $\alpha = 0.05$). in contrast, NOM 4 (Pacific Ocean HPOA) increased the aggregation of PtNP20 in MHW and formed significantly larger aggregates relative to the aggregate size in absence of any NOM.

6.3.2. Pt influx in *L. stagnalis*: Effect of size and aggregation

Snail Pt background concentration was 3 ± 1 ng g^{-1}, which impeded the detection of Pt accumulation at exposure concentrations lower than 10 ng L^{-1}. For example, the accumulation of Pt in snails exposed to 10 ng l^{-1} of Pt^{4+} and $PtNP_{20}$ was not detectable beyond that of the background Pt concentration. At higher Pt concentrations, however, Pt influx in the snail's soft tissues increased linearly as a function of concentration (>0.01-100 µg L^{1}) for Pt, added as H_2PtCl_6 or $PtNP_{20}$ (1st series of experiment) (**Figure 6.1**). A statistically significant linear relationship ($p < 0.001$) was observed over the entire range of concentrations for both forms of Pt (**Figure 6.1**). The influx rate constants from waterborne exposure (k_{uw} ± SD in µg g^{-1} d^{-1}) were 0.055 ± 0.003 L g^{-1} d^{-1} for dissolved Pt^{4+} (added as H_2PtCl_6) and 0.139 ± 0.007 L g^{-1} d^{-1} for $PtNP_{20}$. Because dissolution of PVP-PtNPs in MHW was < 10%, (which was also the case of all NP tested throughout the study),

these results indicate that Pt accumulation from NP_{20} exposure can be attributed mainly to the nano-form of Pt rather than the dissolved Pt fraction.

Snails exposed to 1 µg L^{-1} PVP-PtNPs of five different sizes (second series of experiments; NP_{20}-NP_{95}, size details in **Table E.2**) significantly accumulated Pt in their tissues. The Pt influx rate constants (k_{uw}) ranged from 0.09 ± 0.01 to 0.75 ±0.34 L g^{-1} d^{-1} and increased as a function of PtNPs hydrodynamic diameter (**Figure 6.2**). The influx rate constants for $PtNP_{20}$, $PtNP_{30}$ and $PtNP_{50}$ were not statistically different (ANOVA, *p-value* > 0.25). The influx rate constant for $PtNP_{95}$ was significantly higher (*p-value* < 0.05) than that for the other PtNPs ($PtNP_{20}$-$PtNP_{75}$). Similarly, the influx rate constant for of the NP_{75} was statistically higher than those for the NP_{20}-NP_{50} (*p-value* < 0.05). The decrease in Pt bioavailability with the decrease in PtNP size is likely due to the increased aggregate size of PtNPs with the decrease in NP size, likely resulting in increased sedimentation of smaller PtNP aggregates. Sedimentation reduces the actual Pt exposure concentration, and thereby reducing the overall PtNP influx. Thus, the apparent size-dependent influx of PtNPs observed here is not necessarily due to particle size, but most likely due to the reduction in actual exposure concentration from NP aggregation.

6.3.3. Physiological loss of accumulated Pt

Snails significantly gained weight during the 10-day depuration period of the physiological loss experiments (**Figure E.1**). Growth rate constants (k_g) varied from 0.04±0.02, 0.07±0.02, and 0.02±0.01 d^{-1}, respectively for dissolved Pt, $PtNP_{20}$, and $PtNP_{95}$, respectively. Losses due to growth dilution (k_g) were subtracted from the observed losses of Pt to determine the actual physiological rate constant for Pt loss (**Table 6.1**).

The physiological elimination of Pt accumulated by *L. stagnalis* after aqueous exposure to dissolved Pt and PtNPs (NP_{20} and NP_{95}) varied between Pt forms and between PtNP sizes. The proportional elimination of Pt follows a one compartment model for dissolved Pt (**Figure 6.3a**), with a Pt elimination (or efflux) rate constant of 0.14±0.03 d^{-1}, indicating snails lost approximately 14% of their tissue burden of Pt per day. In contrast, nearly 30% of the accumulated $PtNP_{20}$ was eliminated during the first 24 h of depuration, and no elimination was detected for the next 3 days (**Figure 6.3b**). Thereafter, snails lost approximately 23% of their body burden of Pt per day. The physiological loss of Pt from accumulated $PtNP_{95}$ followed the same trend as that for $PtNP_{20}$, with initial fast efflux rate (from t=0 to t=1d) followed by a slower efflux rate (from t=3d to t=10d) (**Figure 6.3c**). The rate constant associated with fast efflux (k_{e1}) was calculated by mathematical stripping [330] and the rate constant associated with the slow efflux rate (k_{e2}) was calculated using Eq.2 as described above. The combination of ke_1 and ke_2 describes the overall loss dynamics of Pt accumulated from $PtNP_{95}$. The data presented for 2-component loss of accumulated Pt from NP_{95} are ambiguous and could be interpreted as either a fast efflux rate of Pt (k_{e1}) for 2 days followed by a lower efflux rate (k_{e2}) or as a k_{e1} lasting for 4 days and a k_{e2} in which there is almost no Pt remaining. The later scenario provided a better fit to the net uptake experiment (r^2 = 0.94, compared to r^2= 0.41) and is the interpretation we recommend (**Figure 6.3c**). Thus, Pt accumulated from $PtNP_{95}$ exposure were eliminated at a rate of 1.03 d^{-1} for the first 4 days and 0.1 d^{-1} thereafter with 95% and 5% in the fast and slow loss compartments, respectively. Overall, the efflux rate constant of Pt increased according to the following order dissolved Pt < $PtNP_{20}$ < $PtNP_{95}$.

The physiological elimination of Pt varied significantly between dissolved and particulate form. The PtNPs eliminated efficiently, especially for the NP_{95}. Dissimilarities in elimination rate, along with influx rate, suggest a different fate within the animal for the form of Pt. Platinum eliminated quickly following a linear pattern, with only 24% Pt retention after 10 days (**Figure 6.3a**) of waterborne exposure of dissolved Pt (i.e., H_2PtCl_6). However, *L. stagnalis* has showed higher retention with extremely slow physiological loss when accumulating from other dissolved metal exposures (i.e., Zn, Ag) [203, 324]. This might be due to poor absorption potential for dissolved Pt in the gastronomical tract. The bioavailability of dissolved Pt in the digestive tract of Lewis rats showed that 90-96% of initial Pt was eliminated from the rat's body through feces and/or urine within 48 h [67, 331], inferring the poor retention of dissolved Pt in the digestive tract. Similarly, 85% of initial Pt was eliminated from freshwater isopod, *Asellus Aquaticus*, after the waterborne uptake [67]. The $PtNP_{20}$ influx in *L. stagnalis* was slower relative to $PtNP_{95}$, attributed to the aggregation of $PtNP_{20}$ in MHW. But once entered, the retention of $PtNP_{20}$ in the digestive tract was longer relative to $PtNP_{95}$. This might be because of the higher cellular internalization of smaller NP (i.e., $PtNP_{20}$) [332] and/or more reactivity of the $PtNP_{20}$ with the myriad of ligands in the gut. The $PtNP_{95}$ were stable in exposure media (i.e., MHW), influx to a greater extent, and eliminated readily (i.e., 80% in 24 h, **Figure 6.5c**) compared to the $PtNP_{20}$. Therefore, the $PtNP_{95}$ has a low potential for bioaccumulation and subsequent toxicity, as they are less influenced by the condition.

6.3.4. Effect of NOM composition on Pt influx

The third series of waterborne exposure experiments aimed at examining the effect of NOM isolates from different sources and composition (details in **Table E.4**) on Pt bioavailability (inferred from the influx rate constant). The influx rate constants (k_{uw}) for dissolved Pt in the presence of all NOM isolates were not statistically different ($p > 0.05$) relative to that measured in the absence of NOMs (**Figure 6.4a**). These results contradict with the results reported on the influence of NOM on waterborne metal bioavailability (i.e., Pb, Hg, Cd, Cu, Ag, U, and Co) [333-337]. Suggesting that the formed Pt-NOM complexes (if formed under the experimental condition) are bio-available from the dissolved phase, at least in *L. stagnalis* and NOM alone is not influencing the dissolved Pt influx. NOM 2 (Evergaldes 2B-south HPOA) and NOM 4 (Pacific ocean HPOA) significantly supressed (t-test, $p < 0.05$) Pt bioavailability from $PtNP_{20}$ exposure by 45% and 55%, respectively. However, other NOM isolates (i.e., NOM1, NOM3, NOM5, and NOM6) did not influence the k_{uw} significantly (**Figure 6.4b**, *p-value* > 0.05). In contrast, all NOM isolates suppressed the bioavailability of Pt from the $PtNP_{95}$. The extent of k_{uw} suppresion varied between 39-90% (**Figure 6.4c**). The PtNP-specific and NOM-specific influences on Pt bioavailability can be attributed to **1)** the differences in the NOM molecular composition and properties, which may affect the propoerties of the PtNP NOM-corona, and **2)** differences in aggregation behavior of the PtNPs. For example, the greater suppression (*p-value* < 0.05) of Pt bioavailability from the $PtNP_{20}$ in presence of NOM 2 and NOM 4 can be attributed to increased $PtNP_{20}$ aggregation in the presence of these two NOM isolates. The formation of larger aggregate size in the presence of NOM 2 and NOM 4 may reduce the waterborne Pt exposure concentration via sedimentation. On the other hand, the

stability of $PtNP_{95}$ in the presence of all NOM isolates suggests that the differences in bioavailability observed among NOM isolates might be attributed to differences in NOM properties, and thus the composition of NOM-corona.

6.3.5. Correlating k_{uw} of $PtNP_{95}$ to NOM properties

The NOM isolates used in these experiments represent a diverse array of dissolved HPOAs. Because of the stability of $PtNP_{95}$ in MHW in the presence of all NOM isolates, differences in composition among NOM isolates may explain the difference in Pt bioavailability across NOM isolates. To gain insights into the relationship between k_{uw} and NOM properties, we performed Pearson's correlation analysis between k_{uw} and specific NOM property. Calculated Pearson's correlation coefficient (r) and p-values were used to assess the correlation quality at statistical significance of 0.05 (**Table 6.2**). The NOM parameter producing the best correlation was S content ($r= 0.99$, $p < 0.001$) (**Figure 6.5a, Table 6.2**). Weak or no correlations were observed with the molecular weight, $SUVA_{254}$, C, H, O, N, and inorganic ash content in NOM isolates (**Figure E.3, Table 6.2**).

The sulfur speciation in NOM was investigated using sulfur k-edge X-ray absorption near edge structure spectroscopy (XANES) on the HPOA fractions of NOM, to give more insight about the relationship between k_{uw} and NOM property. Reduced sulfur (S_{red}) content - in form of exocyclic and heterocyclic reduced sulfur- in the NOMs exhibited a strong positive correlation with k_{uw} ($p < 0.001$, **Table 6.2** and **Figure 6.6a,b**). Sulfoxide content (S_{sulfo}) in NOM also exhibited strong positive correlation ($r= 0.99$, $p < 0.001$) with k_{uw} of $PtNP_{95}$ (**Figure 6.6c**). However, other oxidized sulfur (S_{ox}) -in form of sulfonate, sulfone, and organosulfate- exhibited positive correlation with k_{uw}, but none of them is statistically significant ($p > 0.15$) (**Figure E.6, Table 6.2**). The stronger correlation

between k_{uw} and reduced S content may be attributed to the higher affinity of reduced S to PtNP relative to oxidized S. Sulfur is a well-known nutrient and increase in S content in the NOM resulted in an increase in S content on the PtNP surface. Hence, NOM coated stable $PtNP_{95}$ could be acting as a possible nutrient source to the snails, resulting in an increase in Pt influx.

6.4. Conclusions

NP size and NOM plays a pivotal role in determining the behavior and fate of PtNPs in the aquatic environment. The influx rate constant (k_{uw}) and/or bioavailability decreased with decreasing PtNPs size, attributed by the higher aggregation tendency of smaller PtNPs in MHW. Aggregation of smaller NPs resulted in increased sedimentation of NPs aggregates, subsequently reduced the actual Pt exposure concentration, and thereby reduce the overall PtNPs influx. Therefore, the apparent size-dependent influx of PtNPs we observed here is not necessarily due to particle size, but most likely due to the reduction in actual exposure concentration because of NP aggregation. The larger NP (i.e., $PtNP_{95}$) also eliminated readily relative to the smaller NP (i.e., $PtNP_{20}$), inferring the low potential for bioaccumulation and subsequent toxicity. The dissimilarities in the influx rate, along with the elimination rate, suggest a different fate within the snail for the form of Pt (i.e., PtNP vs dissolved Pt and $PtNP_{20}$ vs $PtNP_{95}$). Presence of NOM did not influence Pt uptake from the dissolved Pt waterborne exposure. Significantly reduced k_{uw} (*p-value* < 0.05) from the waterborne exposure of $PtNP_{20}$ in the presence of NOM 2 and 4 (Everglades WCA-2BS and Pacific Ocean HPOA, respectively), relative to k_{uw} in absence of any NOM, was attributed to the increased $PtNP_{20}$ aggregate size. In contrast, $PtNP_{95}$ was stable in MHW, regardless of the presence of NOM. However, k_{uw}'s for the $PtNP_{95}$ were significantly

suppressed (*p-value* < 0.05) by all NOM isolates, which was directly attributed to the difference in NOM properties and the composition of NOM-corona. The k_{uw} for the $PtNP_{95}$ increased incrementally with S content in the NOM isolates and k_{uw} had a statistically significant correlation with the sulfoxide, heterocyclic and exocyclic reduced sulfur forms (Pearson's correlation test, $\alpha = 0.05$).

Taken together, our results illustrate that the bioaccumulation of NP depends on several factors, including NP size and NOM molecular characteristics. The size-dependent uptake of NPs is not necessarily due to primary particle size but might also be due to the aggregation and/or other metal specific behaviors (e.g., dissolution, transformation) of NPs. This study shows the potential importance of interactions between NOM and PtNPs and the consequences of these interactions for NP behavior and bioavailability in aquatic ecosystem. The environmental implications of NP and NOM interactions need to be addressed with a broader spectrum of NOM isolates and with other NPs to gain improved understanding of NP reactivity as a function of NOM composition. Biodynamics has the potential to provide an effective basis from which a quantitative assessment of the metal NPs bioavailability and subsequent potential toxicity under different conditions. Similar biodynamic models for other representative species would provide a tool for regulators to build a comprehensive risk assessment for NPs across diverse aquatic environment (i.e., seawater, freshwater, hard water etc.).

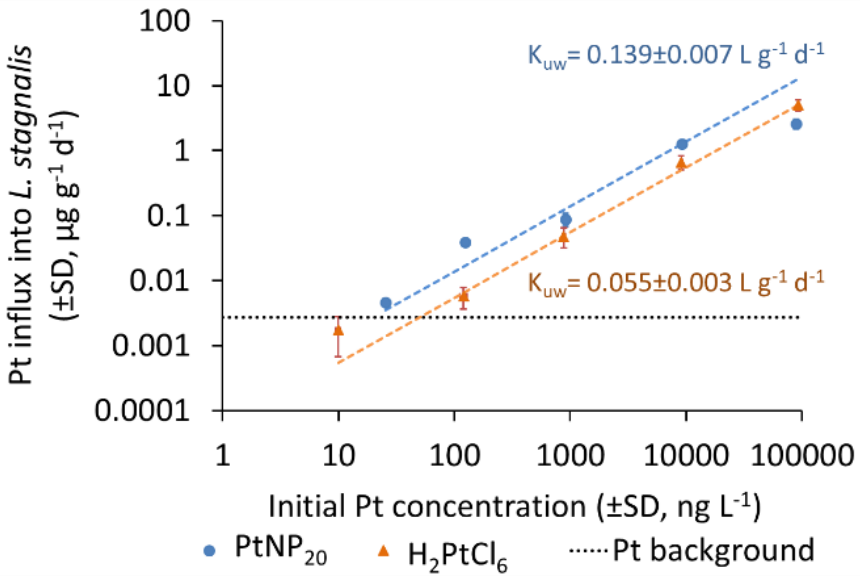

Figure 6.1. Platinum influx rates (µg g^{-1} d^{-1}, ±SD) in *Lymnaea stagnalis* after waterborne exposure to Pt added as H_2PtCl_6 and $PtNP_{20}$ for 24 h. Each point represents Pt mean concentration in 8 individual snails (±SD). The dashed lines represent the linear correlation between Pt influx and Pt exposure concentration.

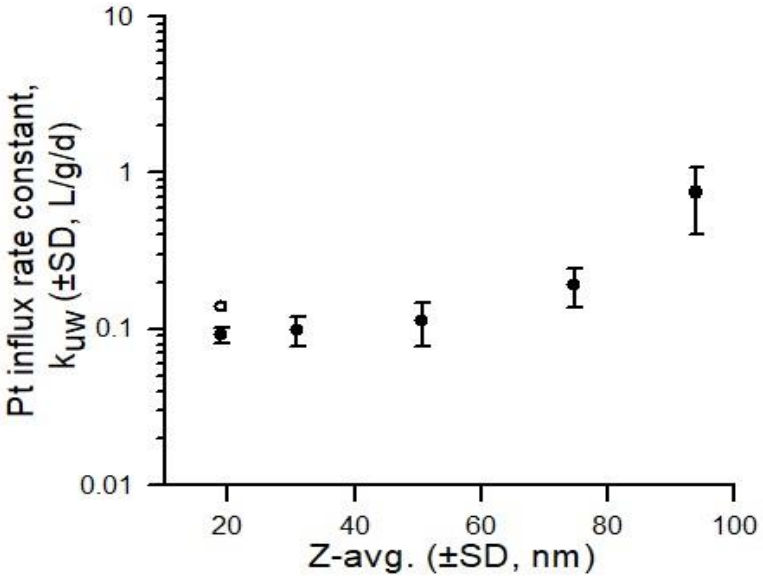

Figure 6.2. Pt influx rate constant, k_{uw} (L g^{-1} d^{-1}, ±SD) as a function of hydrodynamic size following *L. stagnalis* were exposure to 1 µg L^{-1} PVP-PtNPs of 5 different sizes ($PtNP_{20}$, $PtNP_{30}$, $PtNP_{50}$, $PtNP_{75}$, and $PtNP_{95}$) for 24 h. SD was determined by propagating the errors for the measured Pt influx in snails' tissues and the corresponding Pt concentration in the media.

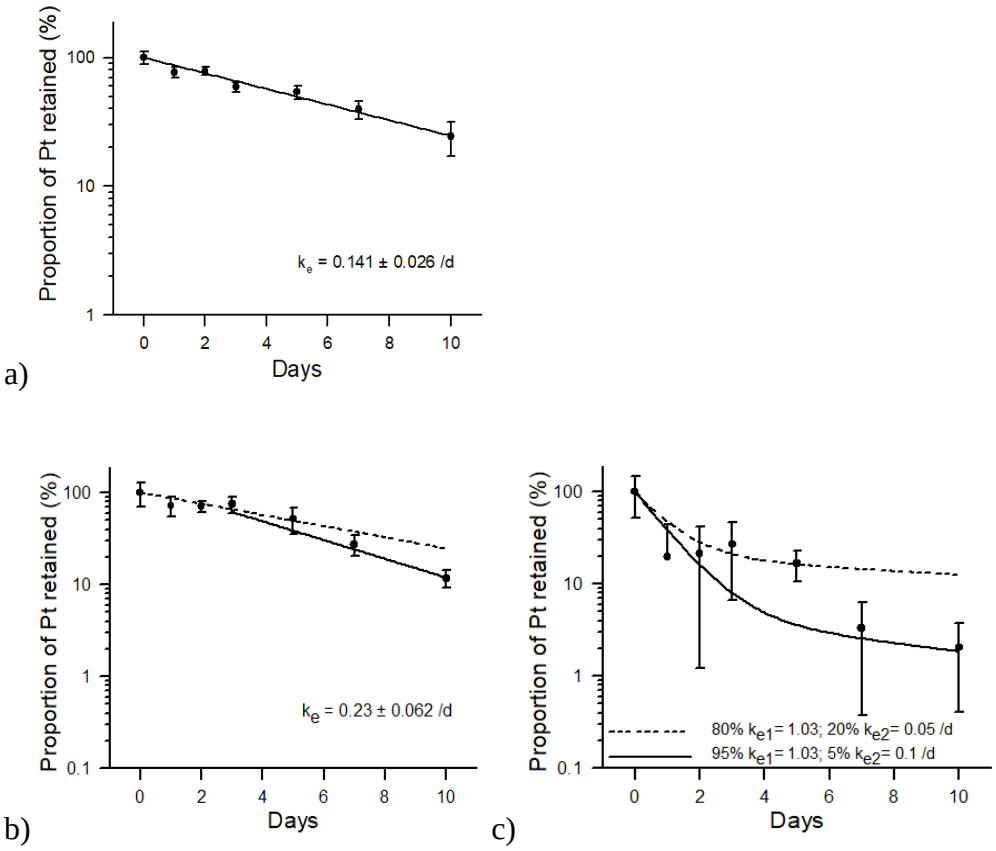

Figure 6.3. Proportional loss of Pt over time in *L. stagnalis* after waterborne exposures to (a) dissolved Pt added as H_2PtCl_6, (b) $PtNP_{20}$, and (c) $PtNP_{95}$. Solid line in "b" represents proportional loss of Pt over time after initial rapid elimination for 1 day followed by lack of significant loss over 3 days and dashed line represents proportional loss of Pt from time 0 to day 10. Solid line in "panel-c" represents 95% loss during initial rapid elimination followed by slower second phase of elimination of the remaining 5%. Dashed line in c represents 80% loss during rapid elimination followed by slower 2nd phase of elimination of the remaining 20%

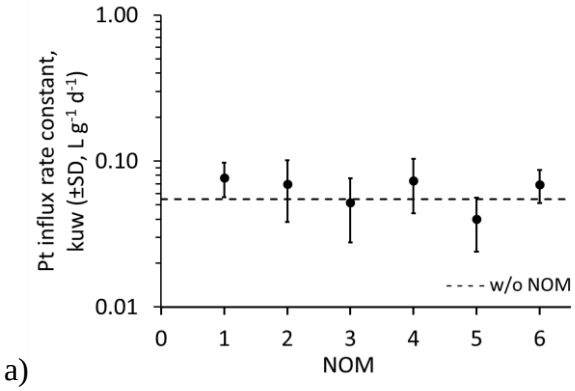

a)

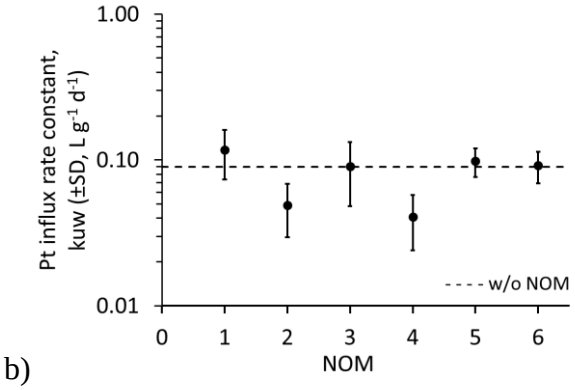

b)

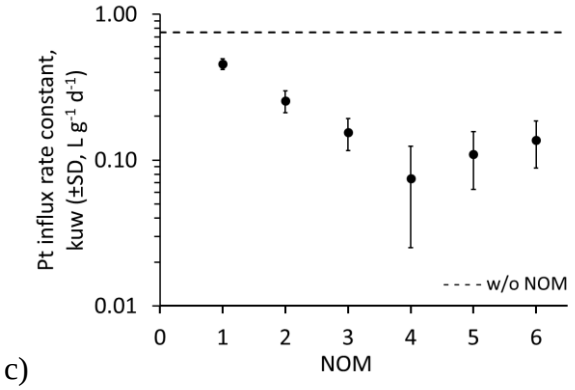

c)

Figure 6.4. Pt influx rate constant, k_{uw} (L g^{-1} d^{-1}, ±SD) in *L. stagnalis* after waterborne exposure to 1 µg L^{-1} (a) dissolved Pt added as H_2PtCl_6, (b) $PtNP_{20}$, and (c) $PtNP_{95}$ for 24 h in presence of 1 mg L^{-1} natural organic material (NOM) isolates. Each point represents mean Pt concentration for 8 individual snails (±SD). Dashed line represents Pt influx rate constant in absence of NOM under the same exposure condition.

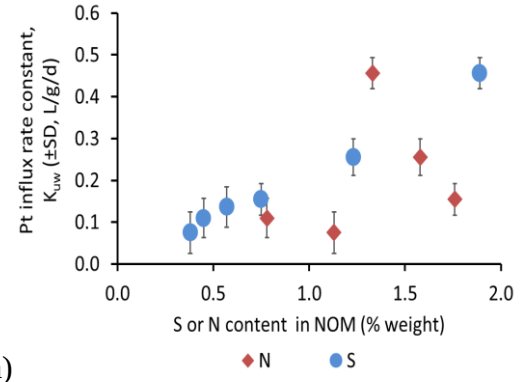

a)

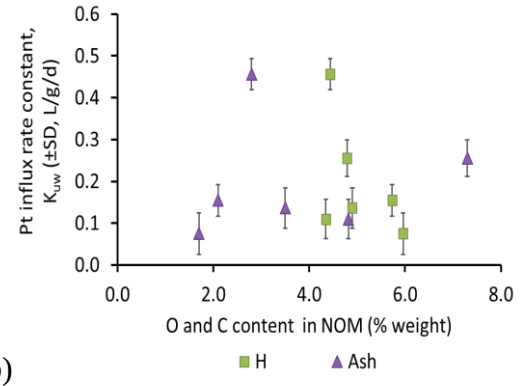

b)

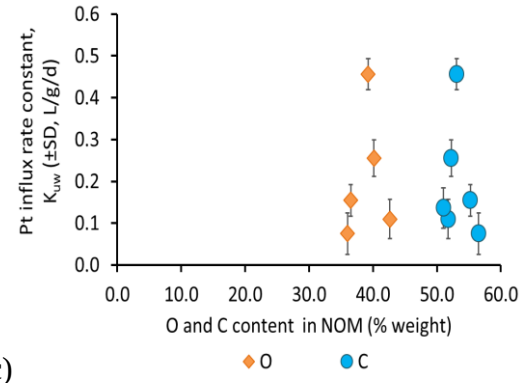

c)

Figure 6.5. Relation between (a) S and N content, (b) H and ash content, and (c) O and C content of NOM isolates and Pt influx rate constant, k_{uw} (L g^{-1} d^{-1}, ±SD) in *L. stagnalis* after waterborne exposure to 1 µg L^{-1} $PtNP_{95}$ in presence of 1 mg L^{-1} NOM for 24 h.

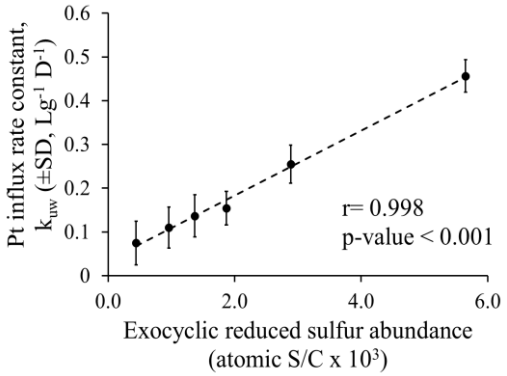

a)

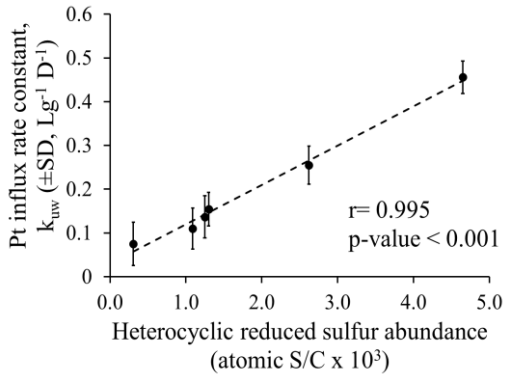

b)

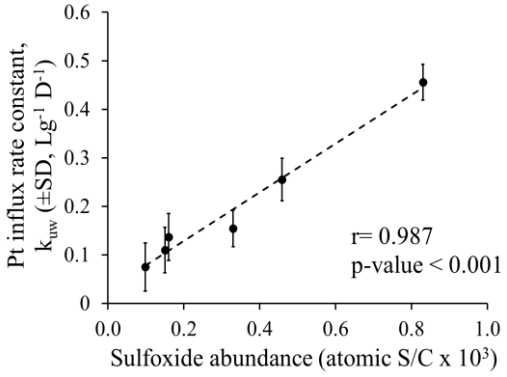

c)

Figure 6.6. Correlation between (a) exocyclic reduced sulfur content (S_{Exo}), (b) heterocyclic reduced sulfur content (S_{Hetero}), and (c) sulfoxide (S_{sulfo}) presented in all 6 NOM and the Pt influx rate constant (k_{uw}, L g^{-1} d^{-1}, ±SD) when *L. stagnalis* exposed to 1 µg L^{-1} $PtNP_{95}$ in presence of 1 mg L^{-1} NOM for 24 h. Each point represents the mean±standard deviation of Pt concentrations in soft tissues of 8 individual snails.

Table 6.1. Biodynamic parameters (±SD) for Pt by *Lymnaea stagnalis*

	Dissolved Pt	$PtNP_{20}$	$PtNP_{95}$
k_{uw} (L g^{-1} d^{-1})	0.06 ± 0.01	0.14 ± 0.01	0.75 ± 0.34
k_e (d^{-1})	0.14 ± 0.03	0.23 ± 0.06	1.03 ± 0.12
k_g (d^{-1})	0.04 ± 0.02	0.07 ± 0.02	0.02 ± 0.01
$k = k_e + k_g$ (d^{-1})	0.18	0.3	1.05

Table 6.2. Analysis results of Pearson's correlation between Pt influx rate constant and NOM properties for the $PtNP_{95}$

Variables	Pearson's correlation coefficient (r)	p-value
$PtNP_{95}$ influx rate constant vs NOM elemental composition		
Molecular weight	-0.28	0.655
$SUVA_{254}$	0.39	0.444
C	-0.21	0.684
H	-0.52	0.293
O	0.17	0.826
N	0.3	0.705
S	0.99	< 0.001 *
Inorganic ash content	0.14	0.793
$PtNP_{95}$ influx rate constant vs organic S content		
Heterocyclic sulfur	0.99	< 0.001 *
Exocyclic sulfur	0.99	< 0.001 *
Sulfoxide	0.99	< 0.001 *
Organosulfate	0.4	0.436
Sulfone	0.6	0.205
Sulfonate	0.66	0.149

CHAPTER 7

CONCLUSIONS

The overall aim of this PhD dissertation was to investigate the effects of particle size and concentration, media characteristics, and NOM molecular properties on the aggregation, dissolution, bioaccumulation, and toxicity of metallic NP at the environmentally relevant conditions. This overarching goal was achieved by addressing the following specific objectives: 1) controlled synthesis and comprehensive characterization of AgNPs and PtNPs using a multimethod approach, 2) evaluating the behaviors of AgNPs and PtNPs in relevant environmental and (eco)toxicological media, and 3) investigating the role of particle size and NOM composition on NP aggregation, bioaccumulation and toxicity.

Citrate coated AgNPs were synthesized by reduction of Ag^+ ions using sodium borohydride as a reducing agent and citrate as a capping agent [165]. Five different size citrate coated PtNPs were synthesized using seed mediated growth approach [192]. PVP coated AgNPs and PtNPs were obtained by a ligand exchange approach using citrate coated AgNPs and PtNPs as precursors, respectively [75]. Then, the concentration-dependent dissolution of AgNPs was investigated in synthetic seawater using UV-vis and ultrafiltration coupled ICP-MS. The colloidal stability of PtNPs were evaluated in different media – moderately hard water, DMEM, and synthetic seawater – using multiple analytical techniques, such as DLS, UV-vis, and sp-ICP-MS. PtNPs bioaccumulation and body burden were measured by ICP-MS following soft tissue digestion in aqua regia. The life-cycle chronic toxicity of AgNP, at sub-lethal exposure concentrations, were evaluated using standardized life-cycle based microplate bioassay methods (ASTM 2012, OECD 2014) [246, 254] and compared to the chronic toxicity of dissolved metal fraction. The overall conclusions of these studies are summarized below:

7.1. Summary of findings

7.1.1. Synthesis

1- Synthesized PVP-AgNPs were monodispersed, spherical, and stable in suspension, with a hydrodynamic size of 21.6±0.3 nm, PDI of 0.27±0.01, zeta potential of -23.4±5.4 mV, and core size of 12.3±2 nm.

2- All five PVP-PtNPs were monodispersed, spherical, and colloidally stable, with hydrodynamic size of 18.9±0.3, 31.4±0.8, 51±0.7, 74.7±0.2, and 93.4±1 nm, PDI of 0.36, 0.19, 0.2, 0.03, and 0.1, zeta potential of -21.7±3.8, -24.2±3.3, -25.6±0.7, 30.1±1, and -31±0.3, and core size of 9.2±1.2, 10.9±0.8, 18.5±5, 44.5±2.7, and 72.5±3.9, respectively for $PtNP_{20}$, $PtNP_{30}$, $PtNP_{50}$, $PtNP_{75}$, and $PtNP_{95}$.

7.1.2. Nanoparticle Characterization

3- A method based on UV-vis spectroscopy analysis was validated for the quantification of sterically stabilized PVP-AgNPs concentration and dissolution in high ionic strength aqueous media (i.e., synthetic seawater) A relationship between AgNP size, maximum absorbance wavelength (λ_{max}), and extinction coefficient (ε) was established, which overcomes the need to measure NP size by more direct measurement method (i.e., TEM). This implies that UV-vis can be used as a detection method to measure AgNPs concentration in SW and potentially in other environmental matrices.

4- The sizes of PtNPs measured using DLS, FlFFF, TEM, AFM, and sp-ICP-MS were all in good agreement whenever, the NP sizes were larger than the size detection limits for each analytical technique. The mean sizes of NPs as measured by five different techniques are different and generally follow the order $d_{AFM} <\sim d_{TEM} < d_{sp\text{-}ICP\text{-}MS} < d_{FlFFFF} < d_{DLS}$. These differences were mainly attributed to the differences in (i) measurement principles, (ii) the obtained measure versus PSD weighting, and (iii) NP structure. The TEM, AFM, and sp-ICP-MS measured the particle core size, whereas, DLS and FlFFF measure NP hydrodynamic diameter (i.e., core size + diffuse layer). Thus, the NP sizes measured by DLS and FlFFF are generally larger than those measured by TEM, AFM, and sp-ICP-MS

7.1.3. Nanoparticle behavior in environmental and toxicological media

5- The aggregation of PtNPs in presence of monovalent (i.e., $NaNO_3$) or divalent electrolytes (i.e., $Ca(NO_3)_2$) was typical of DLVO type aggregation behavior as reported for other types of NPs (i.e., AgNPs, AuNPs, TiO_2-NPs etc.). The critical coagulation concentration (CCC) of PtNPs was independent of particle size, possibly due to differences in PtNPs surface charge as a function of NP size.

6- The aggregation behavior of PtNPs depended on media composition, NP concentration, and ionic strength. PtNPs remained stable in DMEM regardless of NP concentration and surface charge, whereas they aggregated in SW and MHW. At a given concentration, PtNPs mean size increased and the particle number concentration decreased following the order of SW > MHW > DMEM. DMEM media is rich with organic compounds (e.g., amino acids, vitamins, proteins) that are well known to sorb onto NP surfaces to form colloidal stability via steric

stabilization. In contrast, the higher aggregation and surface charge screening in SW is due to the higher ionic strength of SW compared to MHW.

7- PtNPs exhibited an increase in aggregate size with increases in NP concentration in MHW and SW. Despite their aggregation, a fraction of PtNPs remained as primary particles and the % of unaggregated primary NPs increased with the decrease in NP concentration. This was due to the decrease in NP collision frequency, resulting in the formation of smaller aggregates and/or lack of NP aggregation. This finding suggests that NP aggregation became less significant at lower concentrations, and that, NPs may remain as primary particles for an extended period at environmentally relevant concentrations.

8- The dissolution of PtNPs in the different toxicological media after 24 h were only 5-15% of the total Pt concentration. These amounts were variable across samples and not statistically different, indicating limited and/or no dissolution of PtNPs regardless of the NP concentration, ionic strength of the media, and surface coating around the NP. Taken together, limited aggregation and lack of dissolution at environmentally relevant concentrations suggest that PtNPs are an excellent model NP for future fundamental studies of NP environmental transport, fate, deposition, and biological uptake.

9- The dissolution of AgNPs in synthetic seawater varied with particle concentration. At lower concentrations, NP size decreased faster and to a higher extent than at higher NP concentrations. This differential change in NP size should be considered when investigating the toxicological effects and risks of NPs in the environment. Higher dissolution rates and consequently faster reduction in primary NP sizes at

lower concentrations suggest that, NPs and their dissolution products are more bioavailable than has been considered toxicologically in previous studies.

10- PtNP aggregate size increased with the decrease in PtNP size likely due to the lower zeta potential and the higher number concentration of smaller NPs compared to larger NPs at the same mass concentration.

11- The effect of NOM on NP aggregation is size-dependent. Smaller NPs were more impacted by NOM, which might be attributed to the size-dependent NOM-corona composition/properties. Whereas, the 20 nm PtNPs ($PtNP_{20}$) formed aggregates in MHW in presence and absence of NOM, the 95 nm PtNPs ($PtNP_{95}$) remained colloidally stable in MHW, regardless of NOM presence.

12- NOM molecular properties determine the aggregation extent of $PtNP_{20}$. NOM molecular properties associated with higher charge density (i.e. O to C content, O/C), molecular weight (MW), $SUVA_{254}$, condensed hydrocarbon (ConHC), and tannin demonstrated negative correlation with the observed aggregation of $PtNP_{20}$. Higher O/C ratio indicates a higher content of functional groups, such as carboxylic groups [127]. The higher content of these functional groups is likely to enhance NP surface charge and thus increase the electrostatic repulsive forces between NOM-coated PtNPs, and thus enhance NP stability. An increase in MW would presumably lead to thicker adsorbed layers of NOM on NP surface, particularly by forming loop and tail structure and resulting in increased steric stabilization[291-293]. An increase in $SUVA_{254}$ and the relative abundance of ConHC would presumably lead to higher sorption of these molecules on NP surfaces and thus increasing the NP hydrophobicity, and thus may enhance repulsive forces between NPs and

colloidal stability. Tannins are high molecular weight polycyclic aromatic compounds with high O/C ratio and charge density, which are likely to enhance the surface charge and resulting higher stability of NP_{20}. Additionally, the hydrophobic nature and polymer structure of tannins was responsible for the increased colloidal stability and decreased aggregation. The aggregate size of $PtNP_{20}$ increased with the increase in relative abundance of lignin. Lignin is a high molecular polyphenolic compound with hydrophilic regions, such as hydroxyls (–OH), carboxylic (–COOH), and small alkyl chains i.e., methane groups ($–CH_3$). These functional groups and the hydrophobic regions of lignin (e.g., resinol, C-H groups) enable it to bind with organic matter and mineral particles through polar, covalent, and hydrogen bonding as well as Van der Waals forces. These humidified and highly decomposed materials, which are more stable, aid in the formation of microaggregates.

7.1.4. Nanoparticle Uptake and Toxicity

13- A concentration dependent mortality increases in mortality of *A. tenuiremis* were observed in PVP-AgNPs and $AgNO_3$ exposure, at environmentally relevant sub-lethal concentrations. Toxicity of AgNPs were attributed to direct NP effect, release of Ag^+ from AgNPs, or to both. In contrast, the toxicity of $AgNO_3$ were impacted by the Ag^+ concentration in the solution. Sharp decline in the reproduction (i.e., fecundity) were observed in the $AgNO_3$ exposure, whereas, fecundity was not impacted by the PVP-AgNPs exposure. The observed differences in toxicological response for $AgNO_3$ vs PVP-AgNPs were attributed to the dynamics of $[Ag^+]$ change over each 72-h treatment renewal period. For each $AgNO_3$ test

concentration, copepods were exposed for 35 d to the maximal dissolved Ag concentration that could be delivered, and with a significant portion of dissolved Ag rapidly sorbed to the surfaces of algal cell food. For PVP-AgNPs treatments, the actual realized exposure is a combination of intact PVP-AgNPs in suspension and also associated with algal food, plus any released dissolved Ag from NPs' gradual dissolution and sorption to the food. Hence, under similar exposure conditions, PVP-AgNPs exposures likely produced less freely dissolved Ag than $AgNO_3$ exposures, resulting lower toxicity (i.e., survival, development, reproduction, and population growth potential) of PVP-AgNPs on *A. tenuiremis* compared to the severe chronic effects observed for dissolved $AgNO_3$.

14- Although, copepod exposure to PVP-AgNPs had little effect on their ability to survive, reproduce, and increase in population, gradual release of Ag^+ from AgNPs may still pose some risk to marine ecosystems through rapid and complete dissolution of AgNPs in SW at environmentally relevant NP concentrations. Therefore, researchers, policy-makers, and regulators should carefully consider the unintended effects of dissolved Ag release from AgNPs when considering the risks of AgNPs in the environment, released from the consumer products.

15- The Pt influx rate constant (k_{uw}) in *L. stagnalis* increased with the increase of particle size, which was due to the increased aggregate size of PtNPs with the decrease in NP size. Smaller NPs are more prone to aggregation, resulting in sedimentation of smaller PtNP aggregates, and thus reduction in the actual exposure concentration, and a decrease in the overall NP influx. Thus, the apparent primary particle size-dependent influx of PtNPs observed here are not necessarily due to

particle size, but most likely due to the reduction in actual exposure concentration because of small NP aggregation.

16- The Pt influx rate constants (k_{uw}) of dissolved Pt and $PtNP_{20}$ into *L. stagnalis* tissues were not impacted by the presence of NOM. In contrast, k_{uw} for $PtNP_{95}$ were significantly suppressed in presence of NOM. These differences in dissolved Pt, $PtNP_{20}$ and $PtNP_{95}$ influx rate constants were attributed to the differences in NOM molecular composition and properties, which affected the propoerties of the PtNP NOM-corona, and by the aggregation behvaior of PtNPs. The formation of larger aggregate of $PtNP_{20}$ in presence of NOM reduced their concentration in the water column via sedimentation. Whereas, the colloidal stability of $PtNP_{95}$ in all NOM isolates suggests that the difference in $PtNP_{95}$'s k_{uw} were attributed to the differences in NOM properties, and thus the composition of NOM-corona. Sulfur (S) and Nitrogen (N) content in NOM exhibited positive correlation with the k_{uw} of $PtNP_{95}$. N and S are well known nutrients and increase in N and/or S content in the NOM resulted an increase in N, S content in the PtNP surface. Hence, NOM-corona on the surface of -$PtNP_{95}$ could act as a possible nutrient source to the snails, resulting an increased Pt influx with the increase in NOM N and S content. Moreover, reduced sulfur (S_{red}) content - in form of exocyclic and heterocyclic reduced sulfur- in the NOMs exhibited a strong positive correlation with k_{uw}, which was attributed to the higher affinity of reduced S to PtNPs relative to the oxidized S.

7.2. Outlook

The overall outcome of this work suggests that the effect of NP's physiochemical and environmental factors on the fate, behavior, transformation, and toxicity of metallic NP is a complex process. This cannot be described by an individual parameter, such as NP size, exposure concentration, ionic strength of media, NOM's concentration, source, and composition, that has been a focus of many studies in the literature. NP's colloidal stability and subsequent toxicity should be determined by a combination of NP and media physiochemical properties.

NP size and exposure concentration play important roles in determining NP fate as discussed above. At lower concentrations, NP size (i.e., AgNP) decreases faster and to a higher extent than at higher NP concentration, which has been used in majority of the previous studies. The differential change in NP size should be considered when investigating the toxicological effects and risks of NPs in the environment. For instance, smaller NPs are more efficient in crossing biological barriers and for toxicological assays, the nature of toxicant (e.g., dissolved, aggregated, number and size of primary NPs) will be different at different concentrations due to their concentration-dependent aggregation and/or dissolution behavior. Toxicity results obtained at high concentrations might produce inaccuracies in risk assessments when extrapolated to the often much lower but environmentally-relevant concentrations seen in the field or vice-versa. In order to approach realism and to avoid underestimation of potential risks, this study suggests that NP environmental fate and effects studies, and the characterization of NPs underpinning these studies, should be performed at environmentally-relevant NP concentrations.

Although, the exposure to AgNPs had negligible effect on *A. tenuiremis* survival, reproduction, and overall population growth. Environmental release of AgNPs form consumer products would, however, still pose risk to aquatic ecosystems through the rapid and complete dissolution. Therefore, regulators should carefully consider unintended effects of dissolved Ag release from AgNPs. For a more informed risk assessment, future studies should evaluate whether dissolved Ag and AgNPs exhibit similar reproductive and population toxicity patterns for a broader spectrum of chronically exposed invertebrate phyla. Such population-relevant data, along with others, could be used to produce a more useful holistic model for predicting AgNPs risks to estuarine and aquatic ecosystems. Future studies can also evaluate the similar reproductive toxicity patterns for a broad range of NPs, which might behave differently in the media.

NOM plays another pivotal role in determining NP environmental behavior such as aggregation, dissolution, uptake, and toxicity. Previous studies have focused on effects of different isolates of NOMs on NP aggregation, dissolution, uptake, and toxicity. However, few studies have focused on the effect of molecular level characteristics of NOM on NP aggregation. This study indicates that the aggregation of PtNPs depend on several factors, including primary NP size and NOM molecular characteristics, which ultimately affected the bioavailability of the PtNPs. Therefore, the molecular properties and components of NOM determine, to a greater extent, NP colloidal stability, bioavailability, and toxicity in the aquatic environment. However, the number (six) of NOM isolates used in this study is relatively low (nonetheless, they are more and better-characterized than those used in the large majority of previous studies) to provide the statistical power required to produce a statistically reliable correlation between uptake and NOM properties due to their

variability. Hence, future studies are needed using a larger number of NOM isolates, which will give more statistical power, to develop quantitative structure activity relationships between NOM molecular properties and NP environmental behaviors and effect.

REFERENCES

1. Auffan, M.; Rose, J.; Bottero, J.-y.; Lowry, G. V.; Jolivet, J.-P.; Wiesner, M. R., Towards a definition of inorganic nanoparticles from an environmental, health and safety perspective. *Nature Nanotechnology* **2009,** *4* (10), 634-641.
2. Klaine, S. J.; Alvarez, P. J. J.; Batley, G. E.; Fernandes, T. F.; Handy, R. D.; Lyon, D. Y.; Mahendra, S.; McLaughlin, M. J.; Lead, J. R., Nanomaterials in the environment: Behavior, fate, bioavailability, and effects. *Environmental Toxicology and Chemistry* **2008,** *27* (9), 1825-1851.
3. Nowack, B.; Bucheli, T. D., Occurrence, behavior and effects of nanoparticles in the environment. *Environ Pollut* **2007,** *150* (1), 5-22.
4. Benn, T.; Cavanagh, B.; Hristovski, K.; Posner, J. D.; Westerhoff, P., The Release of Nanosilver from Consumer Products Used in the Home Supplemental data file available online for this article. *Journal of Environmental Quality* **2010,** *39*, 1875-1882.
5. Kessler, R., Engineered nanoparticles in consumer products: understanding a new ingredient. *Environmental health perspectives* **2011,** *119* (3), a120-a125.
6. Mu, L.; Sprando, R. L., Application of nanotechnology in cosmetics. *Pharmaceutical research* **2010,** *27* (8), 1746-1749.
7. Lu, P.-J.; Huang, S.-C.; Chen, Y.-P.; Chiueh, L.-C.; Shih, D. Y.-C., Analysis of titanium dioxide and zinc oxide nanoparticles in cosmetics. *Journal of Food and Drug Analysis* **2015,** *23* (3), 587-594.
8. Carrillo-Inungaray, M. L.; Trejo-Ramirez, J. A.; Reyes-Munguia, A.; Carranza-Alvarez, C., Chapter 15 - Use of Nanoparticles in the Food Industry: Advances and Perspectives. In *Impact of Nanoscience in the Food Industry*, Grumezescu, A. M.; Holban, A. M., Eds. Academic Press: 2018; pp 419-444.
9. Gao, J.; Liang, G.; Zhang, B.; Kuang, Y.; Zhang, X.; Xu, B., FePt@CoS2 Yolk−Shell Nanocrystals as a Potent Agent to Kill HeLa Cells. *Journal of the American Chemical Society* **2007,** *129* (5), 1428-1433.
10. Dong, Y.; Feng, S.-S., In vitro and in vivo evaluation of methoxy polyethylene glycol–polylactide (MPEG–PLA) nanoparticles for small-molecule drug chemotherapy. *Biomaterials* **2007,** *28* (28), 4154-4160.
11. Mirshahghassemi, S.; Lead, J. R., Oil Recovery from Water under Environmentally Relevant Conditions Using Magnetic Nanoparticles. *Environmental Science & Technology* **2015,** *49* (19), 11729-11736.
12. Dunne, P. W.; Starkey, C. L.; Munn, A. S.; Sikder, M.; Luebben, O.; Shvets, I.; Lester, E. H., Transition metal doped anatase nanocrystals: Continuous-flow hydrothermal synthesis and photocatalytic activity. *Journal of Environmental Chemical Engineering* **2016,** *4* (3), 2665-2670.

13. Nowack, B.; Ranville, J. F.; Diamond, S.; Gallego-Urrea, J. A.; Metcalfe, C.; Rose, J.; Horne, N.; Koelmans, A. A.; Klaine, S. J., Potential scenarios for nanomaterial release and subsequent alteration in the environment. *Environ Toxicol Chem* **2012,** *31* (1), 50-9.
14. Scown, T. M.; van Aerle, R.; Tyler, C. R., Review: Do engineered nanoparticles pose a significant threat to the aquatic environment? *Crit Rev Toxicol* **2010,** *40* (7), 653-70.
15. Moore, M. N., Do nanoparticles present ecotoxicological risks for the health of the aquatic environment? *Environment International* **2006,** *32* (8), 967-976.
16. Fabrega, J.; Luoma, S. N.; Tyler, C. R.; Galloway, T. S.; Lead, J. R., Silver nanoparticles: behaviour and effects in the aquatic environment. *Environ Int* **2011,** *37* (2), 517-31.
17. Lead, J. R.; Batley, G. E.; Alvarez, P. J. J.; Croteau, M. N.; Handy, R. D.; McLaughlin, M. J.; Judy, J. D.; Schirmer, K., Nanomaterials in the environment: Behavior, fate, bioavailability, and effects-An updated review. *Environ Toxicol Chem* **2018,** *37* (8), 2029-2063.
18. Prabhu, S.; Poulose, E. K., Silver nanoparticles: mechanism of antimicrobial action, synthesis, medical applications, and toxicity effects. *International Nano Letters* **2012,** *2* (1), 32.
19. Chen, X.; Mao, S. S., Titanium Dioxide Nanomaterials: Synthesis, Properties, Modifications, and Applications. *Chemical Reviews* **2007,** *107* (7), 2891-2959.
20. Espitia, P. J. P.; Soares, N. d. F. F.; Coimbra, J. S. d. R.; de Andrade, N. J.; Cruz, R. S.; Medeiros, E. A. A., Zinc Oxide Nanoparticles: Synthesis, Antimicrobial Activity and Food Packaging Applications. *Food and Bioprocess Technology* **2012,** *5* (5), 1447-1464.
21. Zhong Lin, W., Zinc oxide nanostructures: growth, properties and applications. *Journal of Physics: Condensed Matter* **2004,** *16* (25), R829.
22. Cassee, F. R.; van Balen, E. C.; Singh, C.; Green, D.; Muijser, H.; Weinstein, J.; Dreher, K., Exposure, Health and Ecological Effects Review of Engineered Nanoscale Cerium and Cerium Oxide Associated with its Use as a Fuel Additive. *Critical Reviews in Toxicology* **2011,** *41* (3), 213-229.
23. Chen, A.; Holt-Hindle, P., Platinum-Based Nanostructured Materials: Synthesis, Properties, and Applications. *Chemical Reviews* **2010,** *110* (6), 3767-3804.
24. Paciotti, G. F.; Myer, L.; Weinreich, D.; Goia, D.; Pavel, N.; McLaughlin, R. E.; Tamarkin, L., Colloidal Gold: A Novel Nanoparticle Vector for Tumor Directed Drug Delivery. *Drug Delivery* **2004,** *11* (3), 169-183.
25. Ghosh, P.; Han, G.; De, M.; Kim, C. K.; Rotello, V. M., Gold nanoparticles in delivery applications. *Advanced Drug Delivery Reviews* **2008,** *60* (11), 1307-1315.
26. Vance, M. E.; Kuiken, T.; Vejerano, E. P.; McGinnis, S. P.; Hochella, M. F., Jr.; Rejeski, D.; Hull, M. S., Nanotechnology in the real world: Redeveloping the nanomaterial consumer products inventory. *Beilstein Journal of Nanotechnology* **2015,** *6*, 1769-1780.
27. EPA, U. *Emerging Contaminants – Nanomaterials*; US EPA: Washington D.C., 2010.
28. Benn, T. M.; Westerhoff, P., Nanoparticle Silver Released into Water from Commercially Available Sock Fabrics. *Environmental Science & Technology* **2008,** *42* (11), 4133-4139.

29. Kaegi, R.; Sinnet, B.; Zuleeg, S.; Hagendorfer, H.; Mueller, E.; Vonbank, R.; Boller, M.; Burkhardt, M., Release of silver nanoparticles from outdoor facades. *Environ Pollut* **2010,** *158*.
30. Kaegi, R.; Sinnet, B.; Zuleeg, S.; Hagendorfer, H.; Mueller, E.; Vonbank, R.; Boller, M.; Burkhardt, M., Release of silver nanoparticles from outdoor facades. *Environmental Pollution* **2010,** *158* (9), 2900-2905.
31. Mackevica, A.; Olsson, M. E.; Hansen, S. F., Silver nanoparticle release from commercially available plastic food containers into food simulants. *Journal of Nanoparticle Research* **2016,** *18* (1), 5.
32. Gottschalk, F.; Kost, E.; Nowack, B., Engineered nanomaterials in water and soils: A risk quantification based on probabilistic exposure and effect modeling. *Environmental Toxicology and Chemistry* **2013,** *32* (6), 1278-1287.
33. Gottschalk, F.; Sun, T.; Nowack, B., Environmental concentrations of engineered nanomaterials: Review of modeling and analytical studies. *Environmental Pollution* **2013,** *181*, 287-300.
34. Chen, S. F.; Zhang, H. Y.; Lin, Q. Y., Effect of different water conditions on dissolution of nanosilver. *Water Science and Technology* **2013,** *68* (8), 1745-1750.
35. Li, X.; Lenhart, J. J., Aggregation and Dissolution of Silver Nanoparticles in Natural Surface Water. *Environmental Science & Technology* **2012,** *46* (10), 5378-5386.
36. Cheng, Y. W.; Yin, L. Y.; Lin, S. H.; Wiesner, M.; Bernhardt, E.; Liu, J., Toxicity Reduction of Polymer-Stabilized Silver Nanoparticles by Sunlight. *Journal of Physical Chemistry C* **2011,** *115* (11), 4425-4432.
37. Navarro, E.; Piccapietra, F.; Wagner, B.; Marconi, F.; Kaegi, R.; Odzak, N.; Sigg, L.; Behra, R., Toxicity of Silver Nanoparticles to Chlamydomonas reinhardtii. *Environmental Science & Technology* **2008,** *42* (23), 8959-8964.
38. Kittler, S.; Greulich, C.; Diendorf, J.; Koller, M.; Epple, M., Toxicity of Silver Nanoparticles Increases during Storage Because of Slow Dissolution under Release of Silver Ions. *Chemistry of Materials* **2010,** *22* (16), 4548-4554.
39. Ma, R.; Levard, C.; Marinakos, S. M.; Cheng, Y. W.; Liu, J.; Michel, F. M.; Brown, G. E.; Lowry, G. V., Size-Controlled Dissolution of Organic-Coated Silver Nanoparticles. *Environmental Science & Technology* **2012,** *46* (2), 752-759.
40. Chappell, M. A.; Miller, L. F.; George, A. J.; Pettway, B. A.; Price, C. L.; Porter, B. E.; Bednar, A. J.; Seiter, J. M.; Kennedy, A. J.; Steevens, J. A., Simultaneous dispersion-dissolution behavior of concentrated silver nanoparticle suspensions in the presence of model organic solutes. *Chemosphere* **2011,** *84* (8), 1108-1116.
41. Xiu, Z. M.; Zhang, Q. B.; Puppala, H. L.; Colvin, V. L.; Alvarez, P. J. J., Negligible Particle-Specific Antibacterial Activity of Silver Nanoparticles. *Nano Letters* **2012,** *12* (8), 4271-4275.
42. Angel, B. M.; Batley, G. E.; Jarolimek, C. V.; Rogers, N. J., The impact of size on the fate and toxicity of nanoparticulate silver in aquatic systems. *Chemosphere* **2013,** *93* (2), 359-365.
43. Merrifield, R. C.; Stephan, C.; Lead, J., Determining the Concentration Dependent Transformations of Ag Nanoparticles in Complex Media: Using SP-ICP-MS and Au@Ag Core–Shell Nanoparticles as Tracers. *Environmental Science & Technology* **2017,** *51* (6), 3206-3213.

44. Lowry, G. V.; Gregory, K. B.; Apte, S. C.; Lead, J. R., Transformations of Nanomaterials in the Environment. *Environmental Science & Technology* **2012,** *46* (13), 6893-6899.
45. Peijnenburg, W.; Baalousha, M.; Chen, J. W.; Chaudry, Q.; Von der kammer, F.; Kuhlbusch, T. A. J.; Lead, J.; Nickel, C.; Quik, J. T. K.; Renker, M.; Wang, Z.; Koelmans, A. A., A Review of the Properties and Processes Determining the Fate of Engineered Nanomaterials in the Aquatic Environment. *Critical Reviews in Environmental Science and Technology* **2015,** *45* (19), 2084-2134.
46. Elzey, S.; Grassian, V. H., Nanoparticle Dissolution from the Particle Perspective: Insights from Particle Sizing Measurements. *Langmuir* **2010,** *26* (15), 12505-12508.
47. Levard, C.; Mitra, S.; Yang, T.; Jew, A. D.; Badireddy, A. R.; Lowry, G. V.; Brown, G. E., Effect of Chloride on the Dissolution Rate of Silver Nanoparticles and Toxicity to E. coli. *Environmental Science & Technology* **2013,** *47* (11), 5738-5745.
48. Li, Y.; Niu, J. F.; Shang, E. X.; Crittenden, J., Photochemical Transformation and Photoinduced Toxicity Reduction of Silver Nanoparticles in the Presence of Perfluorocarboxylic Acids under UV Irradiation. *Environmental Science & Technology* **2014,** *48* (9), 4946-4953.
49. Liu, J. Y.; Hurt, R. H., Ion Release Kinetics and Particle Persistence in Aqueous Nano-Silver Colloids. *Environmental Science & Technology* **2010,** *44* (6), 2169-2175.
50. Zhang, W.; Yao, Y.; Sullivan, N.; Chen, Y. S., Modeling the Primary Size Effects of Citrate-Coated Silver Nanoparticles on Their Ion Release Kinetics. *Environmental Science & Technology* **2011,** *45* (10), 4422-4428.
51. Baalousha, M.; Sikder, M.; Prasad, A.; Lead, J.; Merrifield, R.; Chandler, G. T., The concentration-dependent behaviour of nanoparticles. *Environmental Chemistry* **2016,** *13* (1), 1-3.
52. Vikesland, P. J.; Heathcock, A. M.; Rebodos, R. L.; Makus, K. E., Particle Size and Aggregation Effects on Magnetite Reactivity toward Carbon Tetrachloride. *Environmental Science & Technology* **2007,** *41* (15), 5277-5283.
53. Liu, J.; Aruguete, D. M.; Murayama, M.; Hochella, M. F., Influence of Size and Aggregation on the Reactivity of an Environmentally and Industrially Relevant Nanomaterial (PbS). *Environmental Science & Technology* **2009,** *43* (21), 8178-8183.
54. Rubasinghege, G.; Lentz, R. W.; Park, H.; Scherer, M. M.; Grassian, V. H., Nanorod Dissolution Quenched in the Aggregated State. *Langmuir* **2010,** *26* (3), 1524-1527.
55. Tantra, R.; Bouwmeester, H.; Ray-Castro, C.; David, C. A.; Dogne, J.-M.; Jarman, J.; Laborda, F.; Laloy, J.; Robinson, K. N.; Undas, A. K.; Zande, M. v. d., Suitability of analytical methods to measure solubility for the purpose of nanoregulation. *Nanotoxicology* **2015**, 1-12.
56. Hyung, H.; Kim, J. H., Natural organic matter (NOM) adsorption to multi-walled carbon nanotubes: Effect of NOM characteristics and water quality parameters. *Environmental Science & Technology* **2008,** *42* (12), 4416-4421.
57. Quik, J. T. K.; Velzeboer, I.; Wouterse, M.; Koelmans, A. A.; van de Meent, D., Heteroaggregation and sedimentation rates for nanomaterials in natural waters. *Water Research* **2014,** *48*, 269-279.
58. *PGM mrket report: Summary of platinum supply and demand in 2016*; Johnson Matthey PLC: Hertfordshire, 2017.

59. Dubiella-Jackowska, A.; Kudłak, B.; Polkowska, Ż.; Namieśnik, J., Environmental Fate of Traffic-Derived Platinum Group Metals. *Critical Reviews in Analytical Chemistry* **2009,** *39* (4), 251-271.
60. Ravindra, K.; Bencs, L.; Van Grieken, R., Platinum group elements in the environment and their health risk. *Science of The Total Environment* **2004,** *318* (1), 1-43.
61. Pawlak, J.; Łodyga-Chruścińska, E.; Chrustowicz, J., Fate of platinum metals in the environment. *Journal of Trace Elements in Medicine and Biology* **2014,** *28* (3), 247-254.
62. Rühle, T.; Schneider, H.; Find, J.; Herein, D.; Pfänder, N.; Wild, U.; Schlögl, R.; Nachtigall, D.; Artelt, S.; Heinrich, U., Preparation and characterisation ofPt/Al2O3 aerosol precursors as model Pt-emissions from catalytic converters. *Applied Catalysis B: Environmental* **1997,** *14* (1), 69-84.
63. Folens, K.; Van Acker, T.; Bolea-Fernandez, E.; Cornelis, G.; Vanhaecke, F.; Du Laing, G.; Rauch, S., Identification of platinum nanoparticles in road dust leachate by single particle inductively coupled plasma-mass spectrometry. *Science of The Total Environment* **2018,** *615*, 849-856.
64. Bocca, B.; Petrucci, F.; Alimonti, A.; Caroli, S., Traffic-related platinum and rhodium concentrations in the atmosphere of Rome. *Journal of Environmental Monitoring* **2003,** *5* (4), 563-568.
65. Schäfer, J.; Puchelt, H., Platinum-Group-Metals (PGM) emitted from automobile catalytic converters and their distribution in roadside soils. *Journal of Geochemical Exploration* **1998,** *64* (1), 307-314.
66. Morton, O.; Puchelt, H.; Hernández, E.; Lounejeva, E., Traffic-related platinum group elements (PGE) in soils from Mexico City. *Journal of Geochemical Exploration* **2001,** *72* (3), 223-227.
67. Artelt, S.; Creutzenberg, O.; Kock, H.; Levsen, K.; Nachtigall, D.; Heinrich, U.; Rühle, T.; Schlögl, R., Bioavailability of fine dispersed platinum as emitted from automotive catalytic converters: a model study. *Science of The Total Environment* **1999,** *228* (2), 219-242.
68. Barbante, C.; Veysseyre, A.; Ferrari, C.; Van De Velde, K.; Morel, C.; Capodaglio, G.; Cescon, P.; Scarponi, G.; Boutron, C., Greenland Snow Evidence of Large Scale Atmospheric Contamination for Platinum, Palladium, and Rhodium. *Environmental Science & Technology* **2001,** *35* (5), 835-839.
69. Siebel, S.; Dammann, C.; Hiller, W.; Drewello, T.; Lippert, B., Revisiting the head–head dinuclear 1-methyluracil complex of cisplatin: New insights into its solution behavior. *Inorganica Chimica Acta* **2012,** *393*, 212-221.
70. Lamy-Pitara, E.; Barbier, J., Platinum modified by electrochemical deposition of adatoms. *Applied Catalysis A: General* **1997,** *149* (1), 49-87.
71. Biesinger, K. E.; Christensen, G. M., Effects of Various Metals on Survival, Growth, Reproduction, and Metabolism of Daphnia magna. *Journal of the Fisheries Research Board of Canada* **1972,** *29* (12), 1691-1700.
72. Veltz, I.; Arsac, F.; Biagianti-Risbourg, S.; Habets, F.; Lechenault, H.; Vernet, G., Effects of platinum (Pt4+) on Lumbriculus variegatus Muller (Annelida, Oligochaetae): acute toxicity and bioaccumulation. *Arch Environ Contam Toxicol* **1996,** *31* (1), 63-7.
73. Książyk, M.; Asztemborska, M.; Stęborowski, R.; Bystrzejewska-Piotrowska, G., Toxic Effect of Silver and Platinum Nanoparticles Toward the Freshwater Microalga

Pseudokirchneriella subcapitata. *Bulletin of Environmental Contamination and Toxicology* **2015,** *94* (5), 554-558.
74. Wei, C.; Morrison , G. M., Platinum in Road Dusts and Urban River Sediments. *Science of the Total Environment* **1994,** *146*, 169-174.
75. Tejamaya, M.; Romer, I.; Merrifield, R. C.; Lead, J. R., Stability of Citrate, PVP, and PEG Coated Silver Nanoparticles in Ecotoxicology Media. *Environmental Science & Technology* **2012,** *46* (13), 7011-7017.
76. Merrifield, R. C.; Wang, Z. W.; Palmer, R. E.; Lead, J. R., Synthesis and Characterization of Polyvinylpyrrolidone Coated Cerium Oxide Nanoparticles. *Environmental Science & Technology* **2013,** *47* (21), 12426-12433.
77. Behra, R.; Wagner, B.; Sgier, L.; Kistler, D., Colloidal Stability and Toxicity of Gold Nanoparticles and Gold Chloride on Chlamydomonas reinhardtii. *Aquatic Geochemistry* **2015,** *21* (2), 331-342.
78. Moore, T. L.; Rodriguez-Lorenzo, L.; Hirsch, V.; Balog, S.; Urban, D.; Jud, C.; Rothen-Rutishauser, B.; Lattuada, M.; Petri-Fink, A., Nanoparticle colloidal stability in cell culture media and impact on cellular interactions. *Chemical Society Reviews* **2015,** *44* (17), 6287-6305.
79. Chen, K. L.; Smith, B. A.; Ball, W. P.; Fairbrother, D. H., Assessing the colloidal properties of engineered nanoparticles in water: case studies from fullerene C60 nanoparticles and carbon nanotubes. *Environmental Chemistry* **2010,** *7* (1), 10-27.
80. Fabrega, J.; Luoma, S. N.; Tyler, C. R.; Galloway, T. S.; Lead, J. R., Silver nanoparticles behaviour and effects in the aquatic environment. *Environ Int* **2011,** *37*.
81. Nebbioso, A.; Piccolo, A., Molecular characterization of dissolved organic matter (DOM): a critical review. *Analytical and Bioanalytical Chemistry* **2013,** *405* (1), 109-124.
82. Filella, M., Colloidal properties of submicron particles in natural waters. *IUPAC series on analytical and physical chemistry of environmental systems* **2007,** *10*, 17.
83. Keller, A. A.; Wang, H.; Zhou, D.; Lenihan, H. S.; Cherr, G.; Cardinale, B. J.; Miller, R.; Ji, Z., Stability and Aggregation of Metal Oxide Nanoparticles in Natural Aqueous Matrices. *Environmental Science & Technology* **2010,** *44* (6), 1962-1967.
84. Petosa, A. R.; Jaisi, D. P.; Quevedo, I. R.; Elimelech, M.; Tufenkji, N., Aggregation and Deposition of Engineered Nanomaterials in Aquatic Environments: Role of Physicochemical Interactions. *Environmental Science & Technology* **2010,** *44* (17), 6532-6549.
85. Gu, B.; Schmitt, J.; Chen, Z.; Liang, L.; McCarthy, J. F., Adsorption and desorption of different organic matter fractions on iron oxide. *Geochimica et Cosmochimica Acta* **1995,** *59* (2), 219-229.
86. Gibson, C. T.; Turner, I. J.; Roberts, C. J.; Lead, J. R., Quantifying the Dimensions of Nanoscale Organic Surface Layers in Natural Waters. *Environmental Science & Technology* **2007,** *41* (4), 1339-1344.
87. Lynch, I.; Dawson, K. A.; Lead, J. R.; Valsami-Jones, E., Chapter 4-macromolecular coronas and their importance in nanotoxicology and nanoecotoxicology. *Front Nanosci* **2014,** *7*.
88. Mudunkotuwa, I. A.; Grassian, V. H., Biological and environmental media control oxide nanoparticle surface composition: the roles of biological components (proteins and amino acids), inorganic oxyanions and humic acid. *Environmental Science: Nano* **2015,** *2* (5), 429-439.

89. Chanudet, V.; Filella, M., Submicron organic matter in a peri-alpine, ultra-oligotrophic lake. *Organic Geochemistry* **2007,** *38* (7), 1146-1160.
90. Matilainen, A.; Vepsäläinen, M.; Sillanpää, M., Natural organic matter removal by coagulation during drinking water treatment: A review. *Advances in Colloid and Interface Science* **2010,** *159* (2), 189-197.
91. Lützow, M. v.; Kögel-Knabner, I.; Ekschmitt, K.; Matzner, E.; Guggenberger, G.; Marschner, B.; Flessa, H., Stabilization of organic matter in temperate soils: mechanisms and their relevance under different soil conditions – a review. *European Journal of Soil Science* **2006,** *57* (4), 426-445.
92. Al-Abadleh, H. A., Review of the bulk and surface chemistry of iron in atmospherically relevant systems containing humic-like substances. *RSC Advances* **2015,** *5* (57), 45785-45811.
93. Philippe, A.; Schaumann, G. E., Interactions of Dissolved Organic Matter with Natural and Engineered Inorganic Colloids: A Review. *Environmental Science & Technology* **2014,** *48* (16), 8946-8962.
94. Afshinnia, K.; Sikder, M.; Cai, B.; Baalousha, M., Effect of nanomaterial and media physicochemical properties on Ag NM aggregation kinetics. *Journal of Colloid and Interface Science* **2017,** *487*, 192-200.
95. Levard, C.; Reinsch, B. C.; Michel, F. M.; Oumahi, C.; Lowry, G. V.; Brown, G. E., Sulfidation Processes of PVP-Coated Silver Nanoparticles in Aqueous Solution: Impact on Dissolution Rate. *Environmental Science & Technology* **2011,** *45* (12), 5260-5266.
96. Dasari, T. P.; Hwang, H. M., The effect of humic acids on the cytotoxicity of silver nanoparticles to a natural aquatic bacterial assemblage. *Sci Total Environ* **2010,** *408* (23), 5817-23.
97. Fabrega, J.; Fawcett, S. R.; Renshaw, J. C.; Lead, J. R., Silver Nanoparticle Impact on Bacterial Growth: Effect of pH, Concentration, and Organic Matter. *Environmental Science & Technology* **2009,** *43* (19), 7285-7290.
98. Wirth, S. M.; Lowry, G. V.; Tilton, R. D., Natural Organic Matter Alters Biofilm Tolerance to Silver Nanoparticles and Dissolved Silver. *Environmental Science & Technology* **2012,** *46* (22), 12687-12696.
99. Liu, X.; Jin, X.; Cao, B.; Tang, C. Y., Bactericidal activity of silver nanoparticles in environmentally relevant freshwater matrices: Influences of organic matter and chelating agent. *Journal of Environmental Chemical Engineering* **2014,** *2* (1), 525-531.
100. Tadros, T., General principles of colloid stability and the role of surface forces. *Colloid stability: The role of surface forces* **2007,** (Part I), 1-22.
101. He, Y. T.; Wan, J.; Tokunaga, T., Kinetic stability of hematite nanoparticles: the effect of particle sizes. *Journal of Nanoparticle Research* **2008,** *10* (2), 321-332.
102. Zhou, D.; Ji, Z.; Jiang, X.; Dunphy, D. R.; Brinker, J.; Keller, A. A., Influence of Material Properties on TiO2 Nanoparticle Agglomeration. *PLOS ONE* **2013,** *8* (11), e81239.
103. Mulvihill, M. J.; Habas, S. E.; Jen-La Plante, I.; Wan, J.; Mokari, T., Influence of Size, Shape, and Surface Coating on the Stability of Aqueous Suspensions of CdSe Nanoparticles. *Chemistry of Materials* **2010,** *22* (18), 5251-5257.
104. Liu, J.; Legros, S.; Ma, G.; Veinot, J. G. C.; von der Kammer, F.; Hofmann, T., Influence of surface functionalization and particle size on the aggregation kinetics of engineered nanoparticles. *Chemosphere* **2012,** *87* (8), 918-924.

105. Sikder, M.; Wang, J.; Thomas Chandler, G.; Berti, D.; Baalousha, M., Synthesis, Characterization, and Environmental Behaviors of Monodispersed Platinum Nanoparticles. *Journal of Colloid and Interface Science* **2019**.
106. Liu, X.; Chen, G.; Su, C., Effects of material properties on sedimentation and aggregation of titanium dioxide nanoparticles of anatase and rutile in the aqueous phase. *Journal of Colloid and Interface Science* **2011,** *363* (1), 84-91.
107. Baalousha, M., Aggregation and disaggregation of iron oxide nanoparticles: Influence of particle concentration, pH and natural organic matter. *Science of The Total Environment* **2009,** *407* (6), 2093-2101.
108. Sikder, M.; Eudy, E.; Chandler, G. T.; Baalousha, M., Comparative study of dissolved and nanoparticulate Ag effects on the life cycle of an estuarine meiobenthic copepod, Amphiascus tenuiremis. *Nanotoxicology* **2018**, 1-15.
109. Badawy, A. M. E.; Luxton, T. P.; Silva, R. G.; Scheckel, K. G.; Suidan, M. T.; Tolaymat, T. M., Impact of Environmental Conditions (pH, Ionic Strength, and Electrolyte Type) on the Surface Charge and Aggregation of Silver Nanoparticles Suspensions. *Environmental Science & Technology* **2010,** *44* (4), 1260-1266.
110. Verrall, K. E.; Warwick, P.; Fairhurst, A. J., Application of the Schulze–Hardy rule to haematite and haematite/humate colloid stability. *Colloids and Surfaces A: Physicochemical and Engineering Aspects* **1999,** *150* (1), 261-273.
111. Buchholz, A.; Laskov, C.; Haderlein, S. B., Effects of Zwitterionic Buffers on Sorption of Ferrous Iron at Goethite and Its Oxidation by CCl4. *Environmental Science & Technology* **2011,** *45* (8), 3355-3360.
112. Stemig, A. M.; Do, T. A.; Yuwono, V. M.; Arnold, W. A.; Penn, R. L., Goethite nanoparticle aggregation: effects of buffers, metal ions, and 4-chloronitrobenzene reduction. *Environmental Science: Nano* **2014,** *1* (5), 478-487.
113. Li, X.; Lenhart, J. J.; Walker, H. W., Dissolution-Accompanied Aggregation Kinetics of Silver Nanoparticles. *Langmuir* **2010,** *26* (22), 16690-16698.
114. Kent, R. D.; Vikesland, P. J., Controlled Evaluation of Silver Nanoparticle Dissolution Using Atomic Force Microscopy. *Environmental Science & Technology* **2012,** *46* (13), 6977-6984.
115. Zhang, H.; Smith, J. A.; Oyanedel-Craver, V., The effect of natural water conditions on the anti-bacterial performance and stability of silver nanoparticles capped with different polymers. *Water Research* **2012,** *46* (3), 691-699.
116. Asharani, P. V.; Yi, L. W.; Gong, Z. Y.; Valiyaveettil, S., Comparison of the toxicity of silver, gold and platinum nanoparticles in developing zebrafish embryos. *Nanotoxicology* **2011,** *5* (1), 43-54.
117. Lau, B. L. T.; Hockaday, W. C.; Ikuma, K.; Furman, O.; Decho, A. W., A preliminary assessment of the interactions between the capping agents of silver nanoparticles and environmental organics. *Colloids and Surfaces A: Physicochemical and Engineering Aspects* **2013,** *435*, 22-27.
118. Diegoli, S.; Manciulea, A. L.; Begum, S.; Jones, I. P.; Lead, J. R.; Preece, J. A., Interaction between manufactured gold nanoparticles and naturally occurring organic macromolecules. *Science of The Total Environment* **2008,** *402* (1), 51-61.
119. Gondikas, A. P.; Morris, A.; Reinsch, B. C.; Marinakos, S. M.; Lowry, G. V.; Hsu-Kim, H., Cysteine-Induced Modifications of Zero-valent Silver Nanomaterials:

Implications for Particle Surface Chemistry, Aggregation, Dissolution, and Silver Speciation. *Environmental Science & Technology* **2012,** *46* (13), 7037-7045.
120. Mohd Omar, F.; Abdul Aziz, H.; Stoll, S., Aggregation and disaggregation of ZnO nanoparticles: Influence of pH and adsorption of Suwannee River humic acid. *Science of The Total Environment* **2014,** *468-469*, 195-201.
121. Ghosh, S.; Jiang, W.; McClements, J. D.; Xing, B., Colloidal Stability of Magnetic Iron Oxide Nanoparticles: Influence of Natural Organic Matter and Synthetic Polyelectrolytes. *Langmuir* **2011,** *27* (13), 8036-8043.
122. Loosli, F.; Le Coustumer, P.; Stoll, S., TiO2 nanoparticles aggregation and disaggregation in presence of alginate and Suwannee River humic acids. pH and concentration effects on nanoparticle stability. *Water Research* **2013,** *47* (16), 6052-6063.
123. Louie, S. M.; Spielman-Sun, E. R.; Small, M. J.; Tilton, R. D.; Lowry, G. V., Correlation of the Physicochemical Properties of Natural Organic Matter Samples from Different Sources to Their Effects on Gold Nanoparticle Aggregation in Monovalent Electrolyte. *Environmental Science & Technology* **2015,** *49* (4), 2188-2198.
124. Louie, S. M.; Tilton, R. D.; Lowry, G. V., Effects of Molecular Weight Distribution and Chemical Properties of Natural Organic Matter on Gold Nanoparticle Aggregation. *Environmental Science & Technology* **2013,** *47* (9), 4245-4254.
125. Nason, J. A.; McDowell, S. A.; Callahan, T. W., Effects of natural organic matter type and concentration on the aggregation of citrate-stabilized gold nanoparticles. *Journal of Environmental Monitoring* **2012,** *14* (7), 1885-1892.
126. Shen, M. H.; Yin, Y. G.; Booth, A.; Liu, J. F., Effects of molecular weight-dependent physicochemical heterogeneity of natural organic matter on the aggregation of fullerene nanoparticles in mono- and di-valent electrolyte solutions. *Water Res* **2015,** *71*, 11-20.
127. Deonarine, A.; Lau, B. L. T.; Aiken, G. R.; Ryan, J. N.; Hsu-Kim, H., Effects of Humic Substances on Precipitation and Aggregation of Zinc Sulfide Nanoparticles. *Environmental Science & Technology* **2011,** *45* (8), 3217-3223.
128. Gunsolus, I. L.; Mousavi, M. P. S.; Hussein, K.; Bühlmann, P.; Haynes, C. L., Effects of Humic and Fulvic Acids on Silver Nanoparticle Stability, Dissolution, and Toxicity. *Environmental science & technology* **2015,** *49* (13), 8078-8086.
129. Baalousha, M.; Arkill, K. P.; Romer, I.; Palmer, R. E.; Lead, J. R., Transformations of citrate and Tween coated silver nanoparticles reacted with Na2S. *Science of the Total Environment* **2015,** *502*, 344-353.
130. Yang, X.; Jiang, C.; Hsu-Kim, H.; Badireddy, A. R.; Dykstra, M.; Wiesner, M.; Hinton, D. E.; Meyer, J. N., Silver Nanoparticle Behavior, Uptake, and Toxicity in Caenorhabditis elegans: Effects of Natural Organic Matter. *Environmental Science & Technology* **2014,** *48* (6), 3486-3495.
131. Bian, S.-W.; Mudunkotuwa, I. A.; Rupasinghe, T.; Grassian, V. H., Aggregation and Dissolution of 4 nm ZnO Nanoparticles in Aqueous Environments: Influence of pH, Ionic Strength, Size, and Adsorption of Humic Acid. *Langmuir* **2011,** *27* (10), 6059-6068.
132. Wang, L.-F.; Habibul, N.; He, D.-Q.; Li, W.-W.; Zhang, X.; Jiang, H.; Yu, H.-Q., Copper release from copper nanoparticles in the presence of natural organic matter. *Water Research* **2015,** *68*, 12-23.
133. Handy, R. D.; Cornelis, G.; Fernandes, T.; Tsyusko, O.; Decho, A.; Sabo-Attwood, T.; Metcalfe, C.; Steevens, J. A.; Klaine, S. J.; Koelmans, A. A.; Horne, N., Ecotoxicity

test methods for engineered nanomaterials: Practical experiences and recommendations from the bench. *Environmental Toxicology and Chemistry* **2012,** *31* (1), 15-31.
134. Lovern, S. B.; Klaper, R., Daphnia magna mortality when exposed to titanium dioxide and fullerene (C60) nanoparticles. *Environmental Toxicology and Chemistry* **2006,** *25* (4), 1132-1137.
135. Lovern, S. B.; Strickler, J. R.; Klaper, R., Behavioral and Physiological Changes in Daphnia magna when Exposed to Nanoparticle Suspensions (Titanium Dioxide, Nano-C60, and C60HxC70Hx). *Environmental Science & Technology* **2007,** *41* (12), 4465-4470.
136. Schlich, K.; Klawonn, T.; Terytze, K.; Hund-Rinke, K., Effects of silver nanoparticles and silver nitrate in the earthworm reproduction test. *Environ Toxicol Chem* **2013,** *32* (1), 181-8.
137. Handy, R. D.; van den Brink, N.; Chappell, M.; Muhling, M.; Behra, R.; Dusinska, M.; Simpson, P.; Ahtiainen, J.; Jha, A. N.; Seiter, J.; Bednar, A.; Kennedy, A.; Fernandes, T. F.; Riediker, M., Practical considerations for conducting ecotoxicity test methods with manufactured nanomaterials: what have we learnt so far? *Ecotoxicology* **2012,** *21* (4), 933-72.
138. Lowry, G. V.; Espinasse, B. P.; Badireddy, A. R.; Richardson, C. J.; Reinsch, B. C.; Bryant, L. D.; Bone, A. J.; Deonarine, A.; Chae, S.; Therezien, M.; Colman, B. P.; Hsu-Kim, H.; Bernhardt, E. S.; Matson, C. W.; Wiesner, M. R., Long-Term Transformation and Fate of Manufactured Ag Nanoparticles in a Simulated Large Scale Freshwater Emergent Wetland. *Environmental Science & Technology* **2012,** *46* (13), 7027-7036.
139. Asghari, S.; Johari, S. A.; Lee, J. H.; Kim, Y. S.; Jeon, Y. B.; Choi, H. J.; Moon, M. C.; Yu, I. J., Toxicity of various silver nanoparticles compared to silver ions in Daphnia magna. *J Nanobiotechnology* **2012,** *10*, 14.
140. Zhu, X.; Zhu, L.; Lang, Y.; Chen, Y., Oxidative stress and growth inhibition in the freshwater fish Carassius auratus induced by chronic exposure to sublethal fullerene aggregates. *Environmental Toxicology and Chemistry* **2008,** *27* (9), 1979-1985.
141. Hoecke, K. V.; Quik, J. T. K.; Mankiewicz-Boczek, J.; Schamphelaere, K. A. C. D.; Elsaesser, A.; Meeren, P. V. d.; Barnes, C.; McKerr, G.; Howard, C. V.; Meent, D. V. D., Fate and effects of CeO2 nanoparticles in aquatic ecotoxicity tests. *Environ Sci Technol* **2009,** *43*.
142. Templeton, R. C.; Ferguson, P. L.; Washburn, K. M.; Scrivens, W. A.; Chandler, G. T., Life-Cycle Effects of Single-Walled Carbon Nanotubes (SWNTs) on an Estuarine Meiobenthic Copepod. *Environmental Science & Technology* **2006,** *40* (23), 7387-7393.
143. Luoma, S. N.; Stoiber, T.; Croteau, M.-N.; Römer, I.; Merrifeld, R.; Lead, J. R., Effect of cysteine and humic acids on bioavailability of Ag from Ag nanoparticles to a freshwater snail. *NanoImpact* **2016,** *2*, 61-69.
144. Üçer, A.; Uyanik, A.; Aygün, Ş. F., Adsorption of Cu(II), Cd(II), Zn(II), Mn(II) and Fe(III) ions by tannic acid immobilised activated carbon. *Separation and Purification Technology* **2006,** *47* (3), 113-118.
145. Reed, R. B.; Higgins, C. P.; Westerhoff, P.; Tadjiki, S.; Ranville, J. F., Overcoming challenges in analysis of polydisperse metal-containing nanoparticles by single particle inductively coupled plasma mass spectrometry. *Journal of Analytical Atomic Spectrometry* **2012,** *27* (7), 1093-1100.
146. Campbell, P.; Ma, S.; Schmalzried, T.; Amstutz, H. C., Tissue digestion for wear debris particle isolation. *Journal of Biomedical Materials Research* **1994,** *28* (4), 523-526.

147. Arslan, Z.; Ates, M.; McDuffy, W.; Agachan, M. S.; Farah, I. O.; Yu, W. W.; Bednar, A. J., Probing metabolic stability of CdSe nanoparticles: alkaline extraction of free cadmium from liver and kidney samples of rats exposed to CdSe nanoparticles. *J Hazard Mater* **2011,** *192* (1), 192-9.
148. Mitrano, D. M.; Lombi, E.; Dasilva, Y. A. R.; Nowack, B., Unraveling the Complexity in the Aging of Nanoenhanced Textiles: A Comprehensive Sequential Study on the Effects of Sunlight and Washing on Silver Nanoparticles. *Environmental Science & Technology* **2016,** *50* (11), 5790-5799.
149. Kunniger, T.; Gerecke, A. C.; Ulrich, A.; Huch, A.; Vonbank, R.; Heeb, M.; Wichser, A.; Haag, R.; Kunz, P.; Faller, M., Release and environmental impact of silver nanoparticles and conventional organic biocides from coated wooden facades. *Environmental Pollution* **2014,** *184*, 464-471.
150. Quadros, M. E.; Pierson, R.; Tulve, N. S.; Willis, R.; Rogers, K.; Thomas, T. A.; Marr, L. C., Release of Silver from Nanotechnology-Based Consumer Products for Children. *Environmental Science & Technology* **2013,** *47* (15), 8894-8901.
151. Nowack, B.; Baalousha, M.; Bornhoft, N.; Chaudhry, Q.; Cornelis, G.; Cotterill, J.; Gondikas, A.; Hassellov, M.; Lead, J.; Mitrano, D. M.; von der Kammer, F.; Wontner-Smith, T., Progress towards the validation of modeled environmental concentrations of engineered nanomaterials by analytical measurements. *Environmental Science: Nano* **2015,** *2* (5), 421-428.
152. Massarsky, A.; Trudeau, V. L.; Moon, T. W., Predicting the environmental impact of nanosilver. *Environmental Toxicology and Pharmacology* **2014,** *38* (3), 861-873.
153. Gallego-Urrea, J. A.; Hammes, J.; Cornelis, G.; Hassellöv, M., Coagulation and sedimentation of gold nanoparticles and illite in model natural waters: Influence of initial particle concentration. *NanoImpact*.
154. Cheryan, M., *Ultrafiltration and microfiltration handbook*. CRC press: Florida, 1998.
155. Fabrega, J.; Tantra, R.; Amer, A.; Stolpe, B.; Tomkins, J.; Fry, T.; Lead, J. R.; Tyler, C. R.; Galloway, T. S., Sequestration of Zinc from Zinc Oxide Nanoparticles and Life Cycle Effects in the Sediment Dweller Amphipod Corophium volutator. *Environmental Science & Technology* **2012,** *46* (2), 1128-1135.
156. Fabricius, A. L.; Duester, L.; Meermann, B.; Ternes, T. A., ICP-MS-based characterization of inorganic nanoparticles-sample preparation and off- line fractionation strategies. *Analytical and Bioanalytical Chemistry* **2014,** *406* (2), 467-479.
157. Zook, J. M.; Long, S. E.; Cleveland, D.; Geronimo, C. L. A.; MacCuspie, R. I., Measuring silver nanoparticle dissolution in complex biological and environmental matrices using UV-visible absorbance. *Analytical and Bioanalytical Chemistry* **2011,** *401* (6), 1993-2002.
158. Baalousha, M.; Prasad, A.; Lead, J. R., Quantitative measurement of the nanoparticle size and number concentration from liquid suspensions by atomic force microscopy. *Environmental Science-Processes & Impacts* **2014,** *16* (6), 1338-1347.
159. Prasad, A.; Lead, J. R.; Baalousha, M., An electron microscopy based method for the detection and quantification of nanomaterial number concentration in environmentally relevant media. *Sci Total Environ* **2015,** *537*, 479-86.
160. Odzak, N.; Kistler, D.; Behra, R.; Sigg, L., Dissolution of metal and metal oxide nanoparticles in aqueous media. *Environmental Pollution* **2014,** *191*, 132-138.

161. Mitrano, D. M.; Barber, A.; Bednar, A.; Westerhoff, P.; Higgins, C. P.; Ranville, J. F., Silver nanoparticle characterization using single particle ICP-MS (SP-ICP-MS) and asymmetrical flow field flow fractionation ICP-MS (AF4-ICP-MS). *Journal of Analytical Atomic Spectrometry* **2012,** *27* (7), 1131-1142.
162. Haiss, W.; Thanh, N. T. K.; Aveyard, J.; Fernig, D. G., Determination of Size and Concentration of Gold Nanoparticles from UV−Vis Spectra. *Analytical Chemistry* **2007,** *79* (11), 4215-4221.
163. Khlebtsov, N. G., Determination of Size and Concentration of Gold Nanoparticles from Extinction Spectra. *Analytical Chemistry* **2008,** *80* (17), 6620-6625.
164. Liu, X.; Atwater, M.; Wang, J.; Huo, Q., Extinction coefficient of gold nanoparticles with different sizes and different capping ligands. *Colloids and Surfaces B: Biointerfaces* **2007,** *58* (1), 3-7.
165. Romer, I.; White, T. A.; Baalousha, M.; Chipman, K.; Viant, M. R.; Lead, J. R., Aggregation and dispersion of silver nanoparticles in exposure media for aquatic toxicity tests. *Journal of Chromatography A* **2011,** *1218* (27), 4226-4233.
166. Baalousha, M.; Lead, J. R., Rationalizing Nanomaterial Sizes Measured by Atomic Force Microscopy, Flow Field-Flow Fractionation, and Dynamic Light Scattering: Sample Preparation, Polydispersity, and Particle Structure. *Environmental Science & Technology* **2012,** *46* (11), 6134-6142.
167. Domingos, R. F.; Baalousha, M. A.; Ju-Nam, Y.; Reid, M. M.; Tufenkji, N.; Lead, J. R.; Leppard, G. G.; Wilkinson, K. J., Characterizing Manufactured Nanoparticles in the Environment: Multimethod Determination of Particle Sizes. *Environmental Science & Technology* **2009,** *43* (19), 7277-7284.
168. Baalousha, M.; Ju-Nam, Y.; Cole, P. A.; Gaiser, B.; Fernandes, T. F.; Hriljac, J. A.; Jepson, M. A.; Stone, V.; Tyler, C. R.; Lead, J. R., Characterization of cerium oxide nanoparticles—Part 1: Size measurements. *Environmental Toxicology and Chemistry* **2012,** *31* (5), 983-993.
169. Vanhaecke, F.; Vanhoe, H.; Dams, R.; Vandecasteele, C., The use of internal standards in ICP-MS. *Talanta* **1992,** *39* (7), 737-742.
170. Lu, Q. F.; Yu, J.; Gao, J. Z.; Yang, W.; Li, Y., Glow-discharge Electrolysis Plasma Induced Synthesis of Polyvinylpyrrolidone/Acrylic Acid Hydrogel and its Adsorption Properties for Heavy-metal Ions. *Plasma Processes and Polymers* **2011,** *8* (9), 803-814.
171. Zhao, J. H.; Yuan, W. Z.; Xu, A. H.; Ai, F.; Lu, Y. W.; Zhang, Y. M., Perfluorinated sulfonic acid ionomer/poly(N-vinylpyrrolidone) nanofiber membranes: Electrospinning fabrication, water stability, and metal ion removal applications. *Reactive & Functional Polymers* **2011,** *71* (11), 1102-1109.
172. Baalousha, M.; Lead, J. R., Size fractionation and characterization of natural aquatic colloids and nanoparticles. *Science of the Total Environment* **2007,** *386* (1-3), 93-102.
173. Paramelle, D.; Sadovoy, A.; Gorelik, S.; Free, P.; Hobley, J.; Fernig, D. G., A rapid method to estimate the concentration of citrate capped silver nanoparticles from UV-visible light spectra. *Analyst* **2014,** *139* (19), 4855-4861.
174. Byrne, R. H., Inorganic speciation of dissolved elements in seawater: the influence of pH on concentration ratios. *Geochemical Transactions* **2003,** *3* (2), 11-16.

175. Jose Ruben Morones and Jose Luis Elechiguerra and Alejandra Camacho and Katherine Holt and Juan, B. K. a. J. T. R. a. M. J. Y., The bactericidal effect of silver nanoparticles. *Nanotechnology* **2005,** *16* (10), 2346.
176. Sotiriou, G. A.; Pratsinis, S. E., Antibacterial Activity of Nanosilver Ions and Particles. *Environmental Science & Technology* **2010,** *44* (14), 5649-5654.
177. Carlson, C.; Hussain, S. M.; Schrand, A. M.; K. Braydich-Stolle, L.; Hess, K. L.; Jones, R. L.; Schlager, J. J., Unique Cellular Interaction of Silver Nanoparticles: Size-Dependent Generation of Reactive Oxygen Species. *The Journal of Physical Chemistry B* **2008,** *112* (43), 13608-13619.
178. Baalousha, M.; Nur, Y.; Romer, I.; Tejamaya, M.; Lead, J. R., Effect of monovalent and divalent cations, anions and fulvic acid on aggregation of citrate-coated silver nanoparticles. *Science of the Total Environment* **2013,** *454*, 119-131.
179. Römer, I.; Wang, Z. W.; Merrifield, R. C.; Palmer, R. E.; Lead, J., High Resolution STEM-EELS Study of Silver Nanoparticles Exposed to Light and Humic Substances. *Environmental Science & Technology* **2016,** *50* (5), 2183-2190.
180. Van Eerdenbrugh, B.; Alonzo, D. E.; Taylor, L. S., Influence of Particle Size on the Ultraviolet Spectrum of Particulate-Containing Solutions: Implications for In-Situ Concentration Monitoring Using UV/Vis Fiber-Optic Probes. *Pharmaceutical Research* **2011,** *28* (7), 1643-1652.
181. Johansson, J.; Cauchi, M.; Sundgren, M., Multiple fiber-optic dual-beam UV/Vis system with application to dissolution testing. *Journal of Pharmaceutical and Biomedical Analysis* **2002,** *29* (3), 469-476.
182. Cho, J. H.; Gemperline, P. J.; Salt, A.; Walker, D. S., UV/Visible Spectral Dissolution Monitoring by in Situ Fiber-Optic Probes. *Analytical Chemistry* **1995,** *67* (17), 2858-2863.
183. Zhang, Y. J.; Chi, H. J.; Zhang, W. H.; Sun, Y. Y.; Liang, Q.; Gu, Y.; Jing, R. Y., Highly Efficient Adsorption of Copper Ions by a PVP-Reduced Graphene Oxide Based On a New Adsorptions Mechanism. *Nano-Micro Letters* **2014,** *6* (1), 80-87.
184. Poznyak, S. K.; Osipovich, N. P.; Shavel, A.; Talapin, D. V.; Gao, M.; Eychmüller, A.; Gaponik, N., Size-Dependent Electrochemical Behavior of Thiol-Capped CdTe Nanocrystals in Aqueous Solution. *The Journal of Physical Chemistry B* **2005,** *109* (3), 1094-1100.
185. Cai, W.; Zhong, H.; Zhang, L., Optical measurements of oxidation behavior of silver nanometer particle within pores of silica host. *Journal of Applied Physics* **1998**, 1705-1710.
186. Wang, H.; Burgess, R. M.; Cantwell, M. G.; Portis, L. M.; Perron, M. M.; Wu, F.; Ho, K. T., Stability and aggregation of silver and titanium dioxide nanoparticles in seawater: Role of salinity and dissolved organic carbon. *Environmental Toxicology and Chemistry* **2014,** *33* (5), 1023-1029.
187. Homeostasis and toxicology of essential metals. In *Fish Physiology*, Chris M. Wood, A. P. F. a. C. J. B., Ed. Academic Press: 2011; Vol. Volume 31, Part A, p i.
188. Afshinnia, K.; Gibson, I.; Merrifield, R.; Baalousha, M., The concentration-dependent aggregation of Ag NPs induced by cystine. *Science of The Total Environment* **2016,** *557–558*, 395-403.

189. Páscoa, R. N. M. J.; Tóth, I. V.; Rangel, A. O. S. S., Review on recent applications of the liquid waveguide capillary cell in flow based analysis techniques to enhance the sensitivity of spectroscopic detection methods. *Analytica Chimica Acta* **2012,** *739*, 1-13.
190. Baalousha, M.; Lead, J. R., Nanoparticle dispersity in toxicology. *Nature Nanotechnology* **2013,** *8*, 308.
191. Baalousha, M., Effect of nanomaterial and media physicochemical properties on nanomaterial aggregation kinetics. *NanoImpact* **2017,** *6*, 55-68.
192. Bigall, N. C.; Härtling, T.; Klose, M.; Simon, P.; Eng, L. M.; Eychmüller, A., Monodisperse Platinum Nanospheres with Adjustable Diameters from 10 to 100 nm: Synthesis and Distinct Optical Properties. *Nano Letters* **2008,** *8* (12), 4588-4592.
193. Brown, K. R.; Walter, D. G.; Natan, M. J., Seeding of Colloidal Au Nanoparticle Solutions. 2. Improved Control of Particle Size and Shape. *Chemistry of Materials* **2000,** *12* (2), 306-313.
194. Koebel, M. M.; Jones, L. C.; Somorjai, G. A., Preparation of size-tunable, highly monodisperse PVP-protected Pt-nanoparticles by seed-mediated growth. *Journal of Nanoparticle Research* **2008,** *10* (6), 1063-1069.
195. Baalousha, M.; Ju-Nam, Y.; Cole, P. A.; Hriljac, J. A.; Jones, I. P.; Tyler, C. R.; Stone, V.; Fernandes, T. F.; Jepson, M. A.; Lead, J. R., Characterization of cerium oxide nanoparticles—Part 2: Nonsize measurements. *Environmental Toxicology and Chemistry* **2012,** *31* (5), 994-1003.
196. Gatan Incorporation. In *Gatan Digital Micrograph Software Instalation Instructions*, 2018.
197. Franze, B.; Strenge, I.; Engelhard, C., Single particle inductively coupled plasma mass spectrometry: evaluation of three different pneumatic and piezo-based sample introduction systems for the characterization of silver nanoparticles. *Journal of Analytical Atomic Spectrometry* **2012,** *27* (7), 1074-1083.
198. Laborda, F.; Jimenez-Lamana, J.; Bolea, E.; Castillo, J. R., Critical considerations for the determination of nanoparticle number concentrations, size and number size distributions by single particle ICP-MS. *Journal of Analytical Atomic Spectrometry* **2013,** *28* (8), 1220-1232.
199. Hineman, A.; Stephan, C., Effect of dwell time on single particle inductively coupled plasma mass spectrometry data acquisition quality. *Journal of Analytical Atomic Spectrometry* **2014,** *29* (7), 1252-1257.
200. Montaño, M. D.; Olesik, J. W.; Barber, A. G.; Challis, K.; Ranville, J. F., Single Particle ICP-MS: Advances toward routine analysis of nanomaterials. *Analytical and Bioanalytical Chemistry* **2016,** *408* (19), 5053-5074.
201. Elimelech, M.; O'Melia, C. R., Kinetics of deposition of colloidal particles in porous media. *Environmental Science & Technology* **1990,** *24* (10), 1528-1536.
202. OECD, *Test No. 202: Daphnia sp. Acute Immobilisation Test*. OECD Publishing.
203. Croteau, M.-N.; Misra, S. K.; Luoma, S. N.; Valsami-Jones, E., Silver Bioaccumulation Dynamics in a Freshwater Invertebrate after Aqueous and Dietary Exposures to Nanosized and Ionic Ag. *Environmental Science & Technology* **2011,** *45* (15), 6600-6607.
204. OECD. Organization for Economic Co-operation and Development *New Guidance Document on Harpacticoid Copepod Development and Reproduction Test with Amphiascus. Series on Testing and Assessment* [Online], 2014.

http://www.oecd.org/officialdocuments/publicdisplaydocumentpdf/?cote=ENV/JM/MONO(2014)17&doclanguage=en (accessed 2018 18).
205. Curiel, D. T.; Agarwal, S.; Wagner, E.; Cotten, M., Adenovirus enhancement of transferrin-polylysine-mediated gene delivery. *Proceedings of the National Academy of Sciences* **1991,** *88* (19), 8850-8854.
206. Agency, U. S. E. P. *Methods for Measuring the Acute Toxicity of Effluents and Receiving Waters to Freshwater and Marine Organisms*; U.S. EPA: Washington DC, 2002.
207. Pomogailo, A. D.; Dzhardimalieva, G. I., Reduction of Metal Ions in Polymer Matrices as a Condensation Method of Nanocomposite Synthesis. In *Nanostructured Materials Preparation via Condensation Ways*, Springer Dordrecht, 2014; pp 13-89.
208. Borsook, H.; Keighley, G., Oxidation-Reduction Potential of Ascorbic Acid (Vitamin C). *Proceedings of the National Academy of Sciences of the United States of America* **1933,** *19* (9), 875-878.
209. Lee, S.; Bi, X.; Reed, R. B.; Ranville, J. F.; Herckes, P.; Westerhoff, P., Nanoparticle Size Detection Limits by Single Particle ICP-MS for 40 Elements. *Environmental Science & Technology* **2014,** *48* (17), 10291-10300.
210. Wilkinson, K. J.; Balnois, E.; Leppard, G. G.; Buffle, J., Characteristic features of the major components of freshwater colloidal organic matter revealed by transmission electron and atomic force microscopy. *Colloids and Surfaces A: Physicochemical and Engineering Aspects* **1999,** *155* (2), 287-310.
211. Mavrocordatos, D.; Perret, D.; Leppard, G. G., Strategies and Advances in the Characterisation of Environmental Colloids by Electron Microscopy Denis Mavrocordatos. In *Environmental Colloids and Particles*, John Wiley & Sons, Ltd: 2007; pp 345-404.
212. Lead, J. R.; Wilkinson, K. J., Environmental Colloids and Particles: Current Knowledge and Future Developments. In *Environmental Colloids and Particles*, John Wiley & Sons, Ltd: 2006; pp 1-15.
213. Uskoković, V., Dynamic Light Scattering Based Microelectrophoresis: Main Prospects and Limitations. *Journal of dispersion science and technology* **2012,** *33* (12), 1762-1786.
214. Sikder, M.; Lead, J. R.; Chandler, G. T.; Baalousha, M., A rapid approach for measuring silver nanoparticle concentration and dissolution in seawater by UV–Vis. *Science of The Total Environment* **2018,** *618*, 597-607.
215. Baalousha, M.; Manciulea, A.; Cumberland, S.; Kendall, K.; Lead, J. R., Aggregation and surface properties of iron oxide nanoparticles: Influence of ph and natural organic matter. *Environmental Toxicology and Chemistry* **2008,** *27* (9), 1875-1882.
216. Wang, H.; Wang, Y.; Zhu, Z.; Sapi, A.; An, K.; Kennedy, G.; Michalak, W. D.; Somorjai, G. A., Influence of Size-Induced Oxidation State of Platinum Nanoparticles on Selectivity and Activity in Catalytic Methanol Oxidation in the Gas Phase. *Nano Letters* **2013,** *13* (6), 2976-2979.
217. Huynh, K. A.; Chen, K. L., Aggregation Kinetics of Citrate and Polyvinylpyrrolidone Coated Silver Nanoparticles in Monovalent and Divalent Electrolyte Solutions. *Environmental Science & Technology* **2011,** *45* (13), 5564-5571.

218. Fröhlich, E.; Bonstingl, G.; Höfler, A.; Meindl, C.; Leitinger, G.; Pieber, T. R.; Roblegg, E., Comparison of two in vitro systems to assess cellular effects of nanoparticles-containing aerosols. *Toxicology in Vitro* **2013,** *27-360* (1), 409-417.
219. Cedervall, T.; Lynch, I.; Foy, M.; Berggård, T.; Donnelly, S. C.; Cagney, G.; Linse, S.; Dawson, K. A., Detailed Identification of Plasma Proteins Adsorbed on Copolymer Nanoparticles. *Angewandte Chemie International Edition* **2007,** *46* (30), 5754-5756.
220. Sikder, M.; Lead, J. R.; Chandler, G. T.; Baalousha, M., A rapid approach for measuring silver nanoparticle concentration and dissolution in seawater by UV–Vis. *Science of The Total Environment* **2017**.
221. Kim, T.; Lee, C.-H.; Joo, S.-W.; Lee, K., Kinetics of gold nanoparticle aggregation: Experiments and modeling. *Journal of Colloid and Interface Science* **2008,** *318* (2), 238-243.
222. French, R. A.; Jacobson, A. R.; Kim, B.; Isley, S. L.; Penn, R. L.; Baveye, P. C., Influence of Ionic Strength, pH, and Cation Valence on Aggregation Kinetics of Titanium Dioxide Nanoparticles. *Environmental Science & Technology* **2009,** *43* (5), 1354-1359.
223. Phenrat, T.; Saleh, N.; Sirk, K.; Tilton, R. D.; Lowry, G. V., Aggregation and Sedimentation of Aqueous Nanoscale Zerovalent Iron Dispersions. *Environmental Science & Technology* **2007,** *41* (1), 284-290.
224. Baalousha, M.; Manciulea, A.; Cumberland, S.; Kendall, K.; Lead, J. R., Aggregation and surface properties of iron oxide nanoparticles: influence of pH and natural organic matter. *Environ Toxicol Chem* **2008,** *27* (9), 1875-82.
225. Abbasi, E.; Milani, M.; Fekri Aval, S.; Kouhi, M.; Akbarzadeh, A.; Tayefi Nasrabadi, H.; Nikasa, P.; Joo, S. W.; Hanifehpour, Y.; Nejati-Koshki, K.; Samiei, M., Silver nanoparticles: Synthesis methods, bio-applications and properties. *Critical Reviews in Microbiology* **2016,** *42* (2), 173-180.
226. Wei, L.; Lu, J.; Xu, H.; Patel, A.; Chen, Z.-S.; Chen, G., Silver nanoparticles: synthesis, properties, and therapeutic applications. *Drug Discovery Today* **2015,** *20* (5), 595-601.
227. Franci, G.; Falanga, A.; Galdiero, S.; Palomba, L.; Rai, M.; Morelli, G.; Galdiero, M., Silver nanoparticles as potential antibacterial agents. *Molecules* **2015,** *20* (5), 8856-8874.
228. Sørensen, S. N.; Baun, A., Controlling silver nanoparticle exposure in algal toxicity testing – A matter of timing. *Nanotoxicology* **2015,** *9* (2), 201-209.
229. Navarro, E.; Wagner, B.; Odzak, N.; Sigg, L.; Behra, R., Effects of Differently Coated Silver Nanoparticles on the Photosynthesis of Chlamydomonas reinhardtii. *Environmental Science & Technology* **2015,** *49* (13), 8041-8047.
230. Newton, K. M.; Puppala, H. L.; Kitchens, C. L.; Colvin, V. L.; Klaine, S. J., Silver nanoparticle toxicity to Daphnia magna is a function of dissolved silver concentration. *Environmental Toxicology and Chemistry* **2013,** *32* (10), 2356-2364.
231. Stensberg, M. C.; Madangopal, R.; Yale, G.; Wei, Q.; Ochoa-Acuña, H.; Wei, A.; McLamore, E. S.; Rickus, J.; Porterfield, D. M.; Sepúlveda, M. S., Silver nanoparticle-specific mitotoxicity in Daphnia magna. *Nanotoxicology* **2014,** *8* (8), 833-842.
232. Kim, K. T.; Truong, L.; Wehmas, L.; Tanguay, R. L., Silver nanoparticle toxicity in the embryonic zebrafish is governed by particle dispersion and ionic environment. *Nanotechnology* **2013,** *24* (11), 115101.

233. Kwok, K. W. H.; Dong, W.; Marinakos, S. M.; Liu, J.; Chilkoti, A.; Wiesner, M. R.; Chernick, M.; Hinton, D. E., Silver nanoparticle toxicity is related to coating materials and disruption of sodium concentration regulation. *Nanotoxicology* **2016,** *10* (9), 1306-1317.
234. Cox, A.; Venkatachalam, P.; Sahi, S.; Sharma, N., Silver and titanium dioxide nanoparticle toxicity in plants: A review of current research. *Plant Physiology and Biochemistry* **2016,** *107*, 147-163.
235. Cong, Y.; Banta, G. T.; Selck, H.; Berhanu, D.; Valsami-Jones, E.; Forbes, V. E., Toxicity and bioaccumulation of sediment-associated silver nanoparticles in the estuarine polychaete, Nereis (Hediste) diversicolor. *Aquatic Toxicology* **2014,** *156*, 106-115.
236. Yue, Y.; Behra, R.; Sigg, L.; Fernández Freire, P.; Pillai, S.; Schirmer, K., Toxicity of silver nanoparticles to a fish gill cell line: Role of medium composition. *Nanotoxicology* **2015,** *9* (1), 54-63.
237. Ivask, A.; Kurvet, I.; Kasemets, K.; Blinova, I.; Aruoja, V.; Suppi, S.; Vija, H.; Käkinen, A.; Titma, T.; Heinlaan, M.; Visnapuu, M.; Koller, D.; Kisand, V.; Kahru, A., Size-Dependent Toxicity of Silver Nanoparticles to Bacteria, Yeast, Algae, Crustaceans and Mammalian Cells In Vitro. *PLOS ONE* **2014,** *9* (7), e102108.
238. Yue, Y.; Behra, R.; Sigg, L.; Schirmer, K., Silver nanoparticles inhibit fish gill cell proliferation in protein-free culture medium. *Nanotoxicology* **2016,** *10* (8), 1075-1083.
239. Choi, O.; Hu, Z., Size Dependent and Reactive Oxygen Species Related Nanosilver Toxicity to Nitrifying Bacteria. *Environmental Science & Technology* **2008,** *42* (12), 4583-4588.
240. Lotufo, G. R., Toxicity of sediment-associated PAHs to an estuarine copepod: Effects on survival, feeding, reproduction and behavior. *Marine Environmental Research* **1997,** *44* (2), 149-166.
241. Dahl, U.; Gorokhova, E.; Breitholtz, M., Application of growth-related sublethal endpoints in ecotoxicological assessments using a harpacticoid copepod. *Aquatic Toxicology* **2006,** *77* (4), 433-438.
242. Breitholtz, M.; Wollenberger, L., Effects of three PBDEs on development, reproduction and population growth rate of the harpacticoid copepod Nitocra spinipes. *Aquatic Toxicology* **2003,** *64* (1), 85-96.
243. Coull, B. C., Are members of the meiofauna food for higher trophic levels? *Transactions of the American Microscopical Society* **1990**, 233-246.
244. Gee, J., An ecological and economic review of meiofauna as food for fish. *Zoological journal of the Linnean Society* **1989,** *96* (3), 243-261.
245. Coull, B. C.; Chandler, G. T., Pollution and meiofauna: field, laboratory, and mesocosm studies. *Oceanography and Marine Biology: An Annual Review* **1992**.
246. ASTM *Standard Guide for Conducting Renewal Microplate-Based Life-Cycle Toxicity Tests with a Marine Meiobenthic Copepod.* ; ASTM international: West Conshohocken, PA, 2012.
247. Lu, W.; Senapati, D.; Wang, S.; Tovmachenko, O.; Singh, A. K.; Yu, H.; Ray, P. C., Effect of surface coating on the toxicity of silver nanomaterials on human skin keratinocytes. *Chemical Physics Letters* **2010,** *487* (1), 92-96.
248. Foldbjerg, R.; Olesen, P.; Hougaard, M.; Dang, D. A.; Hoffmann, H. J.; Autrup, H., PVP-coated silver nanoparticles and silver ions induce reactive oxygen species, apoptosis and necrosis in THP-1 monocytes. *Toxicology Letters* **2009,** *190* (2), 156-162.

249. Blinova, I.; Niskanen, J.; Kajankari, P.; Kanarbik, L.; Käkinen, A.; Tenhu, H.; Penttinen, O.-P.; Kahru, A., Toxicity of two types of silver nanoparticles to aquatic crustaceans Daphnia magna and Thamnocephalus platyurus. *Environmental Science and Pollution Research* **2013,** *20* (5), 3456-3463.
250. Lang, K., *Monographie der Harpacticiden*. Otto Koeltz Science Publishers: Koenigstein, West Germany, 1948.
251. Green, A. S.; Chandler, G. T., Life-table evaluation of sediment-associated chlorpyrifos chronic toxicity to the benthic copepod, Amphiascus tenuiremis. *Archives of Environmental Contamination and Toxicology* **1996,** *31* (1), 77-83.
252. Bejarano, A. C.; Chandler, G. T., Reproductive and developmental effects of atrazine on the estuarine meiobenthic copepod Amphiascus tenuiremis. *Environ Toxicol Chem* **2003,** *22* (12), 3009-16.
253. Chandler, G. T., High-Density Culture of Meiobenthic Harpacticoid Copepods Within a Muddy Sediment Substrate. *Canadian Journal of Fisheries and Aquatic Sciences* **1986,** *43* (1), 53-59.
254. OECD *New guideline for the testing of chemicals: New Guidance Document on Harpacticoid Copepod Development and Reproduction Test with Amphiascus Tenuiremis*; OECD publisher: Paris, 2014.
255. Chandler, G. T.; Cary, T. L.; Bejarano, A. C.; Pender, J.; Ferry, J. L., Population consequences of fipronil and degradates to copepods at field concentrations: An integration of life cycle testing with Leslie matrix population Modeling. *Environmental Science & Technology* **2004,** *38* (23), 6407-6414.
256. Leslie, P. H., On the Use of Matrices in Certain Population Mathematics. *Biometrika* **1945,** *33* (3), 183-212.
257. Ferson, S.; Ginzburg, L.; Silvers, A., Extreme event risk analysis for age-structured populations. *Ecological Modelling* **1989,** *47* (1), 175-187.
258. Power, M.; Power, G., A modelling framework for analyzing anthropogenic stresses on brook trout (Salvelinus fontinalis) populations. *Ecological Modelling* **1995,** *80* (2), 171-185.
259. ASTM *Standard Guide for Conducting Acute Toxicity Tests on Test Materials with Fishes, Macroinvertebrates, and Amphibians*; ASTM international: West Conshohocken, PA, 2014.
260. Hook, S. E.; Fisher, N. S., Sublethal effects of silver in zooplankton: Importance of exposure pathways and implications for toxicity testing. *Environmental Toxicology and Chemistry* **2001,** *20* (3), 568-574.
261. Navarro, E.; Baun, A.; Behra, R.; Hartmann, N. B.; Filser, J.; Miao, A.-J.; Quigg, A.; Santschi, P. H.; Sigg, L., Environmental behavior and ecotoxicity of engineered nanoparticles to algae, plants, and fungi. *Ecotoxicology* **2008,** *17* (5), 372-386.
262. Griffitt, R. J.; Luo, J.; Gao, J.; Bonzongo, J.-C.; Barber, D. S., Effects of particle composition and species on toxicity of metallic nanomaterials in aquatic organisms. *Environmental Toxicology and Chemistry* **2008,** *27* (9), 1972-1978.
263. Chandler, G. T.; Cary, T. L.; Volz, D. C.; Walse, S. S.; Ferry, J. L.; Klosterhaus, S. L., Fipronil effects on estuarine copepod (Amphiascus tenuiremis) development, fertility, and reproduction: A rapid life-cycle assay in 96-well microplate format. *Environmental Toxicology and Chemistry* **2004,** *23* (1), 117-124.

264. Bielmyer, G. K.; Grosell, M.; Brix, K. V., Toxicity of Silver, Zinc, Copper, and Nickel to the Copepod Acartia tonsa Exposed via a Phytoplankton Diet. *Environmental Science & Technology* **2006,** *40* (6), 2063-2068.
265. Shafir, S.; Tom, M.; Ovadia, M.; Lubzens, E., Protein, Vitellogenin, and Vitellin Levels in the Hemolymph and Ovaries during Ovarian Development in Penaeus semisulcatus (de Haan). *The Biological Bulletin* **1992,** *183* (3), 394-400.
266. A S Raikhel, a.; Dhadialla, T. S., Accumulation of Yolk Proteins in Insect Oocytes. *Annual Review of Entomology* **1992,** *37* (1), 217-251.
267. Reinfelder, J. R.; Fisher, N. S., The assimilation of elements ingested by marine copepods. *Science* **1991,** *251* (4995), 794-6.
268. Hutchins, D. A.; Wang, W.-X.; Fisher, N. S., Copepod grazing and the biogeochemical fate of diatom iron. *Limnology and Oceanography* **1995,** *40* (5), 989-994.
269. Xu, Y.; Wang, W. X., Silver uptake by a marine diatom and its transfer to the coastal copepod Acartia spinicauda. *Environ Toxicol Chem* **2004,** *23* (3), 682-90.
270. Giere, O., *Meiobenthology: The Microscopic Motile Fauna of Aquatic Sediments*. Springer-Verlag: Berlin, 2009.
271. Hicks, G. R. F.; Coull, B. C., The ecology of marine meiobenthic harpacticoid copepods. *Oceanography and Marine Biology. An Annual Review* **1983,** (21), 67-175.
272. Sikder, M.; Wang, J.; Chandler, G. T.; Berti, D.; Baalousha, M., Synthesis, characterization, and environmental behaviors of monodispersed platinum nanoparticles. *Journal of Colloid and Interface Science* **2019,** *540*, 330-341.
273. Leenheer, J. A.; Croue, J. P., Characterizing aquatic dissolved organic matter. *Environ Sci Technol* **2003,** *37* (1), 18a-26a.
274. D'Andrilli, J.; Dittmar, T.; Koch, B. P.; Purcell, J. M.; Marshall, A. G.; Cooper, W. T., Comprehensive characterization of marine dissolved organic matter by Fourier transform ion cyclotron resonance mass spectrometry with electrospray and atmospheric pressure photoionization. *Rapid Communications in Mass Spectrometry* **2010,** *24* (5), 643-650.
275. Filipe, V.; Hawe, A.; Jiskoot, W., Critical Evaluation of Nanoparticle Tracking Analysis (NTA) by NanoSight for the Measurement of Nanoparticles and Protein Aggregates. *Pharmaceutical Research* **2010,** *27* (5), 796-810.
276. Gottschalk, F.; Sonderer, T.; Scholz, R. W.; Nowack, B., Modeled Environmental Concentrations of Engineered Nanomaterials (TiO2, ZnO, Ag, CNT, Fullerenes) for Different Regions. *Environmental Science & Technology* **2009,** *43* (24), 9216-9222.
277. Loosli, F.; Wang, J.; Rothenberg, S.; Bizimis, M.; Winkler, C.; Borovinskaya, O.; Flamigni, L.; Baalousha, M., Sewage spills are a major source of titanium dioxide engineered (nano)-particle release into the environment. *Environmental Science: Nano* **2019**.
278. Moldovan, M.; Rauch, S.; Gómez, M.; Antonia Palacios, M.; Morrison, G. M., Bioaccumulation of palladium, platinum and rhodium from urban particulates and sediments by the freshwater isopod Asellus aquaticus. *Water Research* **2001,** *35* (17), 4175-4183.
279. Aiken, G. R.; McKnight, D. M.; Thorn, K. A.; Thurman, E. M., Isolation of hydrophilic organic acids from water using nonionic macroporous resins. *Organic Geochemistry* **1992,** *18* (4), 567-573.

280. Green, N. W.; Perdue, E. M.; Aiken, G. R.; Butler, K. D.; Chen, H.; Dittmar, T.; Niggemann, J.; Stubbins, A., An intercomparison of three methods for the large-scale isolation of oceanic dissolved organic matter. *Marine Chemistry* **2014,** *161*, 14-19.
281. Huffman, E. W. D.; Stuber, H. A., Analytical methodology for elemental analysis of humic substances. In *Humic Substances in Soil, Sediment, and Water: Geochemistry, Isolation, and Characterization*, Wiley: 1985; pp 433-456.
282. Weishaar, J. L.; Aiken, G. R.; Bergamaschi, B. A.; Fram, M. S.; Fujii, R.; Mopper, K., Evaluation of Specific Ultraviolet Absorbance as an Indicator of the Chemical Composition and Reactivity of Dissolved Organic Carbon. *Environmental Science & Technology* **2003,** *37* (20), 4702-4708.
283. Kujawinski, E. B.; Behn, M. D., Automated Analysis of Electrospray Ionization Fourier Transform Ion Cyclotron Resonance Mass Spectra of Natural Organic Matter. *Analytical Chemistry* **2006,** *78* (13), 4363-4373.
284. Minor, E. C.; Steinbring, C. J.; Longnecker, K.; Kujawinski, E. B., Characterization of dissolved organic matter in Lake Superior and its watershed using ultrahigh resolution mass spectrometry. *Organic Geochemistry* **2012,** *43*, 1-11.
285. El Badawy, A. M.; Scheckel, K. G.; Suidan, M.; Tolaymat, T., The impact of stabilization mechanism on the aggregation kinetics of silver nanoparticles. *Sci Total Environ* **2012,** *429*, 325-31.
286. Lin, S.; Cheng, Y.; Liu, J.; Wiesner, M. R., Polymeric Coatings on Silver Nanoparticles Hinder Autoaggregation but Enhance Attachment to Uncoated Surfaces. *Langmuir* **2012,** *28* (9), 4178-4186.
287. Alexander, C. M.; Dabrowiak, J. C.; Goodisman, J., Gravitational sedimentation of gold nanoparticles. *Journal of Colloid and Interface Science* **2013,** *396*, 53-62.
288. Pettibone, J. M.; Cwiertny, D. M.; Scherer, M.; Grassian, V. H., Adsorption of Organic Acids on TiO2 Nanoparticles: Effects of pH, Nanoparticle Size, and Nanoparticle Aggregation. *Langmuir* **2008,** *24* (13), 6659-6667.
289. Chen, K. L.; Elimelech, M., Influence of humic acid on the aggregation kinetics of fullerene (C60) nanoparticles in monovalent and divalent electrolyte solutions. *Journal of Colloid and Interface Science* **2007,** *309* (1), 126-134.
290. Zhang, H.; Penn, R. L.; Hamers, R. J.; Banfield, J. F., Enhanced Adsorption of Molecules on Surfaces of Nanocrystalline Particles. *The Journal of Physical Chemistry B* **1999,** *103* (22), 4656-4662.
291. Phenrat, T.; Song, J. E.; Cisneros, C. M.; Schoenfelder, D. P.; Tilton, R. D.; Lowry, G. V., Estimating Attachment of Nano- and Submicrometer-particles Coated with Organic Macromolecules in Porous Media: Development of an Empirical Model. *Environmental Science & Technology* **2010,** *44* (12), 4531-4538.
292. Tiller, C. L.; O'Melia, C. R., Natural organic matter and colloidal stability: Models and measurements. *Colloids and Surfaces A: Physicochemical and Engineering Aspects* **1993,** *73*, 89-102.
293. Au, K.-K.; Penisson, A. C.; Yang, S.; O'Melia, C. R., Natural organic matter at oxide/water interfaces: complexation and conformation. *Geochimica et Cosmochimica Acta* **1999,** *63* (19), 2903-2917.
294. Baalousha, M.; Afshinnia, K.; Guo, L., Natural organic matter composition determines the molecular nature of silver nanomaterial-NOM corona. *Environmental Science: Nano* **2018,** *5* (4), 868-881.

295. Avneri-Katz, S.; Young, R. B.; McKenna, A. M.; Chen, H.; Corilo, Y. E.; Polubesova, T.; Borch, T.; Chefetz, B., Adsorptive fractionation of dissolved organic matter (DOM) by mineral soil: Macroscale approach and molecular insight. *Organic Geochemistry* **2017,** *103*, 113-124.
296. Davis, J. A.; Gloor, R., Adsorption of dissolved organics in lake water by aluminum oxide. Effect of molecular weight. *Environmental Science & Technology* **1981,** *15* (10), 1223-1229.
297. Lv, J.; Zhang, S.; Wang, S.; Luo, L.; Cao, D.; Christie, P., Molecular-Scale Investigation with ESI-FT-ICR-MS on Fractionation of Dissolved Organic Matter Induced by Adsorption on Iron Oxyhydroxides. *Environmental Science & Technology* **2016,** *50* (5), 2328-2336.
298. Mwaanga, P.; Carraway, E. R.; Schlautman, M. A., Preferential sorption of some natural organic matter fractions to titanium dioxide nanoparticles: influence of pH and ionic strength. *Environ Monit Assess* **2014,** *186* (12), 8833-44.
299. Zhou, Q.; Maurice, P. A.; Cabaniss, S. E., Size fractionation upon adsorption of fulvic acid on goethite: equilibrium and kinetic studies. *Geochimica et Cosmochimica Acta* **2001,** *65* (5), 803-812.
300. Chin, Y.-P.; Aiken, G.; O'Loughlin, E., Molecular Weight, Polydispersity, and Spectroscopic Properties of Aquatic Humic Substances. *Environmental Science & Technology* **1994,** *28* (11), 1853-1858.
301. Haslam, E., *Practical polyphenolics: from structure to molecular recognition and physiological action*. Cambridge University Press: Cambridge, 1998.
302. Sipponen, M. H.; Lange, H.; Ago, M.; Crestini, C., Understanding Lignin Aggregation Processes. A Case Study: Budesonide Entrapment and Stimuli Controlled Release from Lignin Nanoparticles. *ACS Sustainable Chemistry & Engineering* **2018,** *6* (7), 9342-9351.
303. Lal, R., Mechanisms of Carbon Sequestration in Soil Aggregates AU - Blanco-Canqui, Humberto. *Critical Reviews in Plant Sciences* **2004,** *23* (6), 481-504.
304. Caesar-TonThat, T. C.; Cochran, V. L., Soil aggregate stabilization by a saprophytic lignin-decomposing basidiomycete fungus I. Microbiological aspects. *Biology and Fertility of Soils* **2000,** *32* (5), 374-380.
305. Xiao, C.; Bolton, R.; Pan, W. L., Lignin from rice straw Kraft pulping: Effects on soil aggregation and chemical properties. *Bioresource Technology* **2007,** *98* (7), 1482-1488.
306. Pan, J. F.; Buffet, P. E.; Poirier, L.; Amiard-Triquet, C.; Gilliland, D.; Joubert, Y.; Pilet, P.; Guibbolini, M.; de Faverney, C. R.; Romeo, M.; Valsami-Jones, E.; Mouneyrac, C., Size dependent bioaccumulation and ecotoxicity of gold nanoparticles in an endobenthic invertebrate: The Tellinid clam Scrobicularia plana. *Environmental Pollution* **2012,** *168*, 37-43.
307. Hull, M. S.; Chaurand, P.; Rose, J.; Auffan, M.; Bottero, J.-Y.; Jones, J. C.; Schultz, I. R.; Vikesland, P. J., Filter-Feeding Bivalves Store and Biodeposit Colloidally Stable Gold Nanoparticles. *Environmental Science & Technology* **2011,** *45* (15), 6592-6599.
308. Lankveld, D. P. K.; Oomen, A. G.; Krystek, P.; Neigh, A.; Troost – de Jong, A.; Noorlander, C. W.; Van Eijkeren, J. C. H.; Geertsma, R. E.; De Jong, W. H., The kinetics of the tissue distribution of silver nanoparticles of different sizes. *Biomaterials* **2010,** *31* (32), 8350-8361.

309. Skjolding, L. M.; Kern, K.; Hjorth, R.; Hartmann, N.; Overgaard, S.; Ma, G.; Veinot, J. G. C.; Baun, A., Uptake and depuration of gold nanoparticles in Daphnia magna. *Ecotoxicology* **2014,** *23* (7), 1172-1183.
310. Zhao, C.-M.; Wang, W.-X., Size-Dependent Uptake of Silver Nanoparticles in Daphnia magna. *Environmental Science & Technology* **2012,** *46* (20), 11345-11351.
311. Hao, L.; Chen, L.; Hao, J.; Zhong, N., Bioaccumulation and sub-acute toxicity of zinc oxide nanoparticles in juvenile carp (Cyprinus carpio): A comparative study with its bulk counterparts. *Ecotoxicology and Environmental Safety* **2013,** *91*, 52-60.
312. Suematsu, H.; Kiyomiya, E.; Aoki, M.; Sato, M.; Moritoki, N., Size-dependent toxicity of silica nano-particles to Chlorella kessleri AU - Fujiwara, Kitao. *Journal of Environmental Science and Health, Part A* **2008,** *43* (10), 1167-1173.
313. Chithrani, B. D.; Ghazani, A. A.; Chan, W. C. W., Determining the Size and Shape Dependence of Gold Nanoparticle Uptake into Mammalian Cells. *Nano Letters* **2006,** *6* (4), 662-668.
314. Zhang, X.-D.; Wu, D.; Shen, X.; Liu, P.-X.; Yang, N.; Zhao, B.; Zhang, H.; Sun, Y.-M.; Zhang, L.-A.; Fan, F.-Y., Size-dependent in vivo toxicity of PEG-coated gold nanoparticles. *International journal of nanomedicine* **2011,** *6*, 2071-2081.
315. Adams, L. K.; Lyon, D. Y.; Alvarez, P. J. J., Comparative eco-toxicity of nanoscale TiO2, SiO2, and ZnO water suspensions. *Water Research* **2006,** *40* (19), 3527-3532.
316. Rainbow, P. S., Trace metal concentrations in aquatic invertebrates: why and so what? *Environmental Pollution* **2002,** *120* (3), 497-507.
317. Zhao, J.; Wang, Z.; Dai, Y.; Xing, B., Mitigation of CuO nanoparticle-induced bacterial membrane damage by dissolved organic matter. *Water Research* **2013,** *47* (12), 4169-4178.
318. Kim, J. Y.; Kim, K.-T.; Lee, B. G.; Lim, B. J.; Kim, S. D., Developmental toxicity of Japanese medaka embryos by silver nanoparticles and released ions in the presence of humic acid. *Ecotoxicology and Environmental Safety* **2013,** *92*, 57-63.
319. Ren, C.; Hu, X.; Zhou, Q., Influence of environmental factors on nanotoxicity and knowledge gaps thereof. *NanoImpact* **2016,** *2*, 82-92.
320. Praetorius, A.; Labille, J.; Scheringer, M.; Thill, A.; Hungerbühler, K.; Bottero, J.-Y., Heteroaggregation of Titanium Dioxide Nanoparticles with Model Natural Colloids under Environmentally Relevant Conditions. *Environmental Science & Technology* **2014,** *48* (18), 10690-10698.
321. Wang, Z.; Zhang, L.; Zhao, J.; Xing, B., Environmental processes and toxicity of metallic nanoparticles in aquatic systems as affected by natural organic matter. *Environmental Science: Nano* **2016,** *3* (2), 240-255.
322. Rauch, S.; Morrison, G. M., Platinum uptake by the freshwater isopod Asellus Aquaticus in urban rivers. *Science of The Total Environment* **1999,** *235* (1), 261-268.
323. Luoma, S. N.; Rainbow, P. S., Why Is Metal Bioaccumulation So Variable? Biodynamics as a Unifying Concept. *Environmental Science & Technology* **2005,** *39* (7), 1921-1931.
324. Croteau, M.-N.; Dybowska, A. D.; Luoma, S. N.; Valsami-Jones, E., A novel approach reveals that zinc oxide nanoparticles are bioavailable and toxic after dietary exposures. *Nanotoxicology* **2011,** *5* (1), 79-90.

325. Croteau, M.-N.; Fuller, C. C.; Cain, D. J.; Campbell, K. M.; Aiken, G., Biogeochemical Controls of Uranium Bioavailability from the Dissolved Phase in Natural Freshwaters. *Environmental Science & Technology* **2016,** *50* (15), 8120-8127.
326. Croteau, M.-N.; Misra, S. K.; Luoma, S. N.; Valsami-Jones, E., Bioaccumulation and Toxicity of CuO Nanoparticles by a Freshwater Invertebrate after Waterborne and Dietborne Exposures. *Environmental Science & Technology* **2014,** *48* (18), 10929-10937.
327. Nyström, P.; Pérez, J. R., Crayfish predation on the common pond snail (Lymnaea stagnalis): the effect of habitat complexity and snail size on foraging efficiency. *Hydrobiologia* **1998,** *368* (1), 201-208.
328. Stoiber, T.; Croteau, M. N.; Romer, I.; Tejamaya, M.; Lead, J. R.; Luoma, S. N., Influence of hardness on the bioavailability of silver to a freshwater snail after waterborne exposure to silver nitrate and silver nanoparticles. *Nanotoxicology* **2015,** *9* (7), 918-27.
329. Poulin, B. A.; Ryan, J. N.; Nagy, K. L.; Stubbins, A.; Dittmar, T.; Orem, W.; Krabbenhoft, D. P.; Aiken, G. R., Spatial Dependence of Reduced Sulfur in Everglades Dissolved Organic Matter Controlled by Sulfate Enrichment. *Environmental Science & Technology* **2017,** *51* (7), 3630-3639.
330. Croteau, M.-N.; Luoma, S. N.; Topping, B. R.; Lopez, C. B., Stable Metal Isotopes Reveal Copper Accumulation and Loss Dynamics in the Freshwater Bivalve Corbicula. *Environmental Science & Technology* **2004,** *38* (19), 5002-5009.
331. Ek, K. H.; Morrison, G. M.; Rauch, S., Environmental routes for platinum group elements to biological materials—a review. *Science of The Total Environment* **2004,** *334-335*, 21-38.
332. Gratton, S. E. A.; Ropp, P. A.; Pohlhaus, P. D.; Luft, J. C.; Madden, V. J.; Napier, M. E.; DeSimone, J. M., The effect of particle design on cellular internalization pathways. *Proceedings of the National Academy of Sciences* **2008,** *105* (33), 11613.
333. Trenfield, M. A.; Ng, J. C.; Noller, B. N.; Markich, S. J.; Dam, R. A. v., Dissolved Organic Carbon Reduces Uranium Bioavailability and Toxicity. 2. Uranium[VI] Speciation and Toxicity to Three Tropical Freshwater Organisms. *Environmental Science & Technology* **2011,** *45* (7), 3082-3089.
334. Gheorghiu, C.; Smith, D. S.; Al-Reasi, H. A.; McGeer, J. C.; Wilkie, M. P., Influence of natural organic matter (NOM) quality on Cu–gill binding in the rainbow trout (Oncorhynchus mykiss). *Aquatic Toxicology* **2010,** *97* (4), 343-352.
335. Richards, J. G.; Curtis, P. J.; Burnison, B. K.; Playle, R. C., Effects of natural organic matter source on reducing metal toxicity to rainbow trout (Oncorhynchus mykiss) and on metal binding to their gills. *Environmental Toxicology and Chemistry* **2001,** *20* (6), 1159-1166.
336. Luider, C. D.; Crusius, J.; Playle, R. C.; Curtis, P. J., Influence of Natural Organic Matter Source on Copper Speciation As Demonstrated by Cu Binding to Fish Gills, by Ion Selective Electrode, and by DGT Gel Sampler. *Environmental Science & Technology* **2004,** *38* (10), 2865-2872.
337. De Schamphelaere, K. A. C.; Vasconcelos, F. M.; Tack, F. M. G.; Allen, H. E.; Janssen, C. R., Effect of dissolved organic matter source on acute copper toxicity to Daphnia magna. *Environmental Toxicology and Chemistry* **2004,** *23* (5), 1248-1255.
338. Morel, M., M,F; Hering, J., G, *Principles and applications of aquatic chemistry*. John Wiley & Sons Inc.: New York, 1993.

339. Hutchison, K. J.; Hesterberg, D.; Chou, J. W., Stability of Reduced Organic Sulfur in Humic Acid as Affected by Aeration and pH. *Soil Science Society of America Journal* **2001,** *65* (3), 704-709.
340. Poulin, B. A.; Gerbig, C. A.; Kim, C. S.; Stegemeier, J. P.; Ryan, J. N.; Aiken, G. R., Effects of Sulfide Concentration and Dissolved Organic Matter Characteristics on the Structure of Nanocolloidal Metacinnabar. *Environmental Science & Technology* **2017,** *51* (22), 13133-13142.
341. Manceau, A.; Nagy, K. L., Quantitative analysis of sulfur functional groups in natural organic matter by XANES spectroscopy. *Geochimica et Cosmochimica Acta* **2012,** *99*, 206-223.
342. Rose Williams, K.; Hedman, B.; Hodgson, K. O.; Solomon, E. I., Ligand K-edge X-ray absorption spectroscopic studies: metal-ligand covalency in transition metal tetrathiolates. *Inorganica Chimica Acta* **1997,** *263* (1), 315-321.
343. Ravel , B.; Newville, M., ATHENA, ARTEMIS, HEPHAESTUS: data analysis for X-ray absorption spectroscopy using IFEFFIT. *Journal of Synchrotron Radiation* **2005,** (12), 537-541.

APPENDIX A: SUPPORTING INFORMATION FOR CHAPTER 2

A.1. Fitting particle size distribution

In order to construct measured particle size distribution histogram (PSD), measured heights were classified into interval of 1 nm and log-normal distribution function (see full details in SI section) was used to model the PSD. Main objective of this approach was to smooth out the PSD and to eliminate/minimize any potential artefacts within the PSD; as AFM measured AgNPs' numbers were small compared to total amount of AgNPs in suspension.

$$f(x) = \frac{1}{\sqrt{2\pi}x}\ \frac{1}{x}\ e^{-\left\{\frac{\left[ln\left(\frac{x}{m}\right)\right]^2}{2\sigma^2}\right\}} \quad \text{(Equation A.1.)}$$

Where sigma (σ) is the variance, m is the median of the size distribution density function f(x)

In this approach bimodal log-normal distribution were adopted, in order to accommodate smaller fraction of AgNPs and larger fraction of AgNPs; where F_1 and F_2 represents smaller and larger fractions of AgNPs in MSD respectively.

$$Y_1 = \frac{f(x)}{\sum f(x)} F_1 \quad \text{and} \qquad Y_2 = \frac{f(x)}{\sum f(x)} F_2 \quad \text{(Equation A.2.)}$$

Curve fitting was optimized by minimizing the summation of squared errors (Eq. 9)

$$X^2 = \sum \frac{(O-F)^2}{\sigma^2} \quad \text{(Equation A.3.)}$$

Where, σ^2 is the known variance of the observation, O is the observed data and F (= Y_1+Y_2) is the fitted data from the model.

A.2. Dissolution modeling

The obtained data were fitted using a first-order kinetic equation modified from Kittler et al. (2010)[38], which is an empirical equation describing different parts of dissolution curve of a dissolving solid particles. According to Morel and Hering, the dissolution rate of a solid material is proportional to the concentration gradient of its dissolved species between the NP surface and the bulk solution [338] and can be expressed as

$$\frac{dC}{dt} = K(C_{max} - C_x) \quad \text{(Equation A.4)}$$

Where, C_{max} is maximum equilibrium concentration and C_x is the concentration of dissolved species in bulk solution. Assuming that when t= 0 then C_x= 0 and C_{max}= C_{AgNPs}, Eq. 4 can have a general solution of:

$$\frac{C_x}{C_{max}} = 1 - e^{-kt} \quad \text{(Equation A.5)}$$

Assuming, PVP-Ag NPs dissolution proceeds with a constant dissolution rate (k); thus Eq. 5 can be written as

$$\frac{C_x}{C_{max}} = 1 - \mathrm{A} * e^{-k_1 t} \quad \text{(Equation A.6)}$$

Where, A represents fitted coefficient at the electrolyte concentration applied

The weighted square of fitting errors was calculated using Eq. 7

$$X^2 = \sum \frac{(O-E)^2}{\sigma^2} \quad \text{(Equation A.7)}$$

Where, σ^2 is the variance of the measured dissolved Ag fractions.

The fitting parameters (A and k) in Eq. 8 were optimized by minimizing the weighted square error using Solver software in Microsoft Excel. The model parameters (A and k) were plotted as a function of Ag NPs concentration.

A.3. Supporting figures and tables

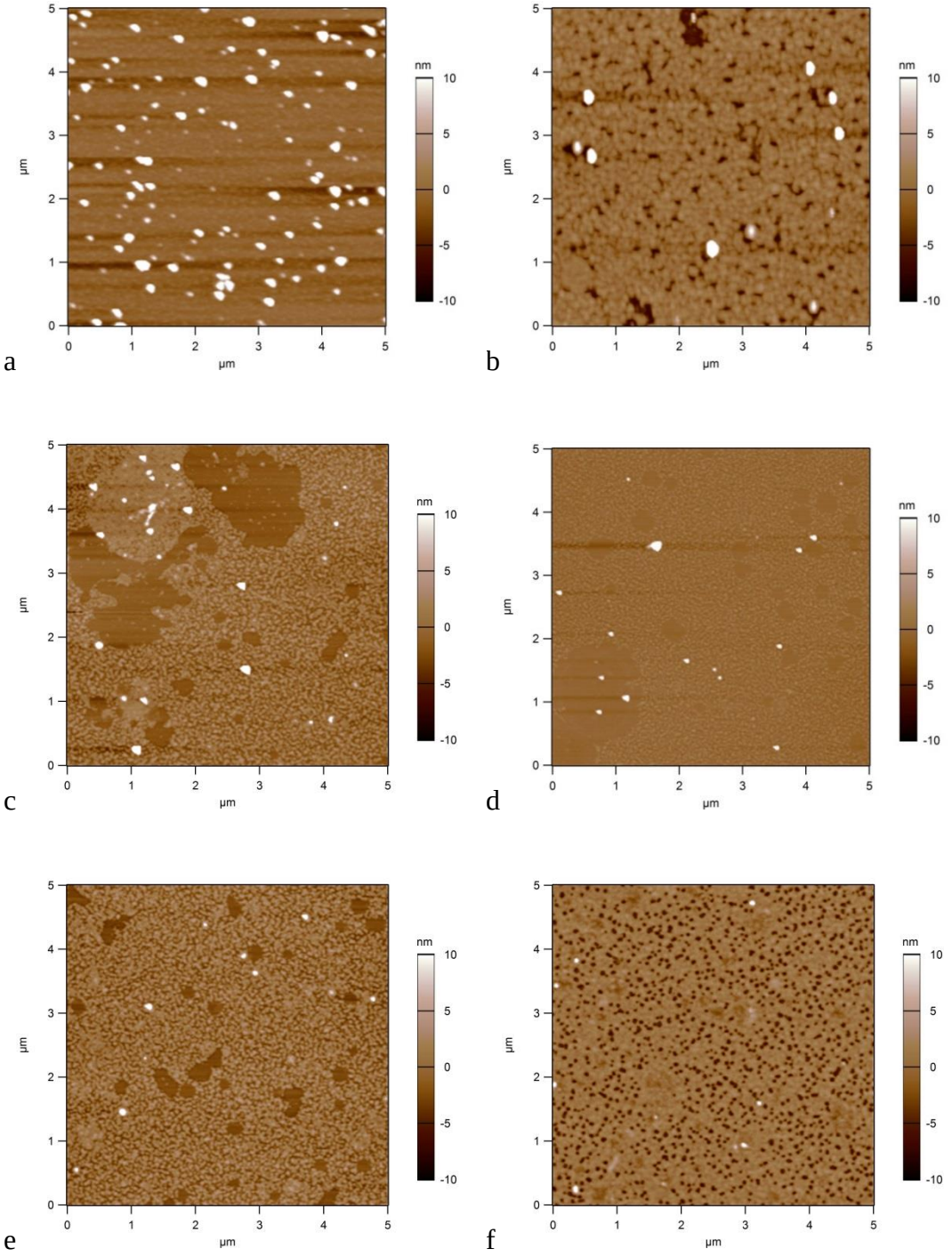

Figure A.1. Representative AFM micrographs of 10 ppb PVP-Ag NPs (a) in UPW and (b-f) in 30 ppt SW at (b) 0 hour, (c) 24 hour, (d) 48 hour, (e) 72 hour and (f) 96 hour

Table A.1. Position of maximum absorbance (λ_{max}) for UV-vis spectra of PVP-Ag NPs after mixing with SW

Sample	**Maximum absorbance (au)**	**λ_{max} (nm)**
NPs in SW at 0 hr.	0.081 ± 0.001	404
NPs in SW at 24 hr.	0.039 ± 0.001	403
NPs in SW at 48 hr.	0.031 ± 0.001	400
NPs in SW at 72 hr.	0.021 ± 0.001	399
NPs in SW at 96 hr.	0.016 ± 0.001	395

Table A.2. Dissolution rate (k) and fitted coefficient (A) of PVP-Ag NPs in 30 ppt SW depending on initial concentration

Initial Concentration (ppb)	**Dissolution rate (k), h^{-1}**	**Fitted Parameter (A)**
25	0.03 ± 0.007	1
50	0.02 ± 0.006	1.1
500	0.011 ± 0.004	1.03
1000	0.006 ± 0.003	0.96
1500	0.0013 ± 0.001	1

Table A.3. Calculated dissolved silver concentration depending on initial AgNPs concentration

Time (h)	**25 µg L^{-1}**	**50 µg L^{-1}**	**500 µg L^{-1}**	**1000 µg L^{-1}**	**1500 µg L^{-1}**
0	0	0	0	0	0
24	8.1	5.6	22.4	26.926	44.6
48	12.1	14.6	104.7	142.1	80.2
72	14.2	21.7	168.6	232.6	101.9
96	24.1	27.3	189.2	264.7	111.8

Table A.4. Composition of Synthetic seawater (SW)

Element	Concentration (mg L^{-1})	Element	Concentration (mg L^{-1})
Sodium	10,400	Chloride	18,600
Magnesium	1290	Sulfate	2,600
Calcium	410	Bicarbonate	149
Potassium	380	Carbonate	10
Strontium	12.5	Bromide	6
Boron	4.4	Flouride	1.5
Silicon	2.8	Iodine	0.05
Rubidium	0.19	Barium	0.05
Aluminum	0.17	Zinc	0.014
Lithium	0.11	Molybdenum	0.01
Iron	0.01	Tin	0.003
Lead	0.004	Arsenic	0.003
Selenium	0.0039	Silver	0.003
Vanadium	0.002	Cesium	0.002
Copper	0.001	Cobalt	0.0001
Manganese	0.001	Tungsten	0.0001
Cerium	0.0007	Cadmium	0.0001
Mercury	0.0003	Gallium	0.00007
Antimony	0.0003	Thalium	0.00007
Thorium	0.0002	Uranium	0.00005
Nickel	0.0002	Chromium	0.00005
Beryllium	0.0001		
Following chemical compositions are present in trace amount:			
Argon, Lutetium, Scandium, Radium, Bismuth, Niobium, Dysprosium, Europium, Gadolinium, Krypton, Indium, Lanthanum, Titanium, Germanium, Ruthenium, Samarium, Tantalum, Zirconium, Xenon, Gold, Hafnium, Radon, Neodymium, Helium, Yttrium, Erbium, Dysprosium, Palladium, Protactinium, Praseodymium, and Neon			

APPENDIX B: SUPPORTING INFORMATION FOR CHAPTER 3

B.1. Supporting figures and tables

Table B.1. Hydrodynamic diameter of cit-PtNPs in UPW and 20 mM $NaNO_3$

	$d_{DLS} \pm \sigma_d$ (nm)	
	in UPW	**in 20 mM $NaNO_3$**
$PtNP_{20}$	10.0±0.3	10.1±1.9
$PtNP_{30}$	17.0±0.3	14±0.6
$PtNP_{50}$	31.2±0.2	32.6±1.3
$PtNP_{75}$	59.3±0.3	52.8±0.7
$PtNP_{95}$	83.5±0.3	70.7±0.9

Table B.2. Chemical composition of moderately hard water (MHW)

Chemical constituent	**Concentration (mg. L^{-1})**
Sodium bicarbonate ($NaHCO_3$)	96
Calcium sulfate ($CaSO_4.2H_2O$)	60
Magnesium sulfate ($MgSO_4$)	60
Potassium chloride (KCl)	4

Table B.3. Composition of Synthetic seawater (SW)

Element	Concentration (mg L^{-1})	Element	Concentration (mg L^{-1})
Sodium	10,400	Chloride	18,600
Magnesium	1290	Sulfate	2,600
Calcium	410	Bicarbonate	149
Potassium	380	Carbonate	10
Strontium	12.5	Bromide	6
Boron	4.4	Flouride	1.5
Silicon	2.8	Iodine	0.05
Rubidium	0.19	Barium	0.05
Aluminum	0.17	Zinc	0.014
Lithium	0.11	Molybdenum	0.01
Iron	0.01	Tin	0.003
Lead	0.004	Arsenic	0.003
Selenium	0.0039	Silver	0.003
Vanadium	0.002	Cesium	0.002
Copper	0.001	Cobalt	0.0001
Manganese	0.001	Tungsten	0.0001
Cerium	0.0007	Cadmium	0.0001
Mercury	0.0003	Gallium	0.00007
Antimony	0.0003	Thalium	0.00007
Thorium	0.0002	Uranium	0.00005
Nickel	0.0002	Chromium	0.00005
Beryllium	0.0001		
Following chemical compositions are present in trace amount:			
Argon, Lutetium, Scandium, Radium, Bismuth, Niobium, Dysprosium, Europium, Gadolinium, Krypton, Indium, Lanthanum, Titanium, Germanium, Ruthenium, Samarium, Tantalum, Zirconium, Xenon, Gold, Hafnium, Radon, Neodymium, Helium, Yttrium, Erbium, Dysprosium, Palladium, Protactinium, Praseodymium, and Neon			

Table B.4. Chemical composition of dulbecco's modified eagle's medium (DMEM)

Chemical constituent	**Concentration (mg. L^{-1})**	**Chemical constituent**	**Concentration (mg. L^{-1})**
$CaCl_2$ (anhydrous)	200	L-Serine	42
$Fe(NO_3)_3 \cdot 9H_2O$	0. 10	L-Threonine	95
$MgSO_4$ (anhydrous)	97.70	L-Tryptophan	16
KCl	400	L-Tyrosine·2Na·$2H_2O$	103.79
$NaHCO_3$	1500	L-Valine	94
NaCl	6400	Choline Chloride	4
$NaH_2PO_4 \cdot H_2O$	125	Folic Acid	4
L-Arginine. HCl	84	myo-Inositol	7.2
L-Cystine. 2HCl	62.6	Nicotinamide	4
L-Glutamine	584	D-Pantothenic Acid (hemicalcium)	4
Glycine	30	Pyridoxine· HCl	4
L-Histidine·HCl·H_2O	42	Riboflavin	4
L-Isoleucine	105	Thiamine· HCl	4
L-Leucine	105	D-Glucose	4500
L-Lysine· HCl	146	Phenol Red, Sodium Salt	15
L-Methionine	30	Sodium Pyruvate	110
L-Phenylalanine	66		

Table B.5. Particle diameter and number concentration measured by sp-ICP-MS of cit-PtNPs and PVP-PtNPs after 24 h mixing with different media

Sample name	NP concentration (µg. L^{-1})	Media	Mean size ± SD (nm)	Total particle number concentration (NP/mL)
Cit-PtNPs	20	UPW	72.9 ± 9.9	6.04E+06
		DMEM	73.1 ± 7.6	5.61E+06
		MHW	73.1 ± 9.6	3.15E+06
		SW	79.2 ± 18.8	2.47E+06
	200	UPW	75.2 ± 10	4.98E+07
		DMEM	76.2 ± 10.6	5.31E+07
		MHW	86.7 ± 22.8	1.74E+07
		SW	89.6 ± 23.7	1.39E+07
	2000	UPW	75.2 ± 10	4.98E+08
		DMEM	75.4 ± 10.1	4.78E+08
		MHW	121.9 ± 39.8	5.05E+07
		SW	126.2 ± 46	2.61E+07
PVP-PtNPs	20	UPW	73 ± 10.5	5.15E+06
		DMEM	74 ± 9.7	6.81E+06
		MHW	75 ± 13.8	3.15E+06
		SW	79.1 ± 21.5	2.70E+06
	200	UPW	74.8 ± 10.4	4.95E+07
		DMEM	74.6 ± 10.8	5.31E+07
		MHW	86.4 ± 21.1	1.63E+07
		SW	93.5 ± 28.2	1.53E+07
	2000	UPW	74.8 ± 10.4	4.95E+08
		DMEM	74 ± 10.8	4.99E+08
		MHW	120.1 ± 38.7	4.18E+07
		SW	126.5 ± 45.4	3.24E+07

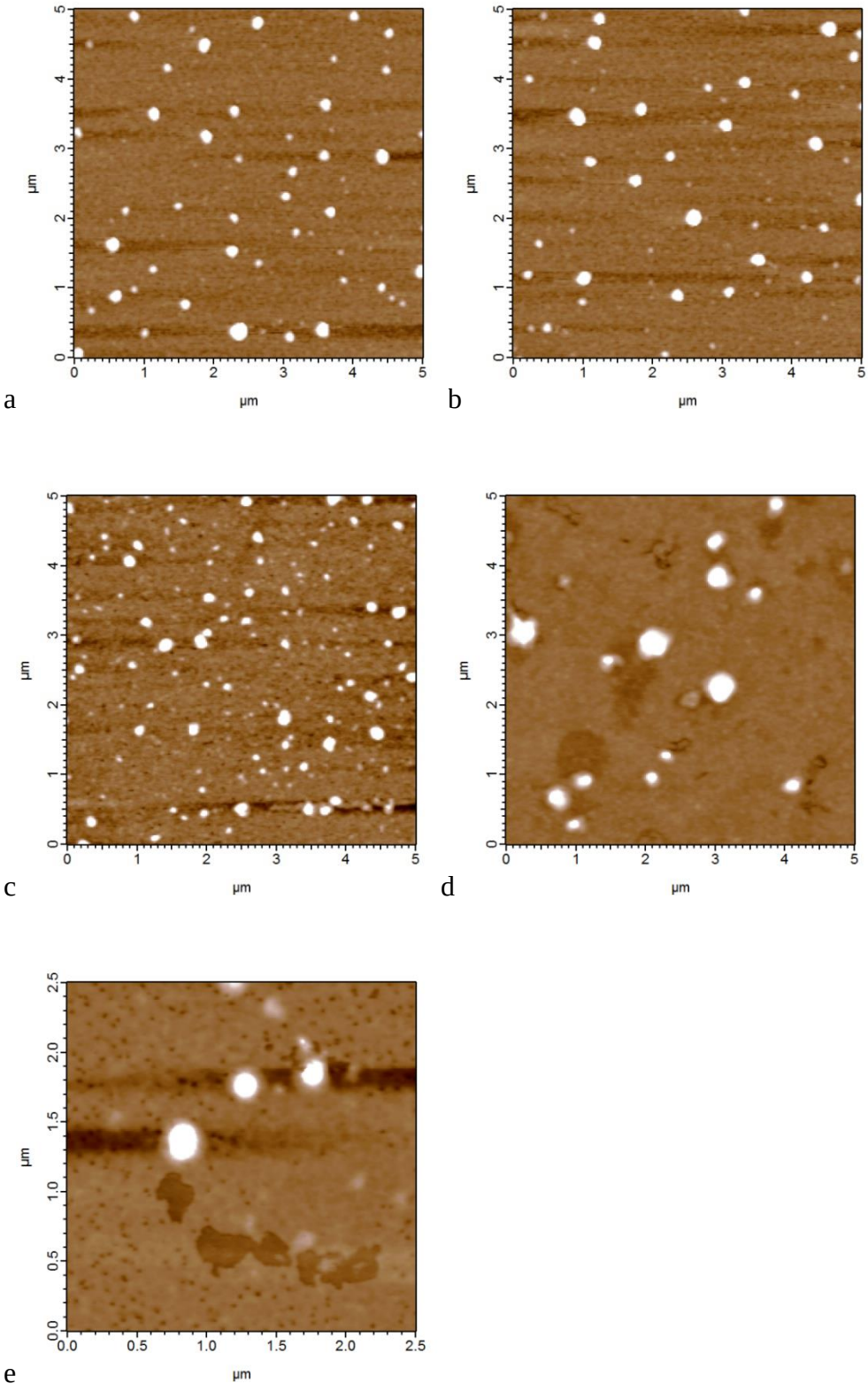

Figure B.1. (a-e) Typical atomic force microscopy (AFM) micrographs of PVP-PtNPs ($PtNP_{20}$, $PtNP_{30}$, $PtNP_{50}$, $PtNP_{75}$, and $PtNP_{95}$, respectively).

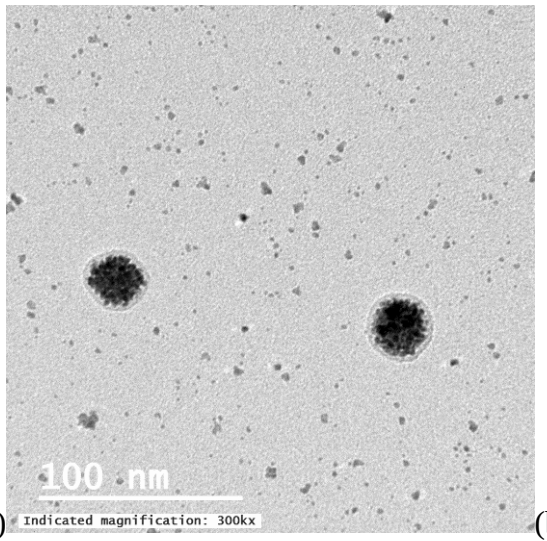

(a)

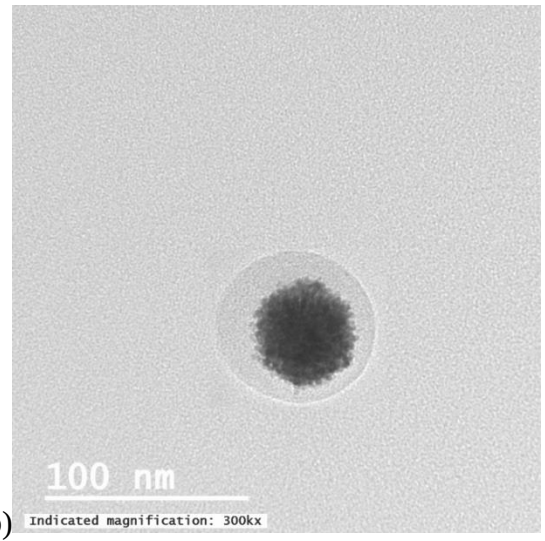

(b)

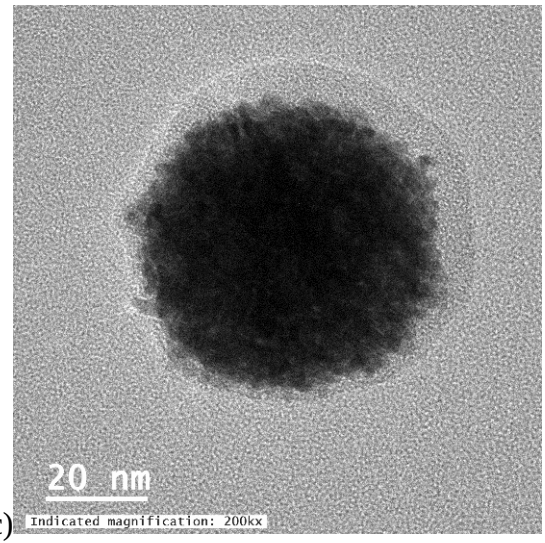

(c)

Figure B.2. Transmission electron microscopy (TEM) micrographs of (a) PVP-$PtNP_{50}$, (b) PVP-$PtNP_{75}$, and (c) PVP-$PtNP_{95}$ illustrating the formation of a thick (2.7-5.6 nm) PVP coating on the surface of PVP-PtNPs.

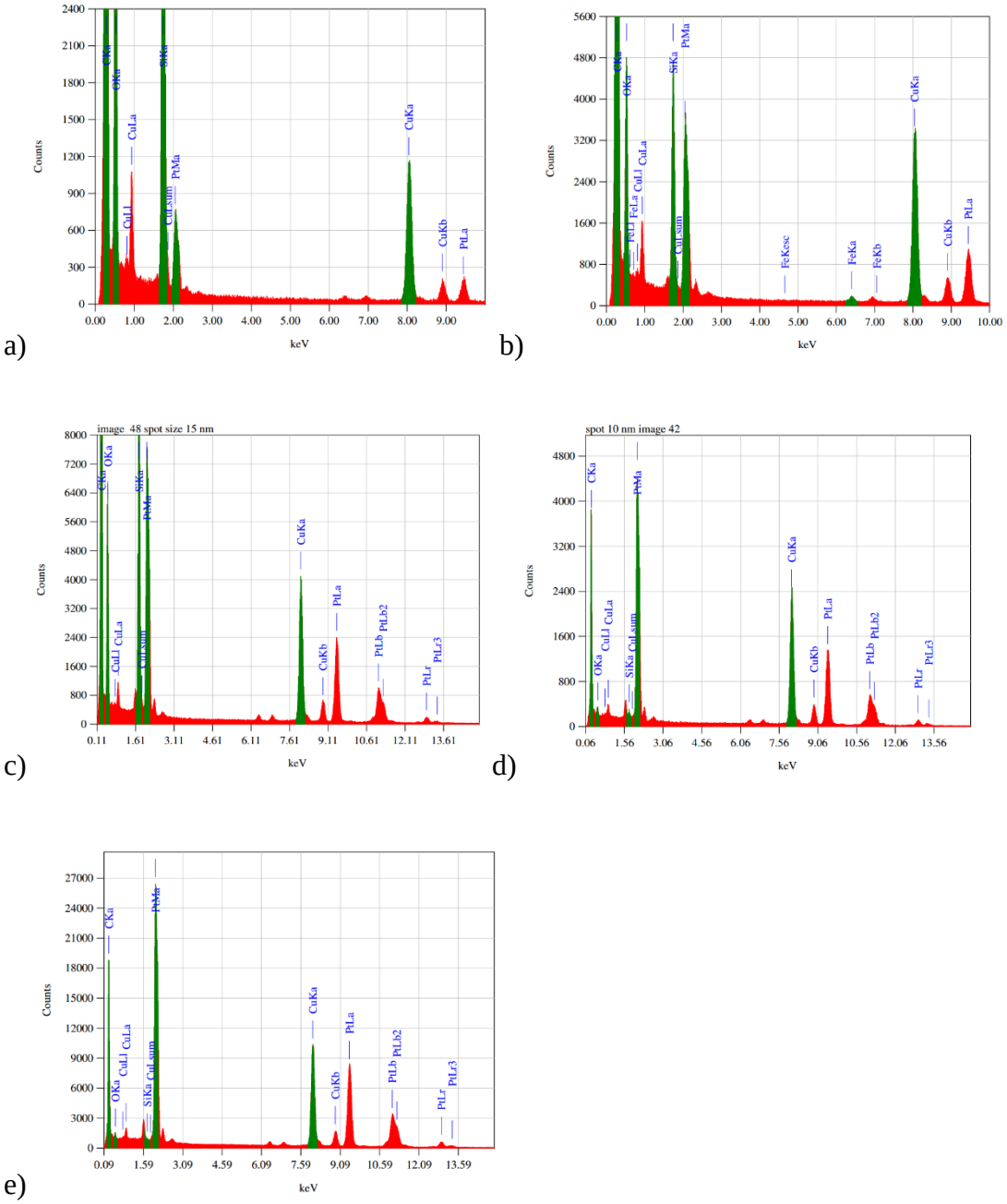

Figure B.3. Energy Dispersive X-ray spectra of (a) $PtNP_{20}$, (b) $PtNP_{30}$, (c) $PtNP_{50}$, (d) $PtNP_{75}$, and (e) $PtNP_{95}$.

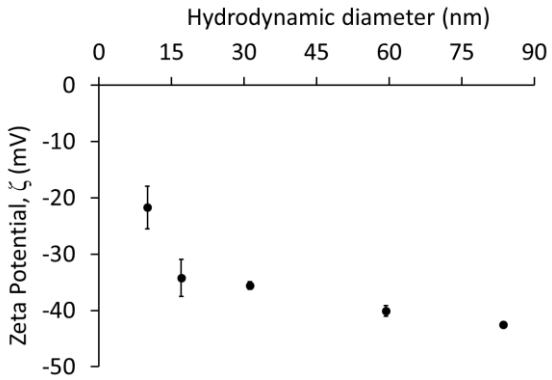

Figure B.4. Zeta potential of cit-PtNPs as a function of NP hydrodynamic diameter (d_{DLS}) in UPW at pH 7±0.1

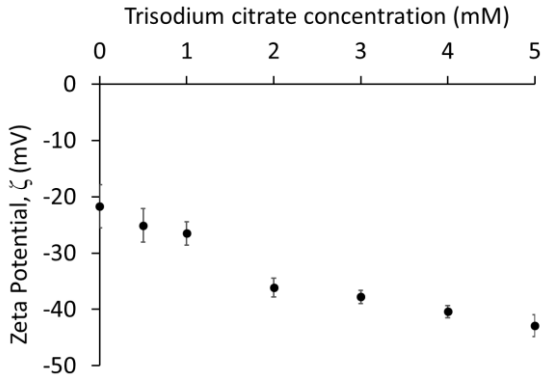

Figure B.5. Zeta potential of $PtNP_{20}$ (d_{DLS}= 10.0±0.3 nm) as a function of the concentration of added trisodium citrate to the synthesized cit-PtNPs.

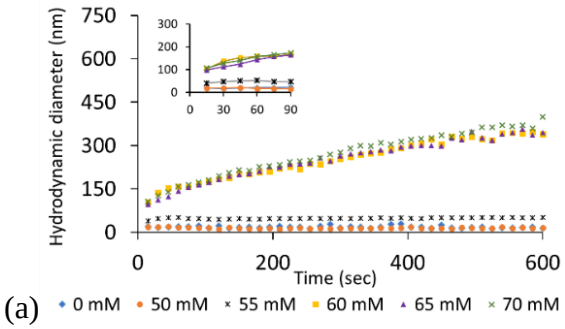
Hydrodynamic diameter (nm)
Time (sec)
0 mM
50 mM
55 mM
60 mM
65 mM
70 mM

(a)

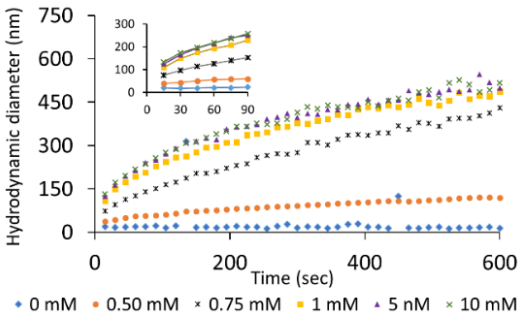
Hydrodynamic diameter (nm)
Time (sec)
0 mM
0.50 mM
0.75 mM
1 mM
5 nM
10 mM

(f)

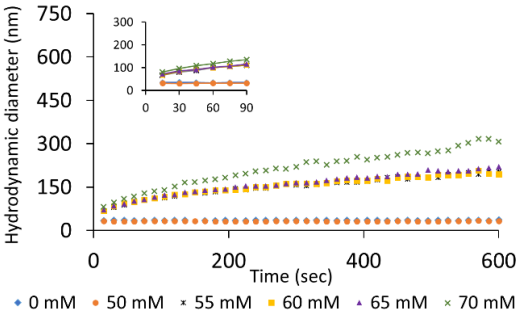
Hydrodynamic diameter (nm)
Time (sec)
0 mM
50 mM
55 mM
60 mM
65 mM
70 mM

(b)

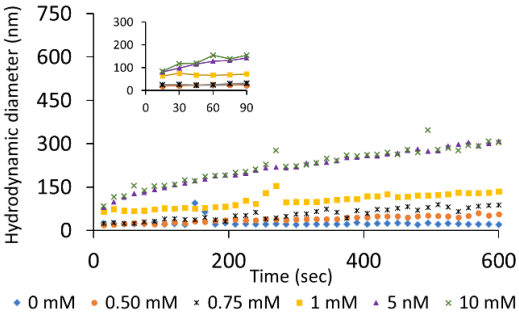
Hydrodynamic diameter (nm)
Time (sec)
0 mM
0.50 mM
0.75 mM
1 mM
5 nM
10 mM

(g)

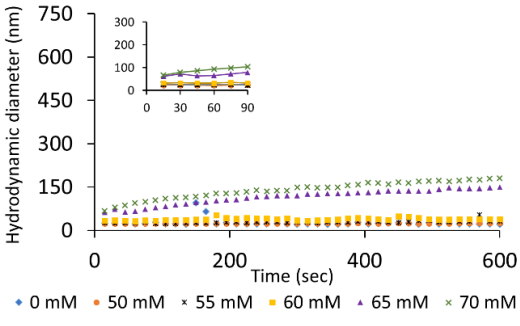
Hydrodynamic diameter (nm)
Time (sec)
0 mM
50 mM
55 mM
60 mM
65 mM
70 mM

(c)

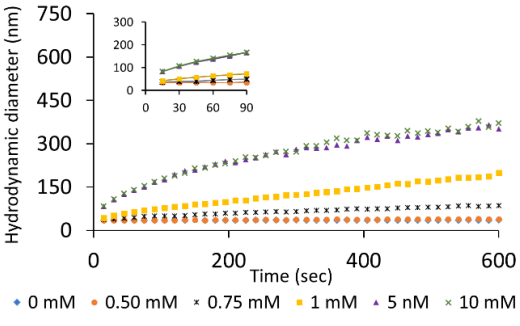
Hydrodynamic diameter (nm)
Time (sec)
0 mM
0.50 mM
0.75 mM
1 mM
5 nM
10 mM

(h)

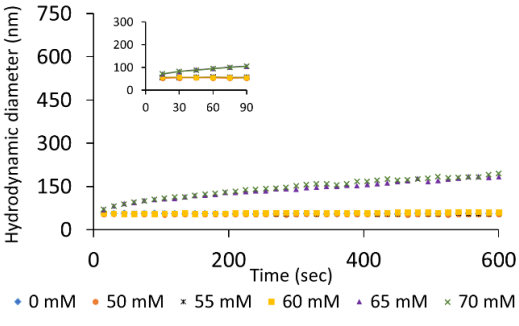
Hydrodynamic diameter (nm)
Time (sec)
0 mM
50 mM
55 mM
60 mM
65 mM
70 mM

(d)

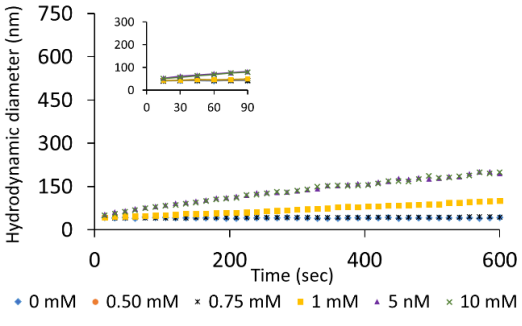
Hydrodynamic diameter (nm)
Time (sec)
0 mM
0.50 mM
0.75 mM
1 mM
5 nM
10 mM

(i)

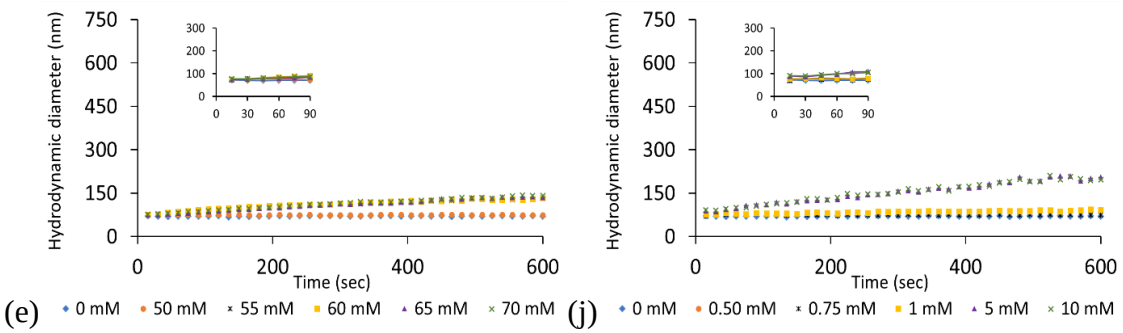

Figure B.6. The growth of the hydrodynamic diameter ($d_{DLS.}$) of cit- PtNPs (10 mg. L^{-1}) as a function of (a-e) $NaNO_3$ and (f-j) $Ca(NO_3)_2$ concentrations: (a,f) cit- $PtNP_{20}$ (d_{TEM}= 9.2 nm), (b,g) cit- $PtNP_{30}$ (d_{TEM}= 10.9 nm), (c,h) cit- $PtNP_{50}$ (d_{TEM}= 18.5 nm), (d,i) cit- $PtNP_{75}$ (d_{TEM}= 44.5 nm), and (e,j) cit- $PtNP_{95}$ (d_{TEM}= 72.5 nm)

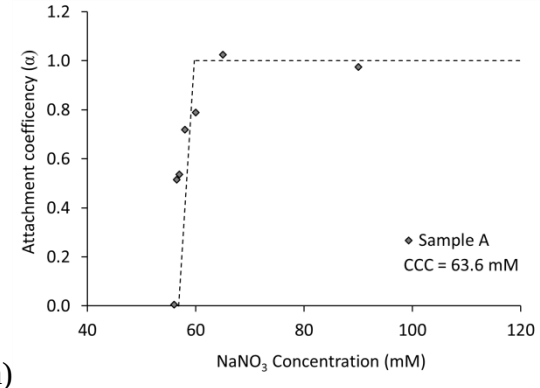
Attachment coefficency (α)
1.2
1.0
0.8
0.6
0.4
0.2
0.0
40
60
80
100
120
NaNO3 Concentration (mM)
Sample A
CCC = 63.6 mM

a)

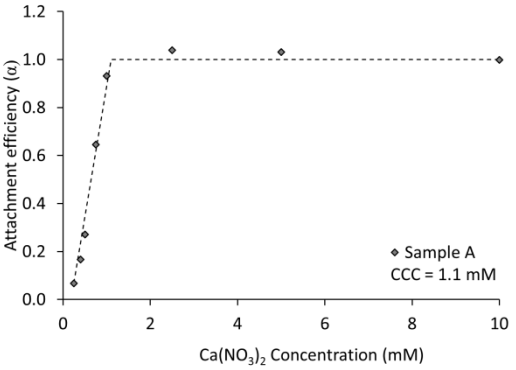
Attachment efficiency (α)
1.2
1.0
0.8
0.6
0.4
0.2
0.0
0
2
4
6
8
10
Ca(NO3)2 Concentration (mM)
Sample A
CCC = 1.1 mM

f)

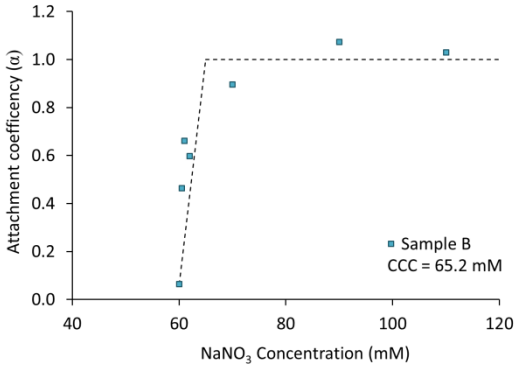
Attachment coefficency (α)
1.2
1.0
0.8
0.6
0.4
0.2
0.0
40
60
80
100
120
NaNO3 Concentration (mM)
Sample B
CCC = 65.2 mM

b)

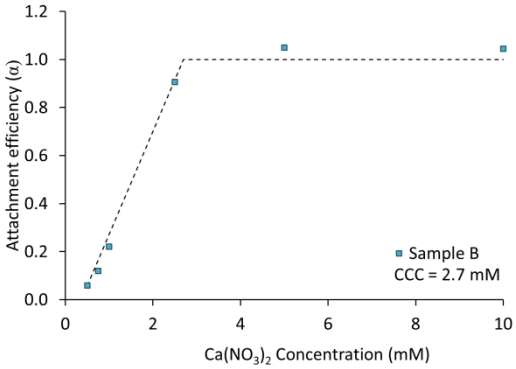
Attachment efficiency (α)
1.2
1.0
0.8
0.6
0.4
0.2
0.0
0
2
4
6
8
10
Ca(NO3)2 Concentration (mM)
Sample B
CCC = 2.7 mM

g)

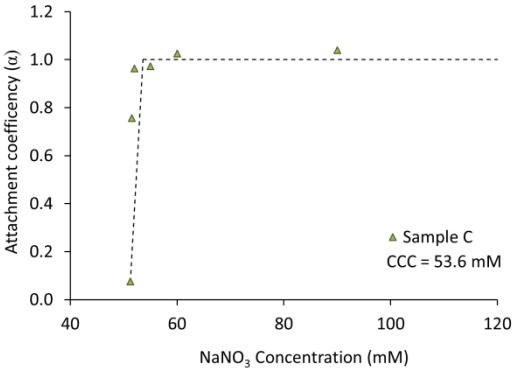
Attachment coefficency (α)
1.2
1.0
0.8
0.6
0.4
0.2
0.0
40
60
80
100
120
NaNO3 Concentration (mM)
Sample C
CCC = 53.6 mM

c)

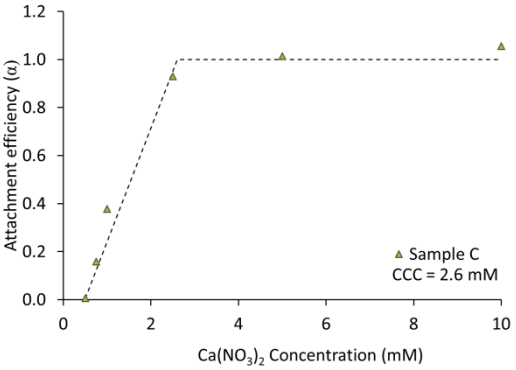
Attachment efficiency (α)
1.2
1.0
0.8
0.6
0.4
0.2
0.0
0
2
4
6
8
10
Ca(NO3)2 Concentration (mM)
Sample C
CCC = 2.6 mM

h)

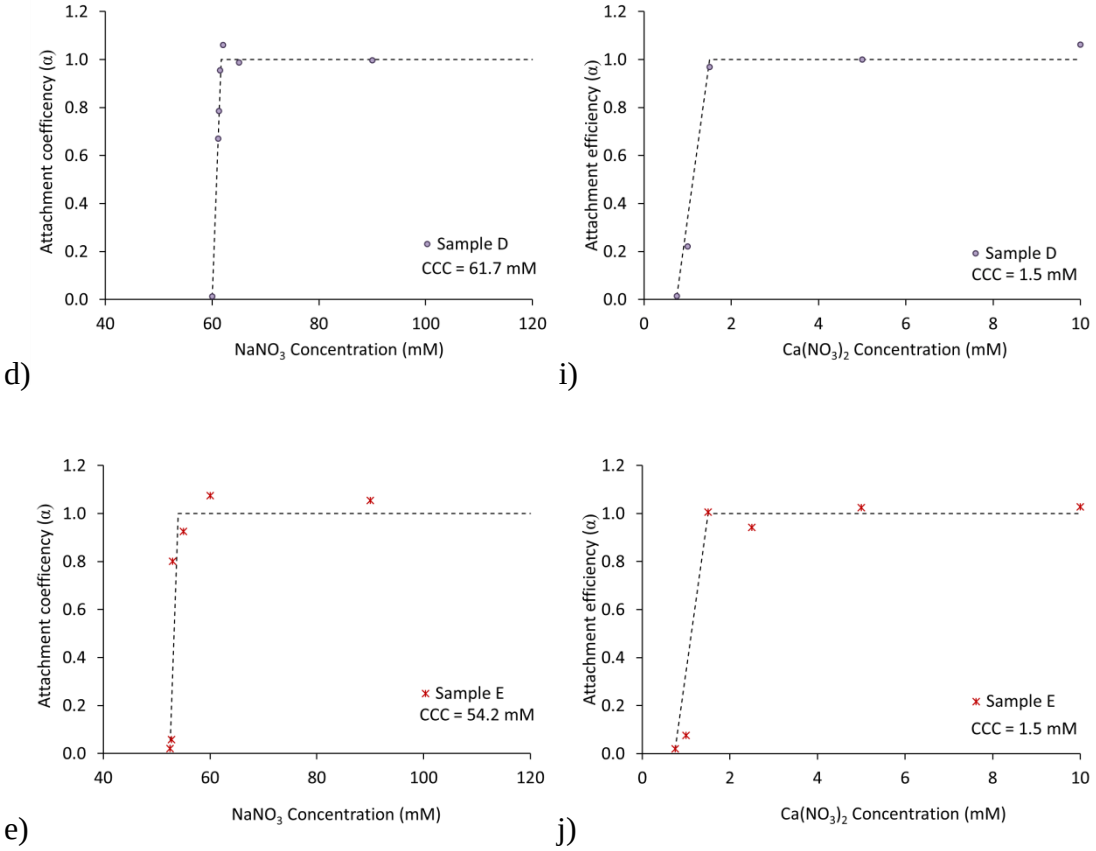

Figure B.7. Attachment efficiency (α) of the cit-PtNPs ($PtNP_{20}$- $PtNP_{95}$) as a function of (a-e) $NaNO_3$ concentrations, and (f-j) $Ca(NO_3)_2$ concentrations. PtNPs concentration was 7.5 mg. L^{-1} and pH was 7±0.1

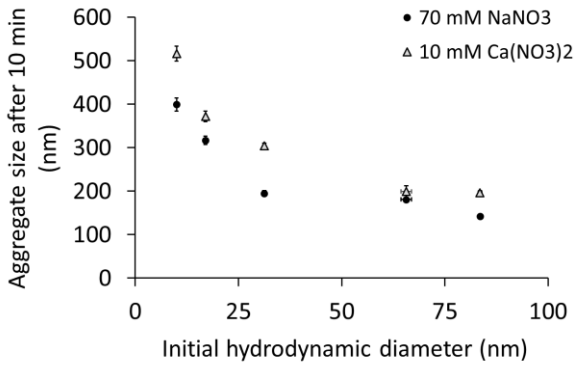

Figure B.8. Aggregate diameter of cit-PtNPs after 10 min of mixing with 70 mM $NaNO_3$ and 10 mM $Ca(NO_3)_2$ electrolyte as a function of initial particle diameter.

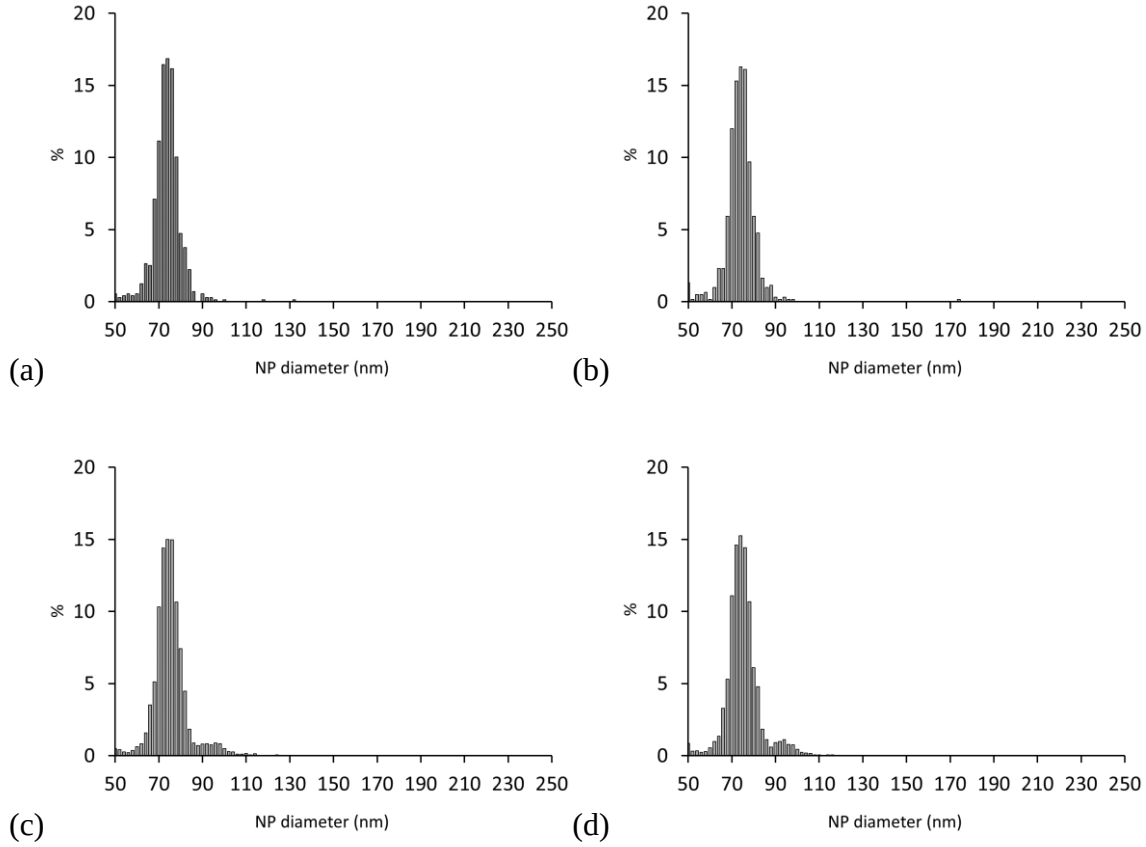

Figure B.9. Number particle size distribution measured by sp-ICP-MS of PVP-PtNPs immediately after mixing with (a) Ultrahigh pure water (UPW), (b) Dulbecco's modified Eagle's medium (DMEM), (c) Moderately hard water (MHW), and (d) 30 ppt synthetic seawater (SW) at 2000 µg. L^{-1} PVP-PtNPs concentration. Presence of smaller tailings (< 5%) in MHW and SW represents initial aggregation of PVP-PtNPs in high ionic strength media, even within 5 mins (required for sample preparation and analysis by sp-ICP-MS).

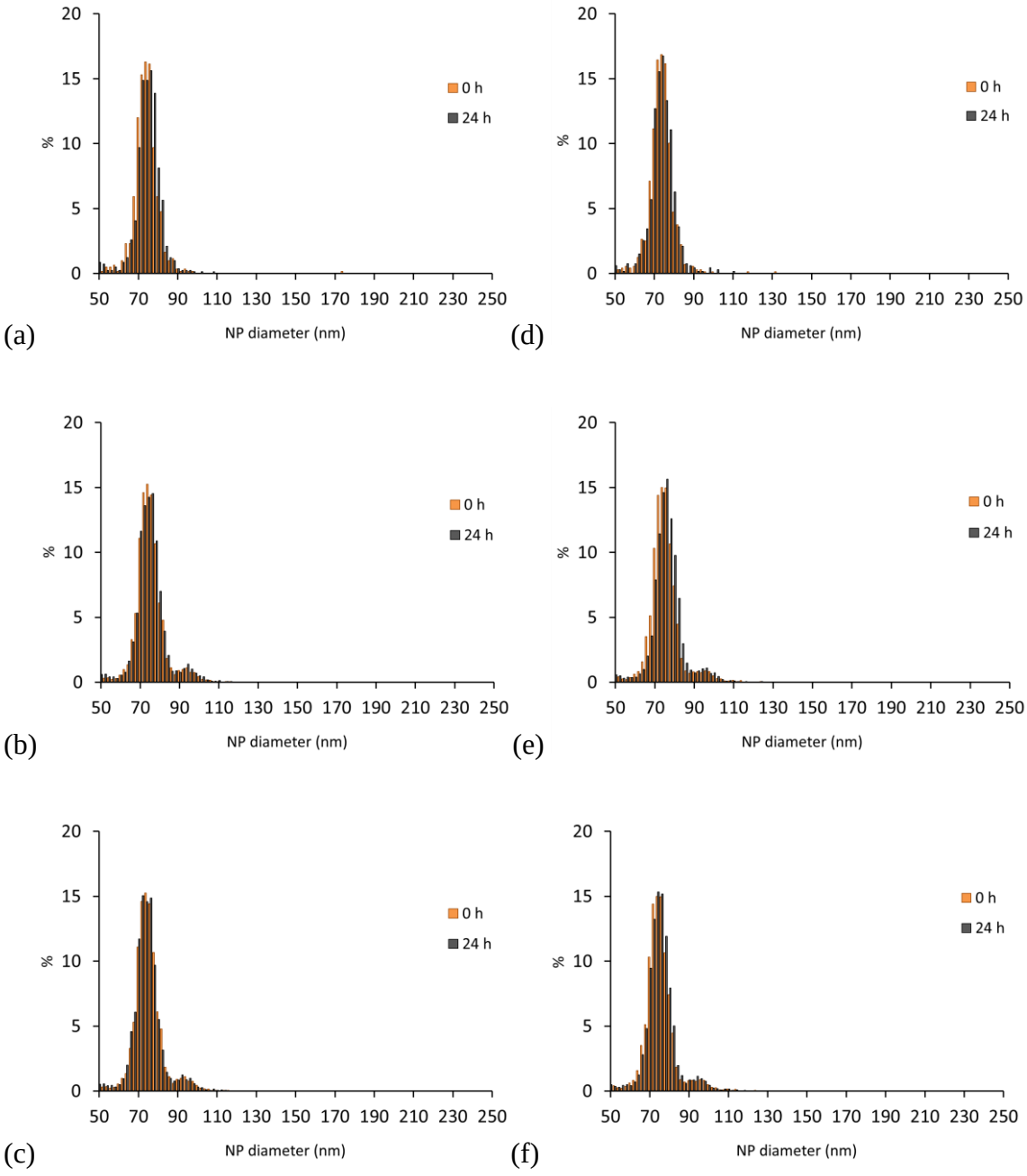

Figure B.10. Number particle size distribution measured by sp-ICP-MS of (a-c) PVP-PtNPs and (d-f) cit-PtNPs at 0 and 24 h after adding PtNPs to Dulbecco's modified Eagle's medium (DMEM) at PtNP concentrations of (a, d) 20 µg. L^{-1}, (b, e) 200 µg. L^{-1}, and (c, f) 2000 µg. L^{-1}.

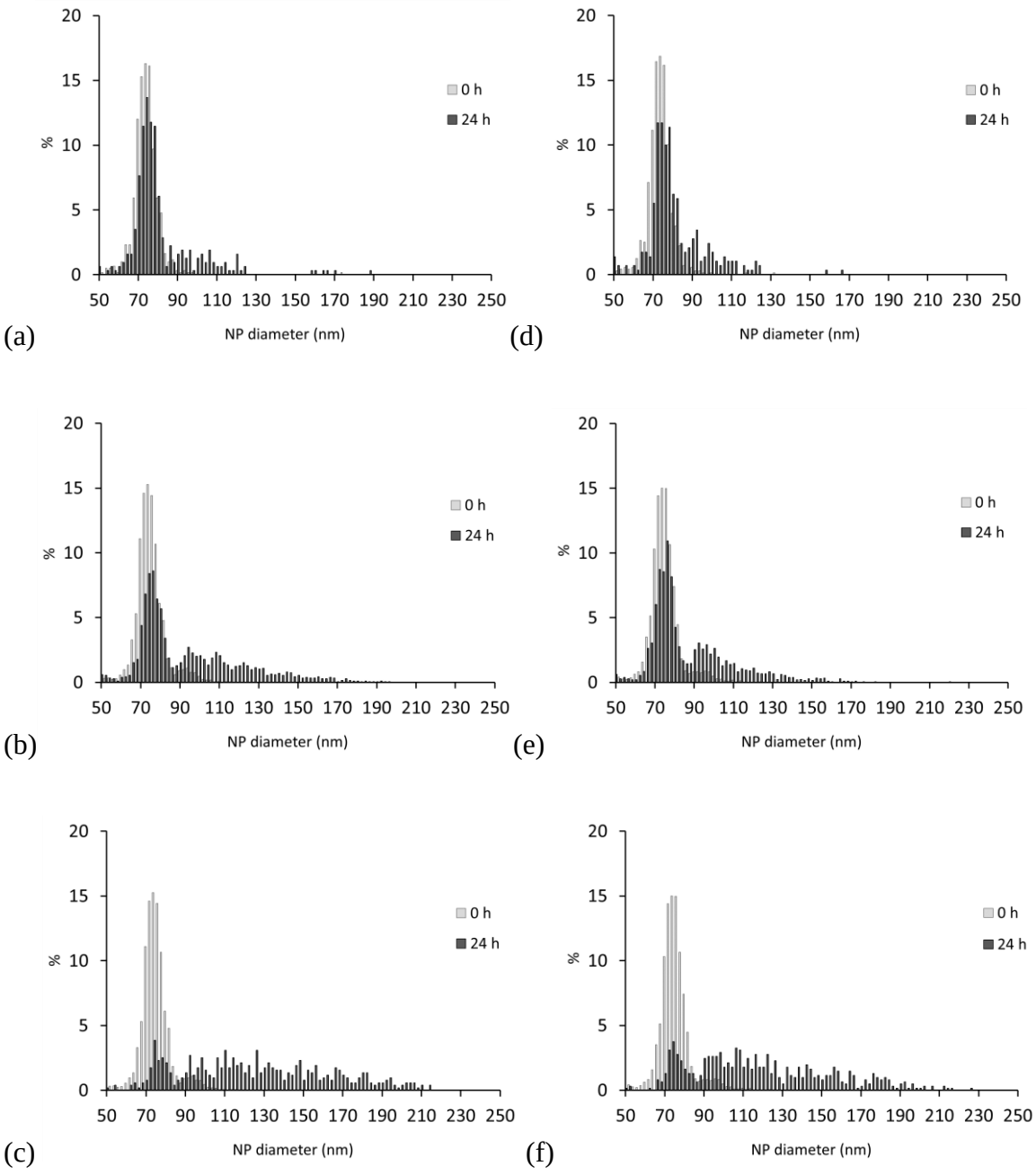

Figure B.11. Number particle size distribution measured by sp-ICP-MS of (a-c) PVP-PtNPs and (d-f) cit-PtNPs after 0 and 24 hours of adding PtNPs to Moderately hard water (MHW) at PtNP concentrations of (a, d) 20 µg. L^{-1}, (b, e) 200 µg. L^{-1}, and (c, f) 2000 µg. L^{-1}.

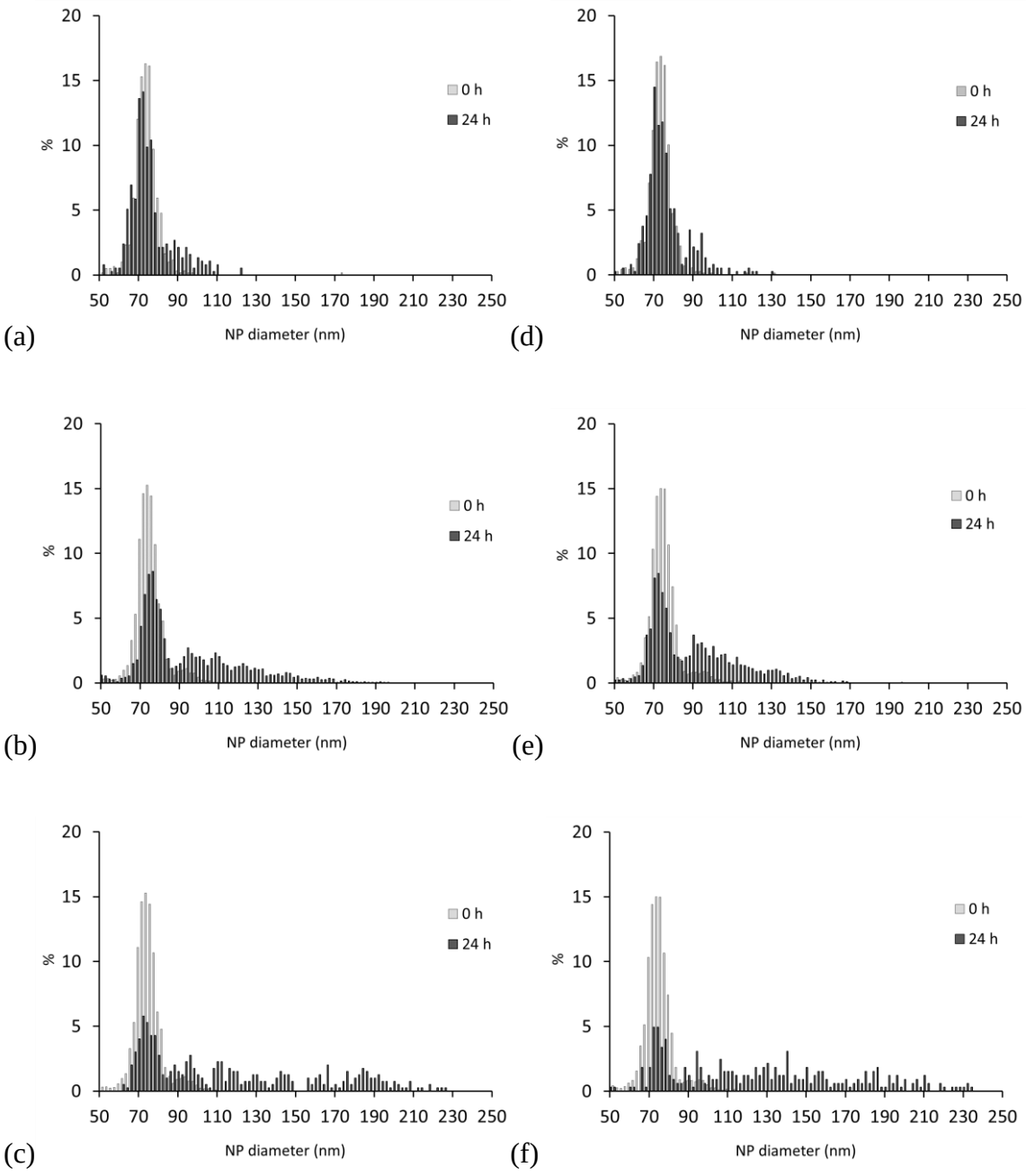

Figure B.12. Number particle size distribution measured by sp-ICP-MS of (a-c) PVP-PtNPs and (d-f) cit-PtNPs after 0 and 24 h of adding PtNPs to 30 ppt synthetic seawater (SW) at PtNP concentrations of (a, d) 20 µg. L^{-1}, (b, e) 200 µg. L^{-1}, and (c, f) 2000 µg. L^{-1}.

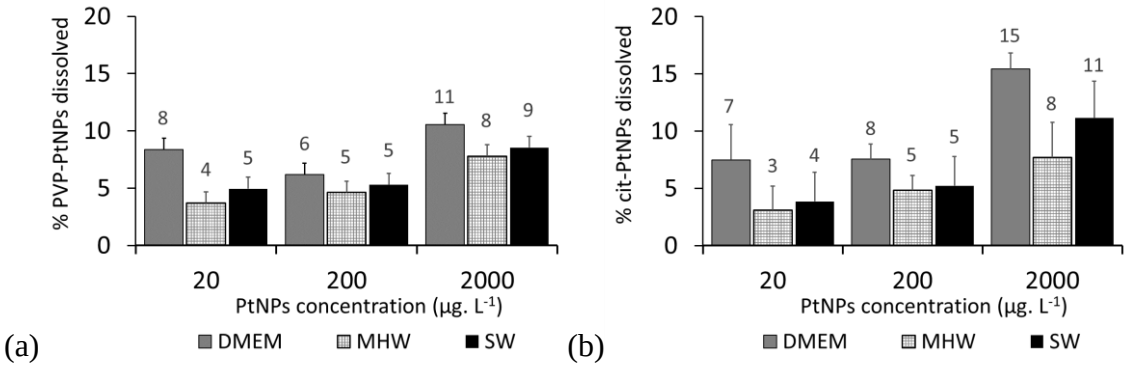

Figure B.13. Dissolved Pt in DMEM, MHW, and SW after 24 h of adding PtNPs to the media for (a) PVP-PtNPs and (b) cit-PtNPs. Dissolved Pt is expressed as % of total PtNPs concentration at 0 h.

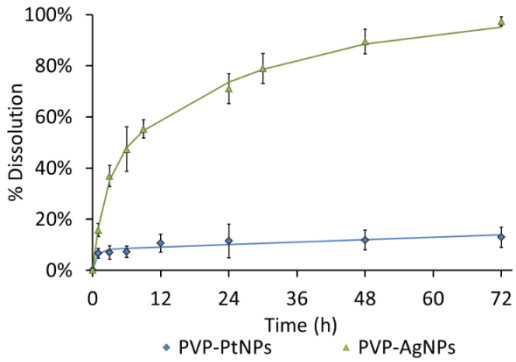

Figure B.14. Dissolution of 20 µg. L^{-1} PVP-PtNPs ($PtNP_{20}$, core size= 9.2 nm) and PVP-AgNPs (core size= 10.1 nm) in 30 ppt SW after 72 h

APPENDIX C: SUPPORTING INFORMATION FOR CHAPTER 4

C.1. Supporting figures

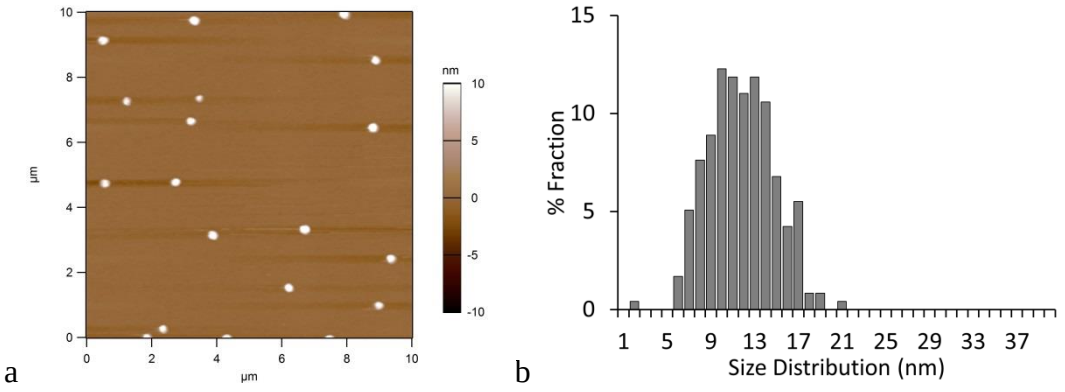

Figure C.1. a) Representative image, and b) particle size distribution (PSD) of synthesized PVP-AgNPs in UPW. Measured by Atomic force microscopy (Average size= 11.3 ± 3 nm, PDI= 0.26)

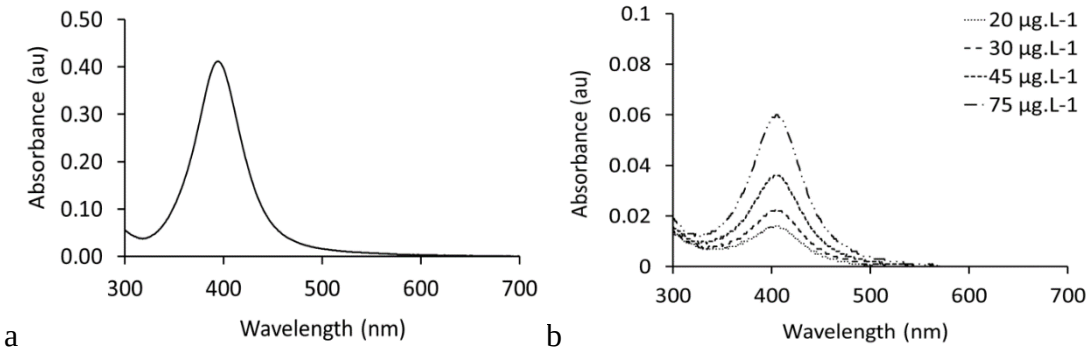

Figure C.2. UV-vis surface plasmon resonance (SPR) spectra of (a) stock PVP-AgNPs and (b) PVP-AgNPs in 30 ppt synthetic seawater (SW)

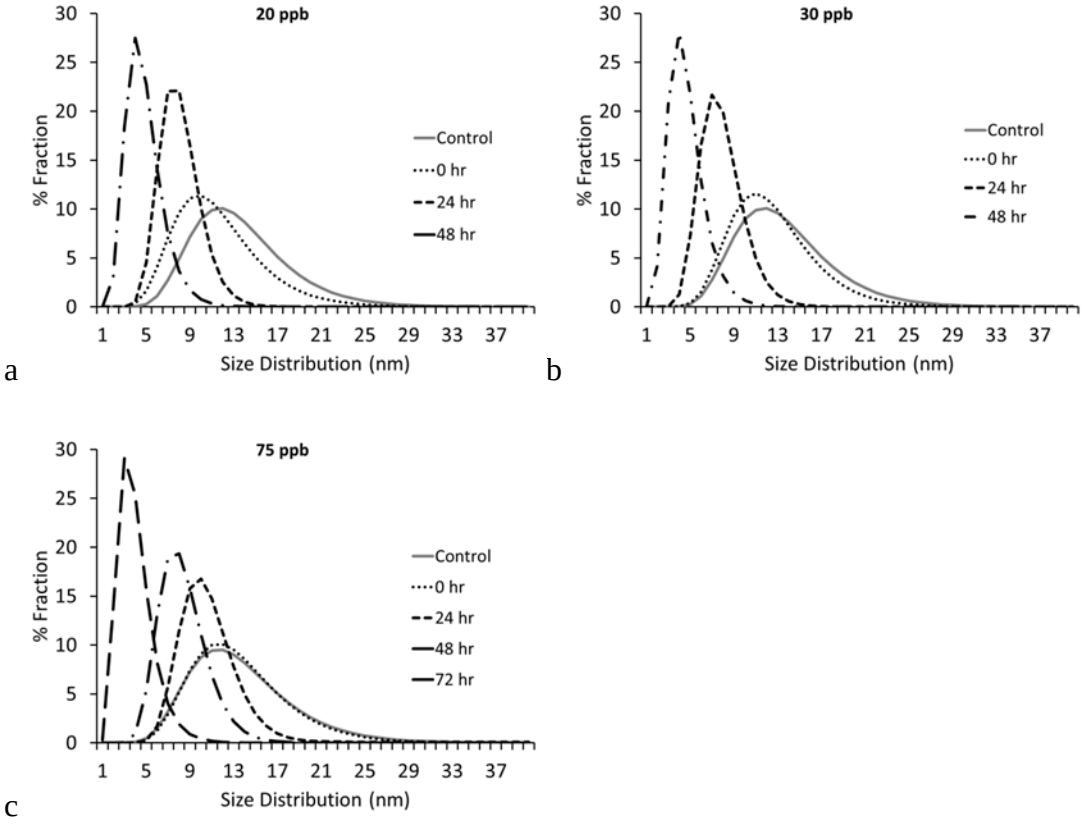

Figure C.3. Size evolution of NPs in SW after (a) 20 µg L^{-1}, (b) 30 µg L^{-1}, and (c) 75 µg L^{-1} PVP-AgNPs mixed in SW (measured by AFM)

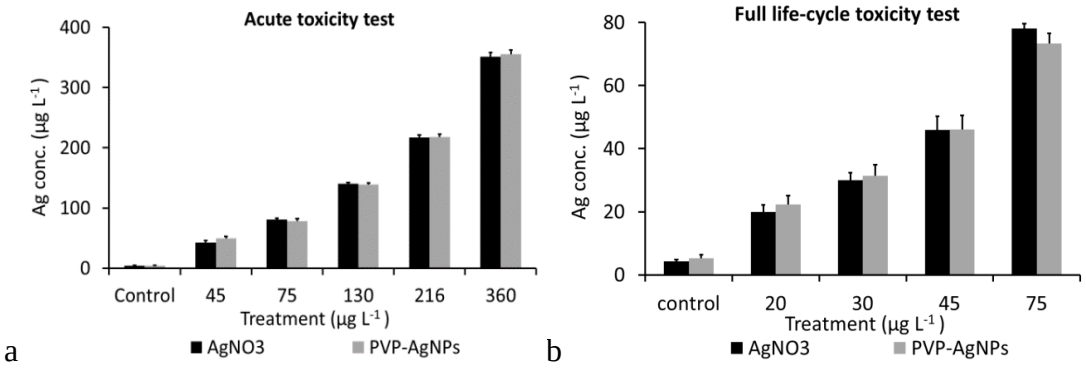

Figure C.4. Measured Ag concentration during (a) acute toxicity test and (b) life-cycle toxicity test

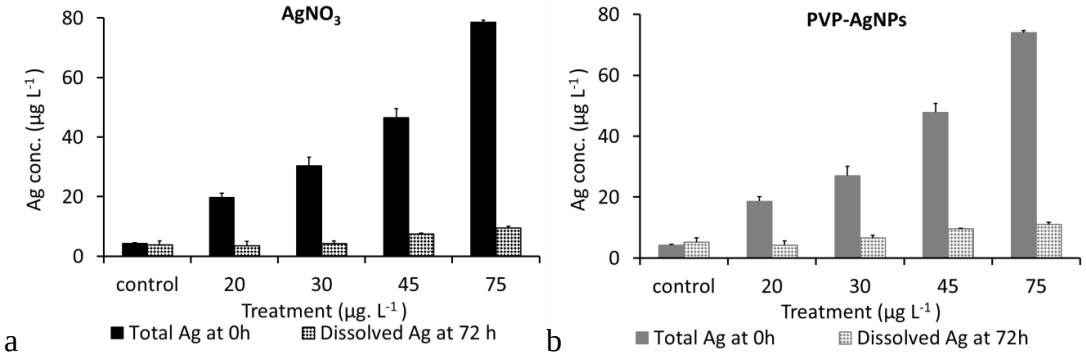

Figure C.5. Dissolved Ag concentration collected from microplates after 72 h as (a) $AgNO_3$ and (2) PVP-AgNPs were exposed to copepods during life-cycle bioassay.

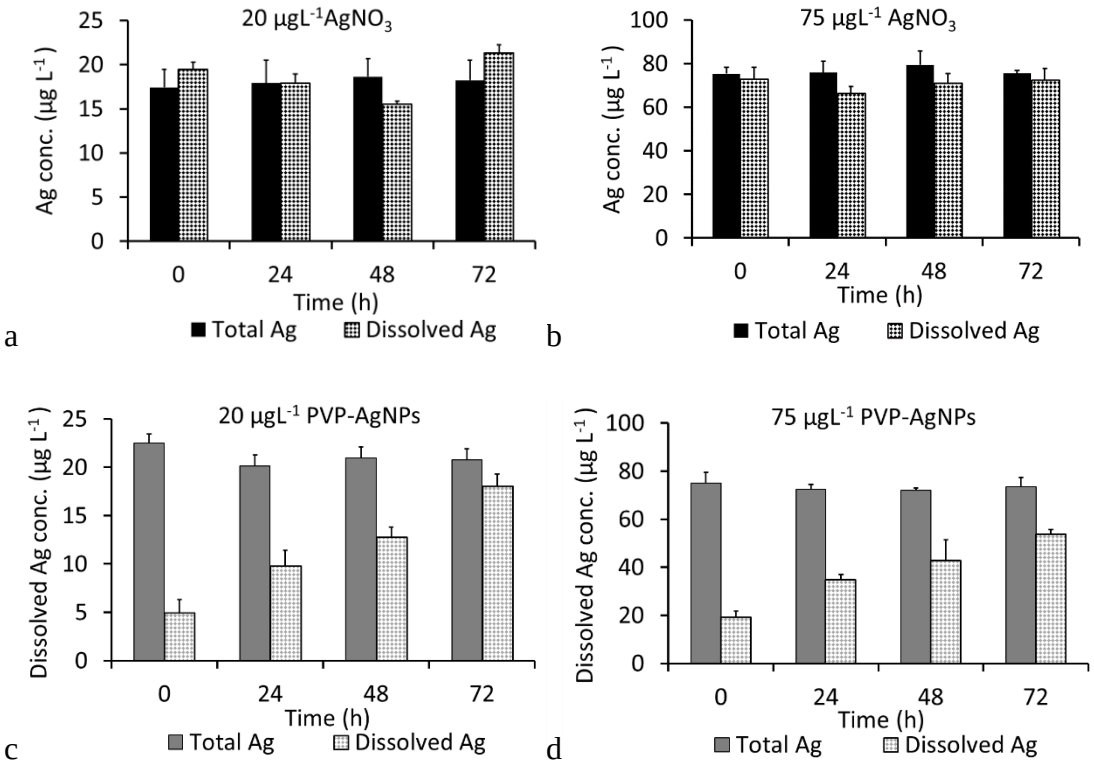

Figure C.6. Total Ag concentrations when (a,b) $AgNO_3$ and (c,d) PVP-AgNPs added and corresponding dissolved (< 3kDa) Ag collected from microplates at different time points

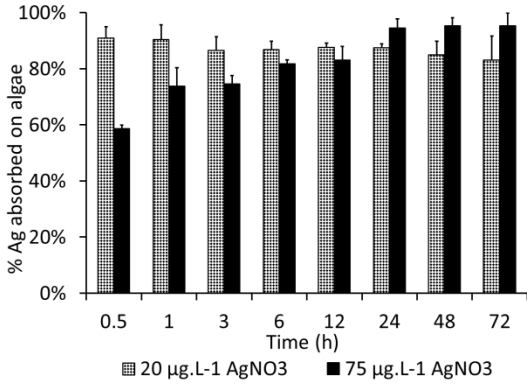

Figure C.7. % Ag absorbed on algae when 20 and 75 µg L^{-1} $AgNO_3$ added to SSW in presence of algae

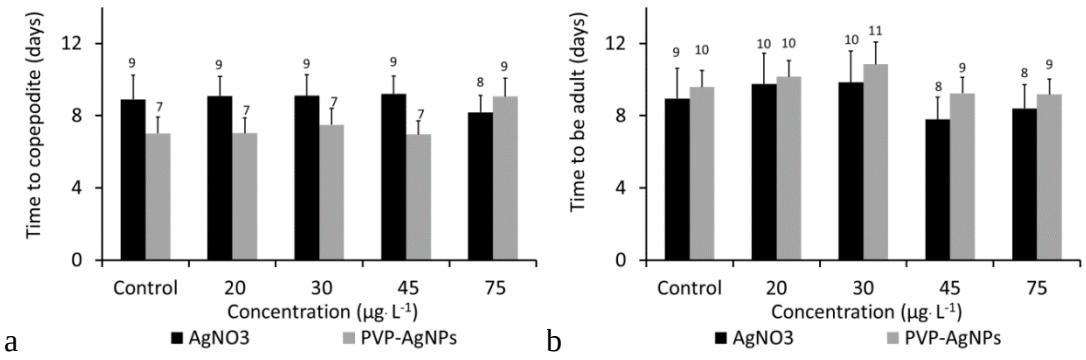

Figure C.8. (a) Time required for naupliar-to-copepodite stage and (b) time required for copepodite-to-adult stage in $AgNO_3$ and PVP-AgNPs exposures.

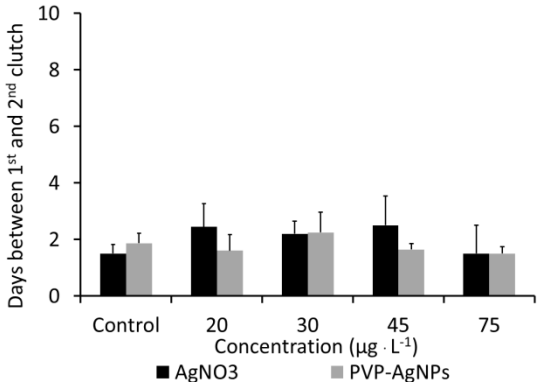

Figure C.9. Time required between two successive (1st and 2nd) naupliar broods by treatments

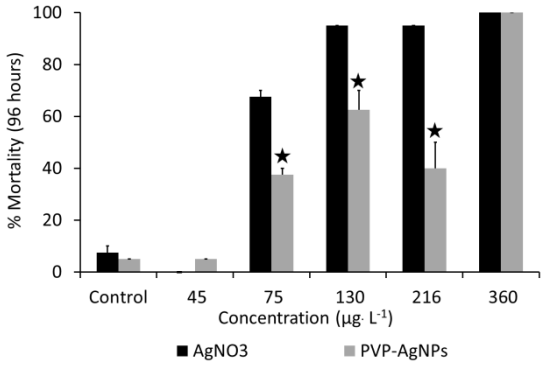

Figure C.10. Adult *A. tenuiremis* mortality in a 96-hour acute exposure to $AgNO_3$ and PVP-AgNPs (* indicates statistically significant difference between mean responses within a given Ag-treatment concentration; *p-value* < 0.05)

APPENDIX D: SUPPORTING INFORMATION FOR CHAPTER 5

D.1. Collection of water samples for NOM isolation

Water samples for natural organic matter (NOM) extraction were collected from four different environments including marshlands, seepage lake, blackwater river, and ocean (Table S1). Water samples were collected from marchlands at the air-water interface from three different sites in Everglades representing pristine, relatively pristine, and eutrophic environments. Oceanic water (Pacific Ocean; NOM 4) was collected at the Natural Energy Laboratory of Hawaii Authority (NELHA) on the island of Hawaii, USA (near Kailua-Kona). At NELHA, surface (5 m depth) oceanic waters were pumped continuously at a rate of more than 0.5 m^3 s^{-1} through high-density polyethylene (HDPE) distribution systems. Water was transferred from HDPE pipelines to the laboratory through polyvinylchloride (PVC) pipes that were flushed continuously for several days before and throughout the study. The temperatures of surface water at NELHA was 24 to 28.5 °C.

D.2. Solid phase extraction of natural organic matter (NOM)

The hydrophobic organic acid fraction (HPOA) was isolated from the six water samples according to procedure described in Aiken et al. (1992) under ambient atmosphere [279] and are labeled NOM 1 to 6 as summarized in **Table D.1**. The isolation procedure was consistent with recommendation of the International Humic Substances Society (IHSS) to isolate humic and fulvic acids. Samples were acidified to pH 2 with 12 N HCl and loaded

onto a pre-cleaned XAD-8 column. Chloride was removed from the HPOA fraction retained on the XAD-8 column by rinsing with high purity water until the conductivity of the effluent was < 700 µS cm^{-1}. The sample was back eluted off the resin with 0.1 M NaOH through a proton-saturated cation exchange resin (CER; Bio-Rad Laboratories) to remove sodium ions. Eluting the sample directly through a CER column minimized the contact time between the sample and the 0.1 M NaOH to minimize the possibility for oxidation of reduced organic sulfur species [339]. The pH of de-salted HPOA samples was approximately 3.3. HPOA samples were freeze dried at pH 3.3.

D.3. UV-vis optical measurement of NOM

Ultraviolet and visible light (UV-vis) absorption spectra were measured from 190 to 800 nm using spectrophotometer (Agilient Technologies, model 8453) and a 1cm quartz cuvette. Sample spectra were measured with respect to a blank's spectrum, containing ultra-high purity water (UHPW). The specific ultra-violate light absorbance (SUVA) at 254 nm ($SUVA_{254}$) of NOM samples, a proxy aromaticity [282], is defined as the decadic UV absorbance at 254 nm divided by the dissolved organic compound (DOC) concentration. Decadic absorbance values were converted to absorption coefficient as follows:

$$\alpha_\lambda = \frac{A_\lambda}{l} \quad \text{(Equation D.1)}$$

where, α_λ is the absorption coefficient (cm^{-1}), A_λ is the absorbance, and l is the path length (cm). The $SUVA_{254}$ values were calculated by dividing the decadic absorption coefficient at 254 nm (α_{254}) by DOC concentration and reported in units of L mg^{-1} m^{-1}. [282]

D.4. Supporting figures and tables

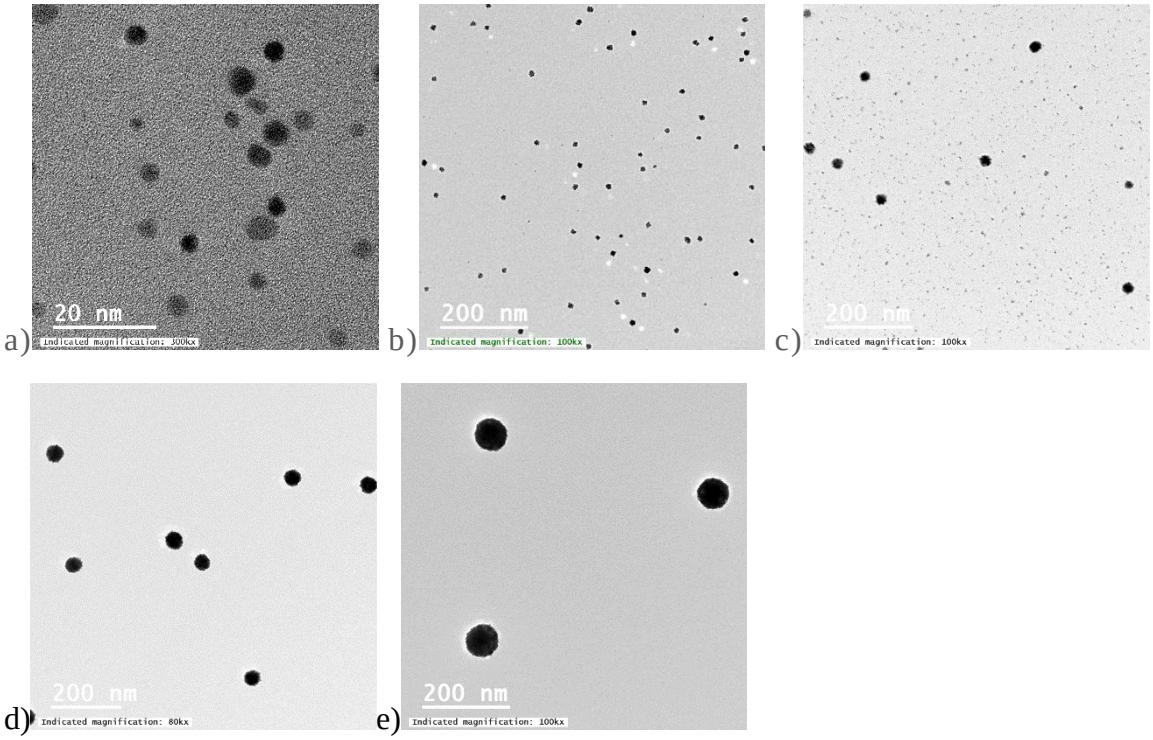

Figure D.1. (a-e) Typical transmission electron microscopy (TEM) micrographs of synthesized PVP-PtNPs ($PtNP_{20}$, $PtNP_{30}$, $PtNP_{50}$, $PtNP_{75}$, and $PtNP_{95}$ respectively) prepared by drop deposition method. Scale bar in TEM micrograph of NP_{20} (a) is 20 nm and in all the other TEM micrographs are 200 nm (b - e).

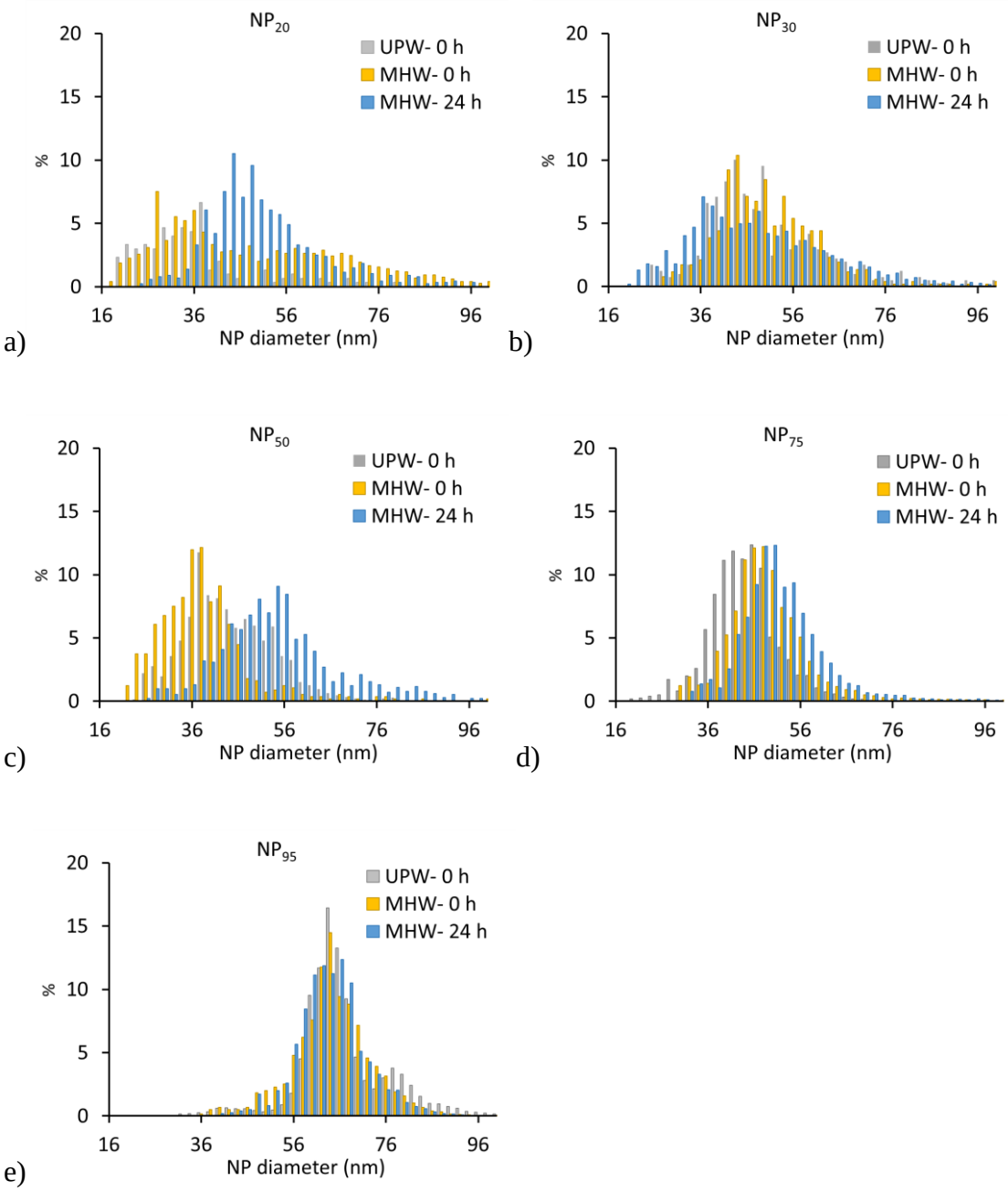

Figure D.2. Aggregation behavior of 1 µg L^{-1} (a) $PtNP_{20}$, (b) $PtNP_{30}$, (c) $PtNP_{50}$, (d) $PtNP_{75}$, and (e) $PtNP_{95}$ in synthetic moderately hard water (MHW) after 24 h.

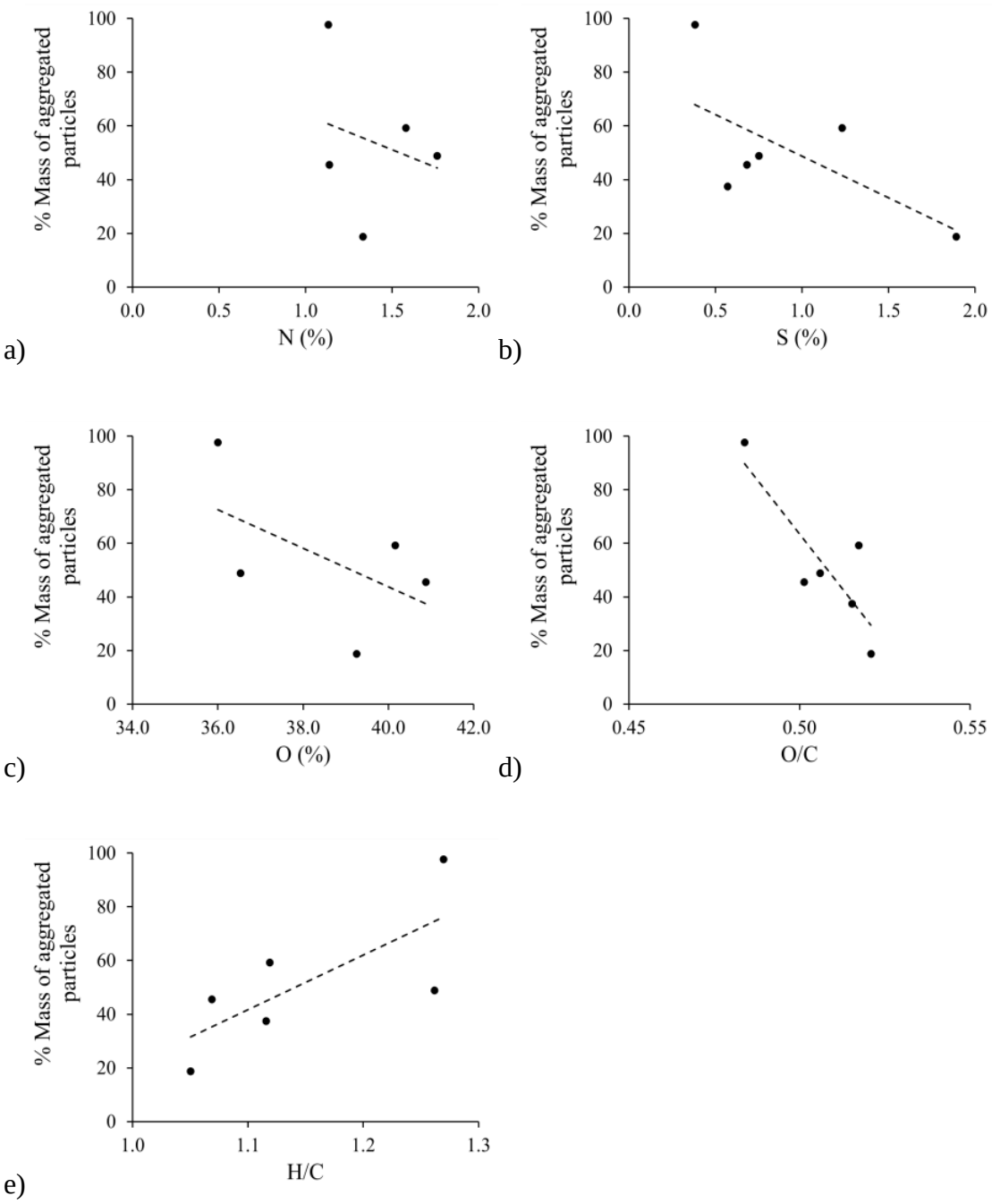

Figure D.3. Correlation between % mass of $PtNP_{20}$ undergoing aggregation and NOM elemental composition: (a) N, (b) S, (c) O/C, and (d) H/C ratio

Table D.1. Sampling site descriptions and chemical characteristics of NOM hydrophobic organic acid (HPOA) samples

NOM ID	Isolate	Sampling site description [a]	Weight % [b]						$SUVA_{254}$ ($L\ mg^{-1}\ m^{-1}$)
			C	H	O	N	S	Ash	
NOM 1	Florida Everglades F1 site HPOA	Eutrophic marshland located in Water conservation Area (WCA) 2A in the northern Everglades. Vegetation dominated by cattails	53.1	4.4	39.3	1.3	1.9	2.8	4.0
NOM 2	Florida Everglades 2B south HPOA	Relatively pristine marshland located in WCA 2B in the northern Everglades. Vegetation dominated by saw grass	52.2	4.8	40.2	1.6	1.2	7.3	3.2
NOM 3	Williams lake HPOA	Seepage lake in North-Central Minnesota. Organic matter dominated by autochthonous sources	55.2	5.7	36.5	1.8	0.8	2.1	1.9
NOM 4	Pacific Ocean HPOA	Sample collected at Natural Energy Laboratory of Hawaii Authority (NELHA) on the island of Hawaii, near Kailua-Kona, from 5 m depth. Organic matter of marine origin	56.5	6	36	1.1	0.4	1.7	0.8
NOM 5	Suwannee river HPOA	Blackwater river draining Okeefenokee Swamp. Sampled at Fargo, Georgia. Vegetation dominated by southern floodplain forest	51.8	4.4	42.7	0.8	0.5	4.8	4.8
NOM 6	Florida Everglades Loxahatchee National Wildlife refuge (LOX) HPOA	Pristine marshland in located in LOX 8 wildlife refuge area in the northern Everglades.	51	4.9	n.m.	n.m.	0.6	3.5	3.5

[a] Site description modified from Poulin et al (2017) [340]

[b] Measured by Huffman Hazen Laboratories (Golden, CO); major elemental composition (*i.e.* C, H, O, N, and S) reported as ash-free dry mass

n.m.= not measured

Table D.2. Relative number abundance of heteroatom classes of compounds determined by FT-ICR-MS

	Sampling site	CHO	CHON	CHOS	CHOP	CHNOS	CHONP	CHONSP	other
NOM 1	Everglades, Site F1, FL	66.1	16.6	7.5	0.4	5.1	3.2	0.3	0.8
NOM 2	Everglades, Site WCA-2BS, FL	61.8	25.6	5.0	0.8	2.9	3.2	0.2	0.5
NOM 3	Williams Lake, MN	65.0	23.4	4.0	4.1	1.9	0.9	0.5	0.2
NOM 4	Pacific Ocean near Hawaii, surface water (NELHA)	67.4	21.7	1.6	2.4	4.4	0.9	1.1	0.4
NOM 5	Suwannee River, GA	73.6	6.4	1.4	1.3	8.1	6.3	0.7	2.1
NOM 6	Everglades, LOX8, FL	68.5	21.0	2.1	1.8	3.9	2.1	0.2	0.4

Table D.3. Relative number abundance of geochemical classes of compounds determined by FT-ICR-MS

	Sampling site	Amino sugar	Carb	ConHC	Lignin	Lipid	Protein	Tannin	Unsat HC	Others
NOM 1	Everglades, Site F1, FL	0.8	0.8	24.5	59.0	0.9	2.3	9.8	0.7	1.2
NOM 2	Everglades, Site WCA-2BS, FL	1.1	0.6	19.9	63.4	0.8	3.3	9.4	0.4	1.0
NOM 3	Williams Lake, MN	1.5	0.4	6.6	72.4	1.9	8.0	8.5	0.3	0.4
NOM 4	Pacific Ocean near Hawaii, surface water (NELHA)	1.4	0.3	1.9	79.6	1.5	8.8	5.4	0.6	0.5
NOM 5	Suwannee River, GA	1.0	1.0	25.0	56.3	0.9	2.9	8.9	2.0	1.8
NOM 6	Everglades, LOX8, FL	0.9	0.7	20.3	62.3	0.9	3.3	10.3	0.6	0.5

*Carb: Carbohydrate
ConHC: Condensed hydrocarbon
Unsat HC: Unsaturated hydrocarbon

Table D.4. O/C, H/C and molecular weight (MW) of NOM isolates calculated as the number average of O/C, H/C, and MW of NOM formulae detected by FT-ICR-MS.

NOM ID	Sampling site	O/C	H/C	MW
NOM 1	Everglades, Site F1, FL	0.52	1.05	391
NOM 2	Everglades, Site WCA-2BS, FL	0.52	1.12	369
NOM 3	Williams Lake, MN	0.51	1.26	372
NOM 4	Pacific Ocean near Hawaii, surface water (NELHA)	0.48	1.27	442
NOM 5	Suwannee River, GA	0.50	1.07	375
NOM 6	Everglades, LOX8, FL	0.52	1.12	383

* ConHC: Condensed hydrocarbon
O/C: Oxygen-carbon ratio
H/C: Hydrogen -carbon ratio

Table D.5. Core size, hydrodynamic size, zeta potential, and pH of synthesized PVP-PtNPs reported as mean ± standard deviation

PVP-PtNPs suspension	Core size measured by TEM, $d_{TEM} \pm \sigma_d$ (nm)	Hydrodynamic size measured by DLS, $d_{DLS} \pm \sigma_d$ (nm)	Zeta potential (mV)	% PtNPs detectable by sp-ICP-MS (> 17 nm)	pH	Polydispersity index (PDI)
$PtNP_{20}$	9.2 ± 1.2	18.9 ± 0.3	-16.9 ± 3.5	0	7.0	0.36
$PtNP_{30}$	10.9 ± 0.8	31.4 ± 0.8	-19.3 ± 1.9	0	6.9	0.19
$PtNP_{50}$	18.5 ± 5.0	51.0 ± 0.7	-22.9 ± 1.4	46	7.1	0.20
$PtNP_{75}$	44.5 ± 2.7	74.7 ± 0.2	-25.1 ± 3.0	100	6.9	0.03
$PtNP_{95}$	72.5 ± 3.9	93.4 ± 1.0	-27.2 ± 1.7	100	6.8	0.10

σ_d is the standard deviation. The standard deviation for core size is that of the size distribution, whereas the standard deviation of hydrodynamic diameter and zeta potential is that of 3 replicates.

Table D.6. Zeta potential of 1 mg L^{-1} PVP-PtNPs at 0 and 24 hours after mixing with MHW. Zeta potential values are reported as mean ± standard deviation of three replicates.

PVP-PtNPs suspension	pH of PtNPs suspension in MHW	Zeta potential in UPW (mV)	Zeta potential in MHW (mV)	
			0 h	24 h
$PtNP_{20}$	8.1	-16.9 ± 3.5	-13.2 ± 0.8	-7.7 ± 0.8
$PtNP_{30}$	7.9	-19.3 ± 1.9	-14.7 ± 1.0	-9.4 ± 2.2
$PtNP_{50}$	8.0	-22.9 ± 1.4	-16.4 ± 1.1	-13.9 ± 0.6
$PtNP_{75}$	8.0	-25.1 ± 3.0	-19.3 ± 0.9	-17.9 ± 4.2
$PtNP_{95}$	8.1	-27.2 ± 1.7	-23.3 ± 0.8	-22.9 ± 1.4

Table D.7. Number concentration of 1 µg L^{-1} PtNPs ($PtNP_{20}$-$PtNP_{95}$) in MHW measured by single particle-inductively coupled plasma-mass spectrometer (sp-ICP-MS) and % of measured PtNPs by sp-ICP-MS relative to the theoretical number concentrations calculated from the measured mass concentration and respective NP diameter

		in UPW- 0 h			in MHW- 0 h			in MHW- 24 h		
Sample ID	Theoretical number conc. ($x10^6$ NP mL^{-1})	Mean size (nm)	Measured number conc. ($x10^6$ NP mL^{-1})	% measured relative to the theoretical conc.	Mean size (nm)	Measured number conc. ($x10^6$ NP mL^{-1})	% measured relative to the theoretical conc.	Mean size (nm)	Measured number conc. ($x10^6$ NP mL^{-1})	% measured relative to the theoretical conc.
$PtNP_{20}$	114.34	26±12	0.31	0.3	31±12	1.77	1.5	38±19	9.99	8.7
$PtNP_{30}$	68.75	30±13	0.83	1.2	31±11	1.05	1.5	48±15	9.09	13.2
$PtNP_{50}$	14.06	34±10	4.65	33.1	38±10	2.63	18.7	54±13	2.61	18.5
$PtNP_{75}$	1.01	44±8	1.09	108.1	59±9	0.50	49.6	62±9	0.44	43.2
$PtNP_{95}$	0.23	77±10	0.23	100.2	74±9	0.23	98.0	74±8	0.18	75.5

Table D.8. Mass based concentrations of 1 µg L^{-1} PtNPs ($PtNP_{20}$-$PtNP_{95}$) in MHW measured by sp-ICP-MS and % of detected PtNP mass by sp-ICP-MS relative to the nominal mass concentration (= 1 µg L^{-1}):

	in UPW- 0 h		in MHW- 0 h		in MHW- 24 h	
Sample ID	Pt conc. (µg L^{-1})	% measured relative to the nominal conc.	Pt conc. (µg L^{-1})	% measured relative to the nominal conc.	Pt conc. (µg L^{-1})	% measured relative to the nominal conc.
$PtNP_{20}$	0.017	1.7	0.209	20.9	0.583	58.3
$PtNP_{30}$	0.082	8.2	0.426	42.6	0.583	58.3
$PtNP_{50}$	0.313	31.3	0.290	29.0	0.046	4.60
$PtNP_{75}$	0.851	85.1	0.813	81.3	0.685	68.5
$PtNP_{95}$	0.824	82.4	0.706	70.6	0.373	37.3

Table D.9. Number concentration of 1 µg L^{-1} $PtNP_{20}$ suspended in UPW and in MHW in presence of 1 mg L^{-1} NOM at 0 and 24 hours post mixing and % of number of detected PtNPs to the theoretically calculated number concentrations. All analyses were performed using sp-ICP-MS.

Sample ID	Theoretical number conc. ($x10^6$ NP mL^{-1})[a]	at 0 h			after 24 h		
		Mean size (nm)	Measured number conc. ($x10^6$ NP mL^{-1})	% measured relative to the theoretical conc.	Mean size (nm)	Measured number conc. ($x10^6$ NP mL^{-1})	% measured relative to the theoretical conc.
in UPW (without NOM)	114.34	32±10	0.44	0.4	34±14	0.80	0.7
in MHW (without NOM)		31±16	0.52	0.5	42±10	15.89	13.9
NOM 1		54±24	0.32	0.3	53±14	12.73	11.1
NOM 2		42±16	0.48	0.4	66±21	22.46	19.6
NOM 3		53±20	0.34	0.3	56±14	17.92	15.7
NOM 4		47±21	0.66	0.6	74±34	58.89	51.5
NOM 5		46±20	0.55	0.5	53±13	19.79	17.3
NOM 6		52±18	0.50	0.4	56±14	14.89	13.0

[a] Theoretically calculated from the mass concentration and NP diameter

Table D.10. Mass concentration of 1 µg L^{-1} $PtNP_{20}$ suspended in UPW and in MHW in presence of 1 mg L^{-1} NOM at 0 and 24 hours post mixing and % measured PtNP mass relative to the actual concentration (= 1 µg L^{-1}). All analyses were performed using sp-ICP-MS.

Sample ID	at 0 h		after 24 h	
	Pt conc. measured by ICP-MS (µg L^{-1})	% measured to the actual conc.	Pt conc. measured by ICP-MS (µg L^{-1})	% measured to the actual conc.
in UPW (without NOM)	0.017	1.7	0.02	2
in MHW (without NOM)	0.033	3.3	0.308	30.8
NOM 1	0.016	1.6	0.188	18.8
NOM 2	0.016	1.6	0.593	59.3
NOM 3	0.019	1.9	0.489	48.9
NOM 4	0.034	3.4	0.978	97.8
NOM 5	0.024	2.4	0.456	45.6
NOM 6	0.02	2.0	0.375	37.5

Table D.11. Number based concentrations of 1 µg L^{-1} $PtNP_{95}$ suspended in UPW and in MHW in presence of 1 mg L^{-1} NOM and % achieved to the theoretically calculated number concentrations, immediately after mixing and after 24 h:

Sample ID	Expected number conc. ($x10^6$ NP mL^{-1})[a]	at 0 h			after 24 h		
		Mean size (nm)	Actual number conc. ($x10^6$ NP mL^{-1})[b]	% measured to the expected conc.	Mean size (nm)	Actual number conc. ($x10^6$ NP mL^{-1})[b]	% measured to the expected conc.
in UPW (without NOM)	0.23	76±10	0.24	102.2	72±10	0.19	82.2
in MHW (without NOM)		72±16	0.25	105.6	71±6	0.18	76.0
NOM 1		74±14	0.22	96.3	74±14	0.23	98.1
NOM 2		72±8	0.19	82.2	72±10	0.21	89.8
NOM 3		73±10	0.17	75.0	73±10	0.19	80.4
NOM 4		77±11	0.20	86.4	77±11	0.21	89.0
NOM 5		76±10	0.24	100.9	76±10	0.23	97.8
NOM 6		72±8	0.18	78.4	72±8	0.19	83.3

[a] Theoretically calculated from the mass concentration and NP diameter

[b] measured by sp-ICP-MS

Table D.12. Mass based concentrations of 1 µg L^{-1} $PtNP_{95}$ suspended in UPW and in MHW in presence of 1 mg L^{-1} NOM and % measured to the actual concentration (= 1 µg L^{-1}), immediately after mixing and after 24 h:

Sample ID	at 0 h		after 24 h	
	Pt conc. measured by ICP-MS (µg L^{-1})	% measured to the actual conc.	Pt conc. measured by ICP-MS (µg L^{-1})	% measured to the actual conc.
in UHPW (without NOM)	1.02	101.6	0.88	88.2
in MHW (without NOM)	1.03	103.1	0.84	84.4
NOM 1	0.88	88.2	0.9	90.3
NOM 2	0.91	91.4	0.96	95.7
NOM 3	0.71	71.5	0.84	83.5
NOM 4	0.83	83.2	0.92	92.1
NOM 5	1	100.3	1.01	100.7
NOM 6	0.77	76.8	0.86	85.5

Table D.13. Criteria applied for molecular assignment of formulae detected by FT-ICR-MS

	H/C	**O/C**
Tannin	0.5-1.25	0.6-0.95
Carbohydrates	1.5-2.0	0.7-1.0
Lipids	1.7-2.25	0-0.22
Lignin	0.75-1.5	0.2-0.6
Protein	1.5-2.0	0.2-0.5
Aminosugar	1.5-1.75	0.55-0.7
Condensed hydrocarbons	0.2-0.75	0-0.7

Table D.14. Chemical composition of moderately hard water (MHW)

Chemical constituent	Concentration (mM)
Sodium bicarbonate ($NaHCO_3$)	1.14
Calcium sulfate ($CaSO_4$)	0.44
Magnesium sulfate ($MgSO_4$)	0.50
Potassium chloride (KCl)	0.05

APPENDIX E: SUPPORTING INFORMATION FOR CHAPTER 6

E.1. Sulfur K-edge XANES spectroscopy

The sulfur speciation in NOM was investigated using sulfur XANES spectroscopy on the HPOA fractions of NOM using beamline 9-BM-B of the advanced Photon Source (APS) (Argonne National Laboratory). Spectra were collected on two International Humic Substances Society (IHSS) reference materials (Suwannee river humic acid II (SRHA; 2S101H), Elliot soil humic acid I (ESHA; 1S102H)) for comparison with spectra measured before at the advanced light source (ALS) (Lawrence Berkley National Laboratory) [341]. NOM samples and IHSS NOM reference materials were pressed as 5.5- and 2.4-mm pellets, respectively, under ambient atmosphere and mounted on sulfur-free carbon tape. At least 10 scans per sample and 5 scans per reference NOM were collected over 2440-2538 eV. The Si(111) crystal monochromator was calibrated with an NaS_2O_3 standard (E_0 = 2,472.02 eV) [342]. Harmonics were rejected by detuning the beam to 50% of its maximum intensity. Between scans, the samples were moved by 0.5 mm to examine previously unexposed material. Spectra were collected in fluorescence yield mode under a Helium (He) atmosphere using a Vortex ME4 detector. Using Athena software [343], scans were averaged, normalized to the absorption from 2515 to 2542.5 eV, and fit by Gaussian curve fitting (GCF) [341]. Atomic fractions of sulfur functionalities, including exocyclic reduced sulfur (S_{Exo}), heterocyclic reduced (S_{Hetero}), sulfoxide (S_{sulfx}), sulfone (S_{SO_2}), sulfonate

(S_{SO_3}), and organosulfate (S_{SO_4}), were calculated with a precision estimated at ≤ 1.6% [341]. Accuracies of atomic fractions of reduced (S_{Exo} and S_{Hetero})and oxidized sulfur functionalities (S_{SO_2}, S_{SO_3}, S_{SO_4}) are estimated at 8% and 4%, respectively [341]. Concentrations of sulfur functionalities relative to carbon were calculated by multiplying the fraction of each sulfur functionality by the atomic S/C. Total reduced (S_{red}) and oxidized sulfur (S_{ox}) were defined as

$$S_{red} = S_{Exo} + S_{Hetero} \quad \text{(Equation E.1)}$$

$$S_{ox} = S_{SO_2} + S_{SO_3} + S_{SO_4} \quad \text{(Equation E.2)}$$

E.2. Gaussian Curve Fitting Spectra

Spectra were fit according to the approach of Manceau and Nagy (2012)6 with two arctangent and six Gaussian functions

$$2A + \sum_{i=1}^{6} G_i \quad \text{(Equation E.3)}$$

Where, A are arctangent functions andGi are Gaussian functions representing exocyclic reduced (S_{Exo}), heterocyclic reduced (S_{Hetero}), sulfoxide (S_{Sulfx}), sulfone (S_{SO_2}), sulfonate (S_{SO_3}), and organosulfate (S_{SO_4}) functionalities. The initial and final positions of arctangent functions, representing the step functions for the continuum of low (S_{Exo} , S_{Hetero} , S_{Sulfx}) and high oxidation state species (S_{SO_2} , S_{SO_3} ,S_{SO_4}), were less than the positions of sulfoxide and the organosulfate Gaussian functions, respectively. Arctangent function positions were fit and widths were co-varied. The nominal energy value was fit for the S_{Exo} Gaussian function, and was fixed for the other five Gaussian functions to previously recommended values within ±0.1 eV [341]. In certain cases, the nominal energies of S_{Sulfx} and S_{SO_2} Gaussian functions deviated from suggested values. For sample spectra, two different widths of

Gaussian functions were used for low (S_{Exo} , S_{Hetero} , S_{Sulfx}) and high oxidation state species (S_{SO_2} , S_{SO_3} , S_{SO_4}), which were co-varied during fitting. For IHSS reference materials, a single width of Gaussian functions was used for Suwannee River humic acid II (SRHA), whereas two widths were used for Elliott Soil humic acid (ESHA) [341]. The quality of fit was evaluated with the normalized sum-squared (NSS) residual:

$$NSS = \frac{\sum(y_{exp} - y_{fit})^2}{\sum y_{exp}^2} \quad \text{(Equation E.4)}$$

Where y_{exp} and y fit are experiment and fit values, respectively. Areas of Gaussian functions were corrected for the change in X-ray absorption cross-section with increasing oxidation state using:

$$y = 0.36481x - 909. \quad \text{(Equation E.5)}$$

where x is the energy of the absorption maximum of a Gaussian function and y is the scaling factor [341].The contribution of each sulfur functionality to total sulfur was calculated by dividing the peak area by the summation of all peak areas. The precision of atomic fractions from Gaussian curve fitting are estimated as follows: S_{Exo} = 1.6 ± 0.2%, S_{Hetero} = 0.5 ± 0.2%, S_{Sulfx}= 0.1 ± 0.0%, S_{SO_2} = 0.3 ± 0.1%, S_{SO_3} = 1.1 ± 0.2%, and S_{SO_4} = 0.7 ± 0.3% [341]. The concentration of each sulfur functionality relative to carbon was calculated by multiplying the percent of each sulfur functionality by the atomic S/C.

E.3. Supporting figures and tables

Table E.1. Chemical composition of moderately hard water (MHW)

Chemical constituent	Concentration (mg L^{-1})
Sodium bicarbonate ($NaHCO_3$)	96
Calcium sulfate ($CaSO_4$)	60
Magnesium sulfate ($MgSO_4$)	60
Potassium chloride (KCl)	4

Table E.2. Core size, hydrodynamic diameter, zeta potential, and pH of synthesized PVP-PtNPs

PVP-PtNPs suspension	Hydrodynamic size measured by DLS, $d_{DLS} \pm \sigma_d$ (nm)	Core size measured by TEM, $d_{TEM} \pm \sigma_d$ (nm)	Zeta potential (mV)	pH	Polydispersity index (PDI)
$PtNP_{20}$	18.9 ± 0.3	9.2 ± 1.2	-16.9 ± 3.5	7	0.36
$PtNP_{30}$	31.4 ± 0.8	10.9 ± 0.8	-19.3 ± 1.9	6.9	0.19
$PtNP_{50}$	51 ± 0.7	18.5 ± 5	-22.9 ± 1.4	7.1	0.2
$PtNP_{75}$	74.7 ± 0.2	44.5 ± 2.7	-25.1 ± 3	6.9	0.03
$PtNP_{95}$	93.4 ± 1	72.5 ± 3.9	-27.2 ± 1.7	6.8	0.1

Table E.3. Change in zeta potential after 24 h exposure of 1 mg L^{-1} PVP-PtNPs in MHW

PVP-PtNPs suspension	pH of PtNPs suspension in MHW	Zeta potential in MHW (mV)	
		0 h	24 h
$PtNP_{20}$	8.08	-13.2 ± 0.8	-7.7 ± 0.8
$PtNP_{30}$	7.89	-14.7 ± 1	-9.41 ± 2.2
$PtNP_{50}$	7.95	-16.4 ± 1.1	-13.9 ± 0.6
$PtNP_{75}$	7.97	-19.3 ± 0.9	-17.9 ± 4.2
$PtNP_{95}$	8.05	-23.3 ± 0.8	-22.9 ± 1.4

Table E.4. Sampling site descriptions and chemical characteristics of NOM hydrophobic organic acid (HPOA) isolates

NOM ID	Isolate	Sampling site description [a]	Weight % [b]						$SUVA_{254}$ ($L\ mg^{-1}\ m^{-1}$)
			C	H	O	N	S	Ash	
NOM 1	Florida Everglades F1 site HPOA	Eutrophic marshland located in Water conservation Area (WCA) 2A in the northern Everglades. Vegetation dominated by cattails	53.1	4.4	39.3	1.3	1.9	2.8	4.0
NOM 2	Florida Everglades 2B south HPOA	Relatively pristine marshland located in WCA 2B in the northern Everglades. Vegetation dominated by saw grass	52.2	4.8	40.2	1.6	1.2	7.3	3.2
NOM 3	Williams lake HPOA	Seepage lake in North-Central Minnesota. Organic matter dominated by autochthonous sources	55.2	5.7	36.5	1.8	0.8	2.1	1.9
NOM 4	Pacific Ocean HPOA	Sample collected at Natural Energy Laboratory of Hawaii Authority (NELHA) on the island of Hawaii, near Kailua-Kona, from 5 m depth. Organic matter of marine origin	56.5	6	36	1.1	0.4	1.7	0.8
NOM 5	Suwannee river HPOA	Blackwater river draining Okeefenokee Swamp. Sampled at Fargo, Georgia. Vegetation dominated by southern floodplain forest	51.8	4.4	42.7	0.8	0.5	4.8	4.8
NOM 6	Florida Everglades Loxahatchee National Wildlife refuge (LOX) HPOA	Pristine marshland in located in LOX 8 wildlife refuge area in the northern Everglades.	51	4.9	n.m.	n.m.	0.6	3.5	3.5

[a] Site description modified from Poulin et al (2017) [340]

[b] Measured by Huffman Hazen Laboratories (Golden, CO); major elemental composition (*i.e.* C, H, O, N, and S) reported as ash-free dry mass

n.m.= not measured

Table E.5. Concentration of different organic sulfur functionalities in NOM samples measured by sulfur k-edge XANES and concurrent $PtNP_{95}$ influx rate constant

Sample	$PtNP_{95}$ influx rate constant, k_{uw} ($L\ g^{-1}\ d^{-1}$)	Concentration of sulfur functionalities (Atomic S/C $x10^3$)					
		Exocyclic reduced sulfur (S_{Exo})	Heterocyclic reduced sulfur (S_{Hetero})	Sulfoxide (S_{Sulfx})	Sulfone (S_{SO_2})	Sulfonate (S_{SO_3})	Sulfate (S_{SO_4})
NOM 1	0.48±0.04	5.7	4.7	0.8	0.3	1.4	0.5
NOM 2	0.28±0.05	2.9	2.6	0.5	0.3	1.9	0.7
NOM 3	0.17±0.04	1.9	1.3	0.3	0.2	0.9	0.5
NOM 4	0.08±0.05	0.4	0.3	0.1	0.2	0.9	0.6
NOM 5	0.12±0.05	1.0	1.1	0.2	0.1	0.7	0.2
NOM 6	0.14±0.05	1.4	1.3	0.2	0.2	0.9	0.3

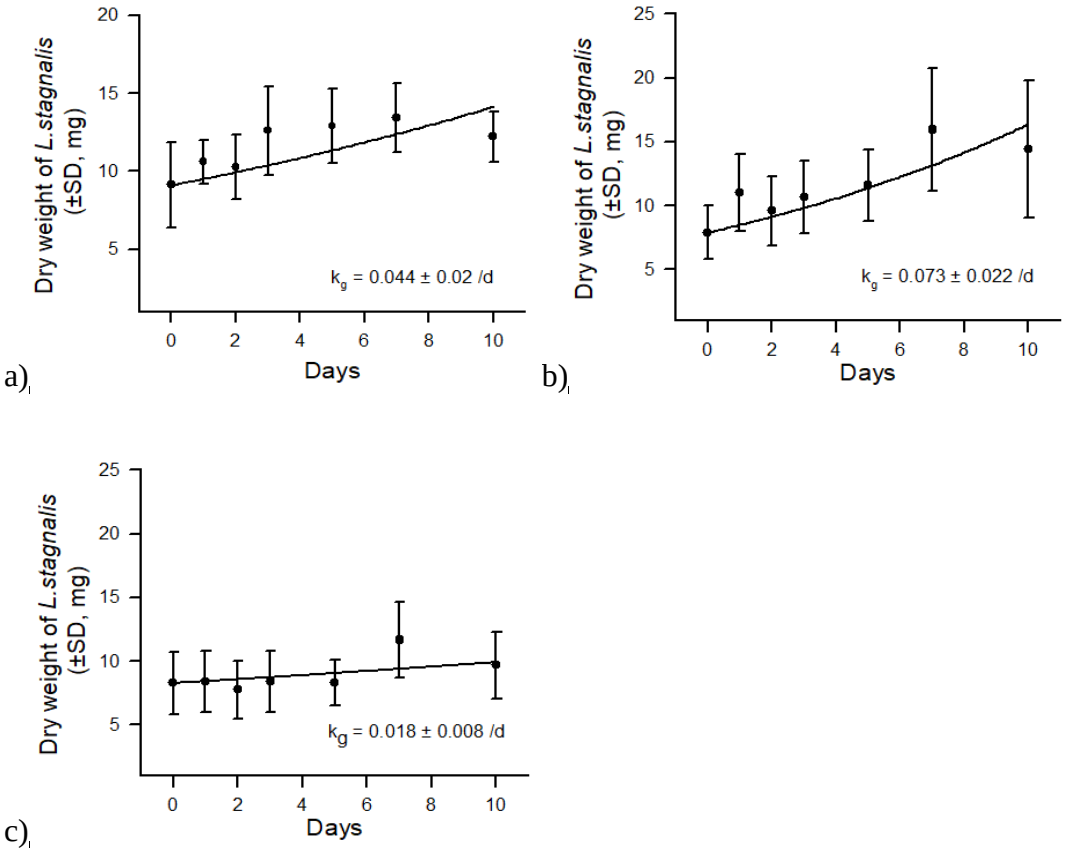

Figure E.1. Snail's dry weight during Pt elimination experimentfollowing exposure to (a) dissolved Pt, (b) $PtNP_{20}$, and (c) $PtNP_{95}$. The solid line represents growth as predicted by equation 4. Each point represents mean Pt concentration for 8 individual snails (±SD).

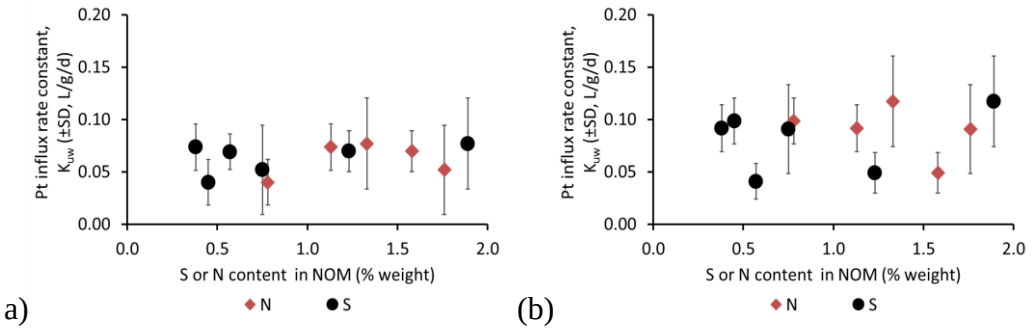

Figure E.2. Correlation between NOM Sulfur (S) and nitrogen (N) content and Pt influx rate constant, k_{uw} (L g^{-1} d^{-1}, ±SD) in *L.stagnalis* after waterborne exposure to 1 µg L^{-1} (a) dissolved Pt (added as H_2PtCl_6), and (b) $PtNP_{20}$ for 24 h. Each point represents mean Pt concentration for 8 individual snails (±SD).

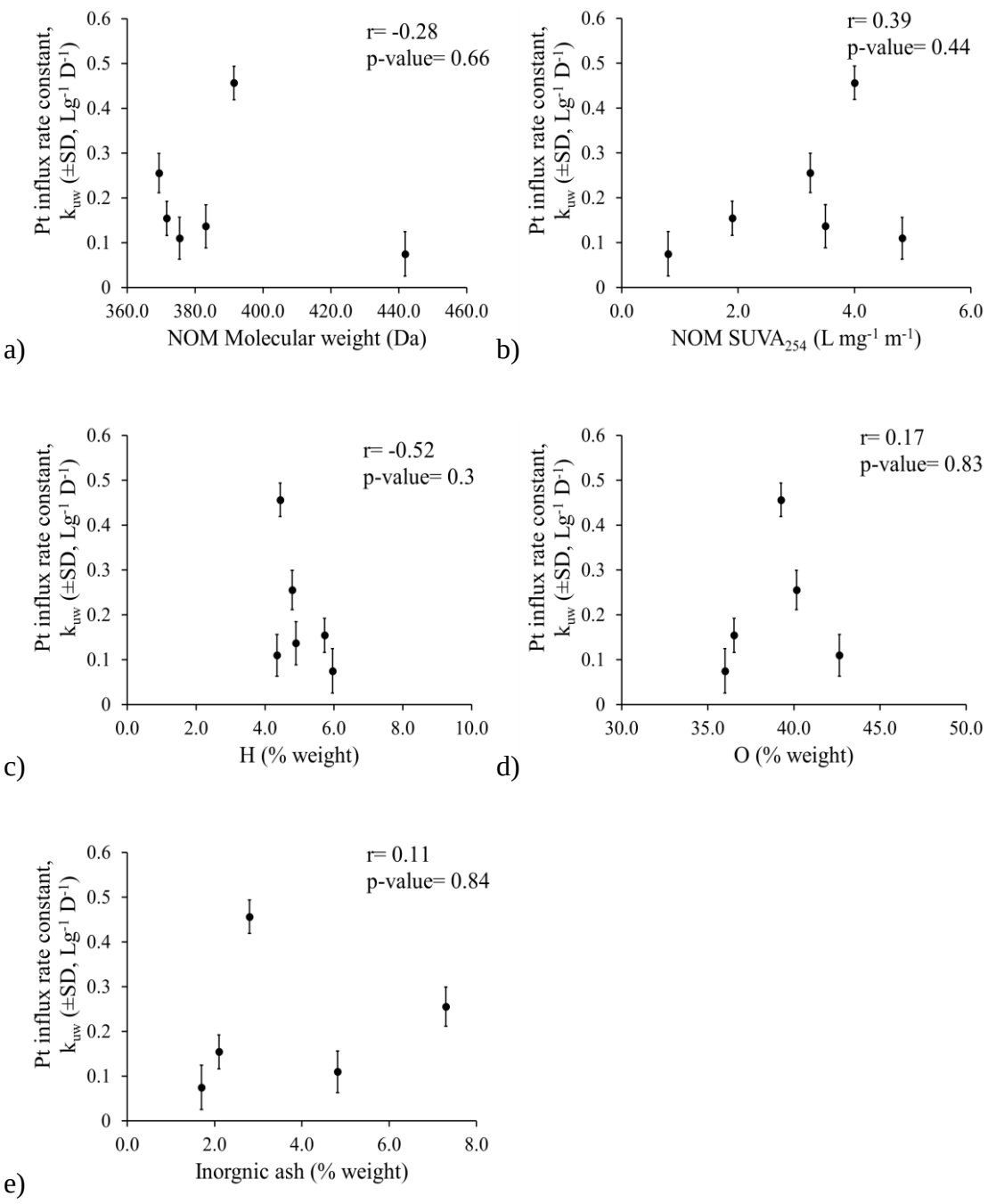

Figure E.3. Relation between (a) molecular weight, (b) $SUVA_{254}$, (c) H content, (d) O content, and (e) inorganic ash content of NOM with Pt influx rate constant, k_{uw} (L g^{-1} d^{-1}, ±SD) in *L.stagnalis* after waterborne exposure to 1 µg L^{-1} NP_{95} in presence of 1 mg L^{-1} NOM for 24 h. Each point represents mean Pt concentration for 8 individual snails (±SD).

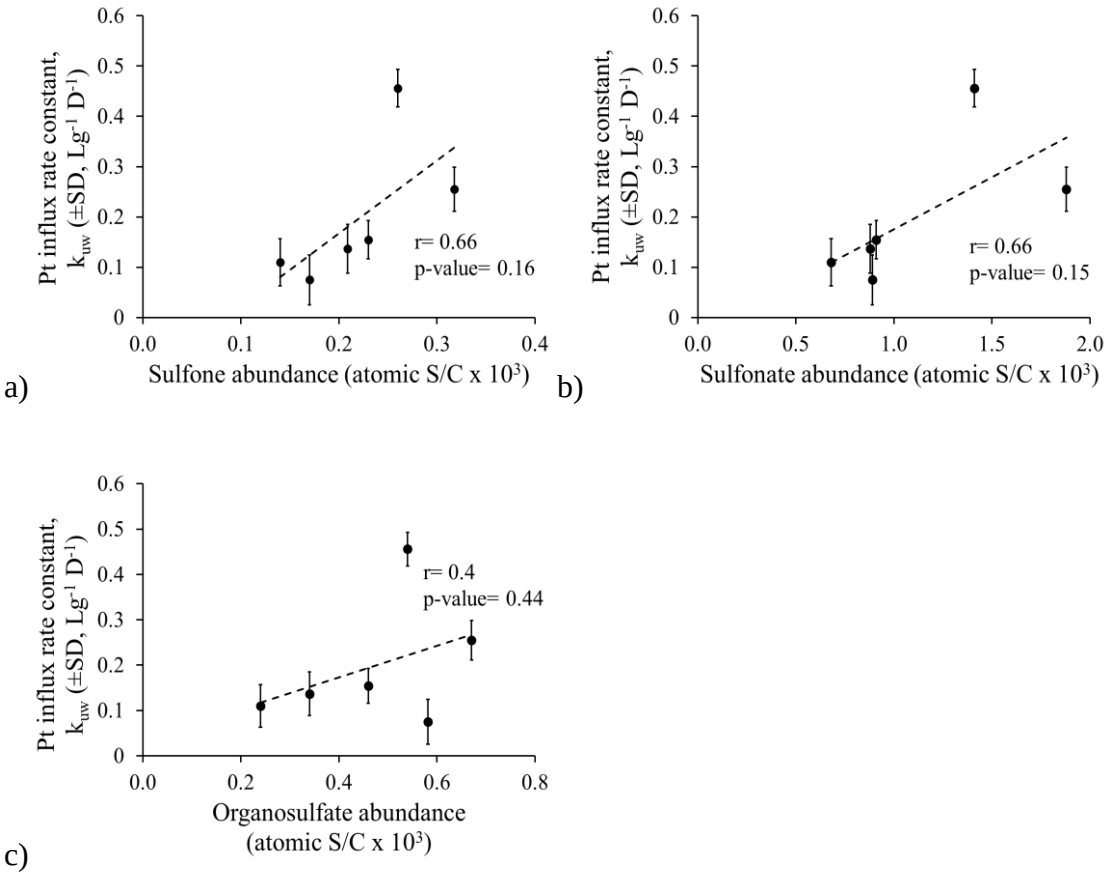

Figure E.4. Correlation between (a) Sulfone (SO_2), (b) Sulfonate (S_{SO_3}), and (c) Sulfate (S_{SO_4}) presented in NOM and Pt influx rate constant, k_{uw} (L g^{-1} d^{-1}, ±SD) in *L.stagnalis* after waterborne exposure to 1 µg L^{-1} $PtNP_{95}$ in presence of 1 mg L^{-1} NOM for 24 h. Each point represents mean Pt concentration for 8 individual snails (±SD).

APPENDIX F: LICENSE AGREEMENT FOR CHAPTER 2

APPENDIX G: LICENSE AGREEMENT FOR CHAPTER 3

APPENDIX H: LICENSE AGREEMENT FOR CHAPTER 4

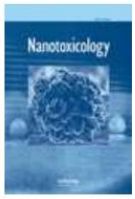

Title: Comparative study of dissolved and nanoparticulate Ag effects on the life cycle of an estuarine meiobenthic copepod, Amphiascus tenuiremis

Author: Mithun Sikder, , Emily Eudy, et al

Publication: Nanotoxicology

Publisher: Taylor & Francis

Date: May 28, 2018

Rights managed by Taylor & Francis

LOGIN

If you're a copyright.com user, you can login to RightsLink using your copyright.com credentials.

Already **a RightsLink user** or want to learn more?

Thesis/Dissertation Reuse Request

Taylor & Francis is pleased to offer reuses of its content for a thesis or dissertation free of charge contingent on resubmission of permission request if work is published.

BACK CLOSE WINDOW